

University of Nottingham
UK | CHINA | MALAYSIA

Improving Dual-Fuel Operation of Natural Gas-Diesel in Compression Ignition Engines under Low-Load Operating Conditions

Taufik Yuwono

Thesis submitted to the University of Nottingham

for the degree of Doctor of Philosophy

September 2022

Abstract

Battery electrified power is predicted to become the dominant mode of propulsion in future passenger cars. For long haul heavy duty transport challenges remain around practical range, payload and total cost. Currently there is no single economically viable decarbonised solution for heavy duty ground vehicles. On a global basis the internal combustion engine will continue to form part of the ideal future mix, in many cases using sustainable fuels and as part of a hybrid electric powertrain. The currently reported work was concerned with dual-fuel (diesel-natural gas/biogas) conversion of a heavy duty diesel engine, while retaining full diesel fall back capability. Such dual-fuel engines employ a small diesel pilot fuel to initiate turbulent combustion at multiple sites in a premixed gaseous fuel/air charge. One of the key challenges of such engines is slow and unstable combustion at typical part load cruising conditions, with the need to switch back to diesel mono-fuel operation to avoid misfires then incurring associated economic and pollutant (NO_x and soot) emissions penalties. An additional concern of dual-fuel operation is methane "slip", with the need to maintain a hot exhaust gas temperature (e.g. >380°C) when running on dual-fuel to ensure effective oxidation of methane via an additional catalyst.

The premise of the work was to improve understanding of a series of novel methods to improve performance of dual-fuel operation at lower engine loads in future heavy duty IC engines, with relevance to future trucks, marine and stationary power generation applications. Experimental work investigated the potential to decarbonise the pilot fuel via the adoption of gas to liquid synthetic diesel fuel, with particular focus on the problematic low load operation where the premixed combustion becomes unstable. Under relatively low gas substitution ratio (58%) it was found that the gas to liquid fuel performed with better pollutant emissions across the board (combustion efficiency increase of ~2%, with lower NO_x, unburned hydrocarbons, soot and carbon monoxide). It was apparent that this fuel has very good potential as a sustainable diesel substitution provided the fuel is readily available and manufactured appropriately (in commercial scale). Additional work was then concerned with the potential to employ cylinder deactivation as a means of elevating the firing cylinder gas pressures and temperatures at lower loads so as to allow yet lower brake loads to be achieved in dual-fuel mode. This analysis was undertaken using the commercial one dimensional simulation package GT-Power, with the modelling employing a dual-fuel variant of a quasi-dimensional combustion model and comparing cylinder deactivation to Miller cycle and part load throttling strategies. The simulation work demonstrated that the low load

dual-fuel limit could be effectively reduced from ~6 to ~3 bar brake mean effective pressure, with elevated exhaust gas temperatures via deactivation by up to 165°C (higher than 6-cylinders operation with throttling) to aid methane oxidation. It was concluded that the adoption of cylinder deactivation would be the most attractive option, especially when combined with electric supercharging as part of a mild hybrid architecture (with brake fuel economy improved by up to 4%). The modelling was then extended to consider the potential benefits of modern thermal barrier coatings applied within the combustion chamber, however only very modest reductions in wall heat transfer were observed (1-2%) at the light load conditions. In final work the benefits of exhaust water removal upon methane oxidation catalyst performance was theoretically evaluated. It was concluded that ~10.7%$_{vol.}$ water removal could be practically achieved through cooling-reheating process via a novel thermal battery arrangement, which could ultimately reduce the catalyst minimum operating temperature by ~60°C. Such an approach may be best suited to applications where additional weight is less critical such as stationary power generation or larger marine engines. Overall, of all the strategies investigated it was clear that cylinder deactivation can provide the best benefits in terms of increasing efficiency and producing higher exhaust gas temperature than conventional strategy in a relatively pragmatic manner.

Contents

Abstract i

Publication Related to This Research viii

Acknowledgements ix

Abbreviations x

Nomenclature xiv

Chapter 1 Introduction 1

1.1 Background 1

1.2 Technical Limitations of Dual-Fuel in Compression Ignition Engines 4

1.3 Aim and Objectives 5

1.4 Thesis Layout 6

Chapter 2 Literature Review 7

2.1 Introduction 7

2.2 Decarbonising The HDV Sector 7

2.3 Potential of Natural Gas for Decarbonising HDV with ICE 15

2.3.1 Properties of NG as fossil fuel 15

2.3.2 Biogas and Biomethane for HDV as Potential CO_2-Neutral Gas 18

2.3.3 Existing Natural Gas Utilisation in ICEs 20

2.4 Improving Compression Ignition Engine Efficiency and Emissions as a Pragmatic Heavy Duty Solution 23

2.4.1 NO_x and Soot Emissions from CI Engines 24

2.4.2 Lean Burn and Low Temperature Combustion Strategies in CI Engines 26

2.5 Diesel-Natural Gas Dual-Fuel as a Lean Burn Strategy in CI Engines 28

2.5.1 The Details of Dual-Fuel Operation of Natural Gas-Diesel 29

2.5.2 Variants of Dual-Fuel Strategies 30

2.5.3 Dual-Fuel Combustion Compared to SI Lean Burn TJI 32

2.5.4 Challenges in Dual-Fuel Combustion 32

2.6 Addressing Poor Combustion in Low Load Operating Conditions 34

2.6.1 Increasing pilot quantity (reducing substitution ratio) 35

2.6.2 Premixed Dual-Fuel Combustion (PDFC) 35

2.6.3 Throttling 36

2.6.4 Intake charge heating 36

2.6.5 Early or Late Intake Valve Closing (Miller Cycle) 37

2.6.6 Exhaust Gas Recirculation (EGR) 38

2.6.7 Cylinder Disablement by Cylinder Cut-out and Cylinder Deactivation (CDA) 40

2.7 The Challenges of Methane Oxidation Catalysis 41
2.8 Summary 43
Chapter 3 Experimental Setup 44
3.1 Introduction 44
3.2 Experimental Facilities 44
3.2.1 Light Duty Engine Test Rig 44
3.2.2 Heavy Duty Engine Test Rig 49
3.2.3 Measurement of Exhaust Gas Emission 58
3.3 Test Fuels 59
3.4 Data Post-Processing 60
3.4.1 Brake Mean Effective Pressure (BMEP) 60
3.4.2 Net Indicated Mean Effective Pressure (Net IMEP) 60
3.4.3 Combustion Stability Indicator 61
3.4.4 Heat Release Rate Calculation 61
3.4.5 Brake and Net Indicated Efficiency 62
3.4.6 Analysis of Exhaust Gas Emission 63
3.4.7 Combustion efficiency 65
3.5 Summary 66
Chapter 4 Phenomenological Modelling of Dual-Fuel Combustion in a Compression Ignition Engine 67
4.1 Introduction 67
4.2 Engine Model and Details 67
4.2.1 Intake and Exhaust Port 69
4.2.2 Intake and Exhaust Valves 71
4.2.3 Electric Supercharger (eSupercharger) and Its Driving Motor 73
4.2.4 Cylinder and Piston Cup Geometry 75
4.2.5 Deactivation Logic 76
4.2.6 Fuel injections 77
4.2.7 Thermal and Friction simulations 78
4.3 Combustion Modelling 79
4.4 Summary 81
Chapter 5 Gas-to-Liquid (GTL) and Diesel Fuel in Conventional Diesel Combustion and Premixed Dual-Fuel Combustion 83
5.1 Introduction 83
5.2 Test Conditions in The Light Duty Engine Test Rig 84
5.2.1 Conventional Diesel Combustion (CDC) Test Conditions in Light Duty Engine 84

5.2.2 Premixed Dual-Fuel Combustion (PDFC) Test Conditions in Light Duty Engine 85
5.3 Results and Discussion on Conventional Diesel Combustion Tests 85
5.3.1 Brake Efficiency by CDC with GTL and Diesel 85
5.3.2 In-cylinder pressure by CDC with GTL and Diesel 86
5.3.3 Net Heat Release Rate (NHRR) by CDC with GTL and Diesel 88
5.3.4 Mass Fraction Burned (MFB) by CDC with GTL and Diesel 91
5.3.5 Maximum Pressure Rise Rate (PRR) by CDC with GTL and Diesel 94
5.3.6 Mean Gas Temperature by CDC with GTL and Diesel 96
5.3.7 Combustion Stability by CDC with GTL and Diesel 98
5.3.8 Exhaust Gas Emission by CDC with GTL and Diesel 99
5.3.9 Combustion Efficiency by CDC with GTL and Diesel 103
5.3.10 Exhaust Gas Temperature by CDC with GTL and Diesel 105
5.4 Results and Discussion on PDFC with GTL and PDFC with Diesel as Pilot Fuel 106
5.4.1 Brake Efficiency by GTL-PDFC and Diesel-PDFC 106
5.4.2 In-cylinder Pressure by GTL-PDFC and Diesel-PDFC 106
5.4.3 Net Heat Release Rate (NHRR) by GTL-PDFC and Diesel-PDFC 107
5.4.4 Mass Fraction Burned (MFB) by GTL-PDFC and diesel-PDFC 109
5.4.5 Mean Gas temperature by PDFC with GTL and diesel 110
5.4.6 Pressure Rise Rate (PRR) by PDFC with GTL and Diesel as Pilot Fuel 110
5.4.7 Combustion Stability by GTL-PDFC and Diesel-PDFC 111
5.4.8 Exhaust Gas Emission by GTL-PDFC and diesel-PDFC 112
5.4.9 Combustion Efficiency by GTL-PDFC and Diesel-PDFC 113
5.4.10 Exhaust Gas Temperature by GTL-PDFC and diesel-PDFC 113
5.5 Summary 114
Chapter 6 The Effects of Cylinder Deactivation on Low Load Dual-Fuel Combustion 116
6.1 Introduction 116
6.2 Simulated Points and Implemented Strategies 116
6.3 Simulation Results at 1200 rpm/6 bar BMEP 119
6.3.1 Intake Manifold Pressure and Temperature at 1200 rpm/6 bar BMEP 119
6.3.2 Dynamic Compression Ratio and IVC in Miller-LIVC at 1200 rpm/6 bar BMEP 121
6.3.3 Individual Load of Firing Cylinder at 1200 rpm/6 bar BMEP 121
6.3.4 Efficiencies at 1200 rpm/6 bar BMEP 123
6.3.5 In-cylinder Pressure and Heat Release Rate at 1200 rpm/6 bar BMEP 124
6.3.6 In-cylinder Pressure and Heat Release Rate at 1200 rpm/6 bar BMEP/λ=1.0 127
6.3.7 Mean Gas Temperature at 1200 rpm/6 bar BMEP/λ=1.0 128
6.3.8 Combustion-Related Parameters at 1200 rpm/6 bar BMEP 129

6.3.9 Maximum Pressure Rise Rate at 1200 rpm/6 bar BMEP 131
6.3.10 Engine Heat Loss at 1200 rpm/6 bar BMEP 132
6.3.11 Exhaust Gas Temperature at 1200 rpm/6 bar BMEP 133
6.4 Simulation Results at 1200 rpm/3 bar BMEP 134
6.4.1 Impact of Simulated Strategies upon Intake Parameters at 1200 rpm/3 bar BMEP 134
6.4.2 Net IMEP and PMEP at 1200 rpm/3 bar BMEP 136
6.4.3 Brake Efficiency and Fuel Economy at 1200 rpm/3 bar BMEP 137
6.4.4 In-cylinder pressure and Heat Release Rate at 1200 rpm/3 bar BMEP 138
6.4.5 Mean Gas Temperature at 1200 rpm/3 bar BMEP 140
6.4.6 Combustion Parameters at 1200 rpm/3 bar BMEP 141
6.4.7 Engine Heat Loss at 1200 rpm/3 bar BMEP 143
6.4.8 Exhaust Gas Temperature at 1200 rpm/3 bar BMEP 144
6.5 Summary 145
Chapter 7 Thermal Barrier Coating (TBC) on Piston and Cylinder Head Surface in Dual-Fuel Combustion 147
7.1 Introduction 147
7.2 Simulation Setting of Dual-Fuel Combustion with TBC 147
7.3 Simulation Results of Dual-Fuel with TBC at 1200 rpm/6 bar BMEP/λ=1.2 148
7.3.1 Changes to The Intake Charge via TBCs at 1200 rpm/6 Bar BMEP 149
7.3.2 Changes to In-cylinder Pressure, Mean Gas Temperature and Heat Transfer at 1200 rpm/6 bar BMEP 150
7.3.3 Combustion Parameters during Dual-Fuel with TBC at 6 bar BMEP 151
7.3.4 Changes of Cylinder Wall Heat Loss by TBC at 1200 rpm/6 bar BMEP 152
7.3.5 Changes in Net IMEP and BMEP by TBCs at 1200 rpm/6 bar BMEP 154
7.3.6 Changes in Exhaust Gas Temperature by TBCs at 1200 rpm/6 bar BMEP 155
7.4 Simulation Results of Dual-Fuel with TBCs at 1200 rpm/3 bar BMEP 156
7.4.1 Changes of The Intake Trapped Mass and Air/Fuel Ratio by Application of TBC at 1200 rpm/3 bar BMEP 156
7.4.2 Changes of The In-cylinder Pressure, Mean Gas Temperature and Crank-Angle Resolved Heat Transfer Changes by TBCs at 1200 rpm/3 bar BMEP 157
7.4.3 Combustion Parameter by Dual-Fuel with TBCs at 3 bar BMEP 158
7.4.4 Changes of Cylinder Wall Heat Loss and Exhaust Gas Temperature by TBCs at 1200 rpm/3 bar BMEP 159
7.4.5 Changes in Net IMEP and BMEP by TBCs at 1200 rpm/3 bar BMEP 160
7.4.6 Changes to Exhaust Gas Temperature by TBCs at 1200 rpm/3 bar BMEP 161
7.5 Summary 162

Chapter 8 Thermodynamic Modelling of Water Removal in Exhaust Gas of Dual-Fuel Combustion 164
8.1 Introduction 164
8.2 Experimental Data for The Thermodynamic Modelling 164
8.3 Cooling and Reheating with PCMs Heat Exchanger as a Thermal Battery 166
8.3.1 Heat Transfer during the Cooling Process 167
8.3.2 Heat Transfer during the Reheating Process 168
8.3.3 Simulated Parameters of the Direct Cooling and Reheating of Exhaust Gas with PCMs 169
8.3.4 Simulation Results of the Direct Cooling and Reheating of Exhaust Gas with PCMs 170
8.4 Simulation of Water Removal Process with Inverted Brayton Cycle and PCM Thermal Battery 171
8.4.1 Processes Calculation 172
8.4.2 Results and Discussion of Water Removal with IBC 175
8.5 Summary 180
Chapter 9 Conclusions and Recommendations for Future Work 182
9.1 Conclusions 182
9.1.1 CDC with Diesel or GTL and PDFC with Diesel or GTL as A Pilot Fuel 183
9.1.2 Dual-Fuel Simulation with Cylinder Deactivation 184
9.1.3 Thermal Barrier Coating (TBC) Strategy in Dual-Fuel Combustion 188
9.1.4 Exhaust Gas Water Removal Process 188
9.2 Recommendations for Future Work 189
Appendix A Formulas for Calculating Humidity and Exhaust Gas Properties 192
A.1 Water Vapour Pressure and Water Vapour Pressure at Saturation 192
A.2 Saturation Humidity Ratio 193
A.3 Dew Point temperature 194
A.4 Specific Heat (Cp) and Constant (R) of Gas Mix 195
References 197

Publication Related to This Research

A. Hegab, T. Yuwono, A. Cairns, J. Hall, R. Cracknell, The effects of cylinder deactivation in future hybridised biogas dual fuel trucks, in: Powertrain Syst. Net-Zero Transp., Institution of Mechanical Engineers, London, 2021.

Acknowledgements

Firstly, I would like to offer my sincere gratitude to Prof. Alasdair Cairns, the Head of Powertrain Research Centre at the University of Nottingham for his patience, encouragement, continuous supports and guidance throughout this research project. My gratitude also goes to the University of Nottingham for allowing to use the experimental and modelling facility.

Secondly, I would like to acknowledge funding for this PhD study from Government of The Republic of Indonesia through RISET-Pro scholarship. I also appreciate the supports from all staffs in the Project Management Office of Riset-Pro and colleagues in BPPT and BT2MP.

Thirdly, I would like to thank Abdo Hegab who introduced me to the green engine and being a helpful colleague in the test cell. Thanks also to Mike McGhee for supporting me in the laboratory in early part of my PhD. I am so grateful for the work of technicians in our laboratory, John Lane and Nigel Sykes. My gratitude also goes to Prof. Paul Shayler who guided me during first year of my PhD prior to his retirement. I thank Nino La Rocca to guide me in early time working in the laboratory and for the supports in the meetings. My thanks also go to all member of Powertrain Research Centre for being good colleagues and nice friends.

Fourthly, I acknowledge support from Shell UK, Ltd that provide the GTL fuel for the experimental tests in this research. I also acknowledge support from nmRC of the University of Nottingham to allow me using the microscope facility.

Last but not least my sincerest gratitude and love to my beloved wife, children, my sister, my mother and all family members who have supported me throughout this period of study. I always remember my late father (Allahuyarham) who encouraged me to pursue a higher education and give contribution to the world of science. I am also appreciative to a warmth relationship from friends within PeDLN during my living at Nottingham.

Abbreviations

AFR	Air/Fuel Ratio
ATDC	After Top Dead Centre
ATDCF	After Top Dead Centre of Firing
BDC	Bottom Dead Centre
BEV	Battery Electric Vehicle
BMEP	Brake Mean Effective Pressure
BSOC	Battery State of Charge
BSCO	Brake Specific Carbon Monoxide
BSHC	Brake Specific Hydrocarbon
$BSNO_x$	Brake Specific Oxides of Nitrogen
BTDC	Before Top Dead Centre
BTE	Brake Thermal Efficiency
CA	Crank Angle
CCS	Carbon Capture and Storage
CDA	Cylinder Deactivation
CDC	Conventional Diesel Combustion
CDF	Conventional Dual-Fuel
CNG	Compressed Natural Gas
CO	Carbon Monoxide
CO_2	Carbon Dioxide
$COV_{IMEPNet}$	Coefficient of Variance in Net Indicated Mean Effective Pressure (%)
CI	Compression Ignition
CIDI	Compression Ignition Direct Injection
CLD	Chemiluminescence Detector
CNG	Compressed Natural Gas
DDI	Dual Direct Injection
DF	Dual-Fuel
DI	Direct Injection
ECE	Economic Commission for Europe
ECU	Engine Control Unit
EGR	Exhaust Gas Recirculation
EGT	Exhaust Gas Temperature
EIVC	Early Intake Valve Closing

ELR	European Load Response
EOC	End of Combustion
ESC	Engine Steady Cycle
EU	European Union
FC	Fuel Cell
FCU	Fuel Conditioning Unit
FID	Flame Ionisation Detector
FMEP	Friction Mean Effective Pressure
FMS	Fuel Measurement System
FPEG	Free Piston Energy Generator
FSN	Filter Smoke Number
GCV	Gross Calorific Values
GDI	Gasoline Direct Injection
GHG	Greenhouse Gas
GHSV	Gas Hourly Space Velocities
GTL	Gas-to-Liquid
GWP	Global Warming Potential
HAJI	Hydrogen Assisted Jet Ignition
HC	Hydrocarbon
HCCI	Homogeneous Charge Compression Ignition Engine
HD	Heavy Duty
HDV	Heavy Duty Vehicle
HEV	Hybrid Electric Vehicle
HFID	Heated Flame Ionisation Detector
HPDI	High-Pressure Direct Injection
HRR	Heat Release Rate
IBC	Inverted Brayton Cycle
ICE	Internal Combustion Engine
IMEP	Indicated Mean Effective Pressure
IVC	Intake Valve Closing
NDIR	Non-Dispersive Infra-Red
LHV	Lower Heating Value
LIVC	Late Intake Valve Closing
LNG	Liquified Natural Gas

LTC	Low-Temperature Combustion
LTHR	Low Temperature Heat Release Rate
MFB	Mass Fraction Burned
MFB50	50% of Mass Fraction Burned
MJI	MAHLE Jet Ignition
MN	Methane Number
MOC	Methane Oxidation Catalyst
Mtoe	Million Tonnes of Oil Equivalent
NDRS	Non-dimensional Rig Swirl
NEDC	New European Driving Cycle
NHRR	Net Heat Release Rate
NO	Nitric Oxide
NO_x	Oxide of Nitrogen
OCE	Off-Cycle Emission
PCCI	Premixed Charge Compression Ignition
PCM	Phase Change Material
PDFC	Premixed Dual-Fuel Combustion
PEMS	Portable Emission Measurement System
PFI	Port Fuel Injected
PM	Particulate Matter
PMEP	Pumping Mean Effective Pressure
PN	Particulate Number
PRR	Pressure Rise Rate
RCCI	Reactivity Controlled Compression Ignition
RCEM	Rapid Compression Expansion Machine
RDE	Real Driving Emissions
RON	Research Octane Number
SI	Spark Ignition
SOC	Start of Combustion
SOI	Start of Injection
SOI_{Main}	Start of Injection of main fuel injection
TBC	Thermal Barrier Coating
TDC	Top Dead Centre
THC	Total Hydrocarbon

TJI	Turbulent Jet Ignition
TTW	Tank-to-Wheel
UHC	Unburned Hydrocarbon
UK	United Kingdom
ULSD	Ultra-Low Sulphur Diesel
UN	United Nations
WHSC	World Harmonised Steady Cycle
WHTC	World Harmonised Transient Cycle
WHVC	World Harmonised Vehicle Cycle
WLTP	World Harmonised Light Vehicle Test Procedure
WMEP	Work-loop Mean Effective Pressure
WOT	Wide Open Throttle
WTT	Well-to-Tank
WTW	Well-To-Wheel

Nomenclature

AFR_{st}	Stoichiometric air/fuel ratio (-)
barA	bar (Absolute)
barG	bar (Gauge)
u_{gas}	Respective constant of exhaust gas constituent for emission calculation
CA50	Location of 50% of mass fraction burned (°CA)
Cf	Flow coefficient (-)
c_{gas}	concentration of exhaust gas constituent (ppm)
COV_{IMEP_N}	Coefficient of Variance in Net Indicated Mean Effective Pressure (%)
$c_{CO,d}$	Dry CO concentration (% or ppm, specified in the equation)
$c_{CO2,d}$	Dry CO_2 concentration (%)
c_v	Specific heat at constant volume (kJ/kg.K)
c_p	Specific heat at constant pressure (kJ/kg.K)
Cv	Valve flow coefficient (-)
C/H	Carbon to hydrogen ratio
gCO_2e	Gram of CO_2 equivalent
H_a	Intake air humidity (g water per kg dry air)
H_2	Hydrogen
$\overline{IMEP_N}$	Mean net IMEP
k_w	dry to wet correction factor in exhaust gas emission calculation
k_{hD}	correction factor for humidity in NO_x emission calculation
$\dot{m}$	Mass flowrate (kg/s)
$\dot{m}_{air,wet}$	Air mass flowrate in wet basis (kg/s)
$\dot{m}_{exh}$	Exhaust mass flowrate (kg/s)
$\dot{m}_{fuel}$	Fuel mass flowrate (kg/s)
M_{exh}	Molar mass of exhaust gas (g/mol)
M_{gas}	Molar mass of gas (g/mol)
NH_3	Ammonia
Pd	Palladium
Pt	Platinum
p_w	Water vapour partial pressure (kPa or hPa, specified next to the equation)

p_{ws}	Saturation of water vapour (kPa)
Zr	Zirconia
Q_g	Gross heat release (J)
Q_n	Net heat release (J)
Q_{ht}	Heat transfer rate (J)
$\dot{Q}_{reheat,required}$	Required heat rate for reheating the gas ($\dot{Q}_{reheat,required}$) to achieve the working temperature of corresponding PCM (W)
$\dot{Q}_{stored}$	The rate of stored heat (W)
r_c	Compression ratio
r_t	Expansion ratio
$r_{M_{H2O}/M_{gas}}$	Mole ratio of water to dry exhaust gas (-)
R	Gas constant (J/g.K)
$\widetilde{R}$	Uuniversal gas constant (8.3143 J/mol.K)
Rh	Rhodium
T_d	Dew point temperature (°C)
$T_{gas,in}$	Gas temperature at the inlet of PCM HE (°C)
$T_{gas,out}$	Gas temperature at the outlet of PCM HE (°C)
$T_{PCM\ HE}$	Working temperature of PCM HE (°C)
T_M	Melting temperature of PCM (°C)
T_{50}	Temperature required to convert 50%$_{vol.}$ of methane within MOC (°C)
V	Volume (m^3)
V_S	cylinder swept volume (m^3)
$\dot{W}_C$	Power consumption of IBC compressor (W)
$\dot{W}_T$	Power generated by IBC turbine (W)
$W_{c,i,Net}$	Net indicated work of a cylinder (J)
W_{humid}	Humidity ratio ($kg_{water}/kg_{dry\ gas}$)
$W_{saturation}$	Saturation humidity ratio ($kg_{water}/kg_{dry\ Gas}$)
$[CO_{2,int}]$	Concentration of intake CO_2 (%)
$[CO_{2,exh}]$	Concentration of exhaust CO_2 (%)
$[CO_{2,exh}]$	Concentration of CO_2 in the ambient air (%)
%$_{mass}$	Percentage by mass
%$_{vol.}$	Percentage by volume
α	Molar ratio of hydrogen to carbon in fuel

γ	Ratio of specific heats (c_p/c_v)
γ_s	Molar ratio of sulphur to carbon in fuel
δ	Molar ratio of nitrogen to carbon in fuel
ε_{HE}	Heat exchanger effectiveness (%)
ε	Molar ratio of oxygen to carbon in fuel
η_c	Isentropic efficiency of the IBC compressor
η_t	Isentropic efficiency of the IBC turbine
θ	Crank angle (°CA)
σ_{IMEP_N}	Standard deviation of the collected Net IMEP data
λ	Air/fuel equivalence ratio (-)
λ_{CNG}	Air/fuel equivalence ratio in CNG basis
ϕ	Fuel/air equivalence ratio (-)

Chapter 1 Introduction

1.1 Background

Local air pollution and climate change are global concerns that requires appropriate response from the stakeholder of automotive industry. Governments in some regions such as the European Union have been tightening the limits of local emissions and assessing more precise measuring methods such as real driving emissions. On 27 June 2019, the UK passed law to commit to reducing greenhouse gas emissions to net-zero by 2050 across all sectors. In the UK, Heavy Duty Vehicles (HDV) and buses contributed around 21% of transport related CO_2 emissions [1]. Meanwhile, HDV in the EU as per 2019 represented 6% of total CO_2 emissions and 25% of road transport emissions [2]. As of 2019, both the UK government and European Commission regulate HDVs to emit a maximum CO_2 target which is set to achieve 15% CO_2 reduction from HDVs by 2025 [3,4]. The UK government set the percentage of reduction relative to average CO_2 emissions by HDVs in 2015 while the EU would use the average value during 1 July 2019–30 June 2020 as a reference. In addition, the EU government planned 30% reduction by 2030 that will be reviewed in 2022. Such ambitious targets require innovative solutions to decarbonise future HDVs.

In recent decades, the automotive industry has been developing Hybrid Electric Vehicles (HEV) and Battery Electric Vehicles (BEV) as lower carbon powertrains. Governments in many countries have been supporting the trend with several policies by giving incentives, tax reduction and implementing low carbon areas (zones) within metropolitan cities. However, so far only the passenger car segment has chosen electrification at mass scale as a reasonable medium-term option. The electrification of the HDV sector remains limited due to several reasons. Heavy weight and large volume of the required battery pack takes a large amount of a typical HD vehicle's payload and space, hence reducing its ability to carry payload. In a recent simulation by Smallbone *et al.* [5] that modelled HDVs with BEV and diesel under World Harmonised Vehicle Cycle (WHVC), showed that the gravimetric and volumetric density of BEV are respectively heavier by 4.15 times (in kg/km) and larger by 4.53 times (in L/km) than diesel HDV. By simulating the operating range from 100 to 500 km, the longer the usage the bigger the difference of densities between BEV and diesel. In other words, longer range of BEV requires heavier battery that reduces the payload. From the simulation of GHG emission by HDVs, its simulation of 500-tonne HDV with BEV using EU electrical mix produced net CO_2 emission by five times of diesel-HDV. In another study by Sacchi et al. [6] that simulated a 40-ton HDV, BEV was reported as a viable option for decarbonising urban delivery (150 km) since 2020. However,

BEV for regional delivery application (400 km) in 2020 produced 24% worse GHG than diesel HDV and just produced less GHG (by 7%) in 2030. In the simulation for long haul (800 km) delivery, BEV application in 2020 and 2030 resulted 168% and 38% higher GHG but then resulted 22% lower GHG in 2050. These studies suggest that Internal Combustion Engine (ICE) is still a favourable option for decarbonising HDV, especially in countries where the electricity mix results worse GHG emission than Europe.

Using lower carbon fuel is an option to reduce CO_2 emission from the ICE. Natural Gas (NG) with lower C/H ratio than diesel and gasoline is a highly potential candidate for decarbonising HDV. Natural gas has been used in the Spark Ignition (SI) engines for many decades. However, the NG-SI engine is typically less efficient than the Compression Ignition (CI) engine due to intake throttling to control the air/fuel ratio and limitations in geometric compression ratio. A CI engine can also use NG in dual-fuel mode, where NG that is injected into the intake port or directly injected into the cylinder is ignited by the in-cylinder direct injected diesel (acting as a pilot fuel). NG with its high-octane rating benefits high compression ratio of the CI engine and multiple ignition source by diesel auto-ignition that provides higher turbulence within combustion chamber [7].

Running a CI engine with NG in dual-fuel mode is not a new concept. Germany used such a strategy during the second world war for the stationary engine. However, increasing oil production and its storage practicality could not compete with diesel fuel [8]. Not only from the technical perspective, natural gas becomes more attractive due to increasing global stock since shale gas discovery in the US [9] and predominantly cheaper than diesel in the recent decade [10]. The recent improvement in LNG storage in a relatively small size for HDV applications has resulted in dual-fuel becoming more applicable. Therefore, dual-fuel of NG-diesel could be a good strategy for decarbonising the HDV sector, especially if combined with biomethane.

One of the few dual-fuel technologies that has been commercially produced is the Volvo dual-fuel engine utilising High-Pressure Direct Injection (HPDI) developed in collaboration with Westport Fuel Systems. In the HPDI system, high pressure natural gas is injected directly into the cylinder immediately after a small quantity of pilot diesel injection. The diesel injection is typically not designed to perform the maximum pressure of the latest injection technology for diesel combustion. Thus, it has eliminated the full potential of diesel single fuel functionality and is limited to being a dedicated dual-fuel setup without full diesel fall back (which remains problematic with currently limited NG infrastructure). Ideally, changing a CI engine to run in dual-fuel mode needs to provide flexibility to revert back to diesel-only operation with

remaining emissions compliance. Therefore, the current reported work has focused upon port injected dual-fuel to attract the market that operates it in areas with rare NG infrastructure.

Methane as the main content of NG is not only available as fossil-fuel, but also could be produced as biogas. Biogas is the product of several natural processes such as anaerobic digestion of organic materials, solid waste decomposition in landfill, and wastewater treatment [11]. Methane content in biogas ranges from 45 to 75 % volume with the remaining gases mainly CO_2 and the other gases in small percentages. It can be upgraded to produce biomethane with more than 95% methane content, hence can be transmitted via the NG grid or directly used for ICE vehicles. Biomethane can also be produced via the biomass gasification process. Biogas and biomethane utilisation in the ICE not only reduces CO_2 emissions, but also contributes to the net-zero CO_2 strategy. GHG emission by dual fuel was investigated in a study by CENEX [12] through trial monitoring of several HDVs with diesel, NG-SI and HPDI where HPDI-HDV using liquid biomethane resulted in lower GHG emission by 76% relative to diesel. From the perspective of biogas potential, International Energy Agency [11] showed that in 2018 the global actual production of biogas and bio-methane was 35 Million Tonnes of Oil Equivalent (Mtoe) while biogas potential was 570 Mtoe and the biomethane potential was 730 Mtoe. This suggests that dual-fuel operation with biomethane could be an advanced strategy to achieve net-zero GHG in 2050 as committed to by the UK and EU governments [4] albeit currently not widely proposed.

The other potential of dual-fuel combustion is NO_x and soot emissions reductions compared to diesel-only operation [13–18]. These two emissions have remained a key problem in diesel combustion. In the heterogeneous air/fuel mixture of diesel injection, the locally leaner mixture at high temperature forms NO_x while the locally richer mixture forms soot. Once formed, NO_x cannot be reduced by any in-cylinder strategy. Meanwhile, the formed soot in the early stage of combustion could be oxidised in the subsequent combustion stage. However, the remaining non-oxidised soot exits the cylinder as an exhaust gas constituent. Both could be significantly reduced through exhaust after-treatment processes to achieve the allowable limits of tailpipe emissions. However, the process requires high cost for catalyst reactant materials, production and maintenance. Substituting diesel fuel with NG in dual-fuel operation can reduce the heterogeneity of the air/fuel mixture. Therefore, running a CI engine in dual-fuel mode at lower combustion temperatures could improve NO_x and soot emissions.

1.2 Technical Limitations of Dual-Fuel in Compression Ignition Engines

Dual-fuel burns the fuels in two different combustion types: auto-ignition of pilot diesel fuel and flame propagation of the premixed air-gas mixture. In a certain condition, it involves the auto-ignition of premixed natural gas. It typically has two main challenges: knocking at high load and poor combustion stability at low load. The rich mixture and high temperature at high load operating conditions cause the gas to auto-ignite prior to the flame propagation, resulting in abrupt and rapidly oscillating pressure events that indicates the knocking phenomenon. If left unchecked this can lead to catastrophic engine damage and the oscillating pressure events damage the in-cylinder structures. On the other hand, at low load operating conditions, a lean fuel/air mixture and low in-cylinder temperature decrease the turbulent flame speed with hence progressively deteriorating combustion stability. At the lowest loads this results in partial or complete misfire and high unburned fuel emissions. Solving the problem of dual-fuel at low load is important as even large trucks spend considerable time operating at lower loads in urban environments. The frequency of operating speed-load range during the World Harmonised Transient Cycle (WHTC) for a Volvo D8 engine is shown in *Figure 1.1*, which would be representative of the powertrain used in a typical small to medium sized urban delivery truck (such trucks typically represent >80% of new UK truck sales). The range with larger bubbles indicates more frequent operation. From the analysis, the load from 0 to 9 bar BMEP covers 57% of the loaded condition.

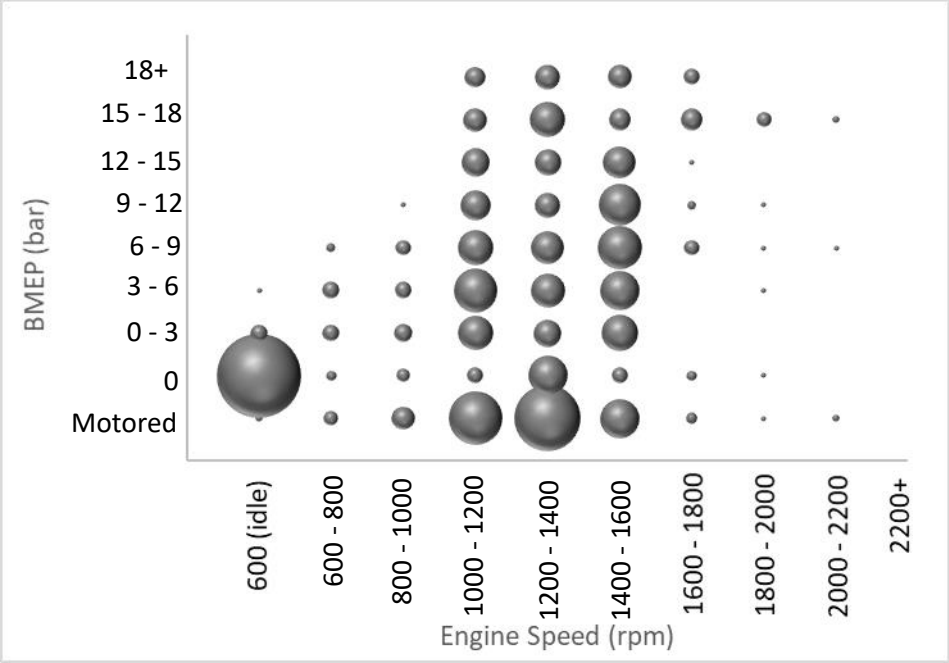


Figure 1.1. Bubble chart showing the frequency of engine operation at certain speed - load range by Volvo Penta D8 engine during World-harmonised Transient Cycle (WHTC)

The unburned fuel in dual-fuel is mostly dominated by methane as the main constituent of natural gas, thus it is referred to as 'methane slip'. Apart from poor combustion performance at low load, the blowby of the premixed gas into the crevice volumes during the compression stroke is another key contributing factor to methane slip [19]. As the in-cylinder pressure decreases, the trapped gas flows back to the cylinder during the expansion stroke then leaves the cylinder unburned. The mechanism happens at any (low to high) operating load of dual-fuel. Methane is a greenhouse gas with 25 times the impact factor in Global Warming Potential within a 100 years period (GWP-100) compared to CO_2 [20]. Therefore, high methane slip by dual-fuel could result in higher total GHG emissions (in CO_2-equivalent) than diesel combustion and negates the CO_2 reduction benefit. With the serious impact of methane slip, its promoting factor by poor combustion quality and crevice volume of dual-fuel combustion should be addressed in order to be a viable solution for decarbonising the HDV sector. All of this neglects the methane losses in the fuel production process, albeit this becomes much less relevant if the strategy is to capture fugitive methane in the future and/or switch at large scale to biomethane.

1.3 Aim and Objectives

The strategy to mitigate methane slip in lower load requires several factors that improve combustion quality. Meanwhile, without changes in piston-ring-cylinder geometry, mitigation of methane slip by the crevice volume requires aftertreatment via a Methane Oxidation Catalyst (MOC). In order to work efficiently, the MOC requires higher temperatures than the other emission catalysts. Therefore, to support the oxidation process in the MOC, the implemented strategy in dual-fuel combustion needs to produce exhaust gas with high temperature (which is counter-intuitive in the backdrop of maximising thermal efficiency).

The currently reported study aims to improve dual-fuel combustion performance and increase the exhaust temperature at low load operating conditions as well as promote the oxidation process in the MOC. This must be achieved while maintaining high thermal efficiency. Experimental engine testing and simulations were conducted with several key objectives:

1. Define the impact of gas-to-liquid (a synthetic diesel fuel from natural gas) as an alternative pilot fuel with respect to performance and emissions
2. Determine the effects of cylinder deactivation strategies on efficiency and exhaust gas temperature with several intake control strategies used to reduce the air/fuel equivalence ratio (λ), including Miller cycle, external Exhaust Gas Recirculation (EGR) and conventional throttling

3. Identify the impact of novel thermal barrier coatings on the piston surface heat transfer, engine efficiency and exhaust gas temperature
4. Assess the impact of the inverted Brayton cycle process and direct cooling/reheating to remove water content to improve the efficiency of the methane oxidation process at lower gas temperature

1.4 Thesis Layout

This thesis consists of 9 main chapters that covers the whole work conducted which aims to mitigate the methane slip in dual fuel combustion by improving low load performance and producing high exhaust gas temperature to support oxidation process within MOC. In Chapter 1 the background of dual-fuel engine operation is introduced leading into project objectives. Presented in Chapter 2 is a summary of the literature reviewed, discussing previous studies and several topics relevant to the objectives. Set out in Chapter 3 are details of the experimental setup including the experimental apparatus, test methodology and calculations in the data analysis. Described in Chapter 4 are details of the engine model developed for simulating dual-fuel combustion under cylinder deactivation and conventional operation with several intake control strategies.

Chapter 5 incorporates the effects of Gas-to-Liquid (GTL) fuel as alternative fuel in conventional diesel and the dual-fuel combustion compared with Ultra Low Sulphur Diesel (ULSD) as a baseline fuel. Discussed in Chapter 6 are the simulation results of cylinder deactivation strategy compared to normal operation. Chapter 7 includes the simulation results of dual-fuel in thermal barrier coating on piston and cylinder head surface compared to the standard engine model. Chapter 8 incorporates discussion on the thermodynamic models of the exhaust gas water removal system including the analysis and discussion.

Finally, a summary is presented in Chapter 9 including conclusions of the experimental and simulation results as an integrated contribution to solve the problems in dual-fuel combustion. Several potential topics for further development are discussed in the recommendation sub-section to suggest future research of methane slip mitigation in dual-fuel CI engines.

Chapter 2 Literature Review

2.1 Introduction

Set out in the following chapter is a review of the relevant prior work in the field of dual-fuel (diesel-natural gas) engine operation, presented within six sub-sections. The first sub-section incorporates a discussion of the key options currently available to decarbonise the Heavy-Duty Vehicle (HDV) sector. The second presents natural gas as a potential candidate fuel for decarbonisation and current commercially established combustion methods for natural gas end use in the Internal Combustion Engine (ICE). The third describes emissions challenges in Compression Ignition (CI), including some alternative combustion strategies. The fourth includes details of dual-fuel combustion of natural gas, when utilising diesel as the pilot fuel. The fifth incorporates a review of methods to address poor combustion performance under low load dual-fuel operating conditions. The sixth describes the challenges in the methane oxidation process within currently available aftertreatment devices. Finally, highlights of each sub-section and potential novel methods for the improvement of dual-fuel combustion are presented.

2.2 Decarbonising The HDV Sector

Innovation in ICE technology and operation has largely governed the direction of the transport sector. From the outset of modern and affordable automobiles, pioneered by Ford and others [21], the ICE displaced range-limited electric alternatives and was mass adopted for passenger cars, heavy-duty vehicles, rail and marine transport [22]. Early advancements were largely focused upon performance and cost. However, as the absolute number of vehicles increased rapidly, attention shifted from the 1970s onwards to degradation in air quality, concerns over diminishing fuel reserves and (relatively more recently) climate change due to the greenhouse effect predominately associated with tailpipe CO_2. Pollutant emissions legislation and fleet averaged fuel consumption targets have since rapidly evolved. Set out below in *Table 2.1* is a summary of the recent history of tightening passenger car emissions legislation within Europe, with the early focus upon CO_2 (albeit targets rather than enforcements) and pollutants including CO, unburned hydrocarbons, NO_x and most recently soot/particulates which is expressed in Particulate Matter (PM) and Particulate Number (PN). From the late 1990s until very recently, diesel engines were rapidly adopted across Europe (above 50% of sales in some states [23]), due to favourable performance, improved fuel consumption and lower CO_2, with additional focus on particulate emissions. However, since the 'dieselgate' NO_x emissions scandal in late 2015 the diesel has rapidly fallen out of favour for passenger cars, with shift towards increased gasoline

[23]. However, particulate emissions from gasoline engines are under growing scrutiny due to their adverse health effects (especially relevant to the high number of smaller sized particles which can penetrate deeper within the human body). The problems of the dieselgate scandal were compounded by the relatively 'gentle' assessments of emissions in Europe, with the New European Drive Cycle resulting in overly optimistic fuel consumption and pollutants relative to real world driving and allowing non-optimal operation of the aftertreatment at higher engine speeds and loads [24]. As such, over the last four years, attention has turned to the establishment of real driving assessments within Europe via the so-called Real Driving Emissions (RDE) test. The RDE test, together with the World Harmonised Light Vehicle Test Procedure (WLTP) are now mandatory [25].

			EU-1	EU-2	EU-3	EU-4	EU-5a	EU-5b	EU-6b	EU-6c
			1992	1996	2000	2005	2009	2011	2014	2017
Test Cycle:			ECE 15.03	ECE 15.04	NEDC	NEDC	NEDC	NEDC	NEDC	WLTC
Positive Ignition Engines (Gasoline)	CO	mg/km	2720	2200	2300	1000	1000	1000	1000	1000
	HC	mg/km			200	100	100	100	100	100
	HC+NOx	mg/km	970	500						
	NOx	mg/km			150	80	60	60	60	60
	NMHC	mg/km					68	68	68	68
	PM only GDI	mg/km					5	4.5	4.5	4.5
	PN	#/km							6E+12	6E+11
Compression Ignition Engines (Diesel)	CO	mg/km	2720	1000	640	500	500	500	500	500
	HC+NOx	mg/km	970	700	560	300	230	230	170	170
	NOx	mg/km			500	250	180	180	80	80
	PM	mg/km	140	80	50	25	5	4.5	4.5	4.5
	PN	#/km						6E+11	6E+11	6E+11
			no change			change			important	

Table 2.1. Changes in emission limits for each stage of European regulation for light duty vehicle (white: no change, yellow: change, red: important change), adapted from Ref. [26]

The regulations for heavy-duty vehicles have also continuously improved from Euro I (1992) to Euro VI (2014). The changes in the testing methods as well as the emission limits from Euro I to Euro VI are shown in*Table 2.2*. The 13-modes of the engine test cycle regulated in Euro I and II have been improved within the Engine Steady Cycle (ESC), Engine Transient Cycle (ETC) and European Load Response (ELR) in Euro III to V operation. In Euro VI, the World Harmonised Steady State Cycle (WHSC), the World Harmonised Transient Cycle (WHTC) and a new real world test procedure became standard. More specifically, the RDE-like procedure must be conducted by running the engine under 15 modes of random points in the Off-Cycle Emission (OCE) mode and an on-road vehicle test with a Portable Emission Measurement System (PEMS) [26]. In addition, since 1 January 2019, HDV manufacturers must declare the new vehicle's CO_2 emissions using a Vehicle Energy Consumption Calculation Tool (VECTO) to calculate the CO_2 at

various operating conditions. The European Parliament also took more progressive action to verify the CO_2 from HDVs with legalisation via Regulation (EU) No. 2019/1242. This clause regulates the improvement in CO_2 limit in 2025 to be 15% lower than the CO_2 average during a reference period (between 1 July 2019–30 June 2020). Such targets will be pushed further, with a target of 30% lower than this reference by 2030 [27].

			EU-1	EU-2	EU-3	EU-4	EU-5	EU-6
			1992	1996	2000	2005	2008	2013
Test Cycles EU-1+2 13 Mode EU-3+4 ESC EU-6 WHSC	CO	g/kWh	4.50	4.00	2.10	1.50	1.50	1.50
	THC	g/kWh	1.1	1.1	0.66	0.46	0.46	0.13
	NMHC	g/kWh						
	CH4	g/kWh						
	NOx	g/kWh	8.00	7.00	5.00	3.50	2.00	0.40
	PM	g/kWh	3.60	0.15	0.10	0.02	0.02	0.01
	NH3	g/kWh				25	25	10
	PN	#/kWh						8E+11
	CO2, FC	g/kWh						no
	NO2	g/kWh						
Test Cycles EU-3+4 ETC EU-6 WHTC	CO	g/kWh			5.40	4.00	4.00	1.50
	THC	g/kWh						0.16
	NMHC	g/kWh			0.78	0.55	0.55	
	CH4	g/kWh			1.6	1.1	1.1	
	NOx	g/kWh			5.00	3.50	2.00	0.46
	PM	g/kWh			0.16	0.03	0.03	0.01
	NH3	g/kWh				25	25	10
	PN	#/kWh						6E+11
	CO2, FC	g/kWh						no
	NO2	g/kWh						
			no change		change		important	

Table 2.2. Changes in emission limits for each stage of European regulation for HDV engine (white: no change, yellow: change, red: important change), adapted from Ref. [26]

Despite these improvements, within Europe the automotive industry has ramped up development of electrified ground transport with the aim of significantly reducing tailpipe emissions, particularly in urban areas. Battery Electric Vehicle (BEV) and Hybrid Electric Vehicle (HEV) technologies are now increasingly being adopted in passenger cars and although absolute numbers still remain relatively low compared to gasoline sales, they are expected to increase rapidly over the next few years. A key advantage is an inherent ability to recover otherwise wasted braking energy via electrical regenerative systems. Despite some key remaining challenges, including severely limited charging and 'green' electricity infrastructure, some governments, including the UK are now proposing to accelerate the mass adoption of BEVs through competing technology bans in a 2030-2040 timeframe. However, some scepticism remains over the viability of full-electric trucks, predominately due to challenges around high embedded greenhouses gases and battery second life/recycling when considered on a life cycle analysis basis [28].

At present, the modern turbo-diesel still dominates the global HDV market [29]. For Heavy Duty, BEV technology has largely been restricted to inner-city buses operating in urban areas on limited range capacities. One key challenge is the relatively poor energy density of the current automotive state of the art lithium-ion-based batteries, which leads to a considerable reduction in payload. For example, the Mercedes E-truck demonstrator had a heavily restricted payload relative to a typical urban truck [30]. In a recent study of heavy-duty alternatives, Smallbone et al. [5] reported the results from the simulation of HDVs with several powertrain options, including a CI engine operating with diesel fuel, a BEV truck with grid electricity, hydrogen with HEVs with ICE, Fuel Cell (FC), Free Piston Energy Generator (FPEG) technologies and also gasoline in HEV and FPEG. The comparison of the gravimetric and volumetric density of the powertrains is set out in *Figure 2.1*. It was shown that BEVs have significantly higher gravimetric and volumetric density than CI engines operating with diesel fuel (shown as ICE-CIDI-Diesel), which had the lowest density among the cases studied. Of the other alternatives, it was shown that hydrogen propulsion might be a preferred HD decarbonised solution to BEV technologies, but this was noted to be highly dependent on the method of hydrogen production, storage and the associated infrastructure capabilities and maturity.

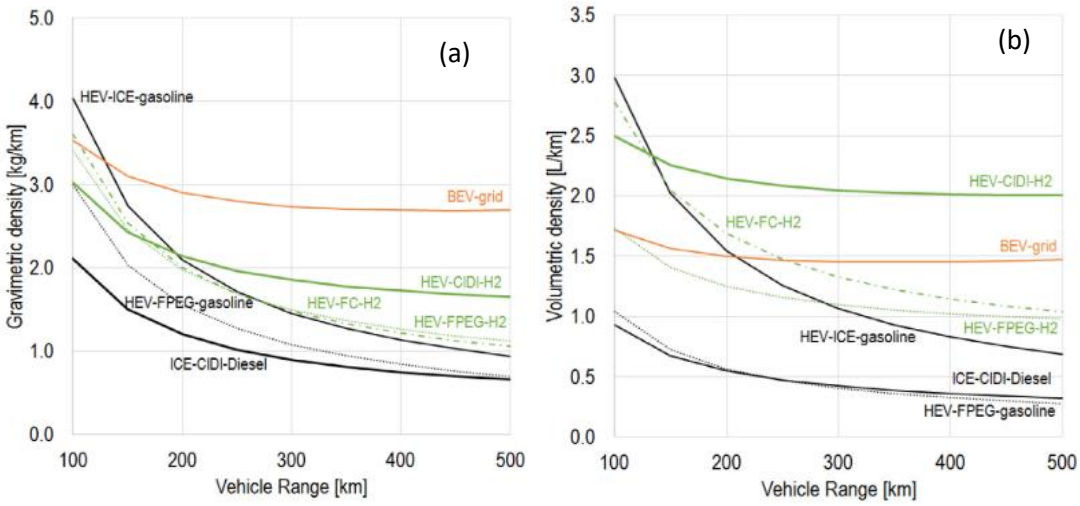


Figure 2.1. (a) Powertrain mass per unit range and (b) Powertrain volume per unit range [5]

Before use phase, BEV production results in higher lifecycle's GHG emission than diesel HDV mainly contributed by battery cell manufacturing processes. Emillsson and Dahloff [31] simulated GHG emission by battery cell production using electricity mix ranges from fully green (0 $kgCO_2e/kWh$) to fossil-rich (1 $kgCO_2e/kWh$). It reported GHG emission ranges from 61 to 106 $kgCO_2e/kWh$ if electric heater is used rather than boiler with natural gas. If natural gas is used for the heating process, GHG emission ranges from 70 to 77 $kgCO_2e/kWh$. The study used a GHG emission of the upstream material by Dai et al. [32]. In another study, Kelly et al. [33] calculated

lifecycle GHG of Nickel-Methane-Cobalt in 1:1:1 ratio of composition (NMC111) lithium ion battery. It resulted 41.8 $kgCO_2e/kWh$ from the best case scenario and 141.5 $kgCO_2e/kWh$ from the worst case scenario. In a holistic context of HDV powertrain production, Wolff et al. [34] put the battery production into cradle-to-gate GWP calculation of HDV production using composition and GHG of NMC111 by Dai et al. [32] and a modelled European electricity mix of 336 gCO_2e/kWh. The GHG emission by the simulated powertrain is depicted in Figure 2.2. Compared to diesel HDV, 40-ton BEV with 450 and 600 km produced GHG by ~4 to ~5 times respectively (in 100 years timeframe GWP). Initially higher GHG emission by BEV production suggest that the use phase should compensate it by producing lower GHG (than by ICE-HDV) to be viable option for decarbonising the HDV sector.

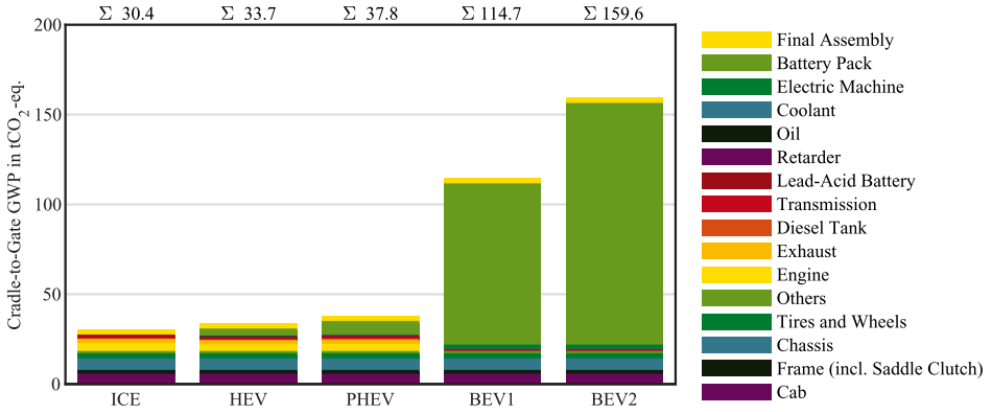


Figure 2.2. Cradle-to-gate GWP by long-haul HDV with diesel (ICE), HEV, PHEV, 450 km range BEV (BEV1) and 600 km range BEV (BEV2) [34]

CO_2 emissions generated by BEVs during the use phase vary wildly depending on the method of electricity generation. In a study by Sacchi et al. [6] simulated phase of 40-ton of HDV with diesel (ICEV-d), SI engine with CNG (ICEV-g), Fuel Cell (FCEV) with hydrogen from electrolysis, and BEV for urban regional, and long haul usage in 2020, 2030, 2050. This study used same BEV components as simulated by Wolff [34]. As illustrated in Figure 2.3, BEV with 36% load factor for urban delivery (150 km) resulted lower GHG than diesel HDV (shown as ICEV-d) since 2020. However, for regional delivery (400 km), ICEV-d was estimated to produce lower GHG until 2030 and BEV would become viable in 2050. For long haul application (800 km) with load, ICEV-d is still viable option for producing lower GHG until 2050. The simulation used 344, 285 and 209 gCO2e/kWh as carbon intensity of electricity mix in 2020, 2030 and 2050 respectively. This suggest that decarbonising HDV with BEV is favourable for short range while diesel is more favourable for medium to long range delivery in short- to mid-term in Europe.

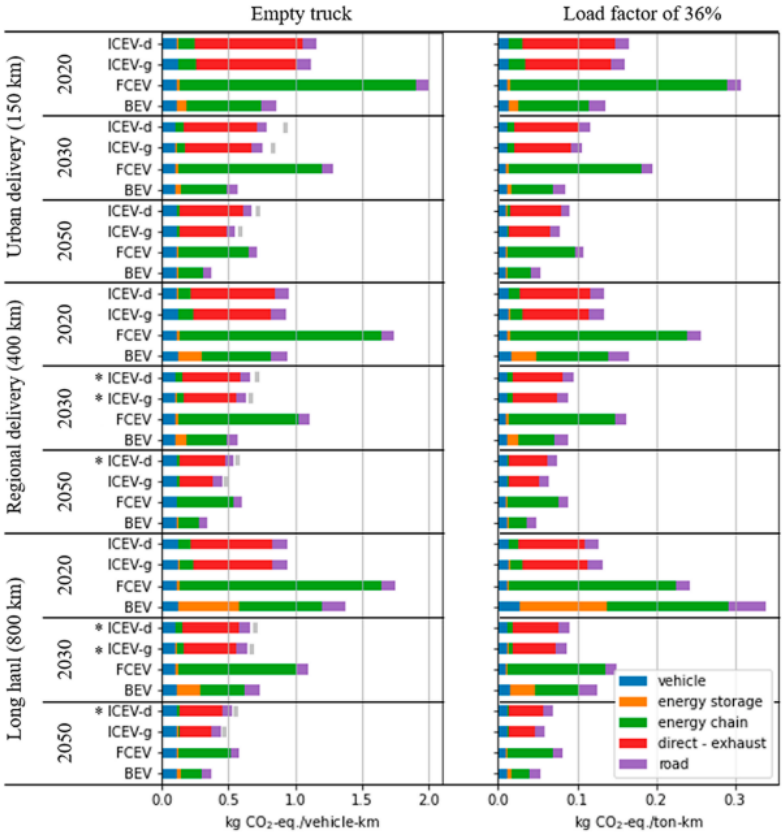


Figure 2.3. Comparison of GHG by 40-ton HDV using diesel (ICEV-d), natural gas (ICEV-g), fuel cell (FCEV) and BEV at 2020, 2030 and 2050 in the equivalent CO2 per vehicle-km (left) for the empty vehicle and ton-km for the loaded vehicle (right) [6]

GHG emission from HDVs was also simulated by Smallbone et al. [5]. The net CO_2 emissions by simulated HDVs for several scenarios are shown in *Figure 2.4*. In comparison of 500 km range HDVs, BEV simulation using average European electricity grid with 136 gCO_2e/MJ (equals to 490 gCO2e/kWh) [35] produces higher lifecycle CO_2 than the other simulated powertrains, except in HEV-FPEG using hydrogen produced via electrolysis with EU electricity grid. Compared to diesel HDV, BEV produced higher GHG emission by ~5 times. They concluded that BEVs could improve the CO_2 emissions to a similar level of the diesel with the scenario of the medium-term target of CO_2 improvement by electrical means to 100 gCO_2/kWh, which they equated to a 2030 timeframe. The study demonstrated how the lifecycle CO_2 emission of BEVs depends highly on the energy mix.

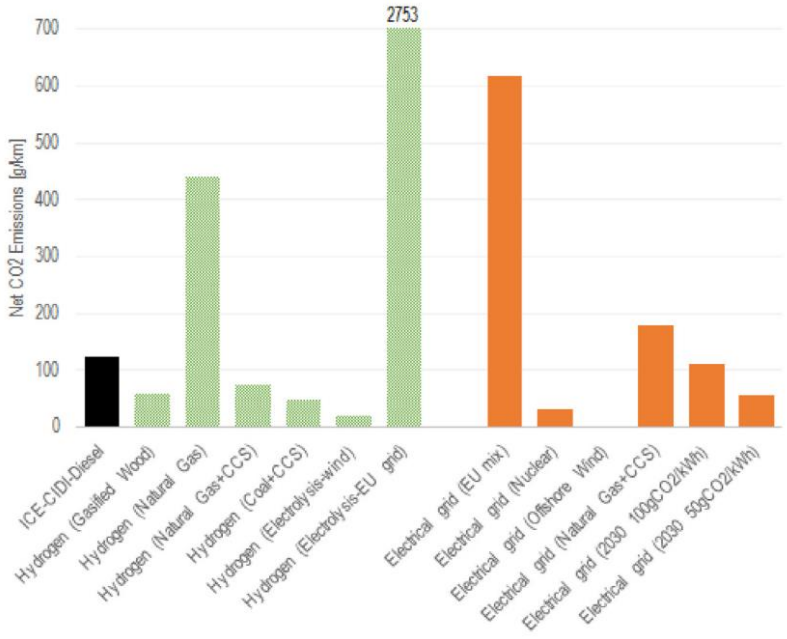


Figure 2.4. Comparison of the Net CO_2 emission by 500 km range of HDV with ICE-CIDI-Diesel, Hydrogen (HEV-FPEG) and BEV with electrical grid with several sources of energy [5]

As shown in *Figure 2.4*, the powertrain that uses hydrogen produces higher CO_2 than the diesel powertrain due to utilisation of natural gas without Carbon Capture and Storage (CCS), which dominates world hydrogen stock production (95%) [36]. The highest GHG emission amongst the simulated powertrains was resulted by HEV-FPEG with hydrogen from electrolysis production. Therefore, low GHG hydrogen production methods must also be developed if hydrogen trucks are ever to be viable. Blue hydrogen is a term now used to denote hydrogen production from fossil fuel with CCS, which may be an alternative during transition to green hydrogen produced using renewable energy and either biomass gasification, electrolysis, solar-to-fuel, or biological methods [36,37]. At the time of writing this thesis considerably uncertainty remains around the viability of mass conversion of heavy duty transport to hydrogen.

The challenges of truck electrification extend to the need to adopt a considerable new high-power charging infrastructure and avoid excessive penalties through repurposing and/or recycling of relatively large battery packs. Some workers have insinuated catenary solutions (e.g. overhead cables with 'trolley' attachments) for future trucks [38,39]. In a simulation study, Hill et al. [39] reported 53% reduction in CO_2 by implementing such technology for the diesel-HEV powertrain on a 40-tonne articulated lorry (compared to diesel). However, the infrastructure does not yet exist on a commercial scale. A trial stage for short distances (5 kilometres) has been recently demonstrated on the highway within several states in Germany for hybrid electric HDVs [40]. On the other hand, the catenary approach could lead to other challenges, including safety if adopted near highly populated areas. For heavy-duty, it would appear that no economically

viable single solution exists for effective decarbonisation and that the ICE will remain part of the mix for several decades to come, albeit in some cases operating on alternative fuels or as part of a hybrid architecture (particularly if frequently operating within highly transient urban areas).

Since CO_2 is a main product of fossil fuel combustion, reducing fuel consumption by increasing engine efficiency is a pragmatic method to reduce CO_2 emissions. For a given engine type this can be achieved through several practical methods such as, for example, improving combustion efficiency by improving fuel mixing, minimising wall heat transfer (e.g., high EGR or novel thermal barrier coatings) and waste heat recovery. In addition to brake efficiency improvements, the accelerated path of decarbonisation needs to consider utilisation of zero or low-carbon fuel for more significant CO_2 reduction. Several zero carbon fuels such as hydrogen (H_2) and ammonia (NH_3) could eliminate CO_2 emissions if produced and transported via renewables. However, their availability is either low or incurs other complex challenges, e.g., efficient production and long-term storage of 'green' H_2 or potentially high toxicity of NH_3 in confined spaces. Natural gas is a hydrocarbon fuel with better availability and a lower C/H ratio (1/4) than diesel or gasoline (~1/2). Despite the fact that infrastructure has not yet been built to the same scale as diesel infrastructure, its availability has been increasing and is easier and vastly cheaper to upgrade (ignoring future carbon capture demands). Of particular note, production has increased significantly after the discovery of significant shale gas in the US since 2007, as shown in *Figure 2.5*. In addition, the predicted increasing trend of natural gas liquefaction by the US and Qatar also increases the world's natural gas supply [41], despite a decreasing production in 2020 could be related to Covid-19 pandemic that hit the economy. The trend of US fuels prices in the recent decade recorded that the price of LNG and CNG is mostly lower than diesel, as illustrated in *Figure 2.5*. This makes natural gas an attractive choice not only for decarbonising the transport sector but also for reducing the operating cost. The details of natural gas including its properties and utilisation are discussed in the following sections. The potential of biogas as a sustainable fuel for decarbonisation is also briefly discussed.

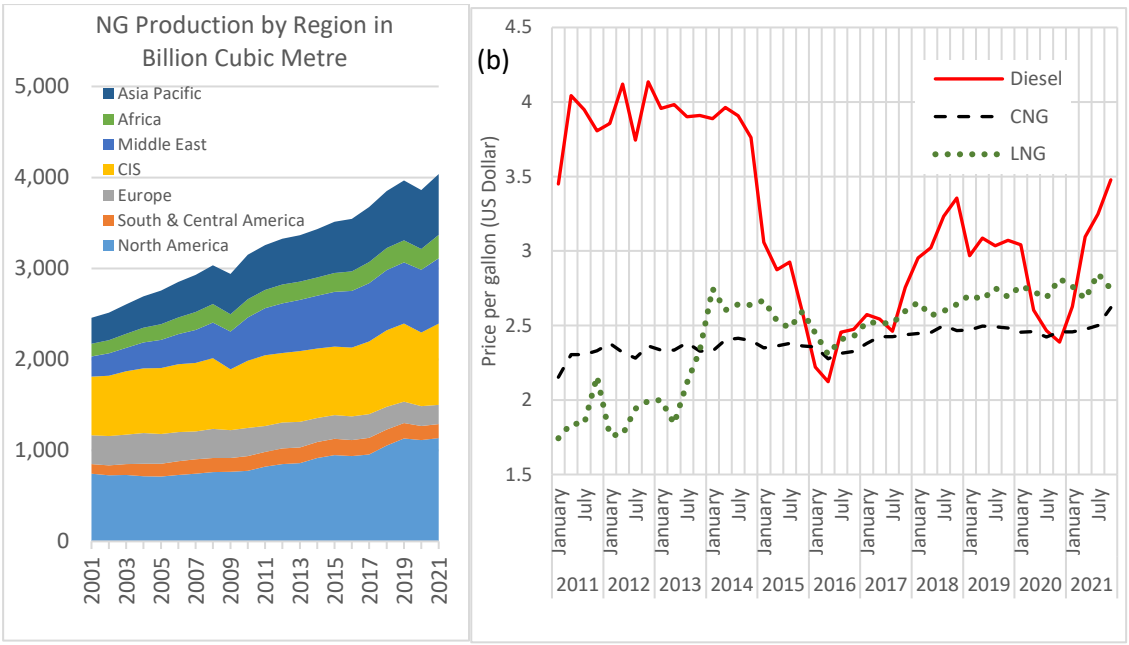


Figure 2.5. (a) NG production by region between 2001 and 2020 (adapted from data in Ref. [9]*), (b) History of Diesel, CNG and LNG Prices in the US in the recent decade (adapted from Ref.* [10]*)*

2.3 Potential of Natural Gas for Decarbonising HDV with ICE

2.3.1 Properties of NG as fossil fuel

Natural gas mainly consists of methane (CH_4) in 80-99 $\%_{vol.}$ proportion with significant amounts of other key hydrocarbons such as ethane, propane, butane, pentane and hexane. Natural gas from many global sources may also contain nitrogen, carbon dioxide, hydrogen sulphide and other pollutant gases like mercaptans, carbonyl sulphide and carbon disulphide [13]. The constituents vary depending on the source. The general properties of natural gas are compared to typical diesel fuel (low sulphur) in *Table 2.3*. Natural gas is typically stored in two ways; as a compressed gas (CNG) or in a liquefied state (LNG). CNG is typically stored at up to 200 bar, while LNG is typically kept under -162 °C in a cold tank. Despite the fact that the Lower Heating Value (LHV) of natural gas is higher than gasoline and diesel (on a mass basis), the lower density of natural gas means it needs more space to be kept either as CNG or LNG to provide the same amount of energy as conventional diesel. LNG's liquefying and storing processes require energy that results in a higher GWP impact than CNG, albeit it is still a lower GWP impact than producing diesel [39,42]. This ignores the challenges of methane slip, which will be returned to later on. The other benefit of natural gas utilisation in the ICE is reduced oil dilution and deposits on the combustion chamber surfaces [43]. From a safety perspective, NG is argued to be safer than

conventional fuel as it has lower energy per volume and high auto-ignition temperature. From a health perspective, it is neither toxic nor carcinogenic [43].

Properties	**Natural Gas** [13]	**Diesel** [44,45]
Carbon content, weight%	73.3	87
Hydrogen content, weight%	23.9	13
Oxygen content, weight%	0.4	0
Hydrogen/carbon atomic ratio	3.0 - 4.0	1.7-1.8
Relative density, at 15 °C (relative to: air for gas, water for diesel)	0.72 - 0.81	0.85
Boiling point, °C	-162	180 – 340
Flash point		60 – 80
Auto-ignition temperature, °C	540 – 560	316
Octane number	120 – 130	-
Methane number	69 – 99	-
Cetane number	-	40-55
Lower heating value, MJ/kg	38 – 50	42.42
Sulphur concentration, weight ppm	<5	15

Table 2.3. Natural gas and low sulphur diesel fuel properties

One key benefit of natural gas usage in a premixed state is a relatively high-octane rating, avoiding premature auto-ignition and knock events in the end-gas that sometimes occur with other premixed fuels. Therefore, it can be used in engines at a higher compression ratio. The Research Octane Number (RON) of natural gas typically varies between 120-130 [43]. An alternative characterisation is the Methane Number (MN) of the blend, which directly relates to the purity of the gas with respect to methane content. The MN is measured by comparing the characteristics of knock intensity of the tested gas to the knock intensity of the mixture of methane and hydrogen in certain volumetric percentage as a reference. The MN test is conducted under closely controlled operating conditions in a spark-ignition test engine. The fuel has a rating of MN100 if it has knock intensity characteristics equivalent to 100% methane, while it has MN0 if it has knock intensity the same as 100% hydrogen [8]. Several methods have been developed to approximate the MN rather than characterising the fuel in the test engine. The AVL method [46] is the first developed MN calculation method based on the composition of gaseous fuel [47]. It has been improved in the most recent calculation methods by including hydrocarbons with carbon content higher than C_4, such as demonstrated previously by MWM [48], GRI [49], Cummins-Westport [50], Caterpillar[51] and Wartsila [52]. As a consequence of the different algorithms used, the different methods can produce considerably different values (more than 5) for the same gas composition [47].

As the MN is highly dependent on the natural gas fuel blend, it varies between global sources. Other key components in natural gas include Ethane (C_2H_6) which has a MN rating of 44 (MN44) and Propane (C_3H_8) that is rated at MN34 [43]. Therefore, higher impurities (non-methane contents) of hydrocarbon species with higher carbon content within natural gas decrease the methane number and increase knocking tendency. Set out in Table 2.4 are values of MN for various global sources of LNG estimated using the MWM method. Varying sources and compositions can incur similar methane numbers for different reasons. Despite MN providing a useful comparative metric, it has recently been shown that variations in knocking intensity can still occur despite similar ratings. For example, Van Alstine et al. [47] reported different natural gas composition with the same MN produced different knock characteristics in dual-fuel natural gas-diesel applications. Therefore, it is important to acknowledge the complex nature and high degree of caution required if reviewing knocking characteristics by methane number alone. Similarly, the Gross Calorific Values (GCV) shown in *Table 2.4* also indicate similar values can be attained from varying constituents, and this also requires caution for haulage operations where small changes may have a large economic impact.

LNG Source	Constituents					MN	Gas GCV (MJ/m^3)
	Methane/ C_1 (%)	Ethane/ C_2 (%)	Propane/ C_3 (%)	C4+ (%)	Nitrogen (%)		
Algeria - Arzew	88.93	8.42	1.59	0.37	0.71	73.02	43.48
Algeria - Bethioua	89.55	8.20	1.30	0.31	0.64	74.01	43.22
Algeria - Skikda	91.40	7.35	0.57	0.05	0.63	78.99	42.30
Australia - Darwin	87.64	9.97	1.96	0.33	0.10	70.98	44.39
Australia - NWS	87.33	8.33	3.33	0.97	0.04	68.00	45.32
Egypt - Damietta	97.25	2.49	0.12	0.12	0.02	90.19	40.87
Egypt - Idku	95.31	3.58	0.74	0.34	0.02	83.03	41.76
Equatorial Guinea	93.41	6.52	0.07	0.00	0.00	82.01	41.95
Indonesia - Arun	91.86	5.66	1.60	0.79	0.08	75.00	43.29
Indonesia - Badak	90.14	5.46	2.98	1.40	0.01	69.00	44.63
Indonesia - Tangguh	96.91	2.37	0.44	0.15	0.13	88.04	41.00
Malaysia	91.69	4.64	2.60	0.93	0.14	73.03	43.67
Norway	92.03	5.75	1.31	0.45	0.46	77.02	42.69
Oman	90.68	5.75	2.12	1.24	0.20	72.07	43.99
Peru	89.07	10.26	0.10	0.01	0.57	75.98	42.90
Qatar	90.91	6.43	1.66	0.74	0.27	74.04	43.43
Russia-Sakhalin	92.53	4.47	1.97	0.95	0.07	74.99	43.30
Trinidad & Tobago	96.78	2.78	0.37	0.06	0.01	88.02	41.05
USA	99.71	0.09	0.03	0.01	0.17	97.01	39.91
Yemen	93.17	5.93	0.77	0.12	0.02	79.99	42.29

Table 2.4. The constituents, GCV and MN of LNG from various sources [53,54]

2.3.2 Biogas and Biomethane for HDV as Potential CO_2-Neutral Gas

While methane is the main constituent of natural gas as a fossil fuel, it can also be available in the form of biogas. Biogas is the product of several natural processes and is typically composed of 45-70% of methane, CO_2, and small amounts of other gases (H_2S and H_2O). At present, it can be readily sourced from three main sources; biodigesters, waste-water treatment plants and closed landfill sites [11]. The International Energy Agency [11] report a current production of biogas of 35 Mtoe, while the biogas and biomethane potential is 570 and 730 Mtoe respectively. In order to make any global impact, renewable sources of NG require strategic policies to increase utilisation, although direct use in transport is only one option for end-use e.g. drop-in solution in the existing gas network [55]. At present, it would appear that there is an insufficient appetite amongst policymakers to unlock the vast potential of biogas for heavy-duty transport.

Biogas is proposed as a carbon-neutral fuel (or near-neutral depending on life cycle) since it is produced from natural sources that rely upon CO_2 captured from the atmosphere. In addition, biogas utilisation for the transport or energy sector is also a valid GHG reduction strategy since several sources such as waste disposal and sewage processing release methane naturally to the atmosphere [56]. The potential climate impact, expressed in Carbon Intensity based on LCA, is shown in *Table 2.5* for diesel, fossil natural gas and biogas from various sources. From this data is can be seen that biogas utilisation enables significant reductions in carbon intensity. The renewable CNG from food and green waste and manure indicates the negative carbon intensity due to the changes in methane as usual disposal pathways.

Fuel	**Average Carbon Intensity (gCO_2e/MJ)**	**Average change of carbon intensity relative to diesel**
Diesel	100	-21%
Fossil CNG	80	-11%
Fossil LNG	90	3.1%
Landfill gas CNG	46	-55%
Manure CNG	-271	-370%
Wastewater CNG	30	-70%
Waste (food and green) CNG	-11	-111%
Landfill gas LNG	54	-46%

Table 2.5. The range of carbon intensity of fossil and renewable vehicle fuels and the relative values to diesel fuel (adapted from EPA [12])

Biogas can be upgraded by removing CO_2 and other contaminants (such as water and H_2S) through several methods, such as absorption, adsorption, membrane filtration, or cryogenic separation to produce biomethane [55]. Biomethane containing methane in more than 95% of its composition can be injected into the natural gas grid to be distributed in the same line as fossil-based NG. Alternatively, it can be used directly for vehicles as it has been increasingly used

in Sweden [55]. The upgrading process and biomethane transmission consume energy that increase the GHG emission, but the lifecycle emission is still lower than fossil fuels. For instance, EPA [42] illustrated that 42.4 gCO_2e/MJ of lifecycle emission by CNG vehicle from landfill gas is contributed to by 17.9 gCO_2e/MJ of processing facility, 16.9 gCO_2e/MJ of pipeline transmission and 3.18 gCO_2e/MJ of compression to CNG. On the other hand, the production cost of biomethane is higher than NG, but narrows over time by more cost-effective production and higher carbon pricing policies [11].

Several studies investigated the potential of biomethane to decarbonise the HDV transport. A study by CENEX [12] compared the GHG emission of several HDV types that comply with Euro VI emission regulation: CNG SI Articulated (Artic), CNG SI Rigid, LNG SI Artic and LNG CI Artic (dual-fuel LNG-diesel). The fuels used were fossil natural gas (standard gas), biomethane and diesel. Each HDV type was compared to the diesel version of the same specification or in the same gross vehicle weight. The distance, refuelling and load conditions were monitored during the road trial. The Well-to-Wheel (WTW) GHG emission by the tested vehicles are depicted in *Figure 2.6*. Compared to the GHG by diesel as a baseline, the standard gas improved GHGs in HDVs for CNG SI Rigid (10%) and LNG CI Artic (13%), but deteriorated GHG emission in CNG SI Artic (4%) and LNG SI Artic (1%). The significant improvements were the result of biomethane usage, ranging from 76% to 81%. The Tank-to-Wheel (TTW) of CNG and LNG SI HDV using biomethane were considered as zero since it was produced from an organic process that captures CO_2 and the emitted CO_2 will be consumed by subsequent production. Meanwhile, the TTW CO_2 from LNG CI using biomethane was taken into account as it requires diesel for the dual-fuel strategy. The electricity consumed in the biogas purification and transportation for biomethane production was included to the GHG of Well-to-Tank (WTT). In another study, Atkins et al. [30] modelled HDV with several powertrains, with resulting GHG emissions in kg-CO_{2e}/100 km as follows: 97.1 for diesel, 51.8 for battery, 89.5 for SI with CNG from grid, 101.0 for SI with LNG from the grid and 23.2 for SI liquid biomethane HDVs. The HDV with spark ignition gas engine using biomethane resulted in less than half of the lifecycle GHG by BEV HDVs. The studies suggest that the ICE HDV with biomethane could be a viable option for the future net-zero carbon emission strategy albeit apparently not a strategy favoured in current UK policy.

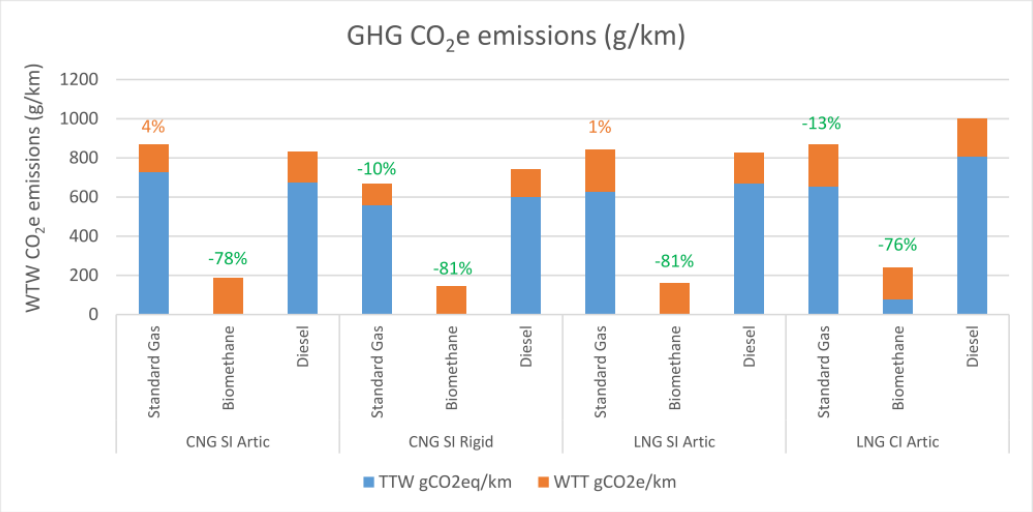


Figure 2.6. The GHG (in g/km of CO2 e) by tested HDV with SI CNG, SI LNG, LNG CI (dual-fuel), and diesel engine; the percentage shown is the relative to diesel [12]

2.3.3 Existing Natural Gas Utilisation in ICEs

Natural gas has been utilised for many decades in SI gas engines for commercial HDVs. Such engines typically operate using a premixed stoichiometric air/fuel mixture by an intake throttling strategy to control the intake air and fuel mixture under varying operating conditions. However, throttling results in significant pumping loss during part-load operation. Some homogenous lean burn concepts have been proposed as a combustion strategy to eliminate pumping loss and improve efficiency, with additional benefits of reduced wall heat losses and reduced NO_x emission due to lower combustion temperatures. However, since the equivalence ratio strongly influences flame speed, as illustrated by the laminar flame speed of methane/air mixtures shown in *Figure 2.7*, the lean mixture deteriorates flame propagation speed. In turn, homogeneous lean-burn results in higher unburned hydrocarbons and poor combustion stability, especially under low load operating conditions [57]. In addition, the three-way catalyst commonly used in existing engine and vehicle systems only works effectively under stochiometric operations for NO_x [45]. Therefore, the lean-burn strategy requires improved exhaust gas aftertreatment methods [58] such as separated NO_x and CO/UHC after-treatment.

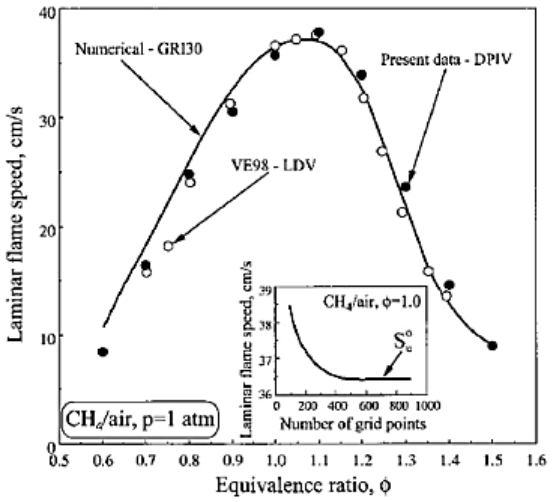


Figure 2.7. Laminar flame speed in the methane/air mixture by numerical and experimental measurement [59]

The general improvement of homogeneous lean burn in SI engines requires ignition sources of higher energy, longer duration and/or multiple locations in the combustion chamber to promote flame propagation and achieve acceptable combustion stability [60]. Several methods have been proposed to improve lean-burn performance, such as twin spark plugs [61], single spark plugs with multiple cores [62], laser ignition [63], multiple events of spark discharge [64] and pre-chamber strategies [60,65–69]. The pre-chamber strategy is described more extensively in this part due to its potential for ignition energy improvement as well as increasing equivalent flame speed in the main chamber. In the pre-chamber ignition concept, combustion is initiated in the pre-chamber to produce reactive jets which are omitted into the main chamber to initiate multiple flame fronts. The pre-chamber ignition concepts can be traced back to the Ricardo Dolphin two-stroke engine, which utilised a pre-chamber and an auxiliary valve to supply a fuel-rich mixture that burns initially and is then exposed to the leaner mixture in the main chamber. The numerous developments of pre-chamber technology up to 2010 are described extensively by Toulson [60]. Hydrogen Assisted Jet Ignition (HAJI) by Watson et al. [66] was developed since the early 1990s, proposed as a unique concept with a small volume pre-chamber of around 1% of the clearance volume. HAJI used hydrogen (~2% of total fuel energy) that was injected into the pre-chamber to produce a flame jet from the ignited mixture, that exits from one or several orifices and burns the lean mixture of air and non-hydrogen fuel in the main combustion chamber. The small pre-chamber concept minimises heat loss from the pre-chamber wall albeit specific losses remain problematic [60]. As an improved concept with non-hydrogen fuel, MAHLE have recently developed a modern turbulent jet ignition system since 2006 [70], which was patented in 2014 by Bunce et al. [67] and later branded MAHLE Jet Ignition (MJI) [70–72].

Several studies of natural gas combustion by Peters et al. [68,72] used a single-cylinder jet ignition engine with Turbulent Jet Ignition (TJI). There are two types of TJI application based upon the availability of a dedicated fuel injector in the pre-chamber: passive and active pre-chamber TJI as illustrated in Figure 2.6. The passive pre-chamber only consists of a spark plug in the pre-chamber, and the fuel that is injected through the intake port or directly to the main chamber flows into the pre-chamber during the compression stroke. Meanwhile, an engine with the active pre-chamber TJI system consists of a pre-chamber with a spark plug and a dedicated miniature fuel injector with a separated fuelling system for the main chamber; either Direct Injection (DI) into the cylinder or Port Fuel Injected (PFI). A small amount of fuel injection into the pre-chamber results in a locally rich mixture. After the spark plug ignites, the fuel in the pre-chamber burns, then the pressure increases higher than the main chamber. The pressure difference causes both combustion radicals and products to exit the pre-chamber through orifices as jets which then ignite the leaner mixture within the main chamber. The jets are highly turbulent, having larger surface area and containing highly reactive radical species with higher temperature. This promotes flame propagation faster than by a spark plug in the standard SI natural gas engine, even with a leaner mixture.

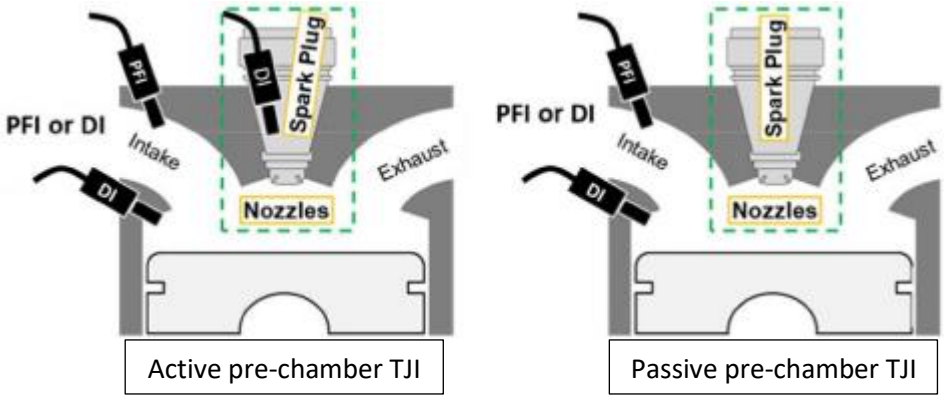


Figure 2.8. Comparison between active pre-chamber and passive pre-chamber TJI [70]

The active pre-chamber TJI concept could extend the lean limit of NG combustion to be ultra-lean by running the engine in the different mixture between the pre-chamber and the main chamber. Peters et al. [68] reported stable combustion at up to λ=1.8 at WOT using TJI with an active pre-chamber, compared to a maximum lean limit of λ=1.6 using a passive pre-chamber in the single cylinder CNG engine test at 900 rpm/1.3 kW. Although further leaner operation with TJI could result in stable combustion (<2% of COV_{IMEP}), it reduced power. An additional benefit was reduction in pumping under leaner operation with a wider open throttle. Compared to stoichiometric operation, TJI at λ=1.8 improved pumping losses by 43% and increased brake efficiency by 1.5%. In another paper, Peters et al. [72] reported the experimental results of the

same engine at a larger operating speed and load area between 900 rpm (1.0 to 1.6 kW) to 1500 rpm (1.0 to 1.9 kW). The leaner operation by TJI improved pumping losses and in-cylinder heat loss but deteriorated exhaust heat loss and friction. The λ sweep showed THC emission improvements from λ=1.0 to λ=1.2, but further leaner operation deteriorated these emissions at λ>1.2. Optimisation of the benefits and losses in several observed parameters resulted in the optimum area of Brake Thermal Efficiency (BTE), where the range of operated λ resulted in similar brake power ($BTE/BTE_{max.}$=0.99-1.0). From their findings, Peters et al. [68] suggested operating the TJI gas engine at a 'sweet spot' to optimise the engine performance at the improved NOx emission. Meanwhile, another study of an active pre-chamber TJI with natural gas in a single-cylinder HD engine by Shah [73] performed sweeps of air/fuel ratio of pre-chamber and different mixtures in the main-chamber and reported that pre-chamber mixture at λ=0.2 (the richest tested) could perform the stable combustion (max. 2% of COV of gross IMEP) to burn fuel in the main chamber at λ=2.65.

An experimental study with a two litre four cylinder engine equipped with an active TJI pre-chamber by Soltic et al. [69] involved testing at 1000 to 4000 rpm from low to full load. The lean mixture (λ=1.7) tested incurred both fast and stable combustion throughout the operating map, from low to full load, without knocking at high load. TJI also resulted in a large speed-load area of high brake efficiency (more than 40%), which is diesel-like efficiency. The lean operation at λ=1.7 by TJI reduced NO_x emissions to be below 2 g/kWh across the operating map, albeit this was still not low enough to avoid aftertreatment. The study also tested full load at the speed range at λ=1.5 that resulted in 45% BTE but with penalties in NO_x emissions by around 5 g/kWh. However, the ultra-lean mixture and the lower in-cylinder temperature are still challenging conditions for complete methane combustion, which deteriorates the combustion efficiency and worsens the unburned methane emission [68,69]. Furthermore, as the lower combustion temperature by TJI decreases the exhaust gas temperature, the methane oxidation in the aftertreatment system becomes more challenging. Therefore, Soltic et al. [69] strongly recommended an innovative aftertreatment system to solve the problem.

2.4 Improving Compression Ignition Engine Efficiency and Emissions as a Pragmatic Heavy Duty Solution

The compression ignition engine is a very efficient internal combustion engine for HDVs, thanks mainly to its high compression and hence expansion ratio, fast combustion and lean operation overall. Therefore, further improving CI engine technology could still be a strategic option for decarbonising the HDV sector in the short-to-medium term, including the improvement of NO_x

and soot that are still the classical problems for diesel combustion. The contributing factors to the NO_x and soot emissions in diesel combustion are discussed in this sub-section. The lean-burn combustion strategies to improve NO_x and soot are also covered, including typical characteristics. The dual-fuel operation of natural gas/diesel is briefly introduced as a lean-burn and low-carbon strategy in the CI engine.

2.4.1 NO_x and Soot Emissions from CI Engines

Diesel combustion consists of several complex processes, starting with the fuel injection through to combustion itself and emissions formation. The prior work by Dec [74] involving an optically accessed diesel engine and non-intrusive laser diagnostics to observe diesel injection and combustion process is one highly cited reference to understand these processes, including the impact of the fuel stratification. The output of the Dec conceptual model with a main injection around TDC is illustrated in *Figure 2.9*. As the fuel is injected into the combustion chamber, it breaks up into small droplets which atomise, vaporise and ultimately are entrained by air. The combustion is initiated by the premixed burn, shown in light blue colour, with fuel/air equivalence ratio in the range of 2-4. During mixing-controlled combustion, the premixed combustion occurs while a diffusion flame occurs within the leaner mixture at the jet periphery. The rich mixture is conducive for soot formation. The soot concentration within the jet is illustrated by the gradient. In the jet periphery, fuel burns as a diffusion flame in a near-stoichiometric mixture at high temperature. This becomes a key source of NO formation, driven by thermal mechanisms as illustrated in the green layer. This is the dominant source of NO_x formation in diesel combustion. However, NO_x is not only formed within this zone, as the high temperature region might also exist in different locations during combustion. Meanwhile, as soot enters the diffusion flame, it oxidises at high temperature with more oxygen availability.

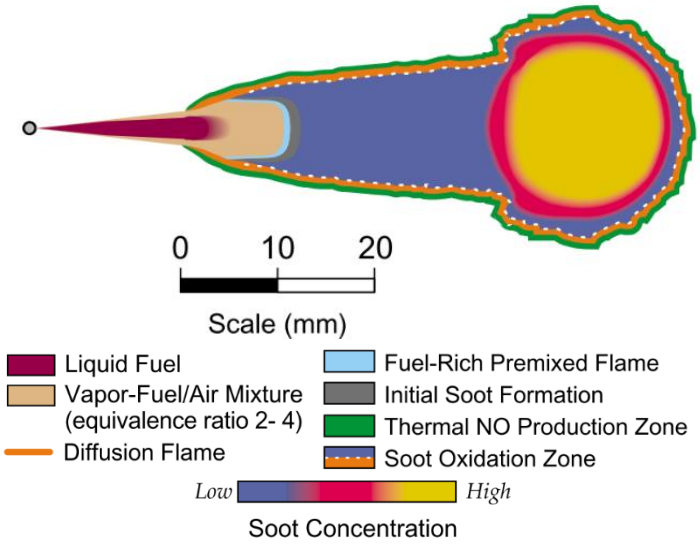


Figure 2.9. Conceptual model of quasi-steady diesel combustion by Dec [74]

NO_x consists of Nitric Oxide (NO) and Nitrogen Dioxide (NO_2). NO constitutes more than 90% of the NO_x emission. There are several chemical pathways of NO formation in the ICE: thermal mechanism, prompt mechanism and converted fuel nitrogen. The thermal process of NO formation follows the extended Zeldovich mechanism at a temperature of more than 2200 K. In the prompt mechanism, NO is formed inside the radical-enriched area in the flame zone, which is usually in the fuel-rich mixture [75]. Meanwhile, nitrogen in the fuel is converted to NO in the flame zone. Among the mentioned mechanisms, according to Musculus [76], considering the high temperature of diesel combustion, the thermal mechanism is the dominant factor of NO formation. Therefore, reducing the combustion temperature is the main method to inhibit NO_x formation.

Soot is formed in the rich mixture zones at temperatures more than 1,600 K [77]. In diesel combustion, the diesel jet's inner plume at the richest mixture contributes to the highest portion of soot formation. Despite the fact that soot formed in the earlier stages of combustion could be oxidised in the later stages, the unburned soot that leaves the cylinder to the exhaust system needs to be processed in an aftertreatment system. Therefore, reducing the over-rich mixture and running at a lower temperature is a preferable method to reduce soot formation.

The variation of local fuel/air equivalence ratio (ϕ) and temperature of the mixture in diesel combustion forms NO_x and soot in different concentrations. The contours of NO_x and soot concentration within their formation islands in a plot of temperature vs fuel/air equivalence ratio (ϕ) are illustrated in *Figure 2.10*, created from a combustion study of the homogeneous mixture of diesel-like fuel and air in the ambient temperature by Akihama et al. [78]. The inner contour with the darker area is the operating condition where the soot and NO are highly

formed in the respective island. It is important to note that different fuel and its composition would produce different islands and contours on the temperature and equivalence ratio plot [79]. Due to the strong influence of both combustion temperature and local equivalence ratio ϕ, recent diesel combustion studies implemented lean-burn and Low-Temperature Combustion (LTC) strategies to avoid the soot and NO_x formation zones, such as discussed in the next section.

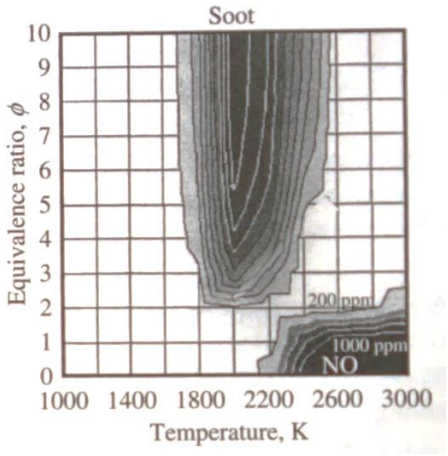


Figure 2.10. Contour of NO_x and soot formation zone in a temperature - local equivalence ratio plot (picture from Heywood [45] *which refers to Akihama et al.* [78]*)*

2.4.2 Lean Burn and Low Temperature Combustion Strategies in CI Engines

The innovations in diesel injection technology with higher injection pressure and electronic control improve the fuel atomisation and provide flexibility to perform multiple injections and various injection profiles at sustained high pressure. This supports further improvement in combustion control. For instance, a small quantity of pilot injection before the main injection could effectively reduce the ignition delay of the main injection, to lower the main combustion's peak pressure and temperature and reduce NO_x. Meanwhile, the post-main injection strategy could promote soot oxidation and increase exhaust gas temperature for the exhaust aftertreatment. To further control the combustion temperature, the diesel engine uses Exhaust Gas Recirculation (EGR) to dilute the intake charge, increasing its specific heat and reducing the combustion temperature.

Many previous studies investigated several combustion strategies to burn diesel fuel at the lean mixture and low temperature by Homogeneous Charge Compression Ignition (HCCI), Premixed Charge Compression Ignition (PCCI) and Rich-LTC. Set out in *Figure 2.11* is an illustration of the possible combustion regimes defined by Neely et al. [80]. This figure is well known and adapted by several authors, some of whom have used different criteria to define the operational area.

In the version shown, the Rich-LTC is mentioned separately from the LTC zone defined by Neely et al. [80] to illustrate a recent variation on this theme.

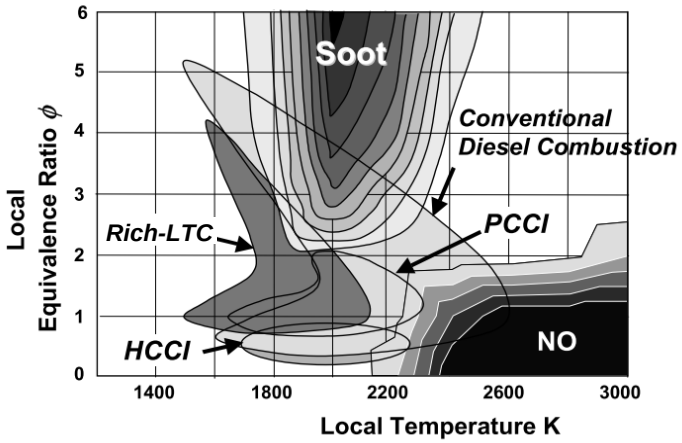


Figure 2.11. Comparison of different alternatives of diesel CI combustion (adapted from [80]*)*

Rich-LTC is a diesel combustion strategy used at low temperature to minimise NO_x and soot at near-stoichiometric conditions. This strategy relies upon EGR to reduce the combustion temperature and avoid soot formation, despite near rich equivalence ratio [78]. However, its operation is in a limited range where the unstable condition becomes the low load boundary and the smoke limit as the high load boundary [80]. HCCI with diesel fuel is a strategy that performs combustion in a homogeneous air/fuel mixture by injecting diesel fuel early in the compression stroke, allowing it to premix before auto-ignition. This reduces the NO_x and soot formation. However, as this strategy heavily relies on the mixture's chemical kinetics, it is complicated to control the combustion phasing, causing difficulty in transient operation. In high load operation, such operation can produce diesel knock and associated unacceptable noise, limiting its application to lower loads. Early diesel injection could detrimentally influence cylinder wall impingement, which deteriorates CO and HC emissions, increases fuel consumption and causes increased lubricant dilution [81]. Alternatively, the PCCI strategy implements the pilot injection that is completely premixed before the start of combustion and combined with a retarded main injection without EGR. This strategy results in improved premixed burn rate and mild combustion to lower the equivalence ratio. PCCI generally operates with a less rich mixture to improve soot emissions [80].

Another lean burn and low-temperature combustion strategy uses two fuels with different reactivity, which was introduced as Reactivity Controlled Compression Ignition (RCCI) by Kokjohn et al. [82]. The fuel with low reactivity (low cetane number) is injected into the intake port, and the high reactivity fuel (high cetane number) is injected early during the compression stroke. The low reactivity fuel, either liquid or gaseous, is injected twice, early (-80 to -50 CA

BTDC) for squish conditioning and between -45 to -30 CA BTDC for igniting the premixed fuel. Since it uses two fuels (either liquid fuel or gaseous fuel), RCCI is a dual-fuel operation in the CI engine with its distinct combustion control characteristics. Both fuels quantity and ratio are controlled depending on the operating condition to perform the optimum combustion performance, efficiency, and emissions. With such a combustion control mechanism, natural gas substitution typically cannot be kept at a high ratio to achieve a high degree of decarbonisation. In addition, such operation leads to a lower exhaust gas temperature (often lower than the aftertreatment working temperature depending on compression/expansion ratio [83]).

Dual-fuel of natural gas as the main fuel and diesel fuel in less quantity is also a strategy to perform lean-burn and LTC in the CI engine. Since natural gas combustion is soot free, substituting diesel with natural gas means operating the CI engine with a leaner mixture could reduce the soot formation through diesel combustion as the pilot fuel. The dual-fuel strategy is the general term that covers combustion of two fuels either operated by single pilot injection, double pilot injection or RCCI to optimise the performance and emissions. The details of dual-fuel combustion are described in the following section.

2.5 Diesel-Natural Gas Dual-Fuel as a Lean Burn Strategy in CI Engines

Dual-fuel operation refers to the use of a diesel pilot to initiate combustion in an otherwise premixed fuel-air mixture, where the secondary premixed fuel is typically a low or 'zero' carbon fuel for environmental benefits. The basic principle is to combine the best features of the fuels, taking advantage of a small diesel pilot to rapidly initiate multiple ignition sites under otherwise pre-mixed lean conditions. Such operation is conducive of high thermal efficiency (diesel-like) and significantly lower pollutant emissions. For natural gas, the engine may be dedicated dual-fuel (such as used in the Volvo High Pressure Direct Injection production system) or alternatively may make use of intake port gaseous fuel injection (albeit with challenges in methane slip for the latter as discussed later on). Regardless of whether dedicated or allowing full diesel fall back, such natural gas engines can operate with high compression ratio, making best use of the relatively high anti-knock index of the gas. The use of natural gas to displace diesel has been reported to reduce CO_2 emissions by approximately 35% on a source to wheel basis for trucks [84] albeit with challenges in methane slip still remaining for global warming. If methane is chosen to represent the natural gas, the calculated CO_2 emission by dual-fuel operation at various substitution ratio of fuel energy (assumed stoichiometric combustion) is shown in *Figure 2.12*.

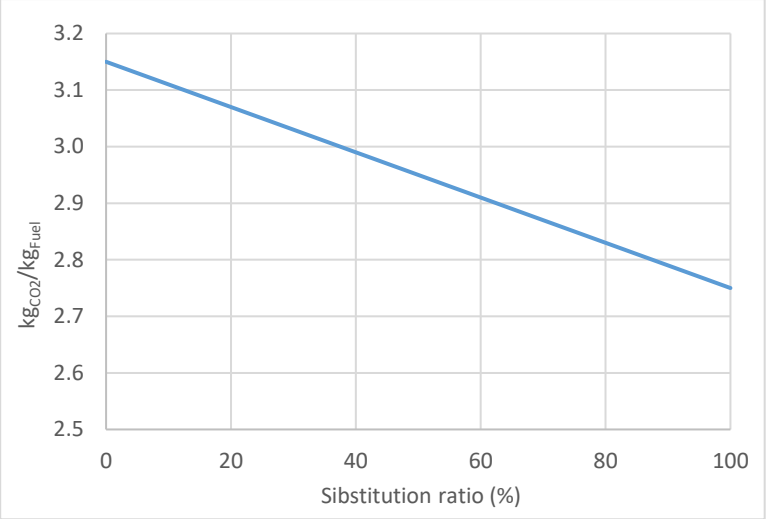


Figure 2.12. CO_2 emission per unit of dual-fuel (methane-diesel) in substitution ratio sweep

2.5.1 The Details of Dual-Fuel Operation of Natural Gas-Diesel

Dual-fuel operation has been used for many decades by injecting the gaseous fuel into the intake port or inlet of intake runner during the intake stroke [8]. The gas, air and EGR (if included) is trapped in the cylinder after intake valve closing. At the end of the compression stroke, pilot diesel fuel is injected into the combustion chamber (historically most typically as a single injection). Then the injection spray breaks up, atomises, vaporises and mixes with the premixed gas (air, NG and residual gas which may also include EGR). After the sequential events during the ignition delay period, the outer part of the diesel jets (at the piston bowl periphery) burns and forms discrete flames that propagate into the surrounding premixed gas (relatively slowly individually but at multiple sites). The remaining part of diesel fuel burns in the next phase, then combustion move towards the injector at the centre of cylinder [85,86]. At high load and high in-cylinder temperature, the auto-ignition of the premixed natural gas in the later stages (so-called end-gas burning) may contribute to the heat release.

Due to the premixed stage, it is clear that the fuel/air equivalence ratio has significant influence over the rate of combustion and arising performance and engine-out emissions. The characteristics of dual-fuel combustion with a constant pilot diesel quantity and sweep of equivalence ratio (by increasing the natural gas quantity) were investigated by Dronniou et al. [85] in an optical single cylinder engine. The apparent Heat Release Rate (HRR) of dual-fuel combustion during a premixed (natural gas/air) equivalence ratio (ø) sweep are illustrated in *Figure 2.13*. The HRR shows the pilot combustion by the noticeable first peak, with another peak at slower speed associated with premixed combustion. Meanwhile, at the richer mixture (closer to stoichiometric), the heat release indicates simultaneous combustion of diesel and gaseous

fuel due to faster flame propagation within the gas/air mixture. At low fuel/air equivalence ratio (ϕ), which indicate the challenging condition for the flame to propagate from the near-wall location to the centre of the cylinder, resulting in highly unburned fuel. Ultimately, this work showed how the equivalence ratio ϕ becomes the key parameter determining flame propagation in dual-fuel mode.

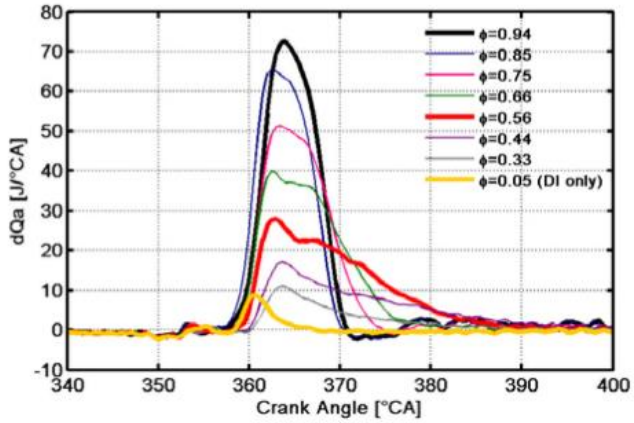


Figure 2.13. The apparent heat release rate (HRR) by single pilot injection dual-fuel at equivalence ratio sweep [30]

However, flame propagation is not the only important factor of dual-fuel combustion performance. Combustion performance of diesel as a pilot fuel providing the ignition source is also another important factor. A relatively richer mixture of natural gas/air is clearly preferable for flame propagation (where peak premixed flame speeds typically occur slightly rich of stoichiometric as shown in *Figure 2.7*). However, dilution of the intake charge with natural gas during dual-fuel combustion prolongs the ignition delay of diesel as reported by Schlatter et. al. [7] via optical combustion studies. Therefore, careful optimisation of injection timing is required to locate the combustion phasing thus producing high efficiency. The low load operating condition is also challenging since the in-cylinder temperature is low, hence increasing the equivalence ratio of natural gas to improve flame propagation could further deteriorate the ignition delay. More details of challenges in dual-fuel combustion and methods to solve it will be discussed further in the next section.

2.5.2 Variants of Dual-Fuel Strategies

Dual-fuel operations are historically classified into several types according to the natural gas supply method into the cylinders: i) intake port injected (premixed) dual-fuel, ii) High-Pressure Direct Injection (HPDI, dedicated dual-fuel in effect), and iii) dual-fuel with low-pressure gaseous fuel direct injection. The differences amongst strategies are described in this sub-section.

2.5.2.1 Intake Port Injected (Premixed) Dual-Fuel

Dual-fuel with intake port injection of natural gas is often simply referred to as 'premixed dual-fuel'. This is the most common type of dual-fuel strategy to date due to its practicality, low cost and ease of retrofit. In this form, a standard diesel engine can be modified by adapting the intake manifold or ports. One or several gas injectors are installed at the inlet of the intake manifold and rely on the mixing in the intake manifold. Alternatively, several gas injectors are installed nearer to the valves in the ports to enable improved fuel distribution across the cylinders. One of the major advantages of this system is ability to revert to conventional diesel operation when gas is not readily available. However, a key challenge is methane slip due to forward and reverse blowby events during compression and the power stroke respectively.

2.5.2.2 High Pressure Direct Injection (HPDI)

The HPDI dual-fuel engine was developed by Westport initially and aims to improve combustion performance by injecting both natural gas and diesel directly into the combustion chamber at high pressure (with gaseous injection up to 600 bar [87]). The pilot fuel injection uses relatively lower pressure than the recent common rail diesel injection technology. McTaggart-Cowan et al. [87] reported that the diesel fuel rail pressure is about 30 bar higher than gas rail pressure. In its commercial application by Volvo, the pilot fuel is injected before natural gas injection. Therefore, natural gas enters the combustion chamber as the pilot fuel has already initiated multiple combustion sites. Such a mechanism aims to minimise the methane slip from the crevice volume and reduces the knocking potential via faster combustion. However, HPDI fully changes the compression ignition engine to be a gas engine without the ability to revert to diesel-only operation. Volvo therefore refers to this technology as "a gas engine based on diesel technology" [88]. One key point to note is this technology is compliant with Euro VI type 1A of duel fuel engine (with substitution ratio≥90%) [89], whereas premixed dual-fuel is not (due to excessive methane slip being considered in this legislation for the first time).

2.5.2.3 Dual Direct Injection (DDI) with Low Pressure Direct Injection of NG

Dual-fuel combustion with low pressure direct injection of NG into the cylinder was proposed by researchers at the University of Graz, Austria [90,91] with the abbreviation DDI. The DDI system uses gaseous fuel common-rail with a maximum pressure of 18 bar to inject the natural gas during the early stage of the compression stroke and diesel injection system with a maximum rail pressure of 2000 bar [90]. The strategy was proposed in attempt to allow relatively increased control over the stratification of the fuel and improve trade-off between engine efficiency and emissions. Sprenger et al. [91] showed that HC emissions improved via retarded injection timing. The system was proposed to be implemented in a passenger vehicle

system that uses CNG rather than relatively heavy LNG storage. The concept requires significant modification of the cylinder head to install both diesel and NG injectors, including removing one of the standard four valves in the base diesel engine and modifying the camshaft design. The ongoing switch to electrified passenger cars has arguably stalled interest in NG for light duty.

2.5.3 Dual-Fuel Combustion Compared to SI Lean Burn TJI

The previous studies compared natural gas combustion in dual-fuel to the conventional spark ignition and TJI in both real and optical engines to attain insight into the key phenomena during the combustion event. Kikusato et. al. [92] carried out an optical engine study during both spark-ignited and diesel spray ignited natural gas combustion. The study reported the advantages of multiple site ignition by diesel injections in improving combustion rate and efficiency. In addition, the ignition by diesel pilot is arguably more repeatable than spark ignition, especially under leaner mixtures. This leads to shorter delay of combustion initiation and a lower rate of pressure rise and maximum pressure. Another benefit of diesel pilot can be its lower knock tendency. Another study by Schlatter et al. [93] compared natural gas combustion in a lean mixture by TJI and diesel pilot injection in a Rapid Compression Expansion Machine (RCEM). These workers reported shorter ignition delay by TJI, but with the flame area's evolution slowing down as the jet became less turbulent. Meanwhile, the pilot diesel ignition exhibited more consistent flame growth and larger flame area than TJI even at low temperature and pressure, although it suffered a longer ignition delay. The studies indicated that diesel pilot provides more ignition energy and a higher turbulent flow that promotes better flame propagation within premixed NG.

The benefits of lean-burn NG combustion by dual-fuel compared to spark ignition could be considered as a more feasible option for decarbonising the HDV sector in an accelerated path. This argument is also valid with diesel engine domination in the existing medium and heavy commercial sector e.g. 98.3% market share in the European Union in 2019 [29]. The suitability is highly dependent on overcoming the challenges.

2.5.4 Challenges in Dual-Fuel Combustion

Despite dual-fuel combustion showing several significant benefits, as mentioned above, the technique has some challenges that need pragmatic solutions to be a viable alternative to diesel combustion. The key main challenges are poor combustion performance at low load, methane slip and knocking phenomena at high load operation with low/variable methane number gas [8,94].

2.5.4.1 Poor Low Load Performance

Under low load operating conditions, the engine runs with lower injected fuel quantity. In dual-fuel operation with a high substitution ratio of natural gas, such condition causes the engine to run with an ultra-lean mixture that causes low in-cylinder temperature. Since the equivalence ratio dictates flame propagation of within the natural gas, as shown in *Figure 2.7* above, the lean mixture deteriorates the turbulent flame speed. Therefore, low load operation could result in poor combustion performance as indicated by slow and unstable combustion and high unburned hydrocarbons. The combustion performance at low load becomes a concern in this study because the HD CI engine is operated in this condition often in truck applications, as mentioned before in the previous chapter. While a premixed dual-fuel system can revert to diesel only operation this ideally needs to be avoided if possible in urban areas.

2.5.4.2 Knocking at high load and its cause

Knocking in dual-fuel can occur at high load with variable methane number fuels [8,95]. It is indicated by a sudden increase of heat release rate due to end gas auto-ignition that induces pressure oscillations throughout the combustion chamber [96,97]. The end gas refers to the part of the mixture that has not yet been reached by flame propagation. In an excessive scale and persistent occurrence, knocking combustion can damage the engine structure [8]. High load operation with high wall temperature and rich mixture typically causes high in-cylinder temperature. Karim [8] suggests higher mixture temperature is more decisive than richer mixture of combustion. On the other hand, knocking in dual-fuel could be challenging to recognise due to pressure oscillation caused by premixed combustion of diesel (ringing) during the early stage of combustion [96,97]. Apart from the in-cylinder condition, the fuel properties determine the knocking characteristics in dual-fuel combustion. Therefore, gaseous fuel quality control including its composition is important to prevent knocking in dual-fuel combustion [47].

There are several methods to mitigate knocking in dual-fuel. Anderson [71] suggests increasing the pilot quantity (reducing substitution ratio) and retarding combustion phasing to mitigate knocking. The intake strategy to reduce combustion temperatures, such as EGR and Miller cycle, could prevent knocking. Intake dilution with EGR reduces the in-cylinder pressure during compression due to increased specific heat of the charge, resulting in a lower temperature, with an additional chemical effect slowing down the combustion [8]. Miller cycle via either early or late intake valve closing results in lower in-cylinder pressure at TDC, reducing the effective compression ratio [98].

2.5.4.3 *Unburned Hydrocarbon (Methane Slip)*

The unburned hydrocarbon as a constituent of exhaust gas from dual-fuel combustion is dominated by methane, so-called methane slip. Such slip is not only produced by the poor combustion at low load, but also from the contribution of premixed gas flow into the crevice volumes. Several crevice volumes with significant contribution are the top-land crevices between the combustion chamber and the compression piston rings. The premixed gas flows into the crevice volumes during the compression stroke as the in-cylinder pressure increases until the in-cylinder pressure reaches the peak pressure after the main combustion events. Since the crevice volumes are small, the flame propagation fails to reach the trapped charge. The blowby gas that flows back into the combustion chamber as the pressure decreases (so called reverse blowby) may be partially burned in the early part of the expansion stroke. However, as the piston and hence pressure and temperature rapidly fall, a significant proportion of the unburned methane escapes into the exhaust.

The contribution of the top-land crevice volume to methane slip of dual-fuel combustion was investigated by Konigsson et al. [19] in a single cylinder CI engine using a crank-angle resolved hydrocarbon measurement. The study reported that the top-land crevice contributes to around 50% of the unburned HC at stoichiometric conditions and increases as the mixture gets leaner up to λ=1.6. At the leaner mixture and deteriorated flame propagation, the poor combustion performance contributes more to the methane slip than the top-land crevices. If the gaseous fuel in the combustion chamber burns efficiently, the top-land crevice contributes about 75% of the unburned HC.

Dual-fuel operation obviously reduces CO_2 emissions, but methane slip remains a major challenge of decarbonisation. Methane has a 25 times higher global warming impact (CO_2-equivalent for an over 100-year period [20]). Therefore, if the methane slip is converted to its CO_2 equivalent, it negates the CO_2 benefit and worsens the overall greenhouse contribution [99,100]. Therefore, reducing the methane slip is one of the main factors to overcome for dual-fuel combustion to be a viable option.

2.6 Addressing Poor Combustion in Low Load Operating Conditions

This section reviews several methods to improve dual-fuel combustion performance at low load, including the control of intake conditions that determines the equivalence ratio, flame propagation of the gaseous fuel and ignition delay of pilot fuel. Each strategy's consequences will also be reviewed to decide the potential of a novel strategy for further improvement.

2.6.1 Increasing pilot quantity (reducing substitution ratio)

Increasing pilot quantity increases the ignition energy to the premixed gas at low load and lean mixture. This strategy could be implemented during dual-fuel operation of the engine with standard diesel intake without throttling or EGR strategy dedicated for dual-fuel to control the intake charge. The larger pilot fuel quantity improves flame propagation even in a leaner mixture, hence improving combustion efficiency. However, this strategy deteriorates soot emissions due to increased diesel combustion [101–103]. In addition, several studies of the driving cycle of HDVs [99,100] have shown soot deterioration during dual-fuel operation was primarily due to low substitution ratio under low load urban operation. An additional complication is classification of the engine under current emissions legislation; Euro VI demanded a substitution ratio≥90% for type 1A and 1B dual-fuel engine [104].

2.6.2 Premixed Dual-Fuel Combustion (PDFC)

An alternative approach is the adoption of multiple pilot injections via so-called PDFC. During this approach, the first pilot is injected earlier in the compression stroke and sufficiently ahead of the second main pilot, allowing diesel fuel to thoroughly premix and 'seed' the methane with diesel vapour. At the end of the compression stroke, the second pilot is injected to initiate the combustion. As the temperature and pressure increases, the premixed pilot fuel that has spread throughout the combustion chamber auto-ignites and creates flames that propagate into the surrounding premixed charge. The premixed pilot provides multiple ignition sites in the premixed air-gaseous fuel in significant numbers. In prior work at Brunel University London, May et al. [105] illustrated the advantage of PDFC, with up to 60% reduction in methane slip relative to Conventional Dual-Fuel (CDF) with single pilot injection. A similar study by Nithyanandan et al. [86] in an optical engine reported more ignition zones by PDFC even at the relatively lean mixture, thus covering the larger area within combustion chamber than CDF. May [105] illustrated comparison of diesel, CDF and PDFC as shown in *Figure 2.14*.

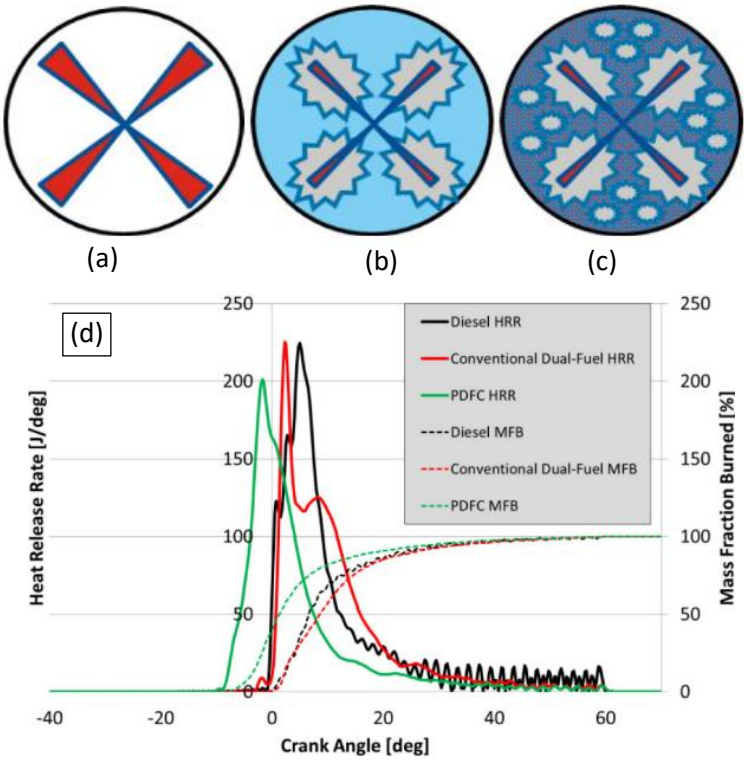


Figure 2.14. Illustrated combustion of: (a) diesel, (b) Conventional Dual-Fuel, (c) PDFC (d) the apparent net HRR and Mass Fraction Burned (MFB) [105]

The HRR of PDFC suggests simultaneous combustion of the pilot and premixed gaseous fuel. PDFC, with a noticeable single peak of HRR, indicates similarity to CDF combustion in the rich mixture, as shown in *Figure 2.13*. Although PDFC is operated at similar air/fuel mixture as CDF (λ~1.4), the premixed pilot accelerates flame propagation within the premixed gaseous fuel, shortening the combustion duration and reducing unburned methane.

2.6.3 Throttling

The throttling strategy limits the intake air flowrate by blocking the intake port, hence decreasing intake airflow in a similar manner to conventional SI engines. Such operation limits the intake manifold pressure and engine volumetric efficiency, burning the combustion nearer towards (or at) stoichiometric conditions which improves the rate of mass burning. The strategy has been investigated in several previous studies [106–109] with reported improvement in unburned methane albeit with pumping losses and deteriorating the net indicated efficiency significantly. Such operation is therefore generally not attractive.

2.6.4 Intake charge heating

The in-cylinder temperature is a decisive factor for flame propagation speeds. The lean mixture and the low fuel quantity at low load produce low in-cylinder temperature. Previous studies

[110,111] proposed intake charge heating to modify the intake conditions. Higher intake charge results in higher compression temperature that promotes flame propagation even in a lean mixture. Higher intake temperature increased the maximum cylinder temperature, reduced the ignition delay, shortened the combustion duration, improved the combustion efficiency and stability. Therefore, it reduced the unburned hydrocarbon and increased exhaust gas temperature. The improvement of combustion efficiency by higher intake temperature is more noticeable at leaner mixture than at richer mixture. However, a higher maximum cylinder temperature could penalise the NO_x emission. In addition, Valladolid et. al. [111] reported that increasing intake temperature from 30 to 90 °C deteriorated brake efficiency by 1.5% at λ_{CNG} =1.5 and worsened at leaner mixture.

2.6.5 Early or Late Intake Valve Closing (Miller Cycle)

The availability of practical variable valve technologies in the last decade or so has led to renewed interest in relative over-expansion achieved efficiently via variable intake valve closing (early or late) with intake boosting to compensate volumetric efficiency. Such operation is now relatively common in premium gasoline passenger cars, where the downsized engine architectures are well suited. For heavy duty, the uptake of variable valve operation has remained limited predominately due to issues with valve clash due to the diesel type piston and limitations in valve overlap. However, future fuels may warrant wider adoption of more flexible valvetrains. For an Early Intake Valve Closing (EIVC) strategy, the valve can be closed early in the intake stroke, with the piston thereafter acting akin to an air spring (minimising pumping losses). One key challenge with this strategy is reduced turbulence intensity for ignition. For Late Intake Valve Closing (LIVC), this decay in turbulence can be avoided but the relative challenge is then avoiding excessive backflow of charge into the intake manifold (which under extreme conditions can increase pumping losses). Regardless of which approach is used, the method is commonly referred to as Miller cycle, named after the inventor, Ralph Miller [112]. In both cases the effective compression ratio is reduced while the expansion ratio can be maintained as an over-expanded cycle, leading to increased thermal efficiency. Additional pre-compression of the intake gases can be achieved via the supercharging or turbocharging system, which typically incurs higher compression efficiency (the IC engine is in fact a relatively inefficient compressor due to the need to maintain top land and ring pack leakage volumes).

May [106] investigated the Miller cycle strategy by the Late Intake Valve Closing (LIVC) for dual-fuel combustion at 1200 rpm and 6 bar Net IMEP, which was the lower load limit for dual-fuel in the thermodynamic heavy duty single cylinder adopted. Retarding IVC to run the engine at

lower λ (varied from 1.77 to 1.22) improved flame propagation as indicated by higher combustion efficiency (7%), shorter combustion duration (10 °CA), vastly reduced improved methane slip (84%) and CO emission (75%). However, with the Miller cycle reducing the compression ratio which in turn resulted in longer ignition delay. Improved combustion speeds also penalised the NO_x emission, which suggested higher in-cylinder temperatures. May [106] also compared Miller cycle to the intake throttling strategy. The LIVC strategy reduced pumping losses and therefore produced higher net indicated efficiency than throttling. With the feature of reducing the compression-end temperature, Miller was also used by Weber et al. [98] in a single-cylinder engine at a higher load to prevent knocking using the EIVC strategy.

One challenge with dual-fuel Miller is detrimental impact upon air and gas exchange between the intake ports and cylinders. As IVC is retarded, a partial amount of gaseous fuel can flow back to the intake manifold and in extreme cases can reach the adjacent cylinder, causing uneven distribution of fuel to each cylinder. An experimental study of such multi cylinder dual-fuel was undertaken by Kassa et al. [86] in a six cylinder 12.4 Litre CI engine at 1200 rpm/16.5 bar BMEP. These workers reported that retarding intake valve closing from 150° to 100 °BTDC increased the cylinder-to-cylinder variation. In the worst case, this variation led to 13% difference in average IMEP, 8% difference in average maximum pressure. Comparing cylinders, the difference between maximum and minimum values was as much as 38% in IMEP, 24% in maximum pressure and 21% in combustion work.

2.6.6 Exhaust Gas Recirculation (EGR)

Dilution of the intake charge with EGR increases the mixture's specific heat, resulting in lower combustion temperatures, reduced wall heat losses and improved NO_x emissions. There are two main types of EGR operation: external EGR and internal EGR. In external EGR, a partial quantity of exhaust gas is recirculated back to the cylinder through a pipe connection between the exhaust and intake manifold, often in a cooled condition by utilising a simple cooler with integrated bypass and throttle valve. For internal EGR, the exhaust gas is typically trapped in the cylinder as increased residual gas via modified valve timing with valve overlap and/or gas re-breathing. Internal EGR is rare for heavy duty, due to limited ability to run significant valve overlap in a typical diesel combustion chamber layout. In the following discussion the term EGR refers to external EGR unless otherwise indicated.

For dual-fuel, the adoption of EGR comes with some challenges. The displacement of fresh charge results in richer combustion unless additional boost pressure is available. In prior work by Song et al. [113], a high percentage of EGR dilution caused significant ignition delay and

longer combustion duration. Elsewhere, an experimental study in a single-cylinder diesel engine by Dev et al. [114] at 1000 rpm/8.1 bar BMEP compared 0% and 10% cooled EGR with a pilot timing sweep from 15 to 21 °CA BTDC. The tests with EGR resulted in decreased maximum rate of pressure rise (0.5 to 1 bar/°CA), reduced unburned methane and non-methane hydrocarbons (by 10%), lower NO_x (by 50%), but longer ignition delay (~1 °CA) and deteriorated brake thermal efficiency (by 1%).

Hot EGR could be another option to increase fuel/air equivalence ratio with another function to increase intake gas temperature relative to non-EGR strategy. Due to lower density, the hotter EGR occupies a larger volume in the cylinder, increasing fuel/air equivalence ratio higher than cooled EGR at a lower EGR percentage. In addition, it has a similar effect to intake charge heating, producing higher in-cylinder temperature that promotes flame propagation. Shim et al. [107] investigated dual-fuel at 1400 rpm/3 bar Net IMEP with 60% substitution ratio, with a hot-EGR sweep up to 50% and cooled-EGR up to 45%. The study resulted in lower THC emissions using hot EGR up to 40%, with cooled EGR only improving the THC at 10% EGR and thereafter deterioration at the higher percentage. These contrasting results suggest that apart from increasing the equivalence ratio, the hot-EGR increased the intake charge temperature, promoted flame propagation while restraining combustion temperature to improve NO_x.

The other strategy with a similar effect as hot external-EGR is internal EGR. The implementation of internal EGR to the dual-fuel combustion was investigated by May [79] in a single-cylinder engine at 1000 rpm/6 bar Net IMEP. The less dense residual gas takes a larger space in the cylinder than cooled EGR. Therefore, dual-fuel combustion could run with internal EGR at lower air/fuel equivalence ratio (λ), although in less EGR percentage than the baseline cooled external-EGR, resulted in higher combustion efficiency and improved ignition delay. However, deteriorated NO_x emissions by an internal-EGR strategy could be related to higher in-cylinder temperature. The study also showed that a combination of both internal EGR and external EGR could improve the combustion efficiency, reducing the unburned methane while improving NO_x emission even at a higher total EGR fraction than the baseline with cooled-EGR only.

EGR can also be implemented in combination with other intake air reducing strategies, such as performed by May [106], who used cooled EGR in combination with throttling or Miller cycle in conventional dual-fuel. Dual-fuel operation at similar λ as a throttling-only strategy indicated that the EGR-throttling operation improves the pumping loss, as would be expected. Meanwhile, the combined EGR-Miller approach increases the effective compression ratio to run the engine at the same λ as the Miller-only strategy because the combined strategy closed the intake valve at an earlier timing. The higher compression ratio also has a positive impact on

improvement in ignition delay. In both combined strategies, the NO_x emission was improved. However, compared to a zero EGR strategy at the same λ, EGR resulted in longer combustion duration, deteriorated unburned methane and CO emissions and reduced combustion efficiency (1.5% to 3.5%). The EGR strategy also resulted in lower exhaust gas temperature and reduced maximum Pressure Rise Rate (PRR) due to slower combustion.

2.6.7 Cylinder Disablement by Cylinder Cut-out and Cylinder Deactivation (CDA)

Low load combustion performance can be improved by firing several cylinders in higher individual cylinder-load and disabling one or several cylinders via a cylinder disablement strategy. As an illustration, if the strategy disables half of the cylinders, the firing cylinders run roughly double the individual load to produce the same brake load. Therefore, the firing cylinder can run under a less lean mixture than in the regular operation, resulting in improved flame propagation for dual-fuel. There are two common methods of cylinder disablement: cylinder cut-out and cylinder deactivation (CDA). Cylinder cut-out disables the fuel injection only. In contrast, CDA disables both fuel injection and valve actuation of the non-firing cylinders, with either residual masses or fresh intake initially trapped in the cylinder (albeit progressively 'leaking down').

A previous study of cylinder disablement by Konrad et al. [115] simulated dual-fuel combustion under a cylinder cut-out strategy in a seven cylinder turbocharged CI engine model. The simulation controlled the air/fuel mixture using a charge blow-off valve between the compressor and the intake manifold. The study simulated dual-fuel with all-cylinders firing versus disablement of one, two and three cylinders. Compared to the conventional operation, cylinder cut-out resulted in less PMEP, lower in-cylinder heat loss and improved brake efficiency. Its simulation with 3 cylinders cut-out at 10% load resulted an increase of brake efficiency by 26% relative to the baseline (all cylinders firing strategy). However, the cylinder cut-out strategy resulted in lower exhaust gas temperature than conventional operation due to exhaust gas dilution with fresh air from the non-firing cylinder. This will affect the methane oxidation catalyst which will be discussed in the next section.

The cylinder cut-out strategy has been implemented in Wartsila 34DF marine dual-fuel engines at low load up to 15% load. It implements a rolling order of cylinder cut-out with up to 3 non-firing cylinders to balance the engine thermal load [116]. Sommer et al. [117] compared two units of a 9-cylinder marine dual-fuel engine at the same load with all-cylinders active and cylinder cut-out from 5% to 92% load (steady state), where cylinder cut-out was implemented

at 5% to 15% load by stopping the fuel injection of 3 cylinders. At 5 to 11% load, the engine that implemented cylinder cut-out strategy improved unburned methane emissions by 50 %.

Compared to the cylinder cut-out strategy, the CDA strategy results in yet higher exhaust gas temperature. CDA operation has been widely investigated in gasoline engines, e.g. Ref. [118] and implemented in commercial engines, such as in Audi 4.0-L V8 TFSI engine [119] and Ford 1.0-L EcoBoost engine [120], for improving efficiency at low load operation. Although the benefit of CDA implementation is marginal in diesel combustion, several studies reported the benefits of improved fuel economy during catalyst warm-up period over the late-injection strategy to produce higher exhaust gas temperature due to a richer mixture of combustion [121,122]. However, CDA application can deteriorate noise, vibration, and harshness aspects of engine operation. Several methods to counter this problem have been developed including active engine mounting technology [119], an integrated pendulum damper system on the dual mass flywheel [120] or a selective (rolling) number/order of firing cylinders based on the speed and firing frequency to avoid the system's resonance [123]. The benefits of CDA suggest its potential for dual-fuel combustion to run at low load with a richer mixture (or higher specific load if boost compensated) to improve combustion efficiency and producing higher exhaust gas temperature for promoting effective process within the methane oxidation catalyst.

2.7 The Challenges of Methane Oxidation Catalysis

Anticipating methane slip by implementing the strategy that improves combustion performance should be the first option to minimise aftertreatment cost. However, minimising methane slip from crevice volumes is challenging. Therefore, an effective aftertreatment process is required to suppress the tailpipe emission. The Methane Oxidation Catalyst (MOC) is an aftertreatment device to oxidise the unburned methane to carbon dioxide and water. One or a combination of noble metals such as Palladium (Pd), Platinum (Pt), Rhodium (Rh) are typically used in the substrate [124–129]. However, such systems are not widely available and typically readily suffer from sulphur poisoning leading to premature unit failure.

The methane conversion process in a MOC typically requires relatively high temperature to perform with high conversion [127], which is challenging for lean-burn dual-fuel operation, which produces exhaust gas temperature of less than 400°C over a significant proportion of the drive cycle. A study of MOC performance by Worth et al. [125] compared six samples of MOCs in a simulated dual-fuel exhaust gas using exhaust gas of a diesel combustion from a 4-cylinders diesel engine with injected methane into the pipe at 5000 ppm, 4.98 % water vapour content and 30,000 h^{-1} Gas Hourly Space Velocities (GHSV). These workers reported a catalyst sample

that required the lowest temperature to convert 50% of methane in the exhaust gas (termed T_{50} or catalysts' light off temperature) of 355°C, which was made of high platinum group metal content (both Pd and Pt) with a ratio of Pd/Pt= 6/1 and the largest catalyst washcoat surface area, albeit with high cost as a consequence. The test with a cheaper Pd catalyst (without platinum) required a higher T_{50} of 410 °C [125]. In a patent of a MOC filed by Tanev et al. [124], a sample of Palladium catalyst, supported with Zirconia (Zr), performed the lowest T_{50} of 387°C (tested in the gas stream with 2000 ppm of CH_4, 15 $\%_{vol.}$ of water vapour and GHSV of 50,000 h^{-1}). However, the catalysts' light-off temperature was higher than predominant exhaust gas temperature from dual-fuel operation, for example, the one from Volvo D13 HD engine under a WHTC cold start test, illustrated in *Figure 2.15*. Therefore, overall an innovative dual-fuel strategy is required to produce a high exhaust gas temperature.

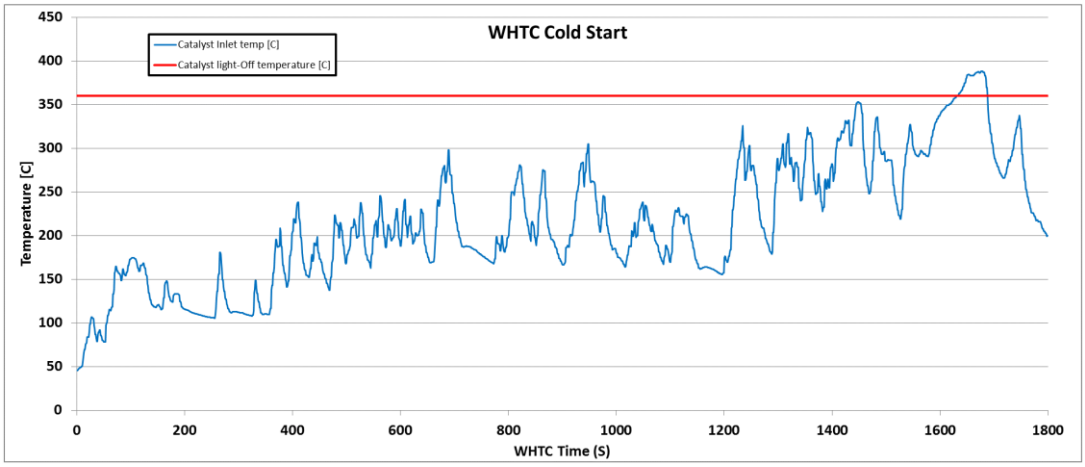
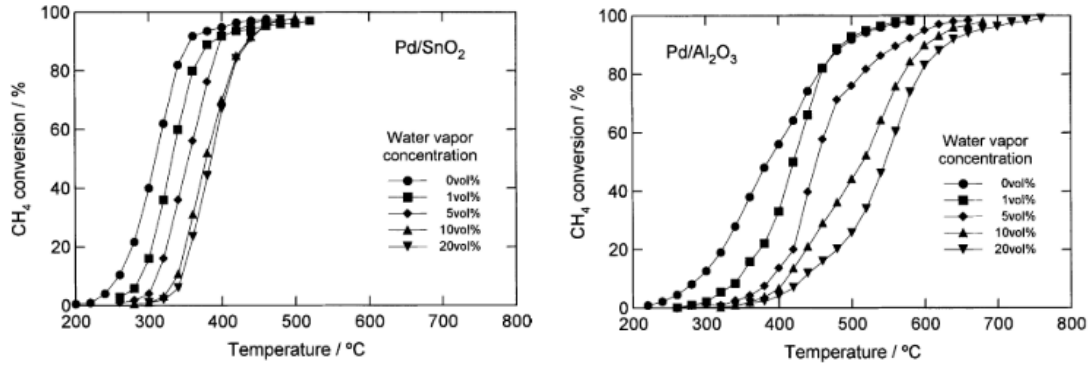


Figure 2.15. Pre-catalyst exhaust gas temperature profile of a 13 litre US2010 compliant dual-fuel truck operating in dual-fuel mode over the WHTC [130]

The challenge for an effective process within a MOC is not only the high exhaust gas temperature requirement but also water content in the exhaust gas [125–129], transient conditions of cyclic oxidation/reduction in the engine and relatively low methane concentration [126]. Water vapour acts as an inhibitor to the oxidation process. Gholami et al. [126] described several mechanisms on how H_2O has detrimental impacts to catalyst performance. Firstly, H_2O adsorption by the catalyst inhibits the methane oxidation. Secondly, $Pd(OH)_2$ formation results in catalyst deactivation. Thirdly, H_2O assists the sintering process at high reaction temperature. In a study by Gelin et al. [127], 10 $\%_{vol.}$ of H_2O decreased the CH_4 conversion in an aged Pd/Al_2O_3 catalyst by 60% (tested at 643 K) and in the aged Pt/Al_2O_3 catalyst by 25% (tested at 843 K). Kikuchi et al. [128] investigated the impact of water vapour concentration on the methane conversion Pd/SnO_2 and Pd/Al_2O_3 catalysts. Some of the results are illustrated *Figure 2.16*. Reducing water vapour concentration passing through the Pd/SnO_2 catalyst from 10 to 1 $\%_{vol.}$

reduced T_{50} by ~60 °C. Meanwhile, reducing water vapour from 10 to 1 $\%_{vol.}$ reduced T_{50} of a Pd/Al_2O_3 catalyst by ~90 °C. As an integral part of methane slip mitigation, removing water content from the exhaust gas is an attractive feature to promote an efficient methane conversion process within a MOC, albeit challenging to implement in a real HDV engine.



(a) (b)

Figure 2.16. Catalytic combustion of methane over 1.1 %(mass) of Pd/SnO_2 (a) and Pd/Al_2O_3 (b) with different concentrations of water vapour [127]

2.8 Summary

Decarbonisation of the HDV sector requires strategic measures to minimise greenhouse gases and provide the most attractive options for the market on a cost versus benefit basis. While electric solutions remain under development, at the time of writing this thesis there is a general consensus that full electric long-range trucks are not viable on a life cycle basis unless infrastructure such as catenary supply is developed at considerable cost. Hydrogen IC engines and fuel cells remain of interest but incur significant challenges in terms of hydrogen production, storage, round trip efficiency and infrastructure. In the short to medium term, natural gas is a highly attractive and retrofit viable solution, with excellent potential to be displaced by biogas in the longer term. Several approaches exist for efficient combustion and low emissions, with dual-fuel one such promising approach also allowing full diesel fall back where natural gas infrastructure is not available. In addition to large trucks, the technology is also attractive for marine and stationary power generation. For retrofit, the key challenge is addressing some of the common pitfalls of premixed dual-fuel operation including poor low load combustion and high methane slip, which was the main focus of the currently reported work.

Chapter 3 Experimental Setup

3.1 Introduction

The experimental apparatus adopted within the currently reported work is described in this chapter. Firstly, the experimental facilities including the equipment in the a) light duty engine test rig b) heavy duty engine test rig and c) exhaust gas analysers are described. In the second section, the key characteristics of the diesel and gaseous fuel used in the experiments are described. Thereafter a description of data processing and associated preliminary analysis is presented. The chapter is concluded with a concise summary of the approach adopted.

3.2 Experimental Facilities

The currently reported work involved the use of two engine test rigs for light duty and heavy duty respectively. The following section includes concise descriptions of the specific rig apparatus followed by an overview of the common equipment adopted.

3.2.1 Light Duty Engine Test Rig

A Ford 2.2 litre 'Puma' diesel engine was installed in the light duty engine test rig for both diesel single fuel and dual-fuel gas/diesel research. The test rig incorporated a DC dynamometer for controlling the speed and load and was accompanied by a standard industry set up for coolant fluid control and key measurements of torque, fuel consumption, engine performance and emissions. A schematic representation of the setup is provided in *Figure 3.1*. The engine coolant was controlled using a typical pit-water indirect heat exchanger arrangement, with control within ±2 °C. The compressed air was cooled by a gas-to-liquid heat exchanger as an intercooler.

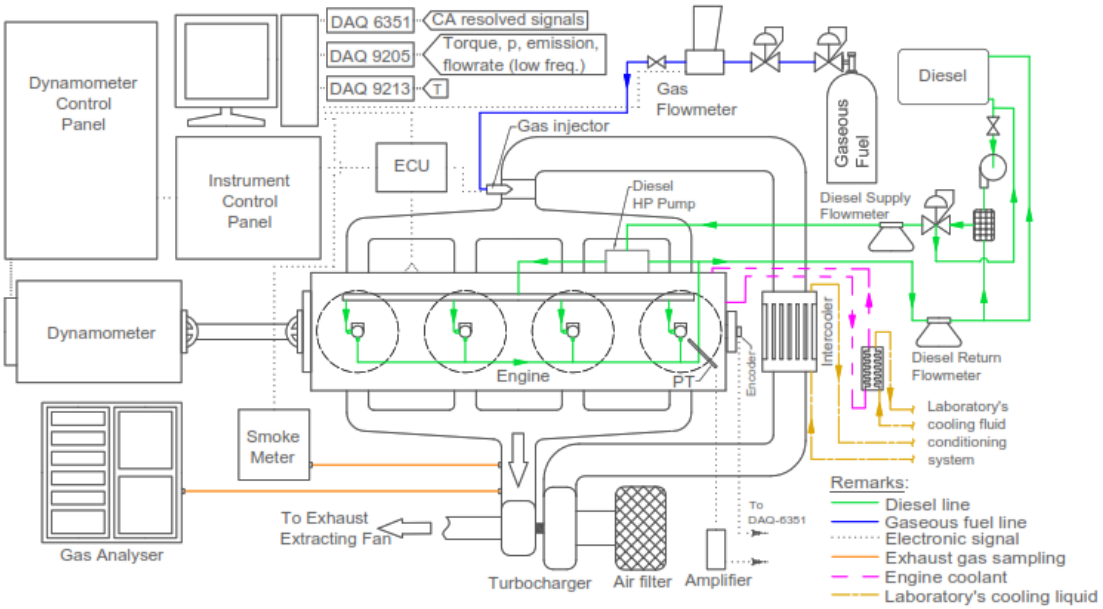


Figure 3.1. Schematic diagram of the light-duty engine test rigLight

3.2.1.1 Light Duty Engine and Dynamometer

The test engine adopted was a model year 2010 Euro 5 four-cylinder 2.2 Litre Ford Puma diesel equipped with common rail direct fuel injection, a variable geometry turbocharger and cooled external EGR. The engine was previously supplied to the university by Revolve Ltd, who adopted this engine to dual-fuel operation of Diesel-Hydrogen in previous UK government funded work with Ford, with the intent of gas conversion of future light commercial vehicles such as the Transit. Key details of the engine specification are set out in *Table 3.1*. The engine was equipped by Revolve with gaseous port fuel injection and associated control, as described in more detail later on.

Brand/Type	Ford/Puma
Swept volume	2198 cc
Bore	86 mm
Stroke	94.6 mm
Connecting rod length	155 mm
Compression ratio	15.5:1
Firing order	1-3-4-2
Injector type/nozzle no.	Piezoelectric/6 holes
Max. rail pressure	1800 bar

Table 3.1. The light-duty diesel engine specification.

A David McClure DC Dynamometer with motoring and absorbing capability was coupled with a propeller shaft to the engine's flywheel. The maximum capacity of the dynamometer was 90 kW at 3000 to 4000 rpm. The dynamometer speed was controlled via a DC control unit that kept it steady (±10 rpm) against changing torque produced by the engine. The dynamometer also

motored the crankshaft for starting the engine then held the crank speed in the absorbing mode as soon as the engine firing.

3.2.1.2 Fuel Delivery System of Light Duty Engine

The fuel delivery system in the light-duty engine test rig consisted of diesel fuel system and gaseous fuel system, as illustrated in *Figure 3.2*. The system enabled the engine to be run either in diesel-only operation or dual-fuel diesel-natural gas operation. The diesel fuel line is shown in the green line. A low-pressure feed pump directed the diesel fuel from a storage tank to the fuel filter. A pressure regulator maintained the pressure at 4 bar before the flowmeter on the supply line to provide 3 barG (±0.5) fuel pressure before the engine's high-pressure pump. A pair of Coriolis flowmeters were used to measure the fuel flowrate to and from the test engine. A Micro Motion CMFS010M was used on the supply line and a Micro Motion CMFS015M on the return line measuring the fuel return from high-pressure pump and injectors. The details of flowmeters' measurement range and accuracy are described later in the instrumentation section.

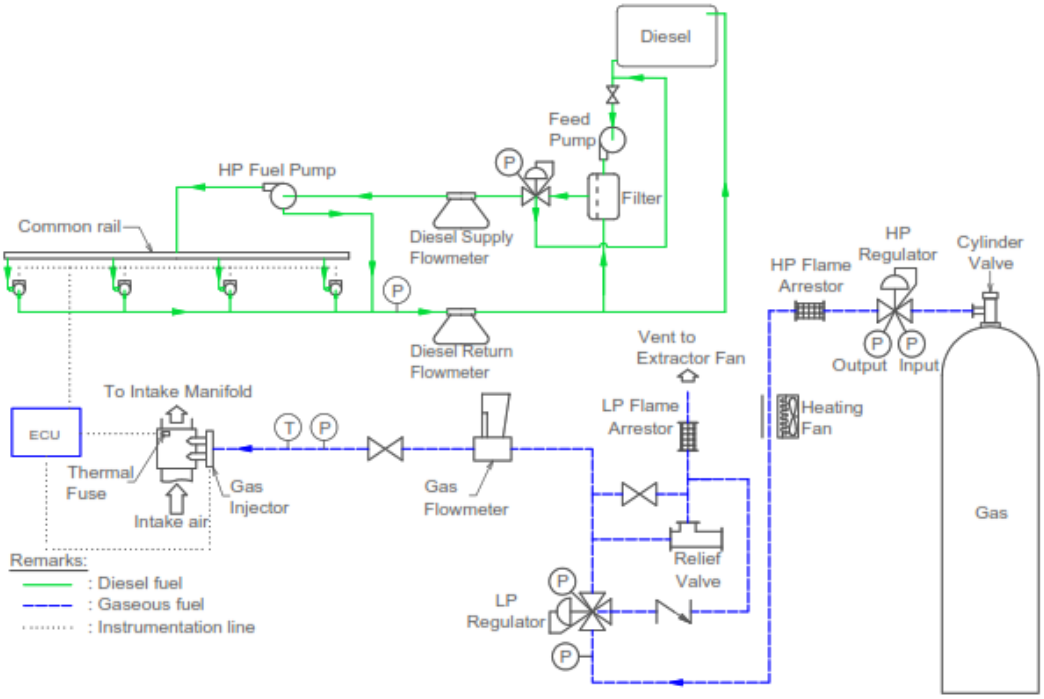


Figure 3.2. Diesel and gaseous fuel delivery system in the light duty engine test rig

The key parts of the gaseous fuel delivery line are illustrated in *Figure 3.2* by the blue line. Several safety devices such as flame arrestors, pressure relief valve and a thermal fuse were in place to ensure system safety during dual-fuel operation. The system was built by Hegab [131] and was not modified during this study. The compressed gas was supplied from a cylinder at 200 barG maximum pressure through the supply line with a High Pressure (HP) regulator at the

outlet of the gas bottle to reduce the pressure to 15 barG (±0.5). After reducing the pressure through the regulator, a heating fan was used to heat up the pipeline against the Joule-Thomson effect, where reducing gas pressure resulted in decreasing gas temperature. Downstream, a Low-Pressure (LP) regulator decreased the pressure further to 6 (±0.5) barG, which was the working pressure of the fuel injector. The gas consumption was measured using a Bronkhorst F-113AI-M50 thermal mass flow meter that communicated with the controller PC via an add-on (developed by Bronkhorst) which was run in a Labview Virtual Instrument (VI). At the end of the gaseous fuel delivery line, the gas injector was installed at the inlet of the intake manifold. The operator controlled the gas injection using NIRA commercial software (in the controlling computer) as an interface of the Engine Control Unit (ECU). Details of the gaseous fuel used in this study will be described later on.

3.2.1.3 Instrumentation of The Light Duty Engine Test Rig

The engine speed was controlled through a dynamometer speed controller at the control panel. To start the engine, the dynamometer drove the engine crankshaft to a certain speed. As soon as the ignition switch was turned on to enable diesel injection, the engine started firing and the dynamometer absorbed the produced torque to hold the speed. The engine torque was controlled through an electric controller “wheel” that worked in principle like the pedal signal in the car, controlling the total fuel quantity. Meanwhile, details of the diesel injection, such as common rail pressure, percentage of pilot/main injection and dwell time, were managed via NIRA-rk software. During the dual-fuel tests, the duration of gaseous fuel injection was controlled via NIRA-rk. The required diesel quantity was adjusted via the diesel electronic controller wheel, while the substitution ratio was monitored in the VI.

The in-cylinder pressure was measured using a Kistler 6055C piezoelectric pressure transducer fitted flush in the glow plug hole of cylinder number 1. The signal from the pressure transducer was amplified using a Kistler K5011 charge amplifier. The pressure transducer was calibrated with a Budenberg deadweight tester under steady state measurement, rated up to 200 barA. This was deemed as sufficient for measurement at low load operation under diesel and dual-fuel combustion.

Pegging of the in-cylinder pressure measurement to produce an absolute pressure was performed using the measured intake manifold pressure at a crank angle position at BDC intake ± 5 °CA as the reference. The intake manifold pressure was measured using a Kulite PT-2054 amplified pressure transducer. Meanwhile, the oil pressure was measured using a Kulite PT-2028 amplified pressure transducer. All pressure transducers were calibrated with the Budenberg deadweight tester under steady state measurement before installation.

Monitoring of the crankshaft's Top Dead Centre (TDC) and Crank Angle (CA) position was performed using a Hohner W2D11R optical shaft encoder with 0.5 °CA increment. The offset measurement between encoder's signal in every revolution (so called "encoder TDC") and the exact engine TDC was carried out using AVL TDC (capacitive) probe. The voltage produced by measuring probe indicated the distance between the probe-end and the piston surface. The TDC offset was the duration between peak voltage as engine TDC indicator and the rising signal of "encoder TDC". The offset value was used in the acquisition program to produce the accurate crank angle degree definition. Afterwards, the recording of in-cylinder pressure was performed under motoring at warm engine temperature. The average of in-cylinder pressure recorded shown that the peak pressure was at 0.8 °CA before the engine TDC, as a defined "thermodynamic loss angle".

The crank-angle resolved signals from the in-cylinder pressure, intake manifold, current clamp and encoder were supplied to a X-series NI USB-6351 data acquisition module. Both signals of TDC mark and half degree mark from the encoder were used as a "clock timer" for data acquisition. Meanwhile, lower frequency signals from the load cell, pressure transducer at oil gallery, gas analyser and Coriolis flowmeters were captured by a NI-9205 analogue input data acquisition device which was attached to the NIDAq-9172 chassis. Temperatures of the gaseous fuel supply, intake manifold, exhaust manifold, engine coolant and lubricating oil were measured by type-K thermocouples and the signals were supplied to the PC via a NI-9213 module, which also connected to the NIDAq-9171 chassis. These low frequency parameters were measured at 100Hz. The signal processing, data monitoring and recording during engine operation were carried out by a VI in the Labview® software that was also used to operate the gaseous fuel flow meter and the smoke meter during dual-fuel tests. Details of the measurements and equipment used in the light-duty engine test rig are described in *Table 3.2*.

DAq. Device	Measurement	Equipment	Range	Accuracy
NI USB-6351	In-cylinder pressure	Kistler 6055C (with Kistler K5011 charge amplifiers)	0 to 250 barA	≤±0.5 % of Full Scale (FS)
	TDC and Crank Angle	Hohner W2D11R		0.5 °CA
	Intake manifold pressure	Kulite PT-2054	0 to 4 barA	0.01%
NI-9205 (on NI-cDAq9178 chassis)	Diesel fuel supply flowrate	Micro Motion CMFS010M	0 to 110 kg/h	±0.25% of Reading (Rd)
	Diesel fuel return flowrate	Micro Motion CMFS015M	0 to 330 kg/h	±0.25% Rd
	Oil pressure	Kulite PT-2028	0 to 7 barA	0.01%
	Dynamometer Load Cell (arm=0.255 m)	BLH Nobel KIS3-5kN	0 to 5 kN	0.02% FS
	Gaseous fuel flowrate	Bronkhorst F-113AI-M50	4 to 750 l_n/min (based on air)	± 0.5 % Rd plus ± 0.1% FS
NI-9213 (on NI cDAq-9171 chassis)	Temperature	K-type thermocouples	-200 to 1250 °C	Above 0 °C: 2.2 °C or 0.75%, below 0 °C: 2.2°C or 2.0%.

Table 3.2. Instrumentations of the light duty engine test rig

3.2.2 Heavy Duty Engine Test Rig

The heavy duty engine test rig was equipped with a 6-cylinder heavy duty diesel engine, AC dynamometer, diesel and gaseous fuel delivery system, instrumentations, as well as the exhaust gas analysers. A schematic diagram of the heavy duty engine test rig is illustrated in *Figure 3.3*. The coolant radiator, intercooler and fan assembly were installed in front of the engine to cool down the engine coolant and compressed air respectively with the air flow provided by the fan. A device called an "Optimiser" was placed after the ECU to manipulate signals to the diesel injectors (will be described in detail later on). The ambient temperature in the test cell was managed via an air ventilation system using a paired roof mounted air supply fan and air extracting fan with 13.3 m^3/s of maximum capacity each. Considering maximum heat rejection by engine through radiation, coolant heat exchanger, and charge air cooler at rated power (2200 rpm) by 204 kW, this would increase the ambient temperature by ~12 °C (higher than supply air temperature). As the work was focused upon part load improvement this limitation was deemed acceptable.

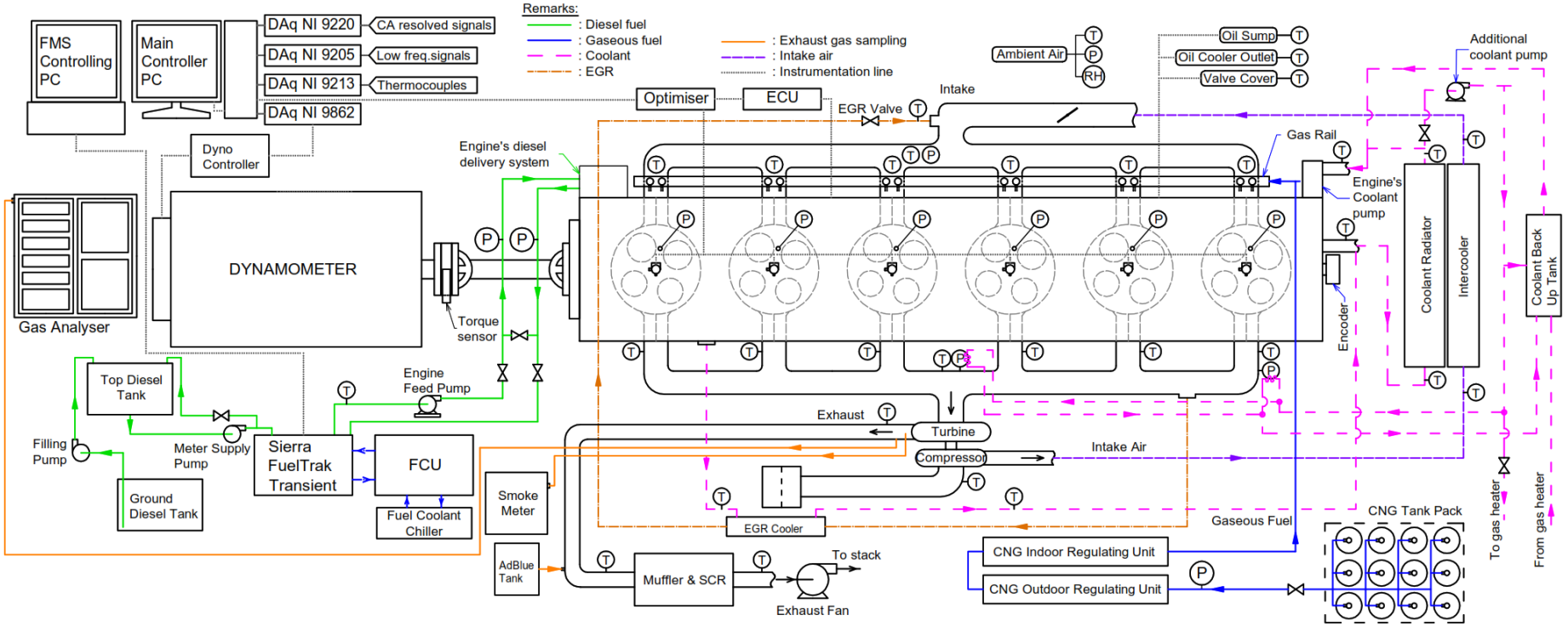


Figure 3.3. Schematic diagram of heavy duty engine test rig with simplified fuel delivery line

3.2.2.1 Heavy Duty Engine and Dynamometer

Towards the start of the PhD a MY 2017 Volvo Penta TAD873VE 6-cylinder inline diesel engine was installed in the heavy duty engine test rig as an entirely new test cell facility (prior empty room). The engine specification is described in *Table 3.3*. The engine was manufactured for running with diesel fuel as a stationary generator set but has a common architecture to the marine variant of the engine. The engine was connected to a Schorch AC dynamometer with dual function for motoring and absorbing. The dynamometer's maximum capacity was 400 kW at 2000 to 3700 rpm. It was capable for running either in steady or transient operating condition.

Brand/Type	Volvo/TAD873VE
Max. Power	235 kW at 2200 rpm (without fan) 220 kW at 1800 (with fan)
Max Torque	1310 Nm at 1450 rpm
Swept volume	7.70 litre
Bore	110 mm
Stroke	135 mm
Compression ratio	17.5:1
Firing order	1-4-2-6-3-5
Injector type/nozzle no.	Piezoelectric/7 holes
Max. rail pressure	2000 bar

Table 3.3. The heavy duty diesel engine specification

3.2.2.2 Fuel Delivery System of Heavy Duty Engine Test Rig

A schematic diagram of the diesel fuel delivery system is illustrated in *Figure 3.4*. Diesel fuel in the reserve tank was pumped to the main supply tank that provided diesel fuel for the engine via a Sierra FuelTrak Transient unit as the Fuel Measurement System (FMS) used in the test rig. The FMS was equipped with a Fuel Conditioning Unit (FCU) that maintained fuel temperature at 25 °C (±2) by passing the fuel to several liquid-to-liquid heat exchangers. To keep the FCU performance, the system was equipped with a chiller that maintained the conditioning liquid temperature of FCU.

Diesel fuel from the FMS was pumped by a feed pump to the engine primary fuel filter. The filtered fuel was then used to cool down the ECU before passing through the engine's low-pressure pump, main filter and high-pressure pump. The high-pressure pump provided the pressurised fuel up to 2000 bar for the common rail that distributed the fuel to each injector. The return fuel from main filter, common rail, and injectors passed back to the Sierra Fuel Trak Transient and conditioned within the FMS to maintain the supply temperature. The working principles of the Sierra FuelTrak Transient unit is described later in more detail.

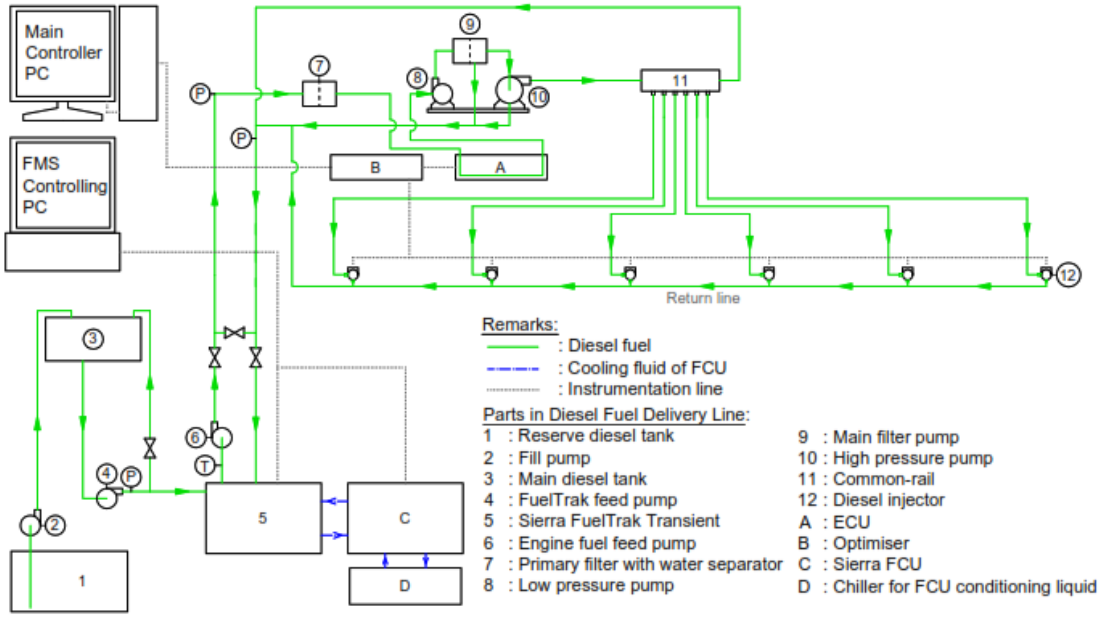


Figure 3.4. Diesel fuel delivery system of heavy duty engine test rig

The Sierra FuelTrak Transient FMS unit consisted of a Coriolis flowmeter for dynamic measurement combined with a gravimetric type of fuel consumption measuring device (Sierra FuelTrak 1000) for steady state measurement. Both flowrate measurement devices worked together to maintain the system's performance depending on the operating conditions. A schematic diagram of fuel measurement by the Sierra FuelTrak Transient unit is illustrated in *Figure 3.5*. The fuel feed from the main supply tank was regulated by a control valve and a fill solenoid valve to maintain the fuel level in the Fuel Measurement System (FMS) vessel in the gravimetric system within a range of level. The engine feed and return fuel passed directly from and to the gravimetric system. To maintain the fuel supply temperature, liquid-to-liquid heat exchangers were fitted in several places such as prior to the fill solenoid valve, on the engine feed line and on the engine return line. The temperature of the conditioning liquid for the heat exchangers was maintained by a Sierra Fuel Conditioning Unit (FCU1000). The Sierra FuelTrak Transient and Sierra FCU1000 were operated by CADET 14.4b software (supplied by Sierra) installed in the FMS controlling PC. The analogue signals of fuel flowrate and temperature from the FMS were sent to the data acquisition device for post-processing in the Labview VI.

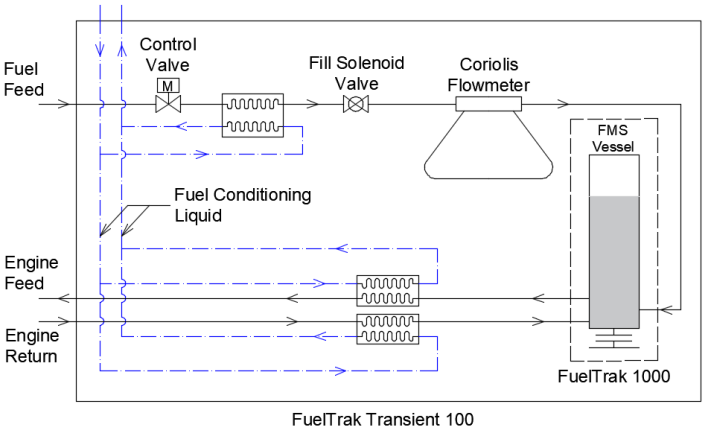
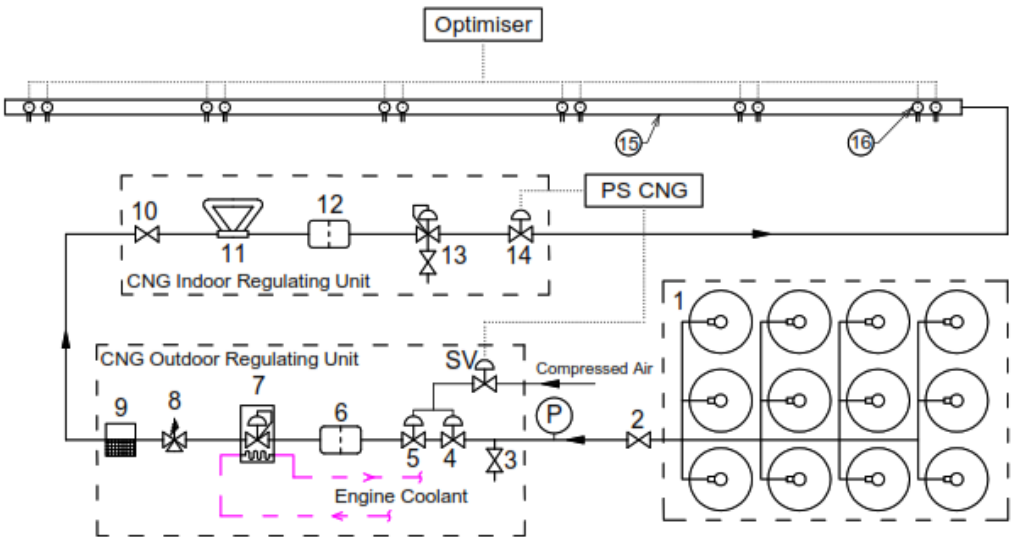


Figure 3.5. Schematic diagram of Sierra FuelTrak Transient unit

The gaseous fuel delivery system of the heavy duty engine test rig with the outdoor and indoor installation is illustrated in *Figure 3.6*, *Figure 3.7* and *Figure 3.8*. The gaseous fuel from a parallel configuration ("rack") of 12 gas bottles (CNG Tank Pack) outside the building was directed to the engine through a pressure gauge, drain-valve, a pair of shut-off valves, gas filter, high pressure regulator, pressure relief valve and flashback arrestor. This assembly was sourced under sub-contract from Clean Air Power, who had considerable prior experience of dual-fuel installations. The gas heater attached to the high pressure (HP) regulator used the engine coolant to heat up the gas out of cylinder which drops its temperature due to Joule-Thomson effect. Meanwhile, the indoor installation consisted of stop valve, Coriolis flowmeter, filter, purge valve and shut-off valve assembly. The LP regulator reduced the pressure to 9 bar for the gaseous fuel rail. The indoor shut-off valve (No. 14) and the outdoor Solenoid Valve (SV) for compressed air that opened and closed the shut-off valves were enabled by a power supply in the control room. On the engine, a gaseous fuel rail distributed the gas to the injectors at each of the inlet of intake runner (two injectors per cylinder). Parts of the indoor and outdoor installations are illustrated in *Figure 3.7* and *Figure 3.8*.



Parts in Gaseous Fuel Delivery Line:

1 : CNG Tank Pack
2 : Stop valve 1 (**Tank Pack Hand Valve**)
3 : Drain valve
4 : Shut-off valve 1 (pneumatic)
5 : Shut-off valve 2 (pneumatic)
6 : Filter 1
7 : HP regulator with gas heater
8 : Pressure relief valve
9 : Flashback arrestor
10: Stop valve 2 (¼ **Turn Hand Valve**)
11: Gas flowmeter
12: Filter 2
13: LP regulator with purge valve
14: Shut-off valve assembly
15: Gaseous fuel common rail
16: Gaseous fuel injector
SV: Solenoid valve
PScng: Power supply, controls SV and valve 14

Figure 3.6. Schematic diagram of gaseous fuel delivery system in the heavy duty engine test rig

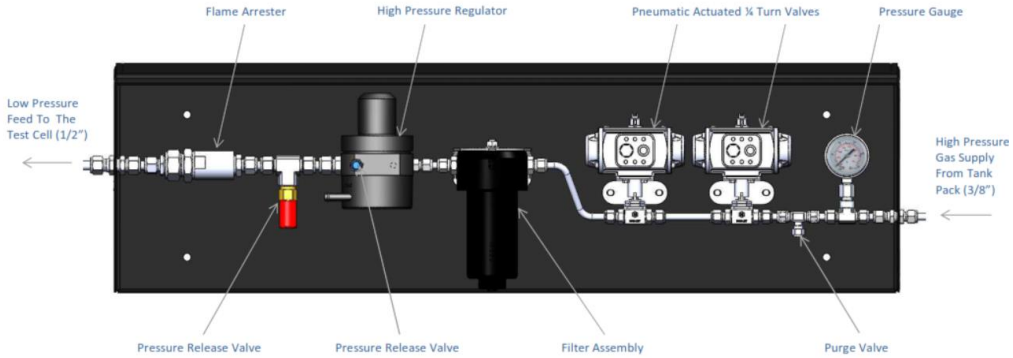


Figure 3.7. Illustrated parts of gaseous fuel outdoor installation (taken from Ref. [132]*)*

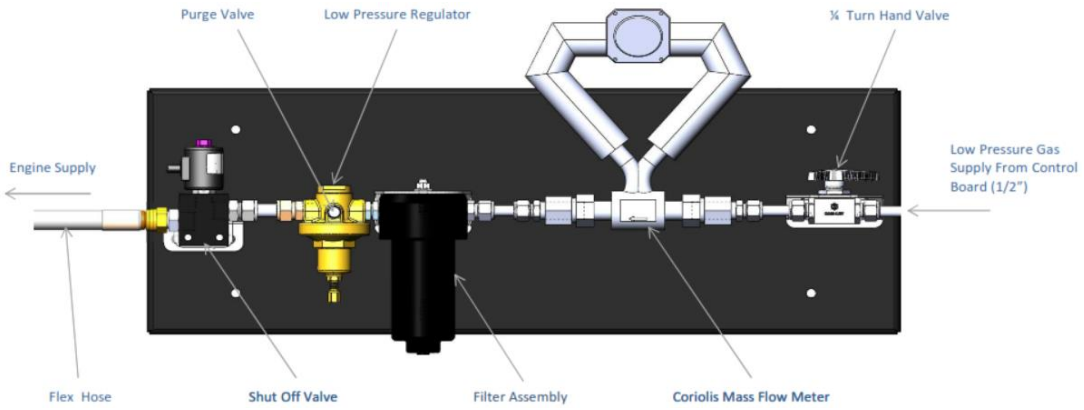


Figure 3.8. Illustrated parts of gaseous fuel indoor installation (taken from Ref. [132]*)*

A G-Volution optimiser as a piggyback ECU was fitted between engine's original ECU and fuel injectors. It worked to interrupt and override the signal to diesel injectors during dual-fuel test. The optimiser worked with setting parameters uploaded into its memory. The setting was used in the engine operation once the 'optimiser controlling mode' was activated, otherwise the diesel injection signal from the ECU was kept as originally prescribed by the engine manufacture. Changing the mode from 'ECU control mode' to 'Optimiser controlling mode' and vice versa was done in a software installed in the control computer. The software was initially developed by R2G2 company in 2019 for dual-fuel operation in a rail engine application, hence it included relatively simple mapping and control parameters. However, to fulfil the research requirement, it needs to be developed in more advanced version to provide fully customisable diesel and gaseous fuel injection parameters. Unfortunately, when this thesis was written and finalised, the optimiser software was still under development (partially delayed due to Covid). Therefore, the dual test could not be performed in the engine in a research-level operation.

3.2.2.3 Instrumentation of Heavy Duty Engine Test Rig

The engine speed and torque were controlled via dyno control panel either using manual knobs and switches available in the control panel or using a Labview VI that communicated with the PC via NI9862 data acquisition device. The torque was measured by a HBM T12 torque sensor. The dyno controller could run the dynamometer either in motoring or absorbing mode, set in the beginning before starting the test. In absorbing mode, the dynamometer could be set to either controlling the speed or torque.

The in-cylinder pressure was measured by Kistler 6125C piezoelectric pressure transducers that were amplified by Kistler charge amplifiers, type 5064D, controlled via Kistler SCP 2852 A/B software in the controlling PC. The transducers were flush mounted with the cylinder head to minimise ringing that might happen if it is installed on a mounting with narrow

passage. Prior to the installation, the pressure transducers were calibrated in a similar way to the ones for light duty engine test rig, as presented in Section 3.2.1.3.

Details of the measuring devices used in the heavy duty engine test rig are listed in *Table 3.4*, including data acquisition devices to capture the signals from the respective devices. The NI 9220 data acquisition device was used to process the crank angle resolved data such as encoder signal and pressure transducers. The lower frequency signals such as exhaust gas concentration from gas analysers, humidity probe and fuel flowmeters were captured by a NI 9205. Meanwhile, two NI 9213 units processed the signals from thermocouples located at the measurement points shown in *Figure 3.3*. A NI 9862 data acquisition device was used for importing and exporting data between the dynamometer control panel and controller computer. All of the data acquisition devices were installed on a NI cDAq-9179 data acquisition chassis. The data acquisition devices were connected to the computer which processed the data in a VI within the Labview software. Digital data was converted by codes in the VI to enable monitoring, ongoing data analysis, and recording during the experiments. The formulas for converting the data will be described in the next section regarding data post-processing.

Data Acquisition Device	Parameter	Equipment	Range	Accuracy
NI 9220	TDC and crank angle	Hohner Encoder	-	0.5 °CA
	In-cylinder pressure (of all 6 cylinders)	Kistler 6125C	0 – 300 bar-Absolute (barA)	≤±0.5 % FS
	Intake manifold pressure	Kulite EWCT-12-312M-10BARA	0 – 10 barA	≤0.5% FS
	Intake runner pressure			
	Exhaust manifold pressure	Kulite EWCT-12-312M-10BARA (Water cooled)	0 – 10 barA	≤0.5% FS
	Exhaust runner pressure			
	Diesel injection current	Fluke i30s AC/DC Current Clamp	Max. Current: 20A RMS Output: 100 mV/A	± 1 % of Reading (Rd) ± 2 mA; Output sensitivity: 100 mV/A
	Gas injection current			
	ECU to optimiser current			
	Optimiser to injection current			
NI 9205	Oil pressure	Druck PMP-4311	0 – 10 barA	0.1% FS
	Diesel flowrate	Sierra FuelTrak Transient (including FuelTrak 1000 gravimetric)	Max. consumption: 100 kg/h; Max. flow to engine: 300 kg/h	Instantaneous: ±0.5% Rd (for 10 to 100 kg/h) Average: ±0.1% Rd
	Gaseous fuel flowrate	Micro Motion CMF025M	Max. 310 kg/h and 440 Nm^3/h) (based on natural gas [133])	±0.25% of rate (linearity 0.20% of rate)
	Ambient temperature	Vaisala HMP110	Temperature: -40 to +80 °C	At 0 to +40 °C: ±0.2 °C, at −40 to 0 °C and +40 to +80 °C: ±0.4 °C
	Ambient relative humidity		Relative humidity: 0 to 100%	±1.5%RH (0 to 90%RH)
	Ambient Pressure	Diplex barometer	930 to 1080 hPa	± 1 hPa
NI 9862	Torque	HBM Stator T12	2 kNm	0% to 20% of nominal torque (M_{nom}): <0.006% Rd; 20% to 60% of M_{nom}: <0.013% Rd; 60% to 100% of M_{nom}: <0.02% Rd;
NI 9213	Temperature at the measurement points shown in Figure 3.3.	K-type thermocouples	-200 to 1250 °C	Above 0 °C: 2.2 °C or 0.75%; below 0 °C: 2.2°C or 2.0%.

Table 3.4. Instrumentation of the heavy duty engine test rig

3.2.3 Measurement of Exhaust Gas Emission

Sample of exhaust gas was taken at the exhaust port after the turbine by two sampling probes, one for the gas analyser and another one for the smoke meter. The sampling gas was passed through a heated line to keep gas temperature at 191 °C and prevented any condensation of unburned hydrocarbon content. In the gas analyser cabinet, as the THC and NO_x were analysed in wet conditions, the sample was kept at high temperature by passing through a Signal 340 distribution oven before each analyser. Meanwhile, for semi-dry analysis of CO_2, CO, O_2, the gas sample was cooled by the Signal 200SM series gas cooler.

All of the exhaust gas constituents either from the light duty engine or heavy duty engine were detected using the same type of devices. CO_2 concentration was analysed using Signal 7000FM Non-Dispersive Infra-Red (NDIR) detectors. Oxygen concentration was analysed using a Signal 8000M Paramagnetic detector. Analysis of NO_x concentration was performed using Signal 4000VM Chemiluminescence Detector (CLD) type gas analyser. Signal 7000FM infrared detectors analysed CO concentration. Total Hydrocarbon (THC) concentration within the exhaust gas of the light-duty engine was analysed using a Signal 3000HM Heated Flame Ionisation Detector (HFID) type, measured up to 4000 ppm Propane Equivalence ($ppmC_3$) during the dual-fuel test. The range and accuracy of the gas analysers are described in *Table 3.5*. Signals from the gas analyser devices were captured by a NI 9205 data acquisition device to be processed in the VI. Apart from exhaust gas analysis, to measure EGR percentage during the tests, the intake CO_2 was measured with a separated Signal 7000FM unit.

Smoke measurement of the exhaust gas was performed using a AVL 415S filter type smoke meter. The device was connected to the controlling computer via a RS-235 port, enabling its operation with the same VI for monitoring the test run. The VI was also used to record the result in Filter Smoke Number (FSN). The smoke meter's range and accuracy are described in *Table 3.5*.

Gas Constituent	Equipment	Range	Accuracy
CO_2	Signal 7000FM NDIR detector	0 to 10%	< ±1 % of FS
CO	Signal 7000FM NDIR	0 to 1%	< ±1 % of FS
NO_x	Signal 4000VM CLD	0 to 3000 ppm	< ±1 % of FS
O_2	Signal 8000M Paramagnetic detector	0 to 25%	±0.01%
Intake CO_2	Signal 7000FM NDIR	0 to 10%	< ±1 % of FS
THC	Signal 3000HM HFID	0 to 3000 ppmC_3	< ±1 % of FS
Smoke	AVL 415S Smoke Meter	0 to 10 FSN	0.002 FSN or 0.02 mg/mm^3

Table 3.5. Gas analyser and smoke measuring devices used in this study

3.3 Test Fuels

The experimental tests in the light duty engine test rig used either Ultra-Low Sulphur Diesel (ULSD) or Shell Gas-to-Liquid diesel (GTL), while methane was used as gaseous fuel used in the dual-fuel tests. In the heavy duty engine, the experimental test was planned to use ULSD and methane/ethane mixture (shown as "gas mix"). The fuels specifications are described in *Table 3.6*.

Property	ULSD	GTL [134,135]	Methane	Gas Mix
Mixture	-	-	99.95% CH_4	CH_4/C_2H_6 in 95/5 %mole
Liquid density at 15 °C (kg/m^3)	820	779		
Gas density at STP (kg/m^3)			0.708	0.749
LHV (MJ/kg)	42.9	44	50	49.78
Cetane Number	45	79.5	-	-
Max. Sulphur (ppm-mass)	10	1	-	-
Auto-ignition temperature (°C)	250	207.2	807	-
Carbon content (% mass)	86.6	84.9	75	66.7
Hydrogen content (% mass)	13.4	15.1	25	33.3

Table 3.6. Properties of fuels for the experiments in this study

In dual-fuel operation, the percentage of gaseous fuel energy to the total consumed fuel energy is called the Substitution Ratio (SR). The calculation involved the measured diesel mass flowrate ($\dot{m}_{Diesel}$), gaseous fuel mass flowrate ($\dot{m}_{Gas}$) and the LHV of respective fuels (LHV_{Diesel} and LHV_{Gas}) as expressed in Equation *(3.1)*.

$$SR = \frac{\dot{m}_{Gas} \times LHV_{Gas}}{\dot{m}_{Gas} \times LHV_{Gas} + \dot{m}_{Diesel} \times LHV_{Diesel}} \quad (3.1)$$

3.4 Data Post-Processing

The recorded data during experimental tests were post-processed to produce other parameters for monitoring during experimental tests or further analysis. The processing was performed by Labview VI or Matlab script using the formulae described in this section.

An additional process was performed on the in-cylinder pressure data. The in-cylinder pressure traces from diesel combustion typically contains signal noise, which is indicated by fluctuating curves after the Start of Combustion (SOC) due to a ringing effect from premixed diesel combustion that resonances in the combustion chamber. This causes difficulties in the analysis of Pressure Rise Rate (PRR) and Heat Release Rate (HRR), since the fluctuation gets worse in the first derivative. Therefore, the in-cylinder pressure traces were filtered using digital low-pass filtering before processed further. Signal analysis with power spectral density using fast Fourier transform was performed to decide the optimum cut-off frequency for the data filtering process on the specific measurement result. The filtered in-cylinder pressure data was processed to calculate the other parameters using the following equations.

3.4.1 Brake Mean Effective Pressure (BMEP)

Brake torque produced by engine is a useful experiment result. However, it would be useful to be converted to BMEP as a comparable load parameter for any engine size. BMEP is expressed in Equation *(3.2)*.

$$BMEP\ (Pa) = \frac{2\pi \times n_r \times T\ (Nm)}{V_d(m^3)} \quad (3.2)$$

Where:

n_r= number of revolutions for a cycle of combustion (2 is used for a 4-stroke engine).

V_d= the engine's displacement volume

3.4.2 Net Indicated Mean Effective Pressure (Net IMEP)

Brake work measured by the dynamometer is used to define the engine performance in general. However, as a result from fuel energy conversion that is transferred through mechanism, there is a certain friction loss in the system. Therefore, further analysis needs to be performed in terms of indicated work that focus on working fluid within the cylinder. The net indicated work of a cylinder ($W_{c,i,Net}$) is an important parameter to get insight of the

working cycle. $W_{c,i,Net}$ is calculated by integrating the multiplication pressure and volumetric increment during a full cycle, which in a four-stroke engine is from the TDC of intake stroke (n) to the next TDC of intake stroke (n+1), as expressed in Equation *(3.3)*.

$$W_{c,i,Net} = \int_{TDCintake(n)}^{TDCintake\ (n+1)} p\frac{dV}{d\theta} \qquad (3.3)$$

The net indicated work is then used in the calculation of Net Indicated Mean Effective Pressure ($Net\ IMEP_{Net}$) to be comparable in any cylinder geometry. The net IMEP is resulted from dividing the net indicated work by cylinder swept volume (V_S) as expressed in Equation *(3.4)*.

$$Net\ IMEP = \frac{W_{c,i,Net}}{V_S} = \frac{\int_{TDCintake\ (n)}^{TDCintake\ (n+1)} p\frac{dV}{d\theta}}{V_S} \qquad (3.4)$$

3.4.3 Combustion Stability Indicator

Processes during the intake, compression, expansion and exhaust strokes in the cylinder, including the fuel injections experience cycle to cycle variation, resulted in varying indicated work of the cylinder. The cycle-to-cycle variation during experimental tests in this study was indicated by the Coefficient of Variation of Net IMEP (COV_{IMEP_N}) from the recorded cycles. COV of Net IMEP is defined as standard deviation of the collected Net IMEP data (σ_{IMEP_N}) divided by mean Net IMEP ($\overline{IMEP_N}$) and multiplied by 100 to express it in percent as expressed by Equation *(3.5)*. The amount of cycle numbers to be processed is described in the respective chapters.

$$CoV_{IMEP_N} = \frac{\sigma_{IMEP_N}}{\overline{IMEP_N}} \times 100 \qquad (3.5)$$

3.4.4 Heat Release Rate Calculation

The in-cylinder charge releases heat during combustion of premixed and directly injected fuels. The heat release calculation of combustion in a cylinder was calculated using the first law of thermodynamics [45]. In a direct injection CI engine, the system is defined as a single open system where:

$$\frac{dQ}{d\theta} - p\frac{dV}{d\theta} + \dot{m}_f h_f = \frac{dU}{d\theta} \qquad (3.6)$$

U in the equation is sensible internal energy of the system and h_f is sensible enthalpy of the fuel. Because $h_{s,f}$≈0, the last part can be neglected. The net heat release rate equals to the

difference between the gross heat release rate in the chamber ($\frac{dQ_g}{d\theta}$) and heat transfer rate to the cylinder wall ($\frac{dQ_{ht}}{d\theta}$).

$$\frac{dQ_n}{d\theta} = \frac{dQ_g}{d\theta} - \frac{dQ_{ht}}{d\theta} = p\frac{dV}{d\theta} + \frac{dU_S}{d\theta} \quad (3.7)$$

If the system inside cylinder is assumed as ideal gas where c_v=du/dT, substitution of dU with ($c_v.dT$) results in:

$$\frac{dQ_n}{d\theta} = p\frac{dV}{d\theta} + mc_v\frac{dT}{d\theta} \quad (3.8)$$

If T is substituted by $T = \frac{pV}{mR}$ where R is assumed constant, then

$$mc_v\frac{dT}{d\theta} = \frac{c_v}{R}\frac{d(pV)}{d\theta} \quad (3.9)$$

Thus, the equation becomes

$$\frac{dQ_n}{d\theta} = \left(1 + \frac{c_v}{R}\right)p\frac{dV}{d\theta} + \frac{c_v}{R}V\frac{dp}{d\theta} \quad (3.10)$$

Replacing $\frac{c_v}{R}$ by its correlation to the ratio of specific heats (γ), where $\frac{R}{c_v} = \gamma - 1$ yields Net of Heat Release Rate (NHRR) as expressed in Equation *(3.11)*.

$$NHRR = \frac{dQ_n}{d\theta} = \frac{\gamma}{\gamma - 1}p\frac{dV}{d\theta} + \frac{1}{\gamma - 1}V\frac{dp}{d\theta} \quad (3.11)$$

Ratio of specific heats (γ) is a function of gas composition and temperature, which is difficult to be accurately defined during the test. According to Heywood [45] that suggest a constant value between 1.3 and 1.35, the appropriate value which produces the most accurate calculation result is not well defined. This study used a constant value γ=1.33 as suggested by Zhao [136]. As a result, the product of the calculation is considered as an apparent (qualitative) value rather than an exact value. Despite the following discussions regarding heat release rate within this thesis refers to the apparent value, it will herein not be mentioned explicitly.

3.4.5 Brake and Net Indicated Efficiency

Brake efficiency is the ratio of brake power (P_{brake}) to the consumed fuel energy for a specific duration as expressed in Equation *(3.12)*.

$$Brake\ efficiency = \frac{P_{brake}}{\dot{m}_{fuel} \times LHV} \quad (3.12)$$

Net indicated efficiency was calculated from net indicated work during an undergoing cycle in a cylinder ($W_{c,i,Net}$), divided by consumed fuel energy per cycle. The net indicated work per cycle can be calculated from Net IMEP multiplied by cylinder swept volume ($V_{s,cyl}$). The net indicated efficiency is expressed in Equation *(3.13)*.

$$Net\ indicated\ efficiency = \frac{W_{c,i,Net}}{\dot{m}_{fuel/cycle} \times LHV} = \frac{IMEP_N \times V_{s,cyl}}{\dot{m}_{fuel/cycle} \times LHV} \quad (3.13)$$

3.4.6 Analysis of Exhaust Gas Emission

Conversion of exhaust gas concentration from concentration to mass flowrate requires the exhaust mass flowrate, either from the calculation or measurement. In this study, the measured fuel mass flowrate and calculated air/fuel ratio were used to produce the exhaust mass flowrate. Stoichiometric air/fuel ratio (AFR_{st}) and air/fuel equivalence ratio (λ) were calculated respectively with Equation *(3.14)* and *(3.15)* from UN ECE Regulation No. 49, Annex 4B [137].

$$AFR_{st} = \frac{138.0 \times \left(1 + \frac{\alpha}{4} - \frac{\varepsilon}{2} + \gamma_s\right)}{12.011 + 1.00794 \times \alpha + 15.9994 \times \varepsilon + 14.0067 \times \delta + 32.065 \times \gamma_s} \quad (3.14)$$

$$\lambda = \frac{\left(100 - \frac{c_{COd} \times 10^{-4}}{2} - c_{HCw} \times 10^{-4}\right) + \left(\frac{\alpha}{4} \times \frac{1 - \frac{2 \times c_{COd} \times 10^{-4}}{3.5 \times c_{CO2d}}}{1 + \frac{c_{COd} \times 10^{-4}}{3.5 \times c_{CO2d}}} - \frac{\varepsilon}{2} - \frac{\delta}{2}\right) \times (c_{CO2d} + c_{COd} \times 10^{-4})}{4.764 \times \left(1 + \frac{\alpha}{4} - \frac{\varepsilon}{2} + \gamma_s\right) \times (c_{CO2d} + c_{COd} \times 10^{-4} + c_{HCw} \times 10^{-4})} \quad (3.15)$$

Where:

α : hydrogen molar ratio (H/C) of the fuel $CH_\alpha O_\varepsilon N_\delta S_{\gamma_s}$

ε : oxygen molar ratio (O/C)

δ : nitrogen molar ratio (N/C)

γ_s : sulphur molar ratio (S/C)

$c_{CO2,d}$: dry CO_2 concentration (%)

$c_{CO,d}$: dry CO concentration (ppm)

c_{HCw} : wet THC concentration (ppm)

The calculated AFR from λ calculation was used to calculate the air mass flowrate ($\dot{m}_{air,w}$) by multiply it with the fuel mass flowrate as expressed in Equation *(3.16)*. Exhaust mass flowrate ($\dot{m}_{exh}$) is the sum of air mass flowrate and fuel mass flowrate as expressed in *(3.17)*.

$$\dot{m}_{air,w} = AFR \times \dot{m}_{fuel} \quad (3.16)$$

$$\dot{m}_{exh} = \dot{m}_{air,w} + \dot{m}_{fuel} \quad (3.17)$$

3.4.6.1 Mass Flowrate Calculation of Exhaust Gas Constituents

Mass flowrate of exhaust gas constituents in this study was calculated using exact equations from UN ECE Regulation No. 49, Annex 4B [137]. In the calculation, the gas concentration from dry measurements such as CO_2, CO and O_2 needs to be converted to wet condition. This was done by multiplying the gas concentration with dry to wet correction factor (k_w) which is expressed in Equation *(3.18)*. NO_x concentration which was already measured in wet condition needs to be corrected with a correction factor for humidity (k_{hD}) as expressed in Equation *(3.20)*.

$$k_{w,a} = \left(1 - \frac{1}{1 + \alpha \times 0.005 \times \left(c_{CO2,d} + c_{CO,d}\right)} - k_{w1}\right) \times 1.008 \quad (3.18)$$

With

$$k_{w1} = \frac{1.608 \times H_a}{1000 + (1.608 \times H_a)} \quad (3.19)$$

$$k_{h,D} = \frac{15.698 \times H_a}{1000} + 0.832 \quad (3.20)$$

Where:

α : hydrogen molar ratio (H/C) of the fuel $CH_\alpha O_\varepsilon N_\delta S_{\gamma_s}$

$c_{CO2,d}$: dry CO_2 concentration (%)

$c_{CO,d}$: dry CO concentration (%)

H_a : intake air humidity (g water per kg dry air)

The specific exhaust gas emission ($\dot{m}_{gas}$) was calculated by Equation *(3.21)*, adapted from the mass emission calculation with exact equations in UN ECE Regulation No. 49, Annex 4B [137].

$$\dot{m}_{gas} = u_{gas} \times c_{gas} \times \dot{m}_{exh} \quad (3.21)$$

Where:

u_{gas} : respective constant of exhaust gas constituent, calculated with Equation *(3.22)*

c_{gas} : concentration of exhaust gas constituent, in ppm

$\dot{m}_{exh}$: exhaust mass flowrate, in kg/s

$$u_{gas} = M_{gas}/(M_{exh} \times 1{,}000) \quad (3.22)$$

Where:

M_{gas} : molar mass of the gas constituent (g/mol)

M_{exh} : the molar mass of exhaust gas (g/mol), calculated with Equation *(3.23)*

$$M_{exh} = \frac{1 + \frac{\dot{m}_{fuel}}{\dot{m}_{air,w}}}{\frac{\dot{m}_{fuel}}{\dot{m}_{air,w}} \times \frac{\frac{\alpha}{4} + \frac{\varepsilon}{2} + \frac{\delta}{2}}{12.011 + 1.00794 \times \alpha + 15.9994 \times \varepsilon + 14.0067 \times \delta + 32.065 \times \gamma_s} + \frac{\frac{H_a \times 10^{-3}}{2 \times 1.00794 + 15.9994} + \frac{1}{M_{air}}}{1 + H_a \times 10^{-3}}} \quad (3.23)$$

Where:

$\dot{m}_{fuel}$: fuel mass flowrate (kg/s)

$\dot{m}_{air,w}$: air mass flowrate in wet basis (kg/s)

H_a : intake air humidity ($g_{water}/kg_{dry\ air}$)

M_{air} : molar mass of air (28.965 g/mol)

3.4.6.2 EGR Percentage

The samples of CO_2 concentration were taken from the intake manifold and from exhaust port after turbine. The concentration data was used to calculate the EGR percentage as expressed in *(3.24)*.

$$EGR\% = \frac{[CO_{2,int}] - [CO_{2,amb.}]}{[CO_{2,exh}] - [CO_{2,amb.}]} \quad (3.24)$$

Where:

$EGR\%$: Percentage of EGR

$[CO_{2,int}]$: concentration of intake CO_2

$[CO_{2,exh}]$: concentration of exhaust CO_2

$[CO_{2,amb.}]$: concentration of CO_2 in the ambient air (assumed at 404 ppm as standard air [45])

3.4.7 Combustion efficiency

The combustion inefficiency is indicated by the ratio of energy content of combustible constituents within exhaust gas (i.e., CO and UHC, with trace H_2 neglected at lean combustion [138]) to the consumed fuel energy. This is used to calculate combustion efficiency (in %) as expressed in Equation *(3.25)*. The mass flowrate of CO and Unburned Hydrocarbon (UHC) were calculated by the algorithm described above. In the dual-fuel analysis, LHV of methane

was used, considering its predominance in the UHC due to poorer combustion of gaseous fuel than diesel.

$$Combustion\ efficiency(\%) = 100 - \left(\frac{\dot{m}_{CO} \times LHV_{CO} + \dot{m}_{UHC} \times LHV_{UHC}}{\dot{m}_{fuel} \times LHV_{fuel}} \times 100\right) \qquad (3.25)$$

3.5 Summary

The experimental methodology for this study was described in this chapter. The work made use of a 4-cylinder light duty CI engine test rig to perform experimental tests of conventional diesel combustion and premixed dual-fuel combustion. Also presented in this chapter are details of a newly built heavy duty engine test facility with a 6-cylinder CI engine that was prepared for dual-fuel testing. However, dual-fuel testing was not possible within the research due to delays in commissioning a third party dual-fuel controller (with the delay partially attributable to Covid). Nonetheless the engine was evaluated in conventional diesel mode, with comparisons then made between other test engines ahead of dual-fuel simulation using data obtained from these alternatives.

Chapter 4 Phenomenological Modelling of Dual-Fuel Combustion in a Compression Ignition Engine

4.1 Introduction

The goal of the simulation work was to develop a correlated one-dimensional thermodynamic engine model for the Volvo Penta HD diesel engine to operate in dual-fuel to assess advanced engine operating strategies to overcome some of the known issues of dual-fuel operation at low load. In particular, the specific objective was to use this model to compare the potential benefits of cylinder deactivation versus Miller cycle operation as a means to efficiently elevating exhaust temperatures under part load urban conditions. The prototype methane oxidation catalyst to be later on fitted to this engine had a 'T50' (50% conversion efficiency) operating temperature of ~380°C, which was relatively high for this otherwise diesel engine architecture. Hence, the elevated temperatures would help reduce methane slip. An additional challenge was inability to remain in dual-fuel operation at the lowest engine loads. In prior work undertaken by Cairns and May [105], it was found that the minimum engine load where dual-fuel operation (with substitution ratio of 83%) could be sustained at typical urban engine operating speeds (e.g. ~1200rpm) was around 6 bar net IMEP. Hence the adoption of higher specific engine load under cylinder deactivation was equally highly attractive for this reason.

In addition to valve operating strategies, the work also considered the potential benefits of electric supercharging as a means to achieving the cylinder deactivation strategy with lean operation for higher efficiency. Finally, a new approach to modelling thermal barrier coatings was also validated, which were under investigation in a parallel funded project and being considered as an additional means to elevate exhaust temperature to help maintain methane oxidation catalyst light-off. All of this modelling work was undertaken using the industry standard one-dimensional software GT-Power (version 2020).

The engine model in this thesis is described firstly in general, followed by the details of the engine sub-systems, components and relevant processes. Secondly, combustion modelling is described with the calibration procedure performed relative to experimental results. The chapter is closed with key conclusions.

4.2 Engine Model and Details

The dual-fuel combustion performance of a 6-cylinder heavy duty engine was simulated using the widely adopted platform, GT Power. The complete setup of the engine model is

illustrated in *Figure 4.1*, which was virtually equipped with an electric supercharger (eSupercharger) to provide intake air boosting to simulate the CDA strategy under variably lean boosted conditions. Parts with a more conventional generator powered eSupercharger, shown in the dashed box (a), were replaced by parts in dashed box (b) in the simulation, with the strategy of using a battery to directly power the eSupercharger, as might be the case in a mild hybrid setup. Details of the engine parts such as intake and exhaust port, intake and exhaust valves, eSupercharger, deactivation logic, fuel injection, thermal and friction simulation are described later on.

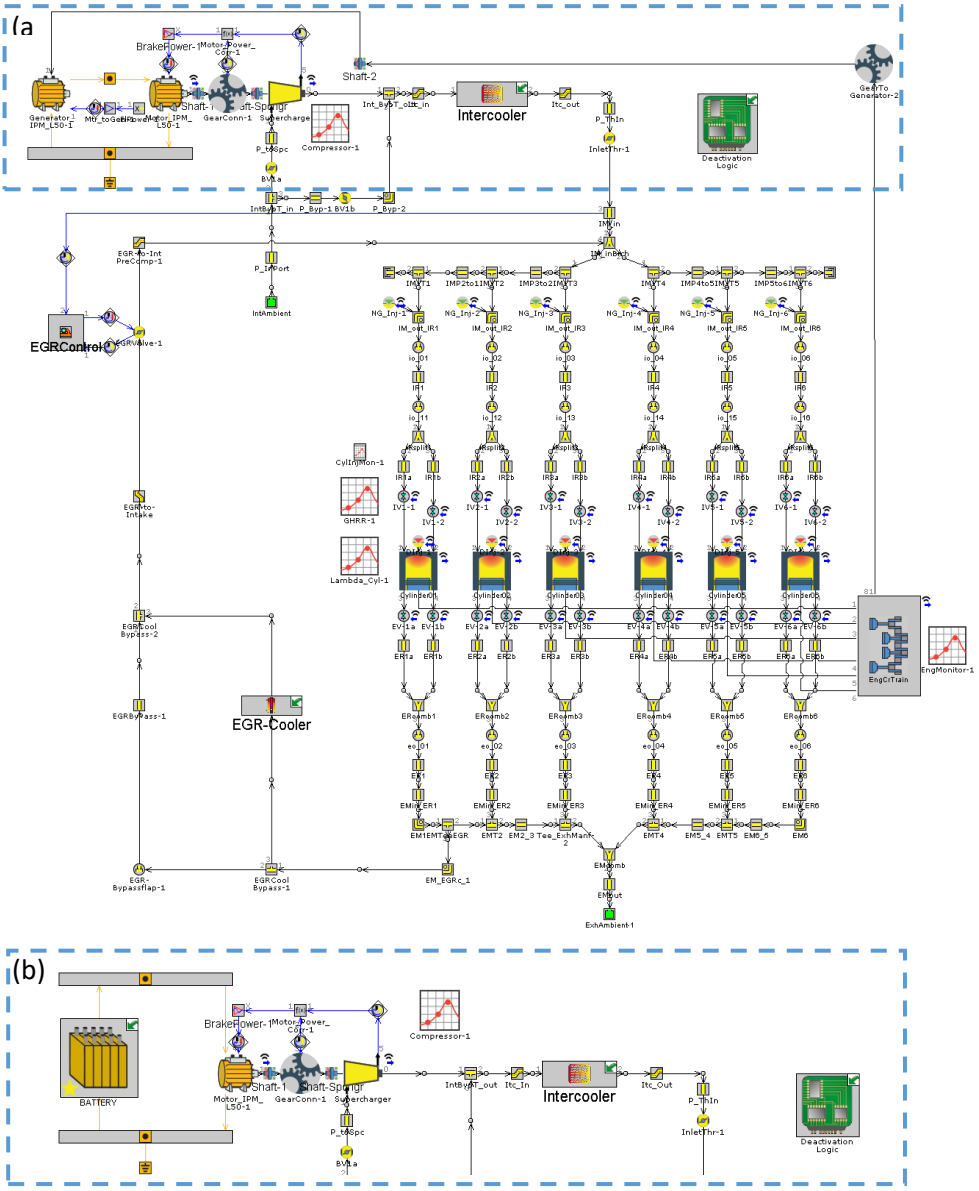


Figure 4.1. The 6-cylinder heavy duty engine model with: (a) generator powered eSupercharger and modified section for simulating a battery powered eSupercharger shown in (b), replacing the parts in dashed box (a).

4.2.1 Intake and Exhaust Port

Upfront of any simulation work the engine intake and exhaust geometries were characterised through manual measurements (using a second identical model engine which was in a teardown state). Geometries of the intake and exhaust ports with rectangular cross-sections and rounded corners were modelled using a “PipeRound” GT-Power template e.g. as circular with the same cross sectional area. The complex geometries of the ports were modelled using the “FlowSplitGeneral” template with similar internal volume. The intake and exhaust valves will be described in the next section.

The intake port of the engine model from the upstream air intake end to intake runner is illustrated in Figure 4.2. The upstream end of the intake ports was simulated with “EndEnvironment” of air at 1 bar and 25 °C. The intake port in the model was equipped with branch pipes and valves at the respective inlet that worked in a substitutive way to manage the intake air flow to the supercharger or bypass directly to intercooler. Details of the supercharger model will be described later in this chapter (being based on a scaled production model). An intercooler that worked as an air-to-air heat exchanger was used to decrease the intake air temperature, providing denser intake air charge for the boosted simulation points. The inlet throttle was placed before the intake manifold, to be adjusted in simulation with a throttling strategy for restricting intake air supply. Part dimensions of the intake manifold and runner were adapted from the measurement, described in *Table 4.2*. In simulations with EGR, cooled EGR was injected into the inlet of the intake manifold. The gaseous fuel injector was located at the outlet of the intake manifold (or inlet of the intake runner) of each cylinder.

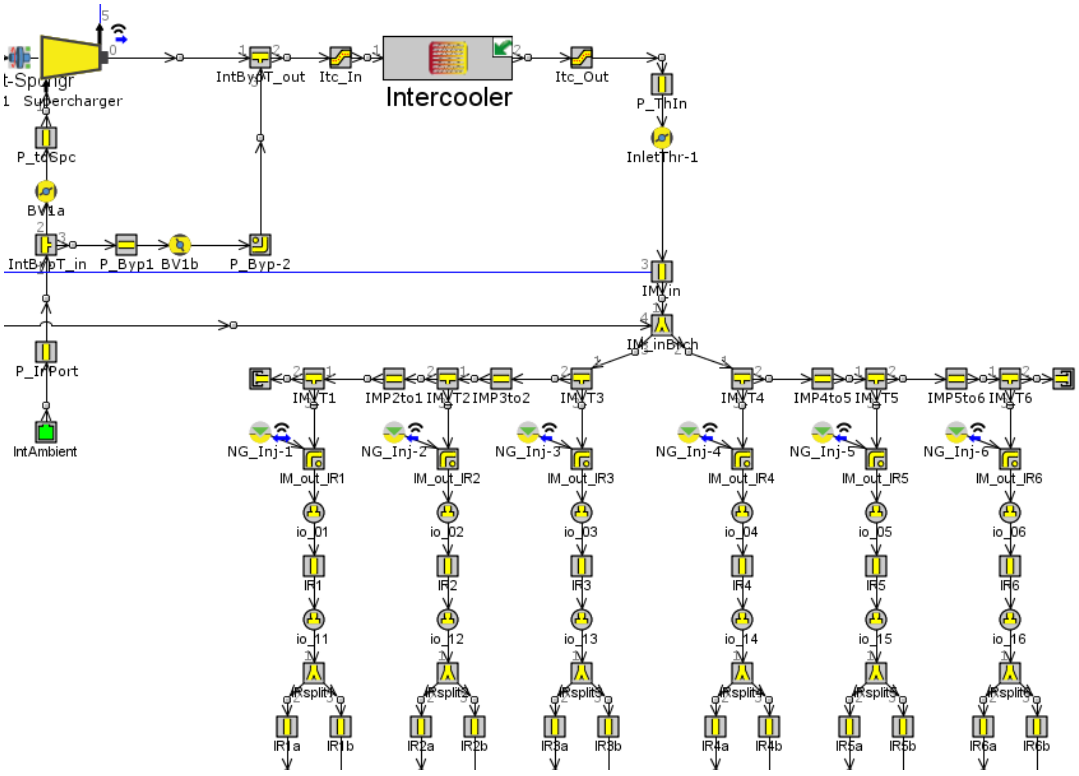


Figure 4.2. Intake ports, manifold and runner of the engine model

Part No.	Dimension				Identical Parts
	Diameter in (mm)	Diameter out (mm)	Length (mm)	Volume (mm^3)	
P_InPort	101.6	101.6	200	101.6	
IntBypT_in	101.6	101.6	150	101.6	
P_toSpc	101.6	101.6	200	101.6	
P_Byp-1	101.6	101.6	50	101.6	
P_Byp-2	101.6	76.2	300	101.6	
IntBypT_out	76.2	76.2	150	76.2	
Itc_In	76.2	76.2	715	76.2	
Itc_Out	76.2	76.2	570	76.2	
P_ThIn	89.39	89.39	100	89.39	
Intake Manifold					
IM_in	89.39	89.39	100		
IM_inBrch				366082	
IMP3to2	60.9	59.7	35.8		IMP4to5
IMP2to1	52.5	49.4	35.8		IMP5to6
IM_out_IR1	61.2	48.4	62.4		IM_out_IR2 to 6
	Diameter 1 (mm)	**Diameter 2 (mm)**	**Diameter 3 (mm)**	**Length**	
IM_T3	89.4	60.9	61.2	94.2	IM_T4
IM_T2	59.7	52.5	61.2	94.2	IM_T5
IM_T1	49.4	0	61.2	62.5	IM_T6
Intake Runner					
IR1	48.4	48.4	40		IR2 to 6
IRsplit1				80000	IRsplit2 to 6
IR1a	34.5	34.5	40		IR(2-to-6)a
IR1b	34.5	40	20		IR(2-to-6)b

Table 4.1. Parts dimensions of intake port of the engine model

The exhaust runner and manifold of the engine model are illustrated Figure 4.3. At the downstream end of exhaust manifold, ExhAmbient was simulated with EndEnvironment. In most simulations, the EndEnvironment was set at 1 bar; the exception was for simulation with EGR, where an exhaust backpressure higher than the intake manifold pressure was required to instigate flow of the EGR.

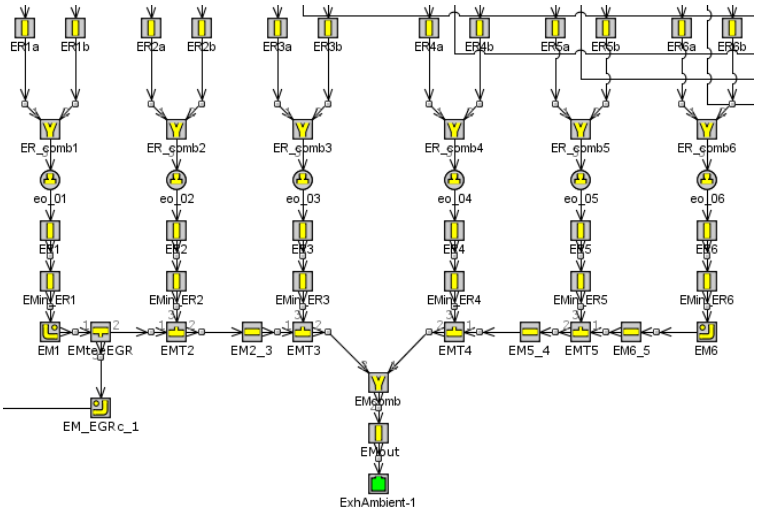


Figure 4.3. Exhaust manifold and exhaust runner of the engine model

Part No.	Dimension				Identical Parts
	Diameter in (mm)	**Diameter out (mm)**	**Length (mm)**	**Volume (mm^3)**	
Exhaust Runner					
ER1a	27.3	27.3	25		ER(2-to-6)a
ER1b	36	36	50		ER(2-to-6)b
ERcomb1				75000	ERcomb2 to 6
ER1	43	43	50		IR2 to 6
Exhaust Manifold					
EMin_IR1	43	43	12		EMin_IR2 to 6
EM1	43	40.38	57.7		EM6
EMcomb				127870	
EMout	64.9	64.9	10		
	Diameter 1 (mm)	**Diameter 2 (mm)**	**Diameter 3 (mm)**	**Length**	
EMteeEGR	40.4	40.4	40	74	
EMT2	43	40.38	40.38	49	EMT3 to 5

Table 4.2. Dimensions of the exhaust runner and manifold of the engine

4.2.2 Intake and Exhaust Valves

Valve lift was measured in a cold condition using a dial gauge at the end of valve stem and the lift was recorded while rotating the crankshaft. Afterwards, the measured intake and exhaust valve lift profiles with standard valve actuation was fed to the engine model. For

simulating Miller cycle with Late Intake Valve Closing (LIVC), the work followed experimental work by May [106], which held the intake lift at 3.1 mm in longer period than the remaining lift curve as the standard until the specified IVC timing to simulate the targeted λ. The lift of exhaust, standard and modified intake valves for LIVC simulation are depicted in *Figure 4.4*, where the intake valve lift with LIVC at 100 °CA before firing TDC is shown as an illustration. The valve timings are listed in *Table 4.3*, fixed at appropriate values from the calculated maximum lift acceleration (2nd derivation of lift).

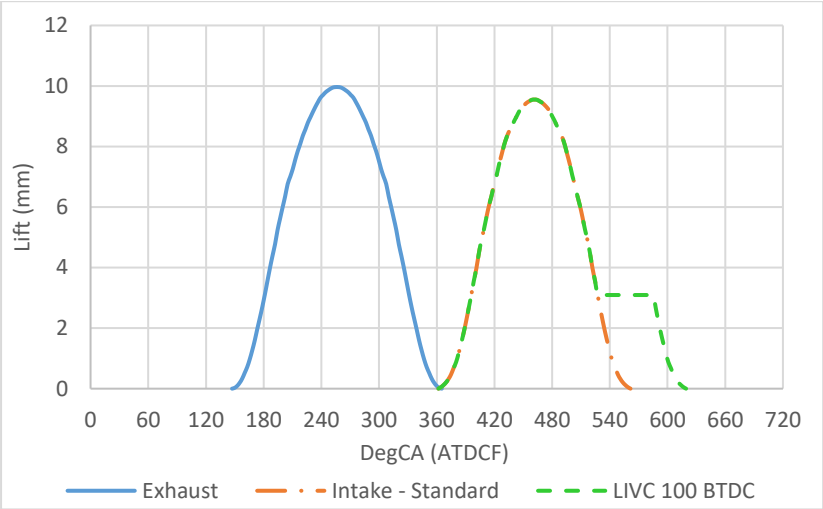


Figure 4.4. The exhaust and intake valve lift of the engine model at standard and an illustrated LIVC mode at 100 °CA BTDC of valve closing.

Valve Event	Timing (°CA ATDCF)
EVO	160.28
EVC	352
IVO	377.6
IVC	545.6

Table 4.3. Valve timings from the lift acceleration

Before simulation work was carried out, flow measurements through the intake and exhaust valve were undertaken through consultancy by MAHLE Powertrain Ltd on the cylinder head and valve assembly for Cylinder 4. The flow coefficients (Cf) through the intake and exhaust valves and swirl characteristics for the respective non-dimensional valve lift are depicted in *Figure 4.5*. Cf describes the ratio of measured mass flow to theoretical mass flow through an ideal convergent nozzle. Meanwhile, the swirl measurement was conducted in a common industrial rig, providing qualitative swirl flow characteristics under steady state conditions, albeit neglecting piston motion and the associated in-cylinder effects. It is expressed inNon-dimensional Rig Swirl, which provides comparison of angular to axial momentum by swirl of the intake valve and intake port assembly. The significant increase in NDRS at low lift was likely caused by the combustion chamber insert counter bore step and chamber relief angle.

The chamber relief angle guides the flow through specific path that generates swirl, while counterbore steps prevent the flow [139]. The flow coefficients and NDRS were entered into the valvetrain model to produce an accurate flow prediction of the intake and exhaust processes during the simulation.

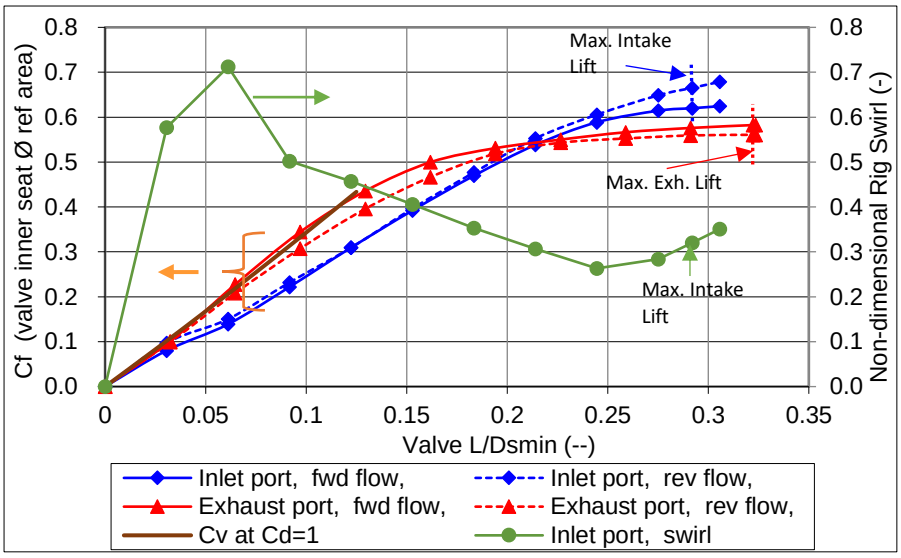


Figure 4.5. Measured flow coefficient (Cf) vs non-dimensional of intake (blue) and exhaust valve (red) and NDRS of the Volvo D8 Engine (green), reproduced from Ref. [139].

4.2.3 Electric Supercharger (eSupercharger) and Its Driving Motor

The eSupercharger was simulated using a performance map available from Aeristech Limited [140], as illustrated in *Figure 4.6*.(a), where the speed is depicted in black lines and efficiency values as contours of varying colour as a function of corrected air mass flow and pressure ratio. The map was chosen as it could fulfil the intake charge up to λ=1.8 at 6 bar BMEP while performed at high efficiency as illustrated in *Figure 4.6*.(b). In addition, it is designed to be driven by a 48 Volt electric motor, a pragmatic system recently developed for mild hybrid electric vehicle systems. Due to relatively low voltage, its application does not need additional requirements as a higher voltage application. The implementation would open the possibility for improvement in the future mild hybrid electric vehicle of heavy-duty engine to be applied in idle and low load operating conditions.

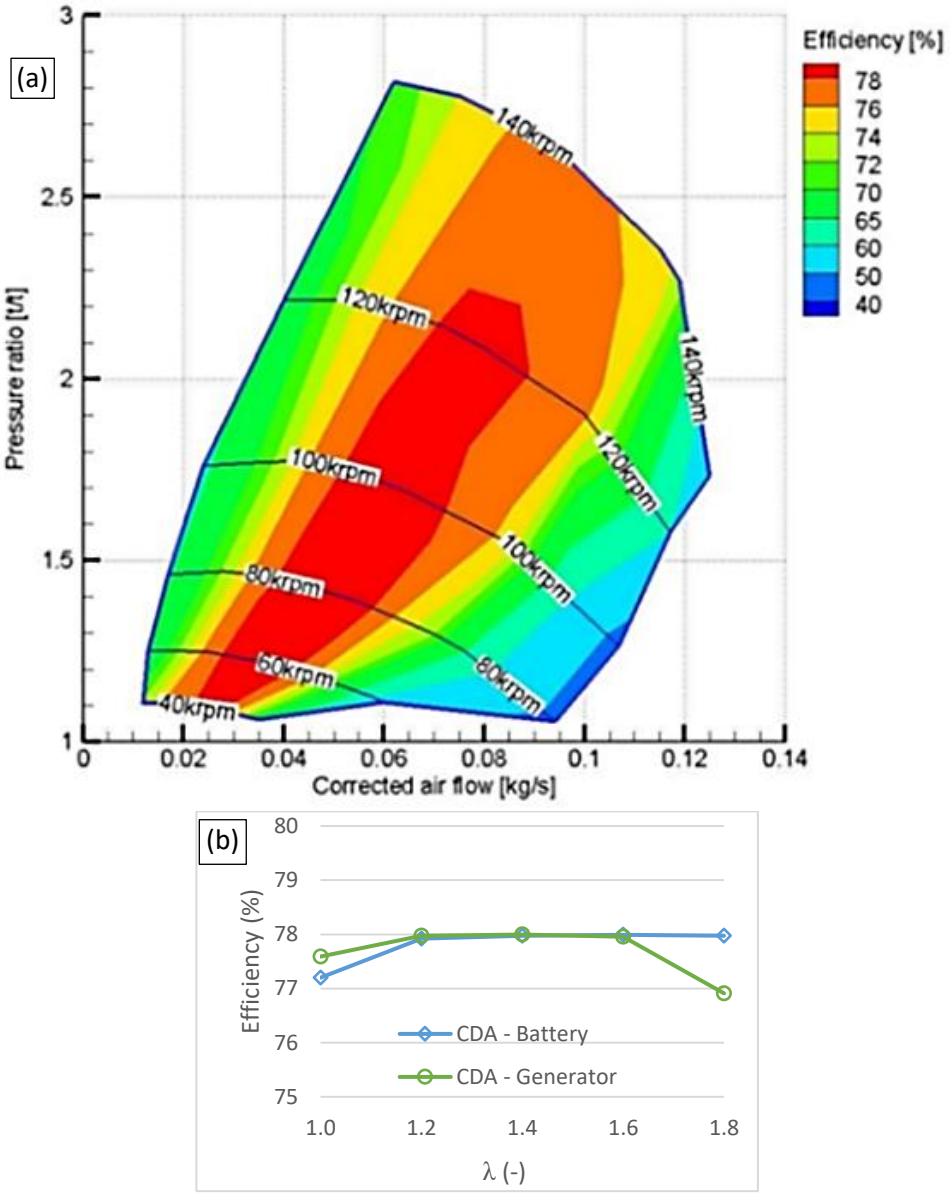


Figure 4.6. (a) Aeristech compressor map to simulate the eSupercharger in the engine model [140]*, (b) The compressor efficiency at simulated points with CDA strategy*

Unfortunately, the electrical machine performance map for the machine was not available. An efficiency map of a similar 48 V – max. 10.5 kW internal permanent magnet electric motor, produced by Ashwoods [141] is shown in *Figure 4.7* and was therefore used for simulating the eSupercharger motor performance. A shaft and gear connection with optimum gear ratio was used to connect motor and compressor shaft and run it at ~93% to minimise the parasitic loss to generate power.

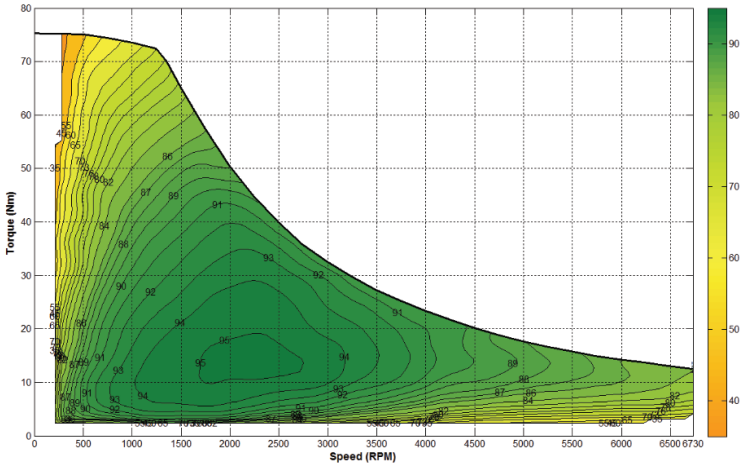


Figure 4.7. A 48 V - max. 10.5 kW of internal permanent magnet motor by Ashwood [141] *to drive eSupercharger.*

The eSupercharger motor was powered in two different ways dependant on the simulation scenario; either with a 48 Volt battery or with a generator driven by the crankshaft via a direct gear connection, as shown in *Figure 4.1*. In CDA simulation using the battery powered electric motor (CDA-Battery), the model was modified to only connect the driving motor to the battery. Several performance maps (Battery State of Charge (BSOC) vs voltage, BSOC vs discharging resistance and BSOC vs charging resistance) were taken from Ref. [142]. As the simulation was only simulating performance at a single point and did not assess for certain durations of engine operation, the battery's state of the charge was set constant at 90%. In this simulation, the battery was assumed to be charged by a regenerative braking mechanism that does not cause additional load to the engine crankshaft. Meanwhile, in the simulation of CDA strategy with the generator powered electric motor (CDA-generator), the generator was simulated using the same motor efficiency map but in reversed (negative) torque mode at the same speed. The electric generator was connected to the engine crankshaft by a shaft and gear connection to simulate the required power by the motor for the eSupercharger, that became an additional load to the crankshaft. An optimum gear ratio was chosen to run the generator at more than 90% efficiency at the simulated points.

4.2.4 Cylinder and Piston Cup Geometry

Cylinder geometry of the engine model was taken from the Volvo D8 engine specification as described in Table 3.3. The measured piston bowl (cup) of the Volvo D8 engine was adapted to the piston cup template in the GT Power as illustrated in *Figure 4.8*. The dimensions of piston cup were 70.6 mm of max. piston cup diameter (max.), 8.45 mm of piston cup depth at maximum diameter, 65.5 mm of piston cup diameter (edge), 7.45 mm of piston cup centre depth.

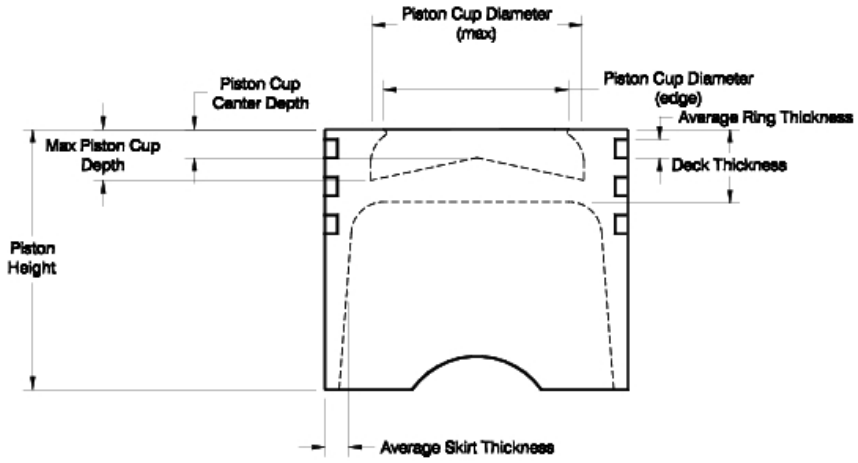


Figure 4.8. Piston cup dimension of the engine model (picture taken from Ref. [143]*).*

4.2.5 Deactivation Logic

In this modelling work, CDA strategy was implemented after a certain number of cycles with all cylinders firing. To enable this method, it was simulated with a logical control to deactivate fuel injection and valve actuation while keeping the other ones activated in the firing cylinders. The logical control is illustrated in *Figure 4.9*, where only wiring to the parts for Cylinder 3 and 4 are shown for the sake of brevity. In the deactivation logic, a number of cycles was set as threshold of delay to enable the deactivating process. As the signal from cylinder was received by the control, once the threshold was met, the logical control held the intake valves actuation, gaseous fuel injection, diesel fuel injection and exhaust valve actuation cylinder for one next cycle before being deactivated. The logical control multiplied the valve lift and fuel injection quantity with zero to deactivate them, while multiplying the other ones with one for the firing cylinders.

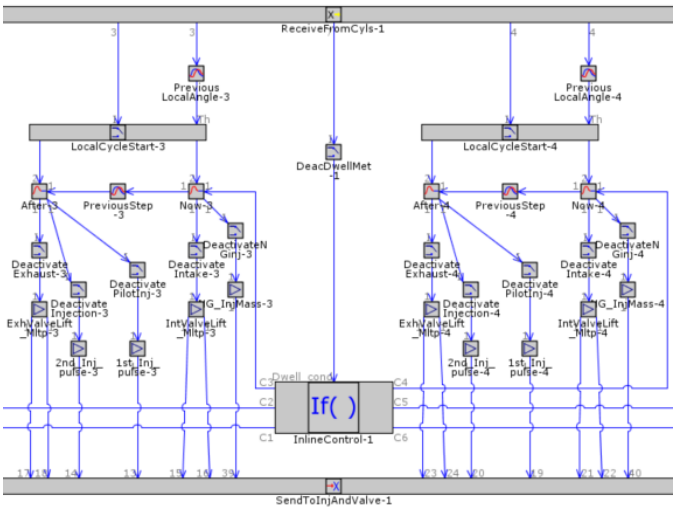


Figure 4.9. Deactivation logic for running CDA strategy with the engine model.

In this simulation work, as the dwell threshold in the deactivation logic was set at 3 cycles, the fourth cycle was the last to incur fuel injection and exhaust valve closing. In other words, the simulation ran four cycles with all cylinders active until exhaust valve closing then started the deactivation upon the fifth cycle. As an illustration, in the fourth cycle the deactivated cylinder injected gaseous fuel, closed the intake valves, injected diesel, burns the fuels then expelled the burned gas during the exhaust stroke. After exhaust valve closing in the fourth cycle, the intake and exhaust valves of the deactivated cylinders remain closed and fuel injections were stopped. With this method, CDA minimised the trapped mass within the deactivated cylinder thus reducing the motoring work to compress and expand the minimum mass in the remaining cycle.

4.2.6 Fuel injections

The gaseous fuel was injected into the inlet of the intake runner of each cylinder. The gaseous fuel was simulated to be injected at a constant flowrate 15 mg/ms. The start of injection was adjusted according to the required quantity and ended at 270 °CA BTDCF (or 90 °CA before intake BDC). A methane/ethane gas mixture at 95/5 %mole ratio was used in all of the simulations.

A diesel fuel injection profile is required in the model to simulate the relevant processes of diesel combustion during dual-fuel operation. A lookup table of injection rate map from GT Power library was adopted in the model. The table contains injection rate profiles (in time vs injection rate graph) prescribed for specific cell of rail pressure (in row) and injection energising time (in column). The profiles had been developed from a combined experimental and simulation by Payri et al. [144] up to 2000 bar of maximum injection pressure. GT Power processed each profile to produce fuel injection mass for each rail pressure and energising time. Hence, the injection mass contour was produced from the integration. During the simulation run, the software calculated the injection profile from the iterated fuel mass. If the injection mass is not found directly from the map, the software interpolates it from the closest points provided and create the injection rate profile accordingly as illustrated in Figure 4.10. Considering limitation of the model with the prescribed injection rate map, another model with different map might produce different result. However, error produced by this approach was expected be minimum since the injected diesel quantity was relatively low at simulation of dual-fuel combustion with 90% substitution ratio.

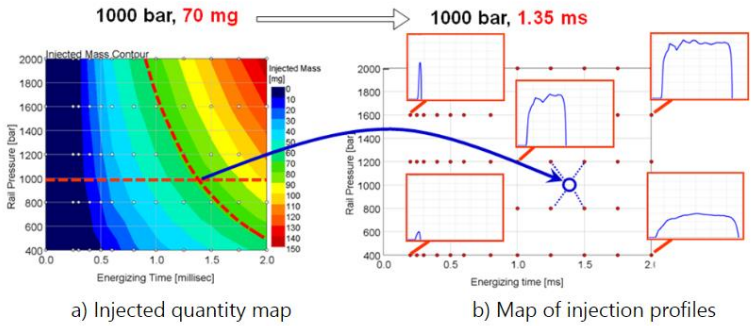


Figure 4.10. Injection profile interpolation process by GT Power (taken from Ref. [143]*)*

4.2.7 Thermal and Friction simulations

Energy losses through cylinder wall heat transfer has significant impact upon fuel economy. In this modelling works, the heat transfer to the cylinder wall was simulated using Finite Element Analysis (FEA) available in GT Power. Both in-cylinder gas temperature and wall temperature were correlatively calculated in the simulation. This aim was to minimise error in prediction, which is normally produced by heat transfer calculation that assumes a constant temperature of the piston, cylinder wall and cylinder head surfaces. The cylinder heat transfer was simulated with the "WoschniGT" template in GT Power, based upon the well-known Woschni correlation [145]. The heat transfer of the working gas to the intake and exhaust ports was simulated with assumed constant temperature of each part's wall.

The engine's friction loss was simulated with "EngFrictionCF" template of GT Power that uses Chenn-Flynn engine friction model [146] using the formula expressed in (4.1). The following values are used: FMEP constant= 0.3, A=0.005, Mean speed factor=0.1 and Mean piston speed squared factor=0.

$$FMEP = FMEP_{Const.} + A.P_{Cyl,max} + B.c_{p,m} + C.{c_{p,m}}^2 \quad (4.1)$$

Where: $FMEP_{Const.}$= Constant part of FMEP

A= The factor of peak in-cylinder pressure

B= The factor of mean piston speed

C= The mean piston speed squared factor

$c_{p,m}$= mean piston speed

$P_{Cyl,max}$= peak of in-cylinder pressure

4.3 Combustion ModellingT

Dual-fuel combustion modelling in this study used “EngCylCombDualFuel”, a predictive combustion template in GT Power. The “EngCylCombDualFuel” combines two combustion modelling templates, i.e. “DIPulse” for simulating diesel combustion and “SITurb” for gaseous fuel combustion [147].

DIPulse combustion modelling discretises the cylinder content into three zones: unburned zone that consists of the trapped mass at intake valve closing, unburned diesel fuel spray and burned zone [147]. It simulates the processes in the diesel combustion: the fuel spray atomisation, fuel entrainment, ignition delay, premixed combustion and diffusion combustion. The processes are dictated by several coefficients (multipliers): entrainment rate, ignition delay, premixed combustion and diffusion combustion multipliers specified prior to the simulation run.

In different combustion template, “SITurb” implements typical two zone combustion modeling where combustion chamber is discretised into unburned and burned zone [147]. The flame propagation within the natural gas/air mixture is modelled as a premixed turbulent combustion event based upon laminar and turbulent burning velocity correlations (i.e. a quasi-dimensional combustion model reliant upon empirical data). The multipliers used to dictate the gaseous fuel burn rate in the template are flame kernel growth, turbulence flame speed, charge dilution and Taylor length scale. Since “SITurb” is coupled by “EngCylCombDualFuel” with “DIPulse”, the function of spark plug was replaced by the simulated spray and burned diesel as pilot fuel that initiates the flame for premixed gaseous fuel combustion. In the turbulent flame speed calculation, the combustion modelling requires a laminar flame speed values to be referred. In the designed model, a formula of methane/ethane gas mixture by Amirante [148] was used to estimate the laminar flame speed at the simulated equivalence ratio.

The combustion multipliers used by the combustion modelling templates are set before the simulation run. In order to produce accurate results, a calibration procedure was performed to validate the multipliers by matching the simulation results with experimental results in some targeted parameters. The simulation using iterated values were performed to produce the targeted parameters that close to the experimental results. Afterwards, the selected multipliers were used in the simulation to model the combustion at the different simulated points.

The experimental results from the previous study of dual-fuel combustion by May et al. [5] were used in the calibration procedure. It was used as reference due to its relatively high substitution ratio of natural gas (85%). In addition, some important data such as intake pressure, λ, EGR, in-cylinder pressure, heat release rate, combustion phasing and duration are provided, although they are not fully complete as ideal requirement for ideal calibration procedure. A key point to note here is that the Volvo engine combustion chamber was similar in type to that employed by May, based upon a four valve layout with typical "ω" piston crown profile. The parity with May is a major assumption but was considered acceptable for the parametric analysis intended. Unfortunately, the Volvo engine had issues with running in dual-fuel to delays in the engine controller setup, which were delayed further by the third party supplier's own delays due to Covid. The experimental results at 1200 rpm/6 bar Net IMEP with CDF and PDFC were used in the calibration process. The calibration in this study was simulated in 6 cylinders model which is expected to provide more stable intake pressure than single cylinder engine used in ref. [5]. The calibration was performed by targeting the same conditions by referring several parameters: Net IMEP, EGR percentage, λ, substitution ratio, $1^{st}/2^{nd}$ pilot quantity ratio.

Comparison of several parameters from the experimental and simulation results produced by the optimum multipliers are shown in *Table 4.4*. Meanwhile, the in-cylinder pressure and net heat release rate produced by experiment and simulation with multipliers that produced closest results are shown in *Figure 4.11*. Difference between measured and simulated peak of net HRR by ~10% was deemed within acceptable range according to several simulation in Ref. [149–151] that reported difference of HRR peak by ~20%. In the figure, the in-cylinder pressure from simulation of CDF indicates higher pressure than the experimental results likely due to limitation of the model to predict end part of combustion accurately with the used multipliers. The error might also be produced by the burned gas from crevice volumes at the end part of combustion which was not predicted well by simulation. In this simulation work, gas from crevice volume cannot be simulated as unburned in the edition of GT Power used (2020 version), since assuming the unburned hydrocarbon caused an error that stopped the simulation.

Parameter	CDF		PDFC	
	Experiment	Simulation	Experiment	Simulation
Max. in-cylinder pressure (bar)	62.69	62.95	78.57	78.96
Max. HRR (J/°CA)	224.44	246.93	199.98	185.748
CA50 (deg. CA ATDC)	8.6	9.1	1.3	1.4
Combustion duration (deg. CA)	23.1	23.5	22	28.37

Table 4.4. Comparison of parameters from the experimental results and the produced calibration results.

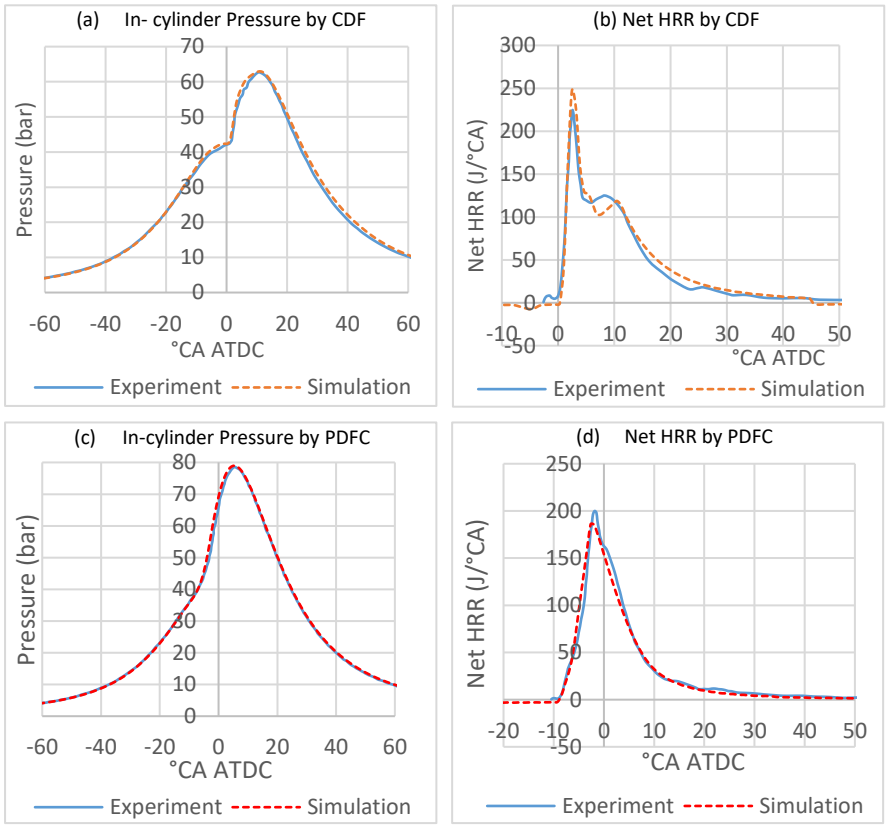


Figure 4.11. Comparison of the experimental and simulation results to calibrate the combustion multipliers: (a) The in-cylinder pressure by CDF, (b) Net HRR by CDF, (c) The in-cylinder pressure by PDFC, (d) Net HRR by PDFC

4.4 Summary

In this chapter, the engine model for simulation works of phenomenological modelling is described. Prior measurements of the engine parts were adapted to the parts model to produce prediction in high accuracy. In the engine model, eSupercharger was used as a proposed boosting device that is potential to be implemented in future mild hybrid powertrain for HDV. Several relevant processes are described, including deactivation logic, fuel injection, thermal and friction simulation. The predictive modelling of dual-fuel

combustion is set out, including calibration of the combustion multipliers to the previous experimental results. The descriptions here were set out to introduce the simulation methods that produce results that will be presented in the next chapter.

Chapter 5 Gas-to-Liquid (GTL) and Diesel Fuel in Conventional Diesel Combustion and Premixed Dual-Fuel Combustion

5.1 Introduction

Diesel composition and injection as a pilot fuel has significant influence over dual-fuel combustion performance. Stratified diesel combustion has no lean limit, which can be manipulated for high thermal efficiency. On the contrary, turbulent premixed flame propagation is limited under lean conditions by slower burning and adverse flame stretch effects, eventually leading to partial and ultimately full flame quench. When operating in dual-fuel, the engine is in effect being operated in a mixed mode, with stratified pilot diesel resulting in multiple ignition sites which help overcome the otherwise adverse slow flame speed via significantly increased overall enflamed area early on in the power stroke. A balancing act arises between sufficiently "seeding" the natural gas with diesel to enable as close to complete combustion as possible. As a consequence, running dual-fuel with a less lean mixture results in deteriorated ignition delay of the pilot fuel [7]. Advancing the pilot injection could be implemented to attain the optimum combustion phasing. However, further advancement of the pilot injection at low load is limited by lower compression pressure and temperature. Ultimately this low temperature leads to very slow flame propagation, partial and ultimately full quench at low engine loads. Therefore, improving ignition delay is important as an integrated strategy to improvement in dual-fuel combustion when using a high natural gas substitution ratio.

Gas-to-Liquid diesel fuel (GTL) is a diesel fuel produced from natural gas via the Fischer-Tropsch process, typically incurring higher cetane number (79) than fossil diesel fuel (45 - 54). This potentially improves ignition delay for a less lean mixture during dual-fuel operation, providing flexibility for optimising combustion phasing. In the previous study on the injection characteristics of GTL, it resulted in shorter liquid penetration, longer vapour penetration, and smaller sauter mean diameter at the same timing than diesel [152,153]. Improved atomisation, vaporisation and air entrainment can reduce local rich combustion, leading to reduced soot formation. Another benefit offered by GTL is that it mostly contains paraffinic hydrocarbon and extremely low aromatic content [134], also expected to produce lower soot. GTL has a lower C/H ratio by 1.6% [134] that could reduce end use CO_2 emissions further in the optimum setting, which is one of the main reasons for dual-fuel implementation. Despite these apparent benefits, it is important to acknowledge potential

full life cycle impacts of the fuel, where GTL incurs relatively high embedded carbon/energy in its manufacturing (relative to conventional diesel). The GHG of GTL is lower than conventional diesel if the credit of negative GHG from coproduct of its production is taken into account [154]. As this is a synthetic product which can be produced not only from natural gas, future production from renewable sources (biomass to liquid) can result in lower GHG and further reduction to be negative GHG can be realised with application of carbon capture and storage technology [155,156]. Apart from discussion of GHG by GTL, the aim of the currently reported work was to understand relative benefits in end use that may justify adoption as a pilot fuel only.

In this chapter, diesel and GTL fuel are compared with Conventional Diesel Combustion (CDC) and PDFC. The operating condition is described in the first sub-section. Presented and analysed in the second sub-section are results from diesel engine combustion testing. In the third sub-section, the results from dual-fuel with diesel or GTL as pilot fuel are presented. In the fourth sub-section, the results are summarised by highlighting the results from CDC and PDFC.

5.2 Test Conditions in The Light Duty Engine Test Rig

5.2.1 Conventional Diesel Combustion (CDC) Test Conditions in Light Duty Engine

Conventional Diesel Combustion (CDC) tests in this study were conducted either with GTL or ULSD (herein referred to as diesel) at 1200 rpm and 5.3 bar BMEP; selected as a calculated low load point of ESC for the Volvo D8 engine and the approximate low load limit in typical modern diesel engines as defined in prior work [106]. CDC was conducted with a single pilot and main fuel injection. The injected pilot quantity was 2 mm^3, which referred to the calibrated quantity for conventional diesel fuel, which may produce a slightly different quantity for GTL injection due to its lower viscosity. The interval between the Start of Injection (SOI) of the pilot and main injections was set at 10 °CA. The average intake manifold pressure was kept at 1.3 barA (±0.02) during the test. The common rail pressure was set at either 600 or 1000 bar based upon prior knowledge of the optimum in this engine at similar speed and load [157]. SOI of the main injection (SOI_{Main}) was swept between -15, -5, 0, 5, 15 °CA ATDC for the 60 MPa rail pressure tests, while for the 100 MPa rail pressure cases this was set at -10, -5, 0, 5, 15 °CA ATDC. The most advanced SOI_{Main} in the test at 100 MPa rail pressure was slightly retarded to limit the maximum Pressure Rise Rate (max. PRR) to 10 bar/°CA in line with typical limits for heavy duty (the engine was light duty but the results

were considered to be relevant to heavy duty operation limits due to the increasing trend towards passenger car electrification and associated diesel bans).

5.2.2 Premixed Dual-Fuel Combustion (PDFC) Test Conditions in Light Duty Engine

Dual-fuel experimental work implemented PDFC with two pilot injections, with the first injection premixed prior to the second injection with a 50/50 ratio in quantity. The PDFC tests were undertaken at 1200 rpm/5.3 bar BMEP. Methane in 99.95 $\%_{vol.}$ was stored in gas bottles at 200 bar maximum pressure and supplied through the gaseous fuel delivery system described in Chapter 3, injected to the inlet of the intake manifold. The diesel rail pressure was kept fixed at 600 bar while the average pressure of the intake manifold was again held to 1.3 bar. The PDFC tests were undertaken under a 58% (±2) natural gas substitution ratio. This was lower than expected and was necessary due to unacceptable combustion stability at higher values. The reason for the lower substitution was not directly uncovered (all monitored engine parameters appeared within acceptable limits) and may have potentially been associated with in-cylinder flow effects, unknown cylinder to cylinder variations (with three cylinders not monitored) or some other unknown. As the engine was still stable with the majority of fuel being natural gas it was decided to proceed. SOI of the second pilot fuel was kept at -3 °CA ATDC and SOI of the first pilot was varied at 40, 50 and 60 °CA ahead.

5.3 Results and Discussion on Conventional Diesel Combustion Tests

The experimental results of CDC are described in this section. Firstly, results of CDC are presented to compare combustion and brake efficiency when using GTL versus diesel. To gain insight several parameters were monitored including the in-cylinder pressure, heat release rate, mass fraction burned and mean gas temperature from 200 consecutive cycles of crank angle resolved data. The exhaust gas emissions are presented and discussed in a subsequent section.

5.3.1 Brake Efficiency by CDC with GTL and Diesel

Brake efficiency by CDC with diesel and GTL are depicted in *Figure 5.1*(a), with the associated fuel consumption shown in *Figure 5.1*(b). Brake efficiency was calculated pressure with an assumed LHV of GTL=44 MJ/kg [135] and LHV of diesel=42.9 MJ/kg [158]. The impact of injection timing to brake efficiency suggests the optimum setting of SOI_{Main} of CDC with GTL (at both 60 and 100 MPa rail pressure) and CDC with diesel with 60 MPa of rail pressure were between -5 °CA ATDC to 0 °CA ATDC, while diesel with 100 MPa rail was at TDC. Comparison

of the results from CDC with two fuels indicated that GTL at the same injection setting generally resulted in lower brake efficiency than diesel, except with SOI_{Main} at 15 °CA ATDC, where GTL with the same rail pressure resulted in higher brake efficiency.

From comparison of different rail pressures, 100 MPa rail pressure resulted in lower brake efficiency at advanced injection timing, similar brake efficiency by SOI_{Main}=5 °CA ATDC but higher brake efficiency than 60 MPa rail pressure at SOI_{Main}=15 °CA ATDC. In CDC with GTL, 100 MPa rail pressure also resulted in lower brake efficiency than by 60 MPa rail pressure, except at SOI_{Main}=15 °CA ATDC. Improvement of efficiency by 100 MPa rail pressure in diesel at SOI_{Main}=15 °CA ATDC was more significant than by GTL. Higher brake efficiency by 100 MPa rail pressure at SOI_{Main}=15 °CA ATDC suggests improved injection spray/atomisation may have improved brake efficiency at low in-cylinder pressure and temperature.

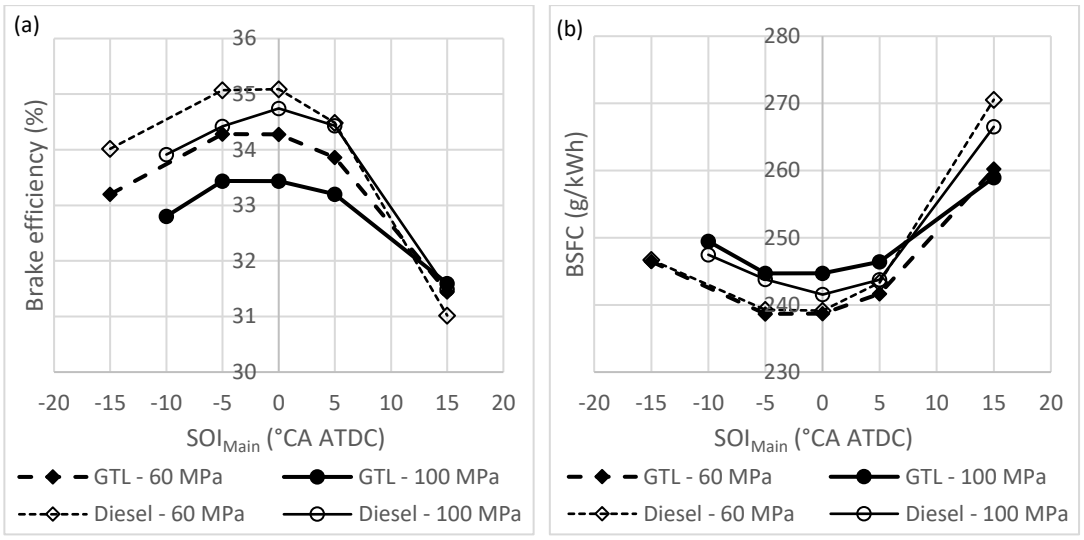


Figure 5.1. (a) Brake efficiency and (b) BSFC of CDC with GTL and diesel

5.3.2 In-cylinder pressure by CDC with GTL and Diesel

In-cylinder pressure is an important data to analyse the phenomena that results in engine performance. Depicted in *Figure 5.2* is a comparison of in-cylinder pressure curves by CDC with GTL and diesel at 60 MPa rail pressure with corresponding SOI_{Main}. Shorter ignition delay of pilot injection was incurred using GTL, with earlier start of increasing pressure than diesel. Pilot combustion of GTL that resulted in higher in-cylinder pressure likely promoted improvement of the main injection events. In addition, GTL resulted in slightly higher maximum pressure than diesel which could be attributed to higher fuel energy by GTL as indicated by lower brake efficiency as shown in *Figure 5.1*.(a). Influence of higher injection pressure to the in-cylinder pressure of CDC with GTL is depicted in *Figure 5.3*. Higher injection pressure resulted in higher in-cylinder pressure during pilot and main fuel

combustion. In addition, higher injection pressure caused higher pressure rise rate. In *Figure 5.4*, a similar trend can be observed with increasing rail pressure for both diesel and GTL to the in-cylinder pressure at SOI_{Main} 5 °CA BTDC and 5 °CA ATDC. However, a different effect was indicated by SOI_{Main} 15 °CA ATDC where the in-cylinder pressure produced by pilot combustion with 60 MPa is higher than with 100 MPa, despite the main combustion of 60 MPa being lower than 100 MPa at the later combustion stage. Higher rail pressure with the same injection timing and dwell time between the pilot and main resulted in higher pressure at the end of compression stroke, which requires higher pressure in the expansion stroke to produce the same load (Net IMEP). Therefore, higher rail pressure deteriorated brake efficiency in many operating conditions, except at SOI_{Main} =15 °CA ATDC. In the presented in-cylinder pressure traces, the same rail pressure with retarded SOI_{Main} resulted in a lower peak of in-cylinder pressure but higher pressure during the expansion stroke.

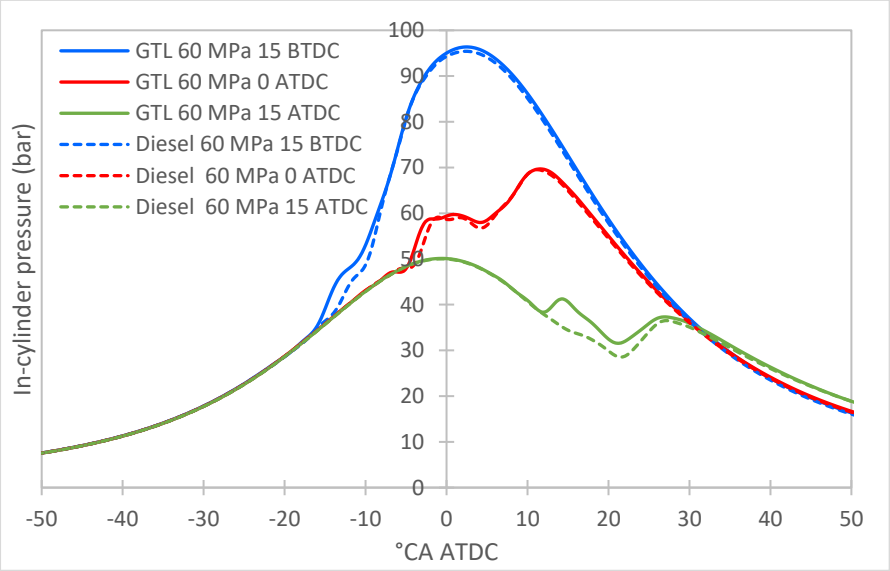


Figure 5.2. The in-cylinder pressure by GTL and diesel at 60 MPa rail pressure at selected SOI_{Main}

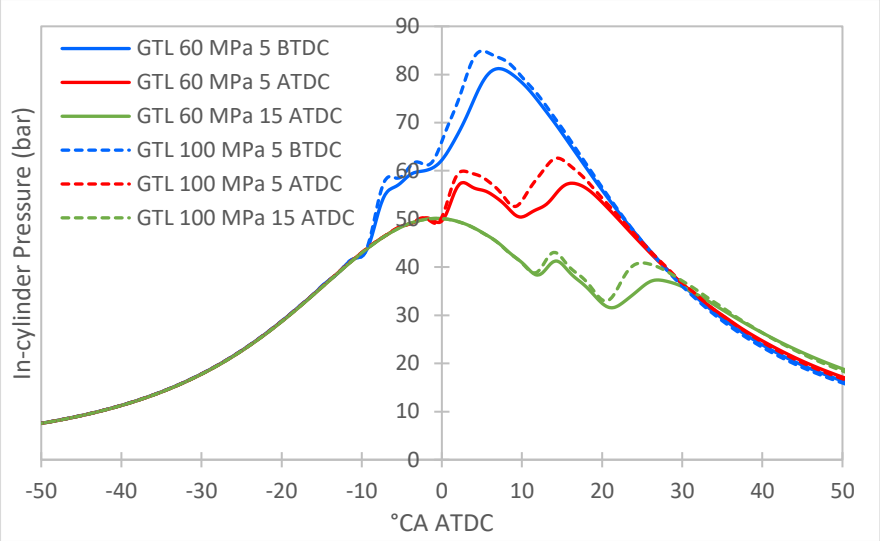


Figure 5.3. Comparison of the in-cylinder pressure between 60 and 100 MPa rail pressure by CDC with GTL at selected SOI_{Main}

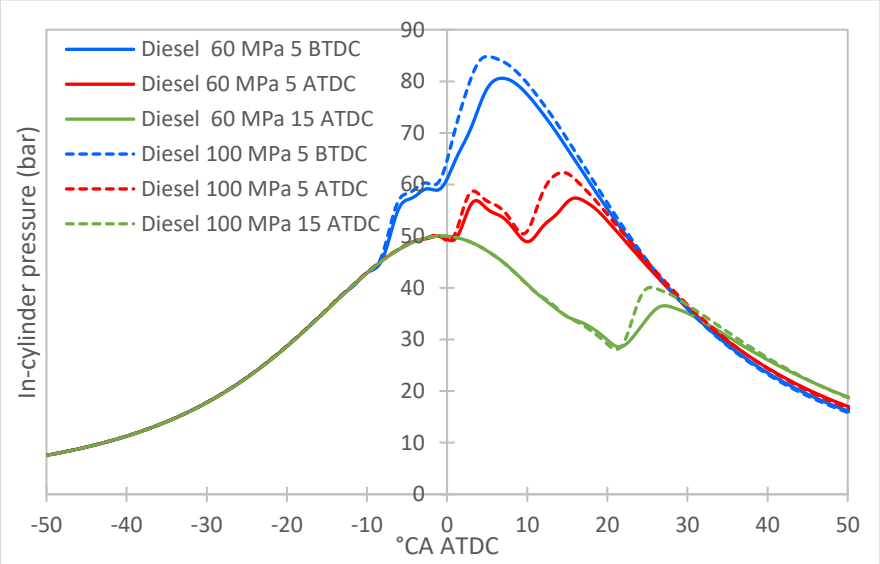


Figure 5.4. Comparison of the in-cylinder pressure between 60 and 100 MPa rail pressure by CDC with diesel at selected SOI_{Main}

5.3.3 Net Heat Release Rate (NHRR) by CDC with GTL and Diesel

Net heat release rate as the product of post-processing on the in-cylinder pressure is one of the key indicators of combustion performance. Net Heat Release Rate (NHRR) by CDC with GTL and diesel at 60 and 100 MPa rail pressure are depicted respectively in *Figure 5.5* and *Figure 5.6*. From comparison of the two fuels with the same injection timing, GTL resulted in shorter ignition delay as indicated by earlier heat release than diesel, both in the pilot and main combustion. The most advanced injection timing with 100 MPa rail pressure at SOI_{Main}= -10 °CA ATDC resulted in dominant premixed combustion of diesel during main fuel combustion, while GTL resulted in higher peak of HRR during mixing controlled combustion.

Higher NHRR for GTL than diesel during pilot combustion can be attributed to higher energy content than diesel. In addition, the same pulse length of pilot injection was expected to result in higher injected fuel quantity due to the lower viscosity of GTL and higher fuel energy due to higher LHV. GTL also resulted in higher heat release rate by pilot injection despite the most retarded injection timing (SOI_{Main}=15 °CA ATDC). Higher heat release by pilot fuel with GTL resulted in higher in-cylinder pressure during the early part of combustion as shown in *Figure 5.2*. This condition resulted in further separation between pilot and main combustion for diesel. Meanwhile, from comparison of the main combustion, longer ignition delay and higher NHRR during the premixed part of the main fuel combustion for diesel is expected due to lower cetane number, with longer ignition delay. GTL, which is more volatile than diesel, resulted in more diffusive combustion, hence reducing the premixed stage of the main combustion. In addition, more evaporated spray of GTL compared to diesel promotes entrainment that enabled combustion to be ready in a leaner mixture near stoichiometric. Therefore, premixed parts that mostly consist of rich mixture ends earlier and then combustion continues in mixing controlled combustion.

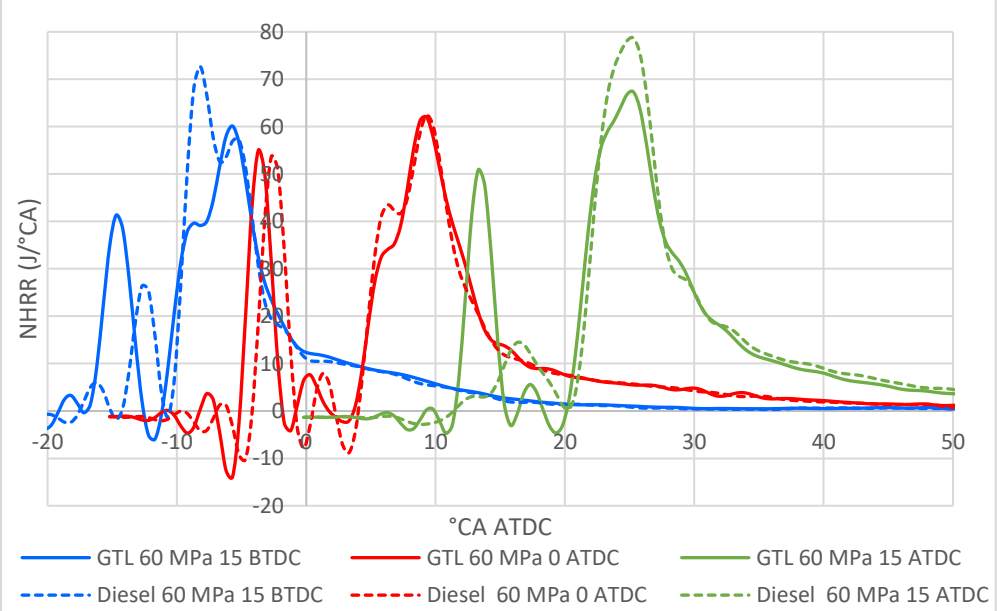


Figure 5.5. Comparison of NHRR of CDC by GTL and diesel at 60 MPa rail pressure, SOI_{Main} at -15, 0, and 15 °CA ATDC

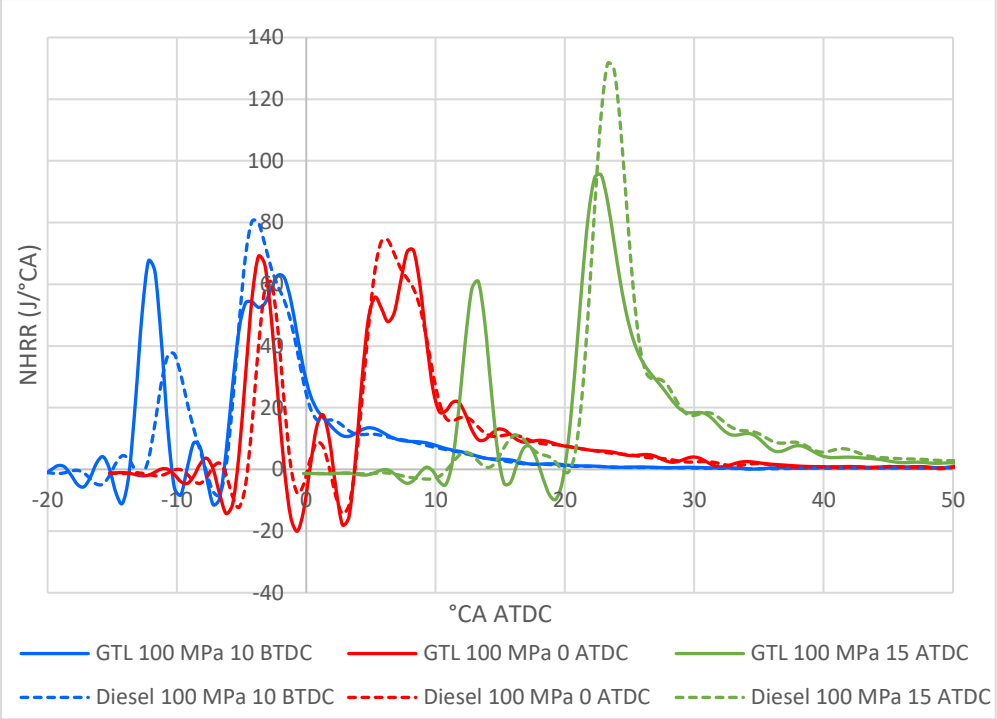


Figure 5.6. Comparison of NHRR of CDC by GTL and diesel at 100 MPa rail pressure, SOI_{Main} at -15, 0, and 15 °CA ATDC

The impact of rail pressure upon NHRR for both GTL and diesel are illustrated in *Figure 5.7* and *Figure 5.8* respectively. Increasing the rail pressure from 60 MPa to 100 MPa generally resulted in shorter ignition delay, higher heat release of premixed combustion and faster combustion overall. According to a prior study on the impact of injection pressure upon spray characteristics by Xu et. al. [159], higher rail pressure increases fuel's liquid and vapour penetration rate. The improved injection characteristics added with higher injection rate by higher rail pressure [160] resulted in shorter ignition delay and higher heat release rate. In turn this was associated with higher peak pressure, as shown in *Figure 5.3* and *Figure 5.4* for each fuel. During CDC with diesel, a higher peak of NHRR occurred via the premixed combustion stage when compared to the peak of mixing-controlled combustion. Higher rail pressure resulted in a higher rate of injection, improved fuel injection and atomisation and ultimately more fuel ready to ignite in a shorter period.

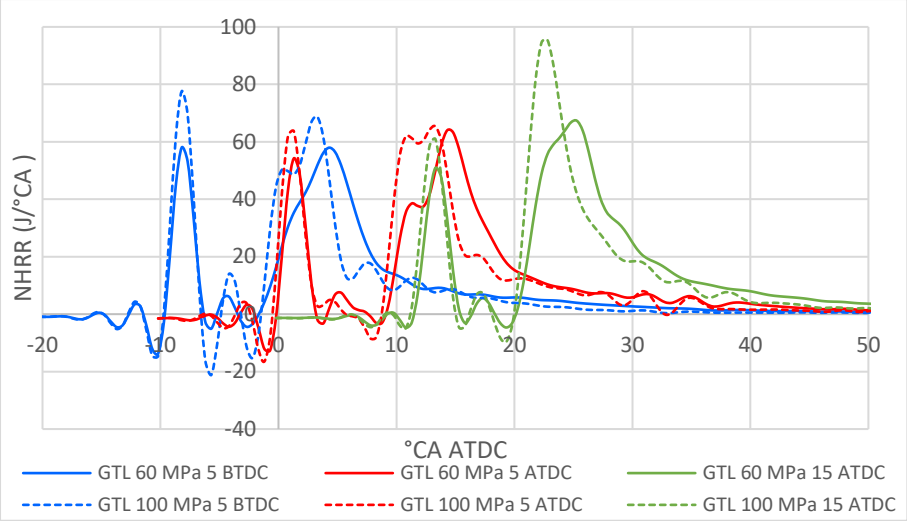


Figure 5.7. Comparison of NHRR of CDC for GTL at 60 and 100 MPa rail pressure with SOI_{Main} at -15, 0 and 15 °CA ATDC

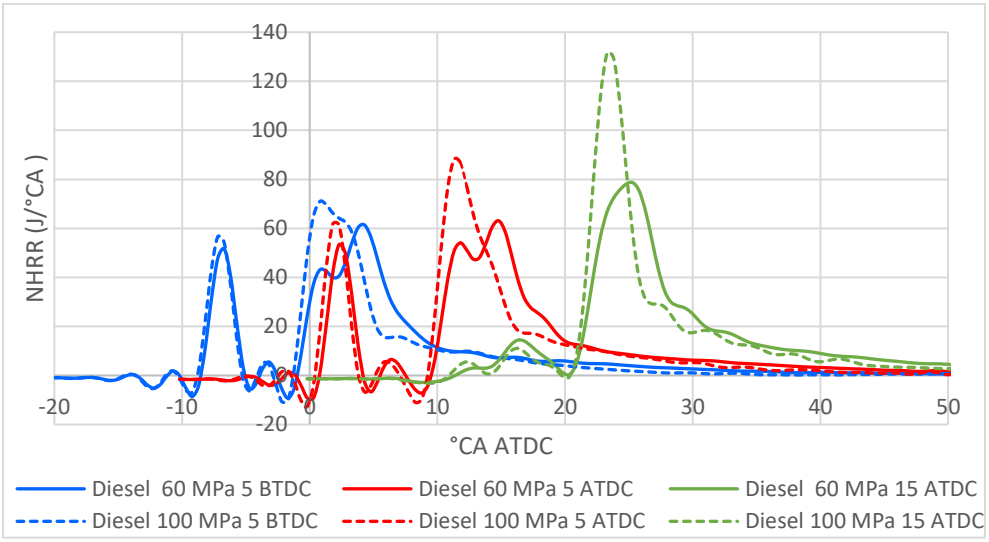


Figure 5.8. Comparison of NHRR of CDC for diesel at 60 and 100 MPa rail pressure with SOI_{Main} at -15, 0, and 15 °CA ATDC

5.3.4 Mass Fraction Burned (MFB) by CDC with GTL and Diesel

Mass Fraction Burned (MFB) was approximated from normalised values of cumulative net heat release from SOC to EOC. SOC was estimated from the location of minimum cumulative net heat release from SOI_{pilot}, while EOC was estimated from the location where NHRR starts to become less than 1 J/°CA. The MFB profiles of diesel and GTL (at selected SOI_{Main} with 60 and 100 MPa rail pressures) are shown in *Figure 5.9* and *Figure 5.10* respectively. GTL incurs a more advanced combustion of pilot fuel than diesel, associated with the shorter ignition delay of GTL. During the main combustion, diesel performed with a faster burn rate during the premixed part of the main combustion event, which accelerated the burn rate albeit with lower heat release rate in pilot combustion. This resulted in earlier or similar timings for the

last part of combustion for GTL, except with SOI_{Main} at 15 °CA ATDC where diesel indicated retarded SOC, later CA50 and a longer end stage of combustion that retarded the EOC further. In addition, at early and late injection timing, GTL indicated a higher ratio of burned pilot fuel to total fuel burned than diesel. This could indicate higher ratio of pilot to total fuel in CDC with GTL than diesel, where more fuel quantity is required at deteriorated brake efficiency by CDC with diesel at SOI_{Main} =15 °CA ATDC, as shown in *Figure 5.1*. For GTL, although the ratio of pilot to total fuel at SOI_{Main} =15 °CA ATDC is less than at earlier SOI_{Main}, the decrease is less significant. This suggests less deterioration of brake efficiency than diesel due to retarded injection timing. The impact of rail pressure upon the MFB of GTL and diesel is shown in *Figure 5.11*. During CDC with both GTL and diesel, increasing rail pressure advanced combustion phasing and shortened the combustion duration (described more later on).

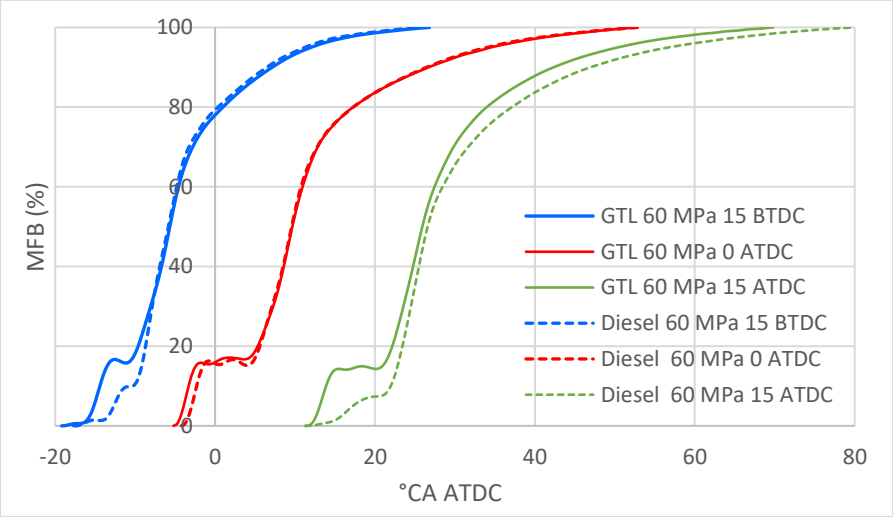


Figure 5.9. MFB of CDC with diesel and GTL at 60 MPa of rail pressure

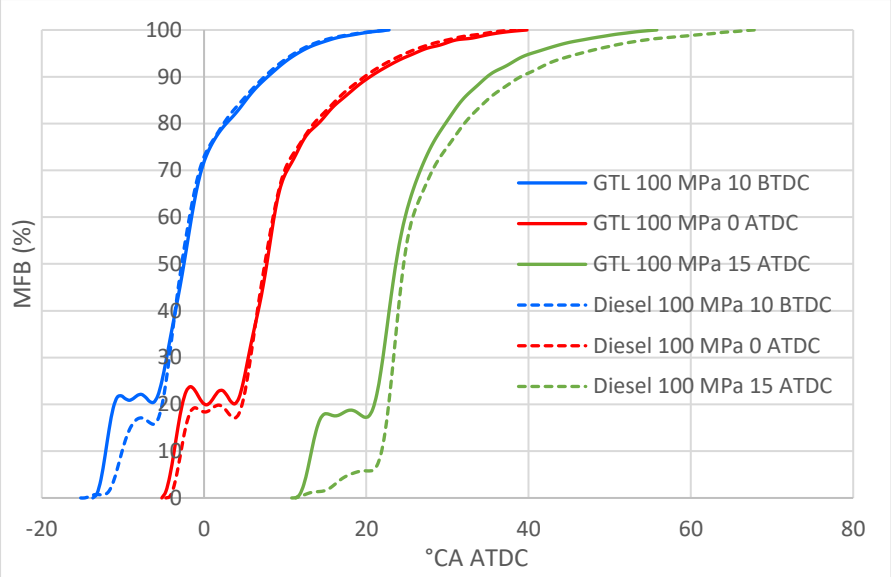


Figure 5.10. MFB of CDC with diesel and GTL at 100 MPa rail pressure

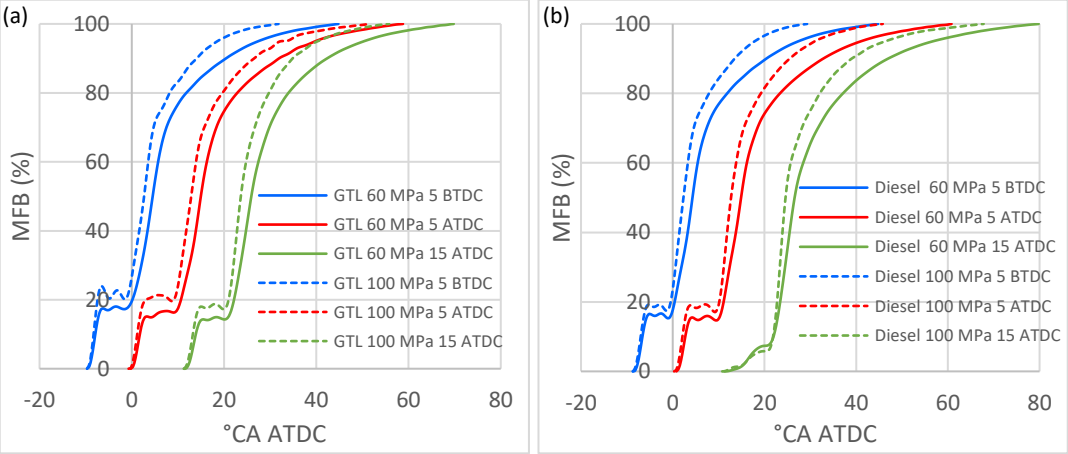


Figure 5.11. MFB for (a) GTL and (b) diesel with 60 and 100 MPa rail pressure

The MFB plots were analysed further to produce combustion phasing and combustion duration as depicted in *Figure 5.12*(a) and (b). Combustion duration was calculated from the duration of 10% to 90% MFB. Meanwhile, combustion phasing is the location where 50% MFB was reached, herein referred to as CA50. The combustion duration of both fuels at the same rail pressure indicated that diesel generally performed with faster combustion than GTL. This was despite GTL incurring shorter ignition delay and higher NHRR of the pilot fuel. The higher premixed stage of the main combustion event with diesel significantly accelerated the combustion, hence resulting in similar combustion phasing as GTL with shorter combustion duration. As shown in the figure, retarding SOI_{Main} resulted in longer combustion duration, except for SOI_{Main}=15 °CA ATDC where longer ignition delay resulted in a highly premixed part of the main combustion event (as shown in *Figure 5.8*). This resulted in shorter combustion duration than the earlier injection timing. Comparing the same fuel with

increased rail pressure, higher rail pressure resulted in accelerated combustion by 7 °CA, with more advanced combustion phasing by around 2 °CA. Shorter combustion duration and more advanced combustion phasing by 100 MPa rail pressure at SOI_{Main}=15 °CA ATDC can be the reason why it resulted higher brake efficiency than 60 MPa rail pressure at the same injection timing as shown in *Figure 5.1*(a).

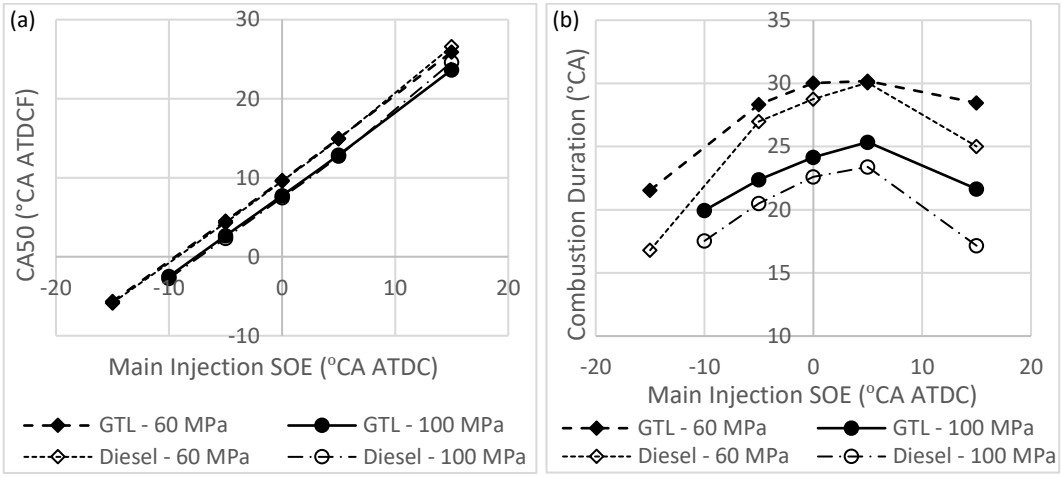


Figure 5.12. (a) Combustion phasing and (b) Combustion duration of CDC with GTL and diesel

5.3.5 Maximum Pressure Rise Rate (PRR) by CDC with GTL and Diesel

A comparison of the max. PRR and its location by CDC with diesel and GTL are depicted in *Figure 5.13*(a). For analysis of the combustion stage contributing to this parameter, their locations are presented in *Figure 5.13*. (b). Max. PRR by CDC with diesel and GTL generally indicated similar trends, with decreasing PRR due to retarded injection timing. However, GTL with 100 MPa rail pressure and SOI_{Main}= 10 °CA BTDC resulted in lower max. PRR than SOI_{Main}= -5 °CA ATDC, with the location of Max. PPR at -12.20 °CA ATDC. This indicates relatively dominant pilot fuel combustion, as indicated by a higher peak heat release rate of the pilot fuel compared to the premixed stage of the main combustion. The comparison indicates that CDC with diesel at the most advanced injection (either at 60 or 100 MPa rail pressure) resulted in the highest max. PRR, which was contributed to by the main fuel combustion. More significant premixed part of the main combustion could be related to the fuel mass built up during ignition delay that in turn ultimately resulted in higher max. PRR. Meanwhile, in comparison of two fuels at the same injection pressure and injection timing, GTL resulted in higher max. PRR than diesel with mid-range injection timing (SOI_{Main}=-5 °CA ATDC to 5 °CA ATDC), which was associated with the premixed combustion of the pilot fuel, but with the effect reduced at the most advanced and retarded settings. Despite same fuel quantity of

pilot injection (2 mm^3), higher LHV of GTL resulted in higher heat release and max. PRR than by diesel.

From the location of max. PRR in CDC with diesel, the main combustion event resulted in max. PRR across several operating conditions; 60 MPa rail pressure and SOI_{Main}=-15, 100MPa rail pressure and SOI_{Main}=-10 and -5 °CA ATDC with both 60 MPa and 100 MPa rail pressure and SOI_{Main}=15 °CA ATDC. Meanwhile, for CDC with GTL, most of the max. PRR events were the result of the pilot combustion, with the exception of 60 MPa rail pressure with SOI_{Main}= -15 °CA ATDC and 100 MPa rail pressure with SOI_{Main}=15 °CA ATDC. The higher cetane number of GTL presumably resulted in shorter ignition delay, with reduced significance of the premixed part of the main fuel combustion event and with higher peak heat release rate during mixing controlled combustion, as shown in *Figure 5.6*. In the GTL case with 100 MPa rail pressure at SOI_{Main}=15 °CA ATDC, the max. PRR at 22.30 °CA ATDC was the result of premixed combustion of the main fuel injection, suggesting a combination of longer ignition delay with retarded injection timing and more fuel for the premixed burn of the main fuel the result of higher rail pressure. In the test with the latest setting of SOI_{Main}= 15 °CA ATDC, all tests except GTL with 60 MPa rail pressure resulted in max. PRR from the main combustion event. Longer ignition delay with low pressure and temperature in the cylinder with retarded injection timing resulted in more significant premixed combustion of the main injected fuel than the pilot fuel. In the test with GTL at 60 MPa rail pressure and SOI_{Main}=15 °CA ATDC, the higher heat release of premixed combustion for the pilot fuel resulted in higher PRR than the premixed part of the main combustion event (which burned at slower speed).

Increasing rail pressure resulted in similar effects either in CDC with diesel or GTL, where higher rail pressure increased the max. PRR due to higher injection rate with improved fuel atomisation. 100 MPa rail pressure during CDC with diesel at the most advanced and most retarded injection timings resulted in higher max. PRR than incurred with 60 MPa. Higher injection pressure improved the fuel atomisation, which resulted in more fuel/air mixture being ready to burn during the premixed part of main injection event. Therefore, ignition delay with the most advanced and retarded injection timings resulted in higher heat release rate during the premixed stage of the main combustion. The test was not run at SOI_{Main}=-15 °CA ATDC because it resulted in a max. PRR higher than the limit of 10 bar/°CA. The impact of higher premixed combustion was shorter combustion duration, as shown in *Figure 5.12*.(b). Meanwhile, max. PRR by diesel fuel with 100 MPa at SOI_{Main}=15 °CA ATDC decreased the effects slightly from the result with SOI_{Main}=5 °CA ATDC. This suggests an improvement in injection performance with higher rail pressure and later injection timing, which resulted

in faster combustion during the premixed stage of the main combustion event, as shown in *Figure 5.8* where accelerated combustion overall is indicated by shorter combustion duration.

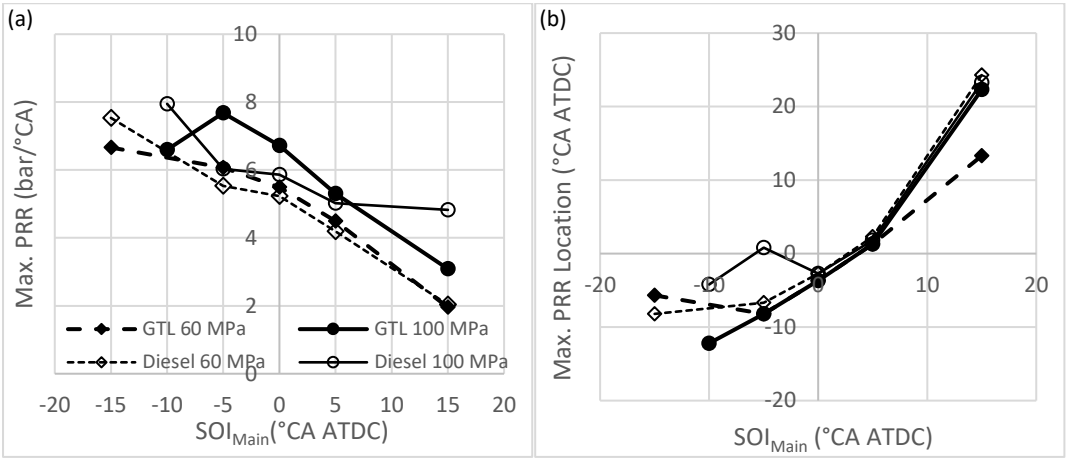


Figure 5.13. (a) Max. PRR and (b) Max. PRR location during CDC with GTL and diesel

5.3.6 Mean Gas Temperature by CDC with GTL and Diesel

The mean gas temperature was calculated using the ideal gas equation, considering the intake trapped mass from the λ calculation and the injected fuel quantities. A comparison of the mean gas temperatures for CDC with diesel and GTL at 60 MPa and 100 MPa rail pressure respectively are depicted in *Figure 5.14* and *Figure 5.15* at selected SOI_{Main} timings. GTL with 60 MPa rail pressure resulted in higher mean gas temperature at all injection timings during both the early and main part of combustion, as indicated by early increasing temperature and peak temperature. In general, the higher injected fuel energy of GTL resulted in higher mean gas temperature than diesel. During early combustion, higher pilot fuel energy with GTL (at the same volumetric quantity) resulted in higher mean gas temperature during premixed combustion than diesel. With 100 MPa rail pressure, despite incurring higher temperature by the pilot injection, GTL resulted in similar maximum mean gas temperature to diesel. Although GTL at this operating condition consumed higher fuel energy than diesel, as indicated by lower brake efficiency in Figure 5.1.(a), more significant impact of the premixed combustion events for diesel resulted in similar maximum values of mean gas temperature. With the latest injection timing of SOI_{Main}=15 °CA ATDC, GTL resulted in higher maximum mean gas temperature. A combination of improved fuel injection by pilot combustion, which resulted in higher mean gas temperature during main injection and higher cetane number, resulted in faster combustion of the main fuel injection as shown in *Figure 5.9* and *Figure 5.10*.

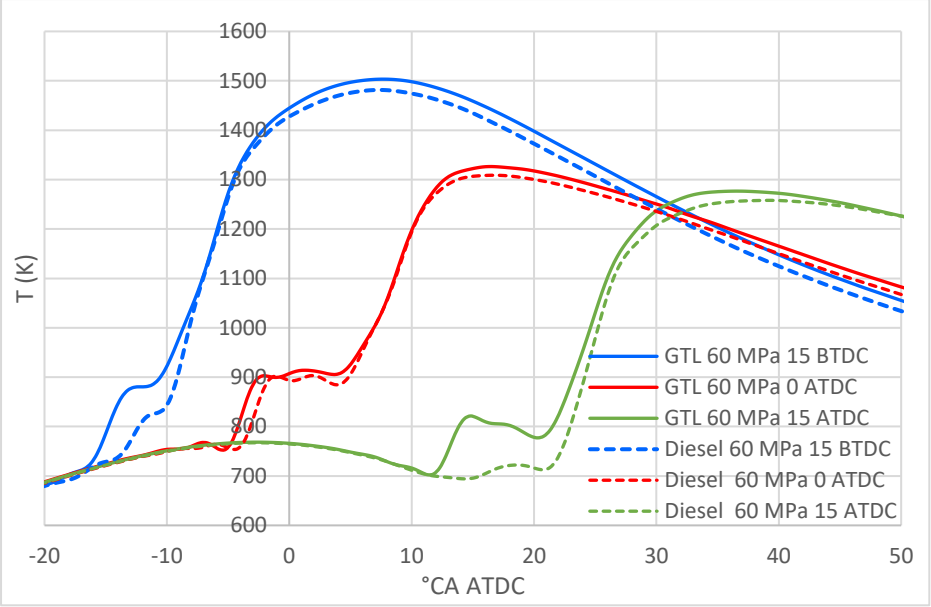


Figure 5.14. Mean gas temperature for GTL and diesel at 60 MPa rail pressure

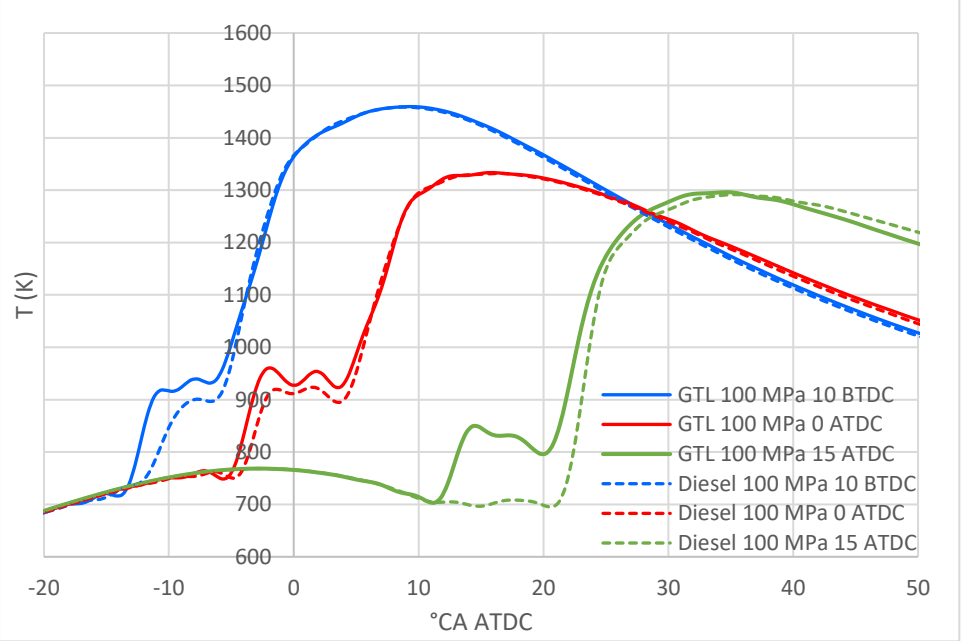


Figure 5.15. Mean gas temperature of GTL and diesel at 100 MPa rail pressure

The impact of rail pressure upon the mean gas temperature of both GTL and diesel are shown in Figure 5.16 and *Figure 5.17* respectively for selected SOI_{Main} settings. Increasing the rail pressure during CDC with both GTL and diesel caused a similar effect, with higher maximum mean gas temperature. In addition, higher temperature at the same timing was the result of more advanced combustion phasing with higher rail pressure. Meanwhile, comparing the same rail pressure with swept injection timing, CDC with GTL and diesel indicated that later injection timing resulted in lower maximum mean gas temperature. However, retarding

SOI_{Main} from 5 to 15°CA ATDC with 100 MPa rail pressure slightly decreased the maximum mean gas temperature.

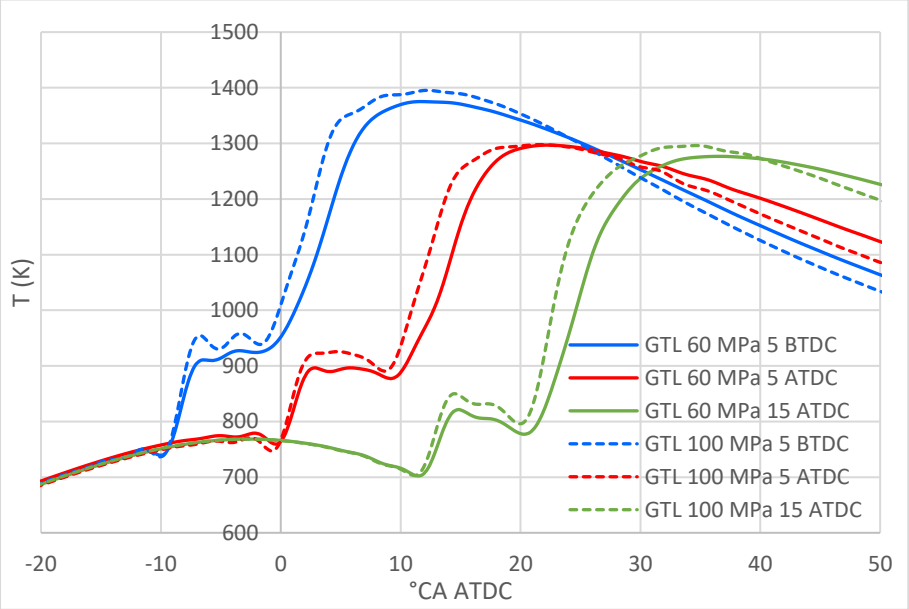


Figure 5.16. Mean gas temperature by CDC with GTL at 60 and 100 MPa of rail pressure

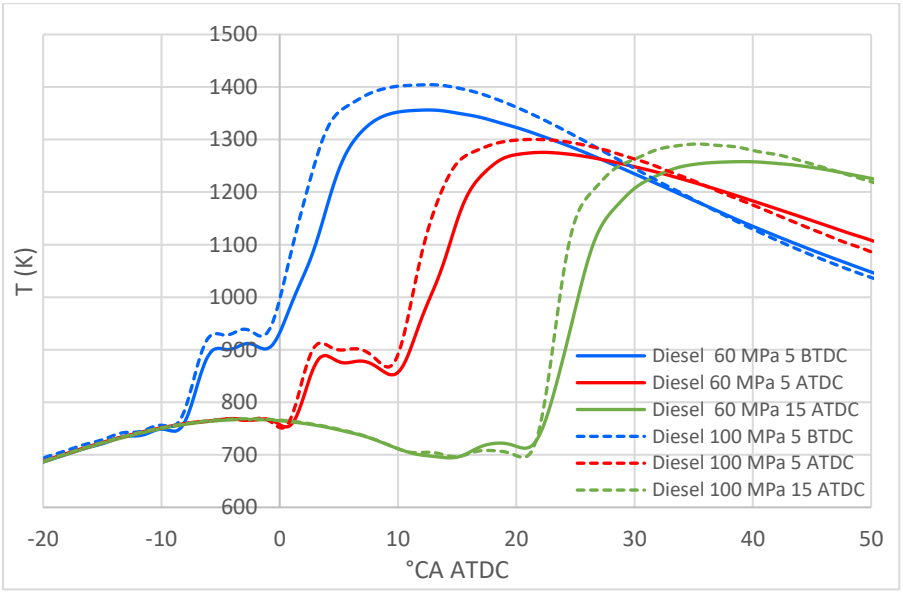


Figure 5.17. Mean gas temperature by CDC with diesel at 60 and 100 MPa of rail pressure

5.3.7 Combustion Stability by CDC with GTL and Diesel

Combustion stability of CDC is quantified from the Coefficient of Variation (COV) of Net IMEP, as illustrated in Figure 5.18. Diesel resulted in the optimum combustion stability at SOI_{Main}=-5 °CA ATDC. On the contrary, setting the SOI_{Main} around TDC in CDC with GTL tended to result in slightly less stable combustion stability than with advanced and retarded injection timing. However, CDC of GTL at all of tested points generally performed with acceptable combustion

stability that was generally better than diesel, with the exception of SOI_{Main}=-5 °CA ATDC that performed similarly to diesel. All values shown were well within acceptable operating limits.

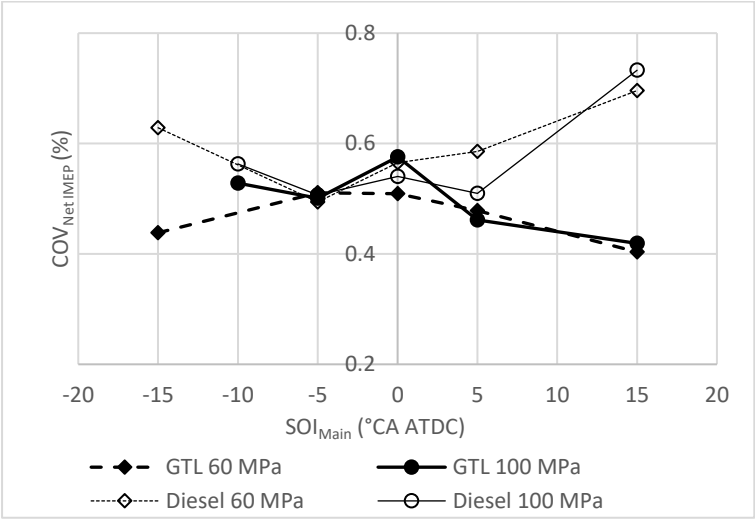


Figure 5.18. Combustion stability in $COV_{Net\ IMEP}$ by CDC with GTL and diesel

5.3.8 Exhaust Gas Emission by CDC with GTL and Diesel

NO_x emissions of CDC with GTL and diesel are depicted in *Figure 5.19* as Brake Specific NO_x ($BSNO_x$). NO_x improvement with retarded injection timing could be attributed to lower combustion temperature, as indicated by mean gas temperature values shown in *Figure 5.14* to *Figure 5.17*. NO_x deterioration with higher rail pressure could be related in a similar way. Comparing both fuels at 60 MPa rail pressure, GTL resulted in lower NO_x than diesel at all injection timings despite higher maximum mean gas temperature than diesel. However, an exception was GTL with 100 MPa rail pressure and SOI_{Main}=-10 °CA ATDC and SOI_{Main}=15 °CA ATDC, resulting in lower NO_x. Similar NO_x levels to diesel were also incurred at -5, 0 and 5 °CA ATDC of SOI_{Main}. Justifying the NO_x improvement of GTL by relating it to predicted mean gas temperature is likely not a viable approach here, since the mean gas temperature may not be an accurate prediction of local temperatures promoting NO_x formation. In addition, higher mean gas temperature with GTL was also produced with advanced combustion phasing due to shorter ignition delay. Meanwhile, higher maximum mean gas temperature could be attributed to more injected fuel energy with GTL but with slower combustion speed during mixing controlled combustion as the more dominant stage of main combustion. Improved NO_x with GTL was likely the result of its lower aromatic content than diesel. Previous studies by Kidoguchi et. al. [161] and Akasaka et al. [162] using fuels with different aromatic contents reported deteriorated NO_x with higher aromatic content. Higher local temperature (that promotes NO_x formation) is likely the result of higher adiabatic flame

temperature due to higher aromatic content of diesel fuel. On the other hand, the effect of cetane number on NO_x emission was not significant [161,162].

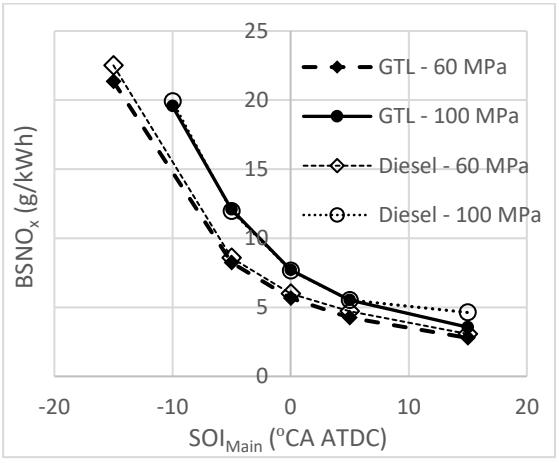


Figure 5.19. NO_x emission by CDC with GTL and diesel

Set out in Figure 5.20 are values of smoke which is expressed in Filter Smoke Number (FSN) for CDC with diesel and GTL at the respective operating condition. For 60 and 100 MPa rail pressure at the same injection timing, GTL resulted in lower FSN than diesel. The higher soot produced with diesel could be attributed to higher aromatic and/or sulphur content of the diesel fuel. Lower vaporisation and entrainment for diesel compared to GTL caused more combustion with a richer mixture that also promotes soot formation. More significant premixed burning with diesel, as indicated by the heat release rate, with a rich mixture also boosts soot formation [74]. In addition, longer combustion duration with GTL with more diffusion combustion could support oxidation of soot formed in the previous stages of combustion (premixed).

Both CDC with diesel and GTL showed a similar effect of improving soot emission with increasing injection pressure from 60 MPa to 100 MPa. This soot improvement was at the cost of NO_x increase, as shown in *Figure 5.19*, which indicates typical the soot-NO_x trade-off. Higher injection pressure improved the fuel atomisation and entrainment that reduced the locally rich mixture combustion and thus improved soot. However, this promotes NO_x formation. The higher injection pressure with diesel improved smoke more significantly than with GTL. This suggests a greater impact of higher rail pressure upon diesel injection performance and hence combustion.

The trend of deteriorating soot with retarded injection timing was exhibited by both diesel and GTL at 60 MPa rail pressure. Meanwhile, less noticeable deteriorating soot was indicated by both GTL and diesel with SOI retardation up to TDC at 100 MPa rail pressure. Retarding

SOI_{Main} from 5 to 15 °CA ATDC during CDC with both GTL or diesel improved soot with 60 MPa rail pressure, but this deteriorated with 100 MPa rail pressure. Improvement of both soot and NO_x for 15 CA ATDC when compared to 5 °CA ATDC with 60 MPa suggested more locally lower temperature that promoted both NO_x and soot formation. To the contrary, the latest injection timing for 100 MPa rail pressure resulted in the NOx-soot trade off; this suggests more combustion occurred with richer conditions and higher temperature.

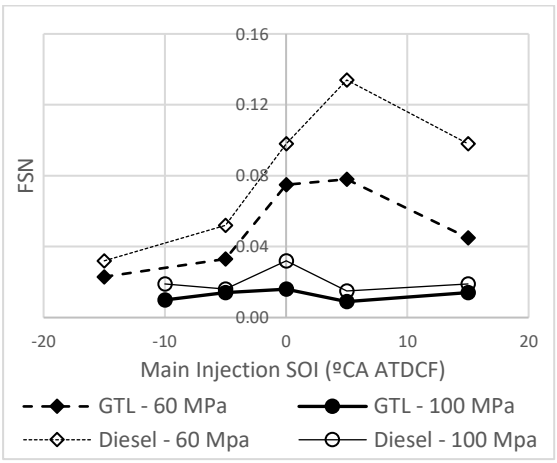


Figure 5.20. FSN by CDC with GTL and diesel

THC emissions for CDC with GTL and diesel are shown in *Figure 5.21* as Brake Specific Hydrocarbons (BSHC). CDC with GTL noticeably resulted in lower THC than diesel for all injection timings. This can be attributed to better atomisation with GTL than diesel. The trend across the injection timing sweep for both GTL and diesel indicates an optimum timing of SOI_{Main}=5 °CA ATDC, with THC deterioration at SOI_{Main}=15 °CA ATDC. Deterioration on THC was more profound for diesel than GTL. Tests with diesel at higher rail pressure improved THC up to SOI_{Main}=0 °CA ATDC, in similar level to 60 MPa rail pressure at SOI_{Main}=5 °CA ATDC, but deteriorated THC with very late injection. Meanwhile, GTL injection at 100 MPa generally improved THC levels, except for SOI_{Main}=0 °CA ATDC. Higher injection pressure for diesel with very late timing and lower in-cylinder pressure and temperature likely caused fuel impingement upon the wall and hence increased THC.

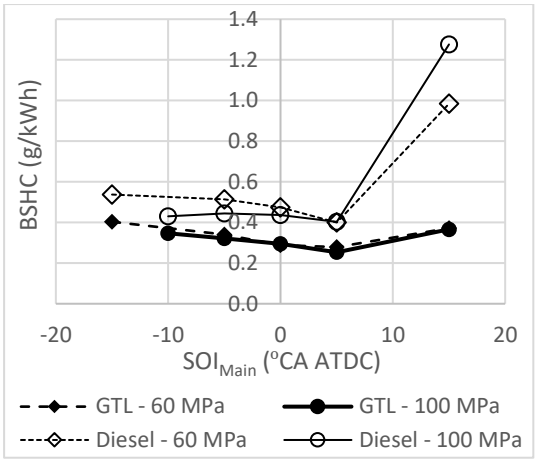


Figure 5.21. THC emission by CDC with GTL and diesel

CO emissions during CDC for both GTL and diesel are presented in *Figure 5.22*. For both GTL and diesel, a retarded SOI_{Main} (from 5 CA ATDC to 15 CA ATDC) exhibits significant increase in CO levels. This strongly suggests relatively poor combustion performance, as also indicated by significant THC increase as shown in *Figure 5.21*. With such very late injection timing, deteriorated injection and entrainment with relatively low pressure and temperature resulted in combustion with locally rich mixtures that formed CO. Unfortunately, this formed CO likely failed to be burned during the late expansion stroke as the pressure and temperature rapidly decreases. Compared to diesel, CDC with GTL at this injection timing resulted in significantly lower CO. Better atomisation during the injection process with GTL [152,153] was attributed to the improved combustion performance, even at low in-cylinder pressure. Improved combustion performance with GTL could be related to its ability to burn with leaner mixture. This is in agreement with a prior study of homogeneous mixtures of diesel and GTL by Lilik et al. [163], undertaken in a modified cooperative fuels research engine with a compression ratio of 8 with a fuel/air equivalence ratio ϕ sweep. It was reported that GTL has lower critical fuel/air equivalence ratio ϕ (0.17) than diesel (0.23), indicated by lowest ϕ where CO emission started to increase significantly due to incomplete combustion [163]. Improved combustion quality with GTL at a critical condition potentially suggests more degrees of freedom to optimise the injection strategy.

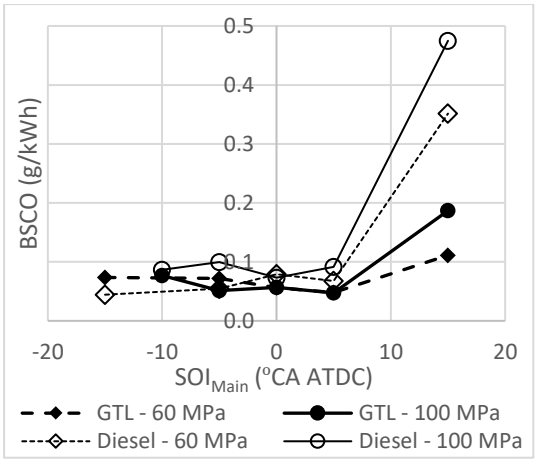


Figure 5.22. CO emission by CDC with GTL and diesel

From the test with the same rail pressure and injection timing sweep, the CO from CDC with GTL was slightly improved as injection timing was retarded up to 5 °CA ATDC and thereafter deteriorated with SOI_{Main}=15 °CA ATDC. In CDC with diesel at 100 MPa, retarding the injection timing with 100 MPa rail pressure led to fluctuating CO up to SOI_{Main}=5 °CA ATDC. Meanwhile, with 60 MPa rail pressure with diesel, retarding SOI_{Main} from -15 to 0 °CA ATDC deteriorated CO albeit slightly improved at SOI_{Main}=5 °CA ATDC. CDC with diesel generally resulted in higher CO emissions than CDC with GTL, except for 60 MPa rail pressure with SOI_{Main}=-15 and -5 °CA ATDC. CDC with Diesel at 60 MPa rail pressure generally resulted in lower CO emissions than 100 MPa rail pressure, except for SOI_{main}=0 °CA ATDC. Changing the rail pressure of the GTL injection did not result in significant changes in CO, except at very late injection timings, where 100 MPa rail pressure resulted in higher CO with either GTL or diesel, which suggests poor combustion via excessively late injection timing. Comparing the same fuel at SOI_{Main}=15 °CA ATDC, with either diesel or GTL at 100 MPa rail pressure, resulted in higher THC and CO than for 60 MPa rail pressure, which suggests deteriorated combustion quality at lower in-cylinder pressures and temperatures.

5.3.9 Combustion Efficiency by CDC with GTL and Diesel

The combustion efficiency during CDC with GTL and diesel fuel (estimated from calculations incorporating combustible constituents in the exhaust gas) is shown in *Figure 5.23*. GTL resulted in marginally higher combustion efficiency than diesel at all injection timings and rail pressures. Similar to the brake efficiency calculation, the calculations were undertaken with an assumed LHV of diesel=42.9 MJ/kg [164] and LHV of GTL=44 MJ/kg [135]. Marginal differences can be incurred with relatively little difference in THC emission and similar CO emission up to 5 °CA ATDC. The difference becomes more significant with SOI_{Main}=15 °CA

ATDC as the THC and CO emission become significantly lower (and BSFC is much lower than diesel). GTL maintained higher combustion efficiency (better than diesel) even with the latest injection timing as indicated by decreased reduction in efficiency across the sweep. This could be attributed to better vaporisation and entrainment using GTL injection [152,153]. The results for both diesel and GTL suggested the optimum SOI timing was SOI_{Main}=5 °CA ATDC.

From comparison between 60 and 100 MPa rail pressures, diesel at 100 MPa with early SOI_{Main} (from -10 °CA ATDC up to 5 °CA ATDC) resulted in slightly higher combustion efficiency than 60 MPa. However, deteriorated performance with 100 MPa rail pressure at the latest injection timing (SOI_{Main}=15 °CA ATDC) resulted in significantly lower combustion efficiency than for 60 MPa. GTL shows a similar effect of varying rail pressure, where 100 MPa resulted in slightly higher combustion efficiency with SOI_{Main} up to 5 °CA ATDC, but deteriorating with SOI_{Main}=15 °CA ATDC to incur slightly lower combustion efficiency than for 60 MPa rail pressure at the same injection timing. Higher rail pressure resulted in higher fuel injection rate and shortened the injection duration, which increases air/fuel mixing and entrainment and could improve combustion performance [160] as shown by early SOI_{Main}. However, higher rail pressure at the latest injection timing in a lower in-cylinder temperature and pressure environment likely caused wall wetting that increased the unburned hydrocarbons (by 30% for diesel) as shown in *Figure 5.21*. GTL with 100 MPa and SOI_{Main}=15 °CA ATDC resulted in less deterioration than diesel at 100 MPa. Higher combustion efficiency with GTL at all test points is an indication of higher combustion performance with GTL. Although GTL resulted in this increased combustion efficiency than diesel, lower brake efficiency occurred at many points. This suggests that additional optimisation of the injection strategy should improve brake efficiency to result in higher brake efficiency than diesel in future work.

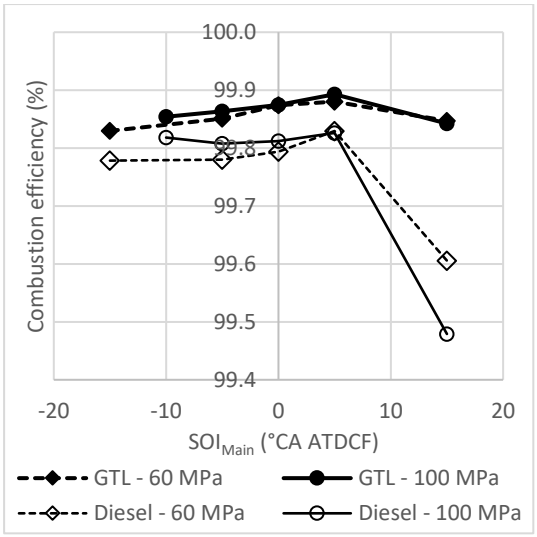


Figure 5.23. Combustion efficiency during CDC with GTL or diesel

5.3.10 Exhaust Gas Temperature by CDC with GTL and Diesel

Exhaust Gas Temperature (EGT) for each fuel at the test conditions are set out in *Figure 5.24*. Longer combustion duration and later combustion phasing for diesel or GTL with 60 MPa rail pressure resulted in higher EGT than for 100 MPa rail pressure. Retarded injection timing resulted in lower in-cylinder temperature, as shown in *Figure 5.14* to *Figure 5.17*. In addition, retarded combustion phasing, as shown in *Figure 5.12*, reduced cylinder wall heat loss, hence resulting in higher exhaust gas temperature. In comparison of GTL and diesel with SOI_{Main}=15 °CA ATDC, diesel suffered longer ignition delay and later end of combustion than GTL. This resulted in lower cylinder wall heat transfer and hence higher EGT than GTL by ~20°C.

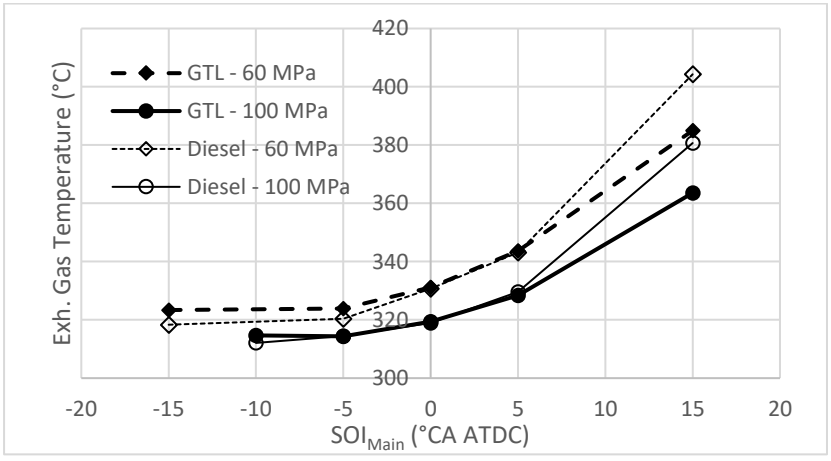


Figure 5.24. Exhaust Gas Temperature by CDC with GTL and diesel

5.4 Results and Discussion on PDFC with GTL and PDFC with Diesel as Pilot Fuel

Test results from PDFC with GTL (GTL-PDFC) or PDFC with diesel (diesel-PDFC) are presented in this section. Post-processing on the crank-angle resolved data recording was carried out on average of 200 consecutive cycles. The analysis and insight to the process are also discussed in this section. Initial analysis was concerned with efficiencies, then in-cylinder pressure and combustion-related parameters such as heat release rate, mass fraction burned, combustion phasing and duration and stability. Exhaust gas emissions are presented, with accompanying discussion of the related processes that contribute to their formation. In the last section the EGT produced with each of the operating points are discussed.

5.4.1 Brake Efficiency by GTL-PDFC and Diesel-PDFC

Shown in *Figure 5.25* are values of brake efficiency produced by GTL-PDFC and diesel-PDFC. A first pilot injection with earlier timing in a longer pilot separation likely resulted in poor atomisation and vaporisation, with deteriorated brake efficiency. Meanwhile, the brake efficiency of GTL-PDFC is higher than for diesel-PDFC in varying significance as shown in *Figure 5.25*. PDFC with either GTL or diesel indicates a similar effect of the pilot separation, where a longer pilot separation resulted in deteriorated combustion and brake efficiency.

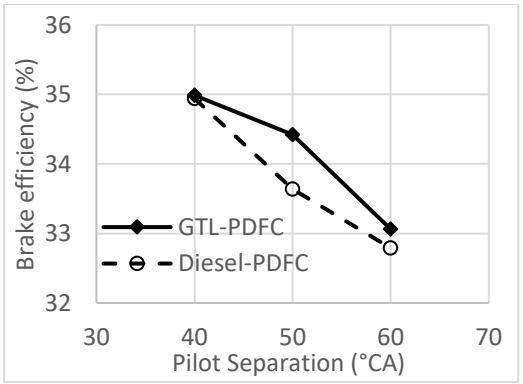


Figure 5.25. Brake efficiency by GTL-PDFC and diesel-PDFC

5.4.2 In-cylinder Pressure by GTL-PDFC and Diesel-PDFC

A comparison of the in-cylinder pressure during PDFC with GTL and diesel with corresponding pilot separation is depicted in *Figure 5.26*. Compared at the same pilot separation, GTL-PDFC resulted in higher peak in-cylinder pressure and earlier start of combustion. This could be related to shorter ignition delay with GTL, which has a higher cetane number than diesel.

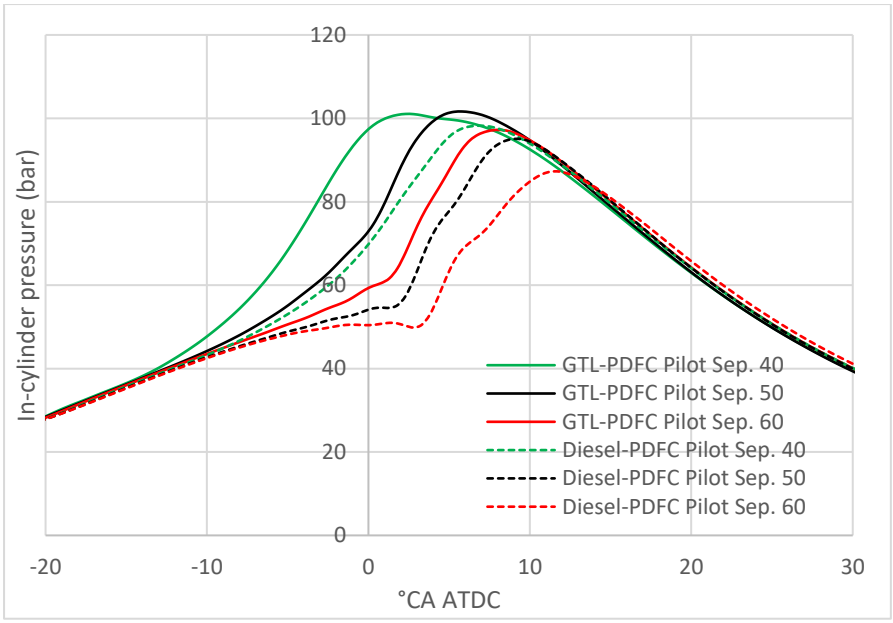


Figure 5.26. In-cylinder pressure by GTL-PDFC and diesel-PDFC at corresponding pilot separation

5.4.3 Net Heat Release Rate (NHRR) by GTL-PDFC and Diesel-PDFC

The net heat release rate of GTL-PDFC and diesel-PDFC is illustrated in *Figure 5.27*. During PDFC combustion with GTL or diesel, the combustion was initiated with Low Temperature Heat Release Rate (LTHR) from the first pilot fuel, as indicated by a small hump between -23 to -15 °CA ATDC. LTHR by GTL-PDFC is higher and of longer duration than diesel-PDFC. The LTHR contributes to the combustion in the next stage. LTHR partially oxidises a small fuel fraction at lower temperature than 850 K, which can increase the air-fuel mixture temperature and hence promote ignition of the additional charge [165]. GTL, with higher paraffinic and less aromatic content than diesel, is more conducive to the two-stage combustion process and incurs larger LTHR during dual-fuel combustion.

NHRR for the diesel-PDFC results indicates that a longer pilot separation delayed the start of combustion. The noticeable gradual increase in NHRR for Diesel-PDFC at 40 °CA separation indicates auto-ignition of the 1st pilot fuel that promotes flame propagation of the surrounding air/gas. In the test with longer separation, contribution of combustion by 1st pilot was diminished and the contribution of the 2nd pilot became more significant, as indicated by higher premixed combustion post 2nd injection. This trend is not only apparent for diesel-PDFC, but also GTL-PDFC. However, due to shorter ignition delay, as a result of lower cetane number, better fuel atomisation, and lower auto-ignition temperature, GTL advanced the combustion and resulted in autoignition of the 1st pilot injection that gradually increased the heat release rate. Earlier SOC and higher heat release from the 1st pilot with

shorter pilot separation possibly suggests a significant turbulence effect from the 1st pilot injection with higher pressure and temperature during the end of compression stage. The effect of higher heat release for GTL-PDFC, due to contribution of the first pilot, was also indicated with 50 °CA pilot separation, with the heat release rate increased further after the second injection which probably suggests a significant impact of local turbulence upon combustion.

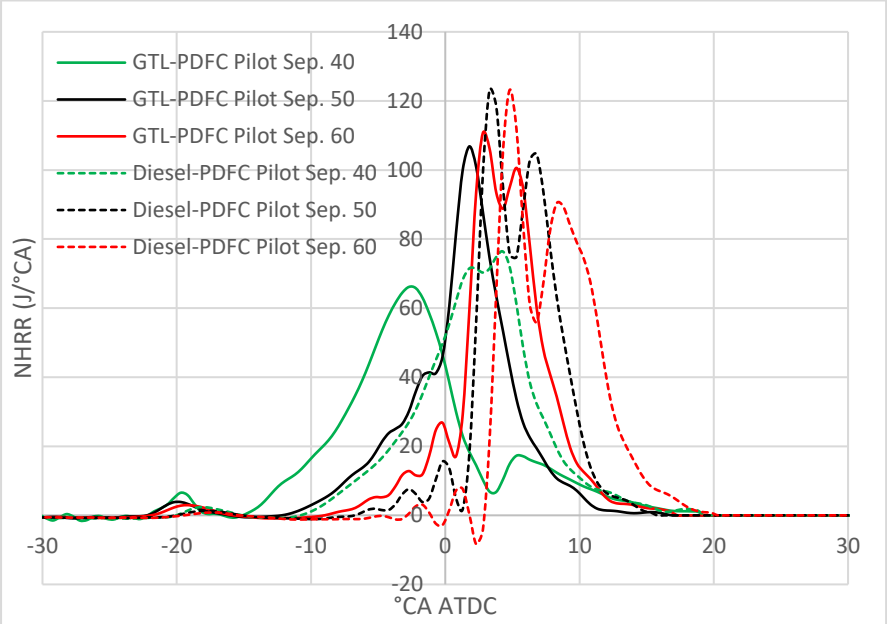


Figure 5.27. Net heat release rate by GTL-PDFC and diesel-PDFC

In comparing the same pilot separation, GTL-PDFC at the respective three pilot separations resulted in higher heat release during the early part of combustion. This suggests autoignition of pilot fuel and flame propagation of gaseous fuel in the vicinity in a more simultaneous way than incurred during diesel-PDFC. GTL injection that vaporises more quickly and that is entrained more easily than diesel likely provided more ignition source for the premixed gaseous fuel. In addition, low second peak of NHRR by 40 °CA pilot separation suggests that during GTL-PDFC the gaseous fuel mostly burned by the first pilot fuel and burned in the second pilot in little proportion. Increasing second pilot ratio to the total fuel quantity for GTL-PDFC may likely signify the contribution of the second pilot to combustion phasing and improving efficiency. Meanwhile, in tests with longer separation (at 50 and 60 °CA separation), the impact of turbulence by the second pilot fuel resulted in higher impact than the first pilot.

5.4.4 Mass Fraction Burned (MFB) by GTL-PDFC and diesel-PDFC

The MFB of GTL-PDFC and diesel-PDFC are depicted in *Figure 5.28*. Further analysis includes the combustion phasing (CA50) and combustion duration (from 10 to 90% MFB) as shown respectively in *Figure 5.29*(a) and (b). GTL as pilot injection fuel during PDFC resulted in advanced combustion phasing (CA50) and longer combustion than diesel-PDFC. However, it is important to note that early combustion initiated via the first pilot injection is noticeably higher for GTL-PDFC, while during diesel-PDFC significant heat release rate occurred after the second pilot injection as shown in *Figure 5.27*. In comparing the MFB with different pilot separations, both diesel-PDFC and GTL-PDFC retarded the SOC and combustion phasing for a longer pilot separation. In combustion with 50 and 60 °CA pilot separation, shorter combustion duration than 40 °CA of pilot separation was contributed to by a more significant turbulence effect of the second pilot injection, as discussed in the previous section.

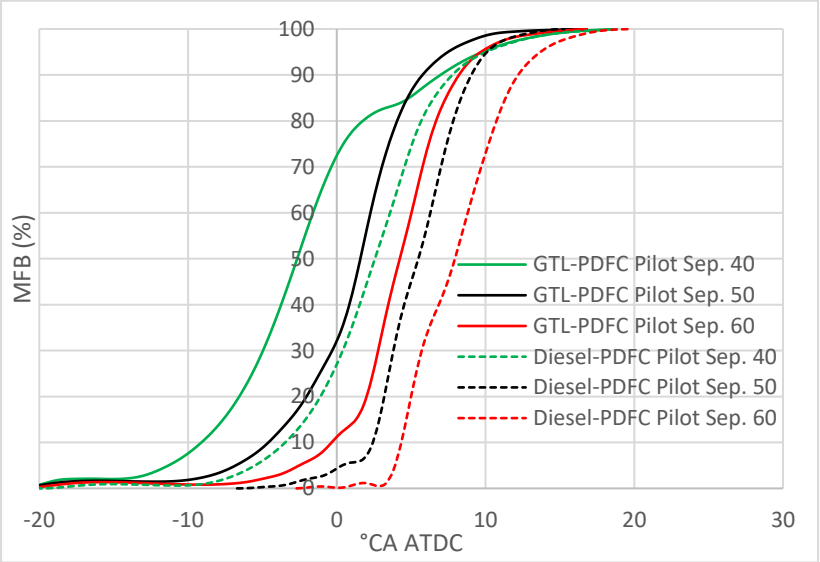


Figure 5.28. MFB by GTL-PDFC and diesel-PDFC

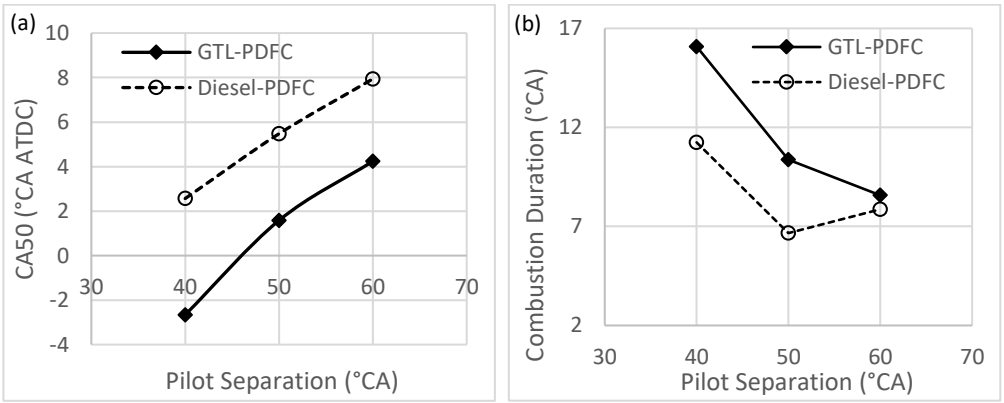


Figure 5.29. (a) Combustion phasing (CA50) and (b) Combustion duration of GTL-PDFC and diesel-PDFC

5.4.5 Mean Gas temperature by PDFC with GTL and diesel

Set out in Figure 5.30 is the mean gas temperature for GTL-PDFC and diesel-PDFC. This was calculated by assuming uniform distribution of premixed gas into every cylinder. Earlier combustion phasing with GTL-PDFC resulted in higher gas temperature at earlier timing, despite lower maximum mean gas temperature. Lower peak with GTL-PDFC suggests a less significant contribution of the second pilot injection to the combustion, hence resulting in little increase in mean gas temperature. At a pilot separation of 50 and 60 °CA, the maximum mean gas temperature of GTL-PDFC is higher than diesel-PDFC due to higher heat release rate at more advanced timing.

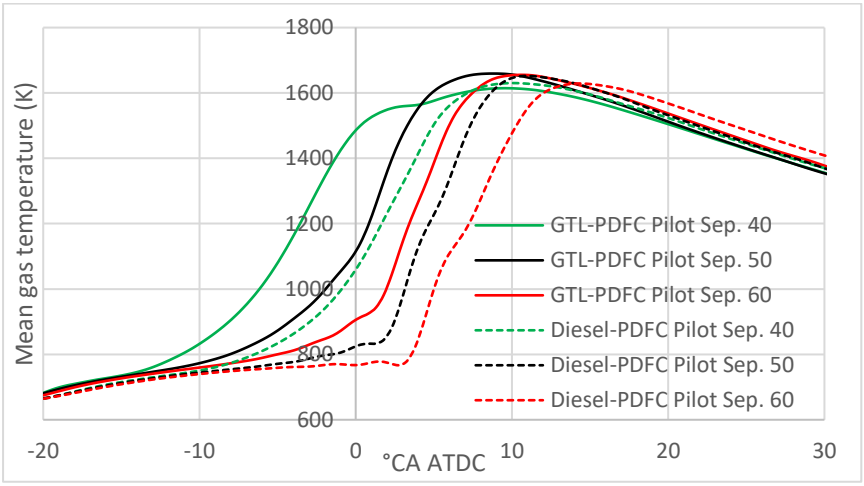


Figure 5.30. Mean gas temperature by GTL-PDFC and diesel-PDFC

5.4.6 Pressure Rise Rate (PRR) by PDFC with GTL and Diesel as Pilot Fuel

Maximum PRR and its location during GTL-PDFC and diesel-PDFC are shown in *Figure 5.31*(a) and (b) respectively. PDFC with GTL resulted in higher max. PRR than diesel-PDFC at 40 °CA pilot separation, while 50 and 60 °CA resulted in lower max. PRR. According to their location, the max. PRR during GTL-PDFC with 40 °CA pilot separation resulted before the second pilot combustion, while in the other test points the max PRR occurred after the second pilot injection. These results could be related to the turbulence effect during fuel injection and combustion. Turbulence is a decisive factor that improves heat release and results in higher max. PRR. A combination of turbulence effects, not only by the first pilot injection that is closer to TDC, but also the pilot autoignition at earlier timing, promoted flame propagation that resulted in high heat release rate and max. PRR before the second pilot injection. Such effects may well be less pronounced with higher gas substitution ratio. During diesel-PDFC with the same injection timing, a higher heat release rate suggests a contribution of turbulence but at lower rate than for GTL, which could be related to the typical longer

ignition delay of diesel that becomes worse in the premixed environment. With 50 and 60 °CA pilot separation, the first pilot was injected at an advanced timing that resulted in less significant turbulence when it autoignited. Therefore, at this operating condition both GTL-PDFC and diesel-PDFC resulted in higher heat release and max. PRR after the second injection as the in-cylinder condition became more turbulent.

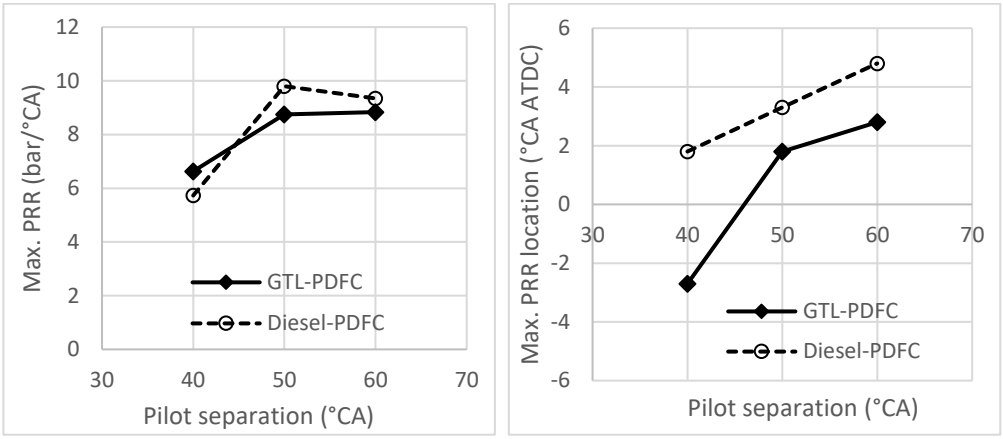


Figure 5.31. (a) Max. PRR and (b) Max. PRR location by GTL-PDFC and diesel-PDFC

5.4.7 Combustion Stability by GTL-PDFC and Diesel-PDFC

Combustion stability during PDFC with GTL or diesel, shown for the calculated COV of Net IMEP of cylinder 1, is shown in *Figure 5.32*. GTL-PDFC and diesel-PDFC at 40 and 60 °CA pilot separation resulted in similar combustion stability. Meanwhile, with 50 °CA pilot separation GTL-PDFC resulted in more stable combustion than diesel-PDFC. At this operating condition, both GTL-PDFC and diesel-PDFC resulted in acceptable cycle-to-cycle variation of less than 4% of $COV_{NetIMEP}$, albeit this is considered as the threshold or acceptable operation in real engines.

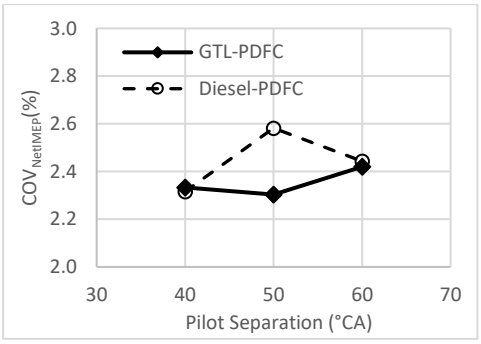


Figure 5.32. Combustion stability from $COV_{NetIMEP}$ by GTL-PDFC and diesel-PDFC

5.4.8 Exhaust Gas Emission by GTL-PDFC and diesel-PDFC

Exhaust gas emissions during GTL-PDFC and diesel-PDFC are shown in Figure 5.33. Comparison of PDFC with GTL and diesel as the pilot fuel generally shows that GTL as the pilot generally resulted in lower emissions than incurred with diesel. In addition, lower CO and THC for GTL indicates improved combustion efficiency than diesel-PDFC. Among the PDFC test points, 40 °CA pilot separation indicates the optimum operating condition with lowest NO_x, FSN, CO and THC, either in GTL-PDFC or diesel-PDFC modes. Better fuel atomisation and entrainment of the injected GTL within premixed gaseous fuel provided more ignition sources for the surrounding gaseous fuel, thus improving flame propagation.

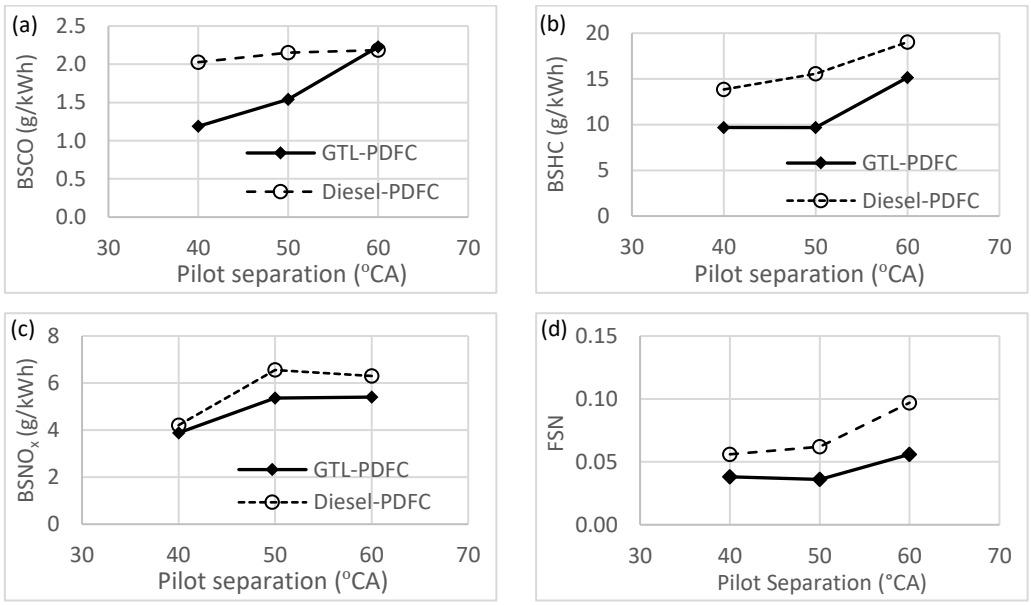


Figure 5.33. Exhaust gas emission by GTL-PDFC and diesel-PDFC: (a) CO, (b) THC, (c) NO_x and (d) FSN

Higher NO_x emissions with 50 and 60 °CA pilot separation (than 40 °CA) for either GTL-PDFC and diesel-PDFC may be related to mean gas temperature, as indicated by the highest peak for each respective fuel shown in *Figure 5.30*, which suggests NO_x deterioration due to thermal mechanisms. However, lower NO_x emissions during GTL-PDFC may not be related directly to the mean gas temperature as this mode incurred higher mean gas temperature than diesel-PDFC. For the respective fuel, the results do not indicate a straightforward NO_x-soot trade-off, since changing the pilot separation from 40 to 50 °CA deteriorated NO_x but with FSN remaining constant. With further pilot separation at 60 °CA, NO_x remained constant but with deteriorated soot. The longer combustion duration of GTL-PDFC and diesel-PDFC with 40 and 50 °CA separation (with earlier combustion phasing) likely promoted soot oxidation.

5.4.9 Combustion Efficiency by GTL-PDFC and Diesel-PDFC

Combustion efficiency values during PDFC with GTL or diesel are depicted in *Figure 5.34*. GTL-PDFC generally resulted in higher combustion efficiency than diesel-PDFC. PDFC-GTL with 40 and 50 °CA pilot separation resulted in similar combustion efficiency while 60 °CA separation decreased it quite significantly. During diesel-PDFC, combustion efficiency decreased during the test with longer pilot separation. Higher combustion efficiency during GTL-PDFC indicates that GTL as pilot fuel improved dual-fuel combustion performance.

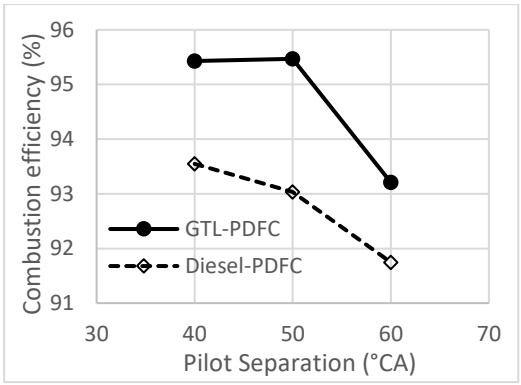


Figure 5.34. Combustion efficiency by GTL-PDFC and diesel-PDFC

5.4.10 Exhaust Gas Temperature by GTL-PDFC and diesel-PDFC

The Exhaust Gas Temperature (EGT) values during GTL-PDFC and diesel-PDFC are shown in *Figure 5.35*. GTL-PDFC at 40 and 50 °CA pilot separations resulted in slightly higher exhaust gas temperature, which could be related to later EOC during GTL-PDFC that lowered the cylinder wall heat losses. At 60 °CA pilot separation, 6°C higher EGT duirng diesel-PDFC was likely due to retarded combustion phasing and the latest EOC amongst the tested operating conditions, thus lower in-cylinder wall heat losses.

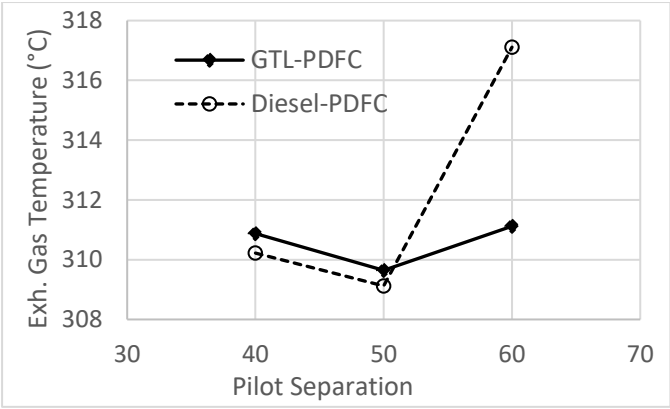


Figure 5.35. Exhaust gas temperature by GTL-PDFC and diesel-PDFC

5.5 Summary

Experimental tests were performed in a light duty CI engine test rig under Conventional Diesel Combustion (CDC) and Premixed Dual-fuel Combustion (PDFC). The tests were undertaken with two pilot fuels, namely ultra-Low sulphur diesel (diesel) and GTL fuel with the rail pressure switched between 60 and 100 MPa for injection timing sweeps. The gas substitution ratio was limited to 58%, which was the highest ratio where acceptable combustion stability could be achieved. CDC with GTL generally resulted in higher combustion efficiency than diesel, but lower brake efficiency at most operating conditions, except at SOI_{Main}=15 °CA ATDC that resulted in higher brake efficiency than diesel at 60 MPa rail pressure. This suggest that optimising injection strategy including pilot/main ratio, pilot quantity and injection timing could result in higher brake efficiency by GTL than diesel. Tests with higher rail pressure increased combustion efficiency but decreased brake efficiency, except at SOI_{Main}=15 °CA ATDC. GTL generally performed with shorter ignition delay and resulted in a reduced premixed stage of the main combustion event compared to diesel. Despite earlier SOC with GTL, the longer ignition delay in diesel resulted in a higher premixed part of the main combustion event that resulted in similar combustion phasing and shorter combustion duration than GTL. With the latest injection timing of SOI_{Main} =15 °CA ATDC, GTL performed with shorter ignition delay than diesel, longer separation of pilot and main combustion and advanced combustion phasing than diesel.

From the exhaust gas analysis from CDC, GTL generally resulted in lower NO_x, smoke, THC and CO than diesel. Increasing rail pressure either in CDC with GTL or diesel at the same injection timing deteriorated NO_x and improved smoke (the typical NO_x-soot trade off in conventional mono-fuel diesel combustion). NO_x emissions for each respective fuel with the same rail pressure were highest with the most advanced injection timings and could be decreased by later injection due to lower peak combustion temperatures. Retarding the injection timing by up to 5 °CA ATDC both during CDC with diesel or GTL at 60 MPa rail pressure deteriorated soot albeit improved with at SOI_{Main}=15 °CA ATDC due to deteriorated combustion performance. Lower NO_x and soot for GTL was apparent at most operating points despite higher mean gas temperature, which potentially suggests a contribution of the aromatic content in the fuel. For the THC emission results, retarding SOI_{Main} up to 5 °CA ATDC improved THC, but more retarded injection timing deteriorated values, where more significant deterioration was observed with diesel. Higher rail pressure during CDC with GTL improved THC at all injection timings, while during CDC with diesel the elevated pressure improved THC values at SOI_{Main} up to 5 °CA ATDC but thereafter deteriorating with at SOI_{Main}

=15 °CA ATDC. From the CO emission results, the highest CO was observed with diesel at 100 MPa rail pressure and SOI_{Main} =0 °CA ATDC, but the impact of injection timing at this injection pressure was less obvious and fluctuated. At most operating points, CO emissions with GTL were lower than diesel even with SOI_{Main} =15 °CA ATDC, which overall indicated improved combustion efficiency.

GTL and diesel were used as pilot fuel during PDFC. GTL-PDFC generally performed with higher combustion and brake efficiency. Tests with longer pilot separation deteriorated both combustion and brake efficiency. GTL, with shorter ignition delay and higher heat release rate during early stages of combustion, advanced the combustion phasing but resulted in lower heat release rate during the end of combustion and overall prolonged combustion duration. From the analysis on exhaust gas emissions, PDFC with GTL emitted lower concentrations of CO, THC, NO_x and soot at all pilot separations. From several parameters of efficiencies, combustion performance and emission, a 40 °CA pilot separation was the optimum operating condition. GTL-PDFC slightly improved cycle-to-cycle variations with acceptable noise levels as indicated by max. PRR. This could be related to higher cetane number which improved the ignition delay and reduced premixed diesel combustion. Overall, the results indicate preferential performance of GTL during dual-fuel operation with relatively lower substitution ratios. Such operation is not preferred but may be relevant in future heavy duty applications, potentially including future marine or stationary power generation four stroke engines switched to dual-fuel and ideally expected to remain in dual-fuel mode across the operating map. The engine was only capable of a relatively low gas substitution ratio, the reasons for which could not be uncovered from the parameters measured in the currently reported work (which warrants further investigation in its own right covering effects such as differences in charge motion or other engine design).

Chapter 6 The Effects of Cylinder Deactivation on Low Load Dual-Fuel Combustion

6.1 Introduction

Set out in this chapter is a detailed description of the correlated simulation work undertaken to improve understanding of the potential impact of cylinder deactivation on dual-fuel combustion. The chapter includes an overview of the operating strategy, followed by summary of the parametric modelling sweeps undertaken in an attempt to expand the low load operating limit to capture and increased proportion of the drive cycle when operating at high natural gas substitution ratio. The chapter is concluded with a summary of the key findings.

6.2 Simulated Points and Implemented Strategies

From prior work it was clear that the typical low load limit of dual-fuel operation when operating around 1200 rpm was approximately 6 bar BMEP. This speed and load can be considered representative of low load cruising operation, where an engine entering an urban environment would still operate at lower loads in a transient manner. The goal of the simulation was therefore to understand if cylinder deactivation could be used to allow operation at roughly half this load (neglecting small differences in pumping, valvetrain friction or to a lesser degree bearing loads due to differences in the in-cylinder pressure profiles). The simulations were therefore undertaken at 1200 rpm and the two load points at 3 and 6 bar BMEP. These points are also appropriately representative of low load operating conditions for the Volvo D8 engine under the WHTC as presented in Chapter 1. Dual-fuel combustion was simulated at 90% substitution ratio of fuel energy by gaseous fuel, which was a target ratio following the implementation of Euro VI legislation. A mixture of methane/ethane with 95/5 $\%_{mol}$ was used in the simulation works to represent typical natural gas composition within the European market. Several parameters were set equivalent for all simulations described in *Table 6.1*, referred previous study in a single cylinder heavy duty engine by May [106] that covered dual-fuel test under CDF, PDFC and Miller cycle.

Parameter	Value
Intake pressure (at inlet end)	1 barA
Intake air temperature (at inlet end)	25 °C
Exhaust manifold outlet pressure (average)	Simulation without EGR: 1 barA
	Simulation with EGR: >1 barA
Standard IVC	-158.4° ATDC (fully closed)
Diesel Rail Pressure	1000 bar
Gaseous fuel injection rate	15 mg/ms
End of injection of gaseous fuel	- 270 °CA ATDCF
Diesel injection timing (SOI)	Iterated to locate CA50 at 8 °CA
Standard IVC (fully closed)	-158.4° ATDC
Oil temperature	90 °C
Coolant temperature	90 °C

Table 6.1. General setting parameters for simulation

Simulations at 1200 rpm/6 bar BMEP were performed under both conventional (all cylinders firing) and CDA operating strategies, with the details are summarised in *Table 6.2*. The 6-cylinder active strategy (6-cyl) was simulated with an air/fuel equivalence ratio (λ) sweep from 1.0 to 1.6 in 0.2 increments and also a simulation point at leanest mixture (no λ control), i.e no EGR, no throttling, and standard IVC. The term air/fuel equivalence ratio (λ) when used in this chapter is the global λ that was calculated from the quantity of diesel, gaseous fuel and air quantity. The intake charge mass under 6-cyl operation was controlled by throttling, EGR or Miller cycle with LIVC. The simulations with throttling, Miller or no λ control were simulated in CDF with a single pilot injection. This injection setting was in accord with prior Miller cycle experimental work by Ian May [106]. Meanwhile, an external EGR operating strategy was also simulated with PDFC, which is presented in this chapter as PDFC-EGR, where the first pilot fuel was injected at 15 °CA prior to the second injection in a 30/70 ratio and the second injection timing swept.

The CDA strategy at 6 bar BMEP was simulated under CDF with a λ sweep from 1.0 to 1.8 in 0.2 increments. In CDA simulations, the eSupercharger speed was iterated to fulfil the required intake air quantity for the target λ. The eSupercharger motor was simulated to be powered by either a battery (marked as CDA-Battery) or by electricity from the crank-driven generator (denoted as CDA-Generator). The simulation of CDA-Battery with battery at high state of charge aimed to predict the performance at condition where the compressor used the electric power without adding more load to the engine crankshaft. The battery energy was assumed to be supplied by regenerative braking. Therefore, the consumed electrical

energy from the battery was not included in the calculation of engine efficiency. This was considered to be an appropriate assumption for urban mild hybrid operation. Meanwhile, the CDA-Generator was simulated to predict the engine performance when the battery is exhausted of power and the motor for the eSupercharger relies on electricity from a crank-driven generator. Due to different eSupercharger speed, the intake manifold pressure in the simulated CDA strategy depended on the simulated λ, while the exhaust manifold pressure was kept at 1 bar. By modelling both of these electric supply scenarios the two extreme cases for battery state of charge could be compared.

	Strategy	DF scenario*	EGR	Throttling	IVC	Simulated λ
CDA (3-cyl. firing)	**CDA-Battery**	CDF	No	No	Standard	1.0, 1.2, 1.4, 1.6, 1.8 (Controlled with eSupercharger)
	CDA-Generator	CDF	No	No	Standard	
6-cyl. firing	**PDFC-EGR**	PDFC	Yes	No	Standard	1.0, 1.2, 1.4, 1.6
	Throttling	CDF	No	Yes	Standard	
	Miller-LIVC	CDF	No	No	LIVC	
	No λ control **	CDF	No	No	Standard	1.7

*) Dual-fuel scenario:
- CDF: single pilot injection
- PDFC: double pilot injections, interval between two injections: 15 °CA, ratio of $1^{st}/2^{nd}$ pilot quantity: 30/70)

**) No intake throttling, no EGR, standard IVC

Table 6.2. Simulated strategies at 1200 rpm/6 bar BMEP

Simulations at 3 bar BMEP were performed with 6-cyl and CDA strategies as listed in *Table 6.3*. The 6-cyl strategies were only simulated at λ=1.8 either with throttling, EGR or a combination of throttling and EGR. The 6-cyl operation was not simulated at lower λ since excessive throttling was required leading to poor thermal efficiency. This study limited throttling to reduce the intake manifold pressure minimum to 0.7 barA. The maximum EGR rate was also limited to 40%, which was exceeded without throttling at this low load. With the throttling strategy, running the engine at 3 bar BMEP and λ=1.8 requires significant intake restriction that results in the very low MAP (~0.67 bar). Simulation with EGR at λ=1.8 required very high EGR rate (34.1%). The combined strategy (Throttle-EGR) was implemented to optimise the strategy, by implementing an intake manifold pressure at 0.8 bar and 15.9% EGR. For Miller cycle operation, it was also not possible to run with the 6-cyl strategy active as very late IVC was required, which caused the engine to run at very low and unrealistic compression ratio. The CDA strategy at 3 bar BMEP was simulated at λ=1.0, 1.2 and 1.4 using several intake control methods including: i) CDA with EGR (in PDFC), ii) CDA

with LIVC (in CDF), and iii) CDA with throttling (in CDF). At the highest simulated λ, CDA strategies were simulated without any intake restriction, either with CDF or PDFC respectively.

	Strategy	DF scenario*	EGR	Throttling	IVC	Simulated λ
CDA (3-cyl. firing)	**CDA-EGR(PDFC)**	PDFC	Yes	No	Standard	1.0, 1.2, 1.4
	CDA-Throttling	CDF	No	Yes	Standard	
	CDA-LIVC	CDF	No	No	LIVC	
	CDA-PDFC	PDFC	No	No	Standard	1.48
	CDA-CDF	CDF	No	No	Standard	1.5
6-cyl. firing	**PDFC-EGR**	PDFC	Yes	No	Standard	1.8
	Throttling	CDF	No	Yes	Standard	
	Throttling-EGR-PDFC	PDFC	Yes	Yes	Standard	
	Throttling-EGR-CDF	CDF	Yes	Yes	Standard	

*) Dual-fuel scenario:
- CDF: single pilot injection
- PDFC: double pilot injections, interval between two injections: 15 °CA, ratio of $1^{st}/2^{nd}$ pilot quantity: 30/70)

Table 6.3. Simulated strategies at 1200 rpm/3 bar BMEP

6.3 Simulation Results at 1200 rpm/6 bar BMEP

The results of the parametric modelling work for 1200 rpm/6 bar BMEP are presented in this section, covering several aspects of relative engine performance. The effect of the implemented strategy to the EGT are also compared. The results of simulation with PDFC are presented with the mark clearly mentioned, while the other ones without PDFC are the results of simulation with CDF.

6.3.1 Intake Manifold Pressure and Temperature at 1200 rpm/6 bar BMEP

The simulation of CDA, PDFC-EGR and throttling with λ sweeps generally resulted in different intake pressures to supply air at the required quantity. The impact of the strategies upon average intake manifold pressure and temperature are presented in *Figure 6.1*. Increasing λ during CDA operation generally required increased intake air mass, thus the eSupercharger needed to operate at higher speed, which increased the intake manifold pressure and temperature. Compared to CDA-Battery, CDA-Generator operated at higher intake manifold pressure and temperature for a given λ , associated with the eSupercharger working at higher speed to supply higher amount of intake air for the slightly higher amount of injected fuel for the same λ. In PDFC-EGR, the intake pressure remained relatively constant while the

temperature was higher at less lean mixtures (from 27 °C at λ=1.6 to 54 °C at λ=1.0) due to more EGR being supplied to the intake port to reduce the intake air quantity. The simulation at a less lean mixture with throttling indicates relatively constant intake manifold temperature and decreasing intake pressure (from 0.94 bar at λ=1.6 to 0.7 bar at λ=1.0) due to more restriction with the less lean mixture. Meanwhile, Miller-LIVC indicated relatively constant intake pressure and higher intake temperature at less lean mixtures due to a certain amount of air being expelled back from the cylinder during the compression stroke.

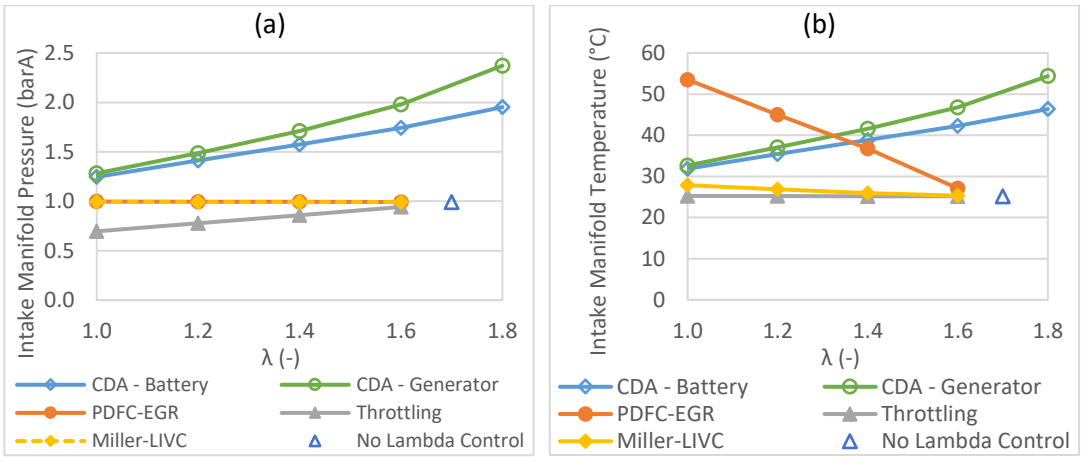


Figure 6.1. (a) Intake manifold pressure and (b) Intake manifold temperature at 1200 rpm/6 bar BMEP

Set out in Figure 6.2(a) are values of Cylinder 1 intake trapped mass for each strategy at 1200 rpm/6 bar BMEP. In all simulated strategies except PDFC-EGR, simulation at less lean mixture (lower λ) reduced the intake trapped mass. Intake dilution with increasing EGR percentage (as shown in *Figure 6.2*(b)) resulted in only slight reduction in total trapped mass when running closer to stoichiometric.

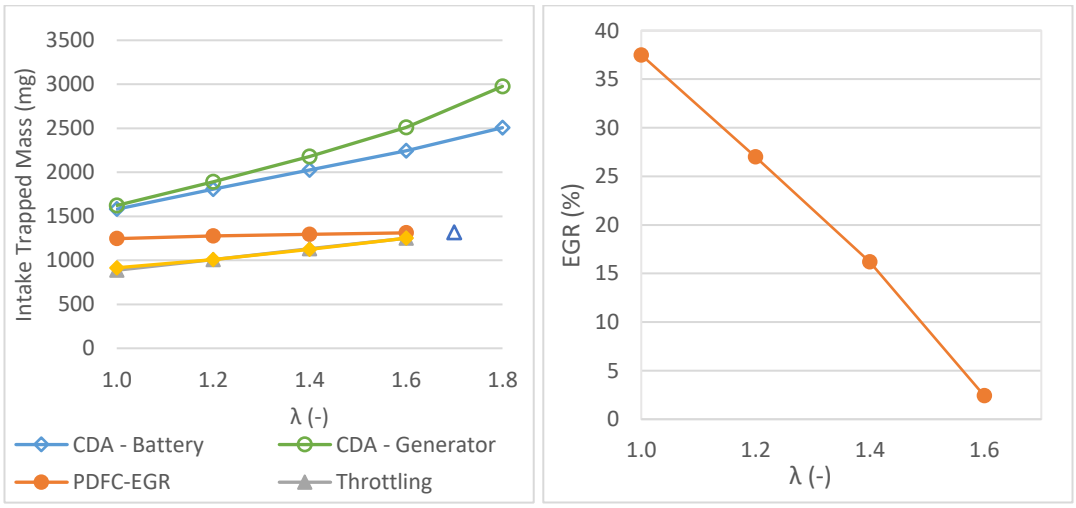


Figure 6.2. (a) Intake trapped mass by simulated strategies and (b) EGR in PDFC-EGR at 1200 rpm/6 bar BMEP

6.3.2 Dynamic Compression Ratio and IVC in Miller-LIVC at 1200 rpm/6 bar BMEP

In the simulation with standard IVC at -158.5 °CA ATDC, non-Miller strategies operated with a "dynamic" compression ratio of 17.1, which is calculated from the volumetric ratio at IVC to TDC. Miller cycle with LIVC decreased the dynamic compression ratio, as illustrated in *Figure 6.3*. Retarding IVC from -121 to – 79 °CA ATDC reduced the dynamic compression ratio from 14.5 at λ=1.6 down to 9.0 at λ=1.0. Going further than this was considered to be unrealistic.

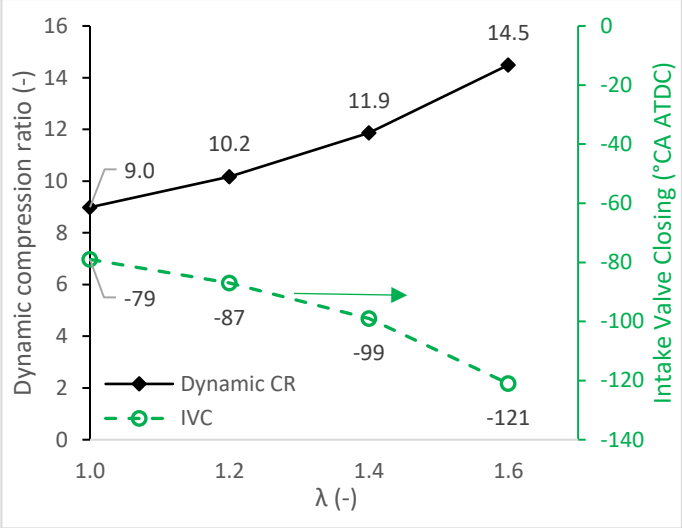


Figure 6.3. Dynamic compression ratio and IVC in Miller-LIVC at 1200 rpm/6 bar BMEP

6.3.3 Individual Load of Firing Cylinder at 1200 rpm/6 bar BMEP

Set out in Figure 6.4 are values of Net IMEP for Cylinder 1 at 1200 rpm/6 bar BMEP. This cylinder was selected as it was one of the three that remained operational throughout all strategies and was therefore representative when considering CDA effects. The Net IMEP under 6-cyl operation showed a relatively constant value around 7.1 bar, roughly half of Net IMEP by CDA-Battery strategies at relatively constant around 14.4 bar. Increasing λ during CDA-Battery operation did not increase Net IMEP since the battery powered the motor for the eSupercharger (hence FMEP by CDA-Battery was relatively constant and did not significantly change the Net IMEP). Meanwhile, the CDA-Generator increased Net IMEP from 14.8 bar at λ=1.0, to 17.9 bar at λ=1.8, covering the increasing parasitic losses for driving the generator that powered motor of eSupercharger at higher speed.

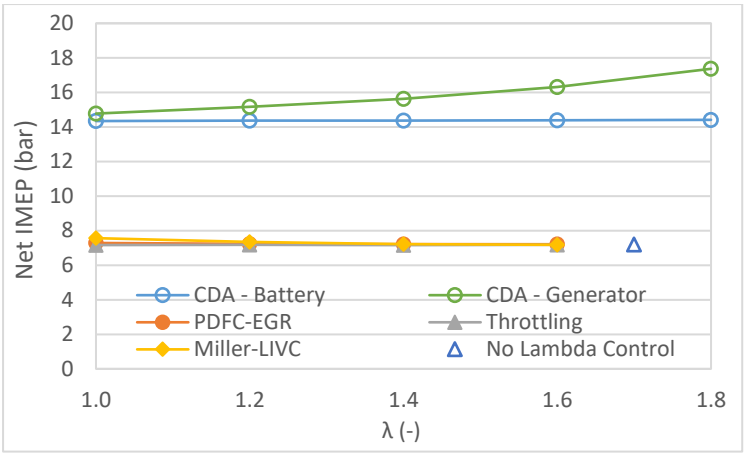


Figure 6.4. Net IMEP of Cylinder 1 at 1200 rpm/6 bar BMEP

The PMEP values generated by the simulated strategies are presented in *Figure 6.5*. The trapped gas of the non-firing cylinders under the CDA strategies underwent compression and expansion processes that produced or required work, expressed as Work-loop Mean Effective Pressure (WMEP), which was included in the PMEP calculation. The simulation results indicate that CDA-Generator operation, with higher intake manifold pressure and constant exhaust manifold pressure at 1 bar, resulted in the highest positive PMEP as a positive contribution to engine efficiency. Since the CDA-Generator strategy was simulated at higher fuel consumption to produce higher individual load, it required higher boosting pressure than CDA-Battery operation at the same λ. Among all of the simulated strategies, the throttling strategy resulted in the worst pumping loss due to lowest intake manifold pressure with the less lean mixture. The pumping losses generated by Miller-LIVC operation were the least amongst the 6-cyl modes at λ=1.0 (since it did not require intake throttling or higher exhaust backpressure as implemented in the EGR strategy).

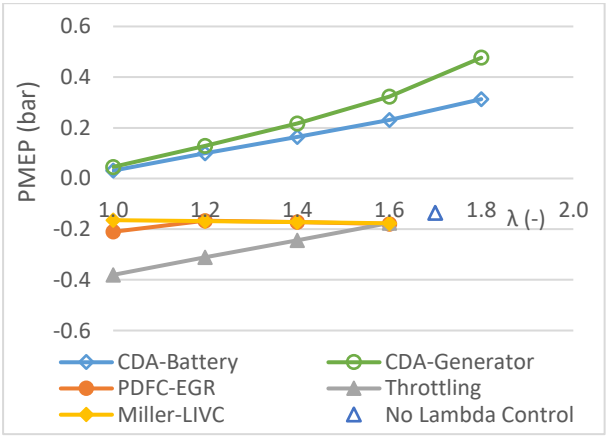


Figure 6.5. Engine PMEP at 1200 rpm/6 bar BMEP (includes WMEP of deactivated cylinders)

6.3.4 Efficiencies at 1200 rpm/6 bar BMEP

The net indicated efficiencies of Cylinder 1 generated by the simulated strategies at 1200 rpm/6 bar BMEP are depicted in *Figure 6.6*. The net indicated efficiency produced via the CDA strategies (except at λ=1.0) were higher than the 6-cyl strategies at most operating points and increased as the mixture was enleaned. CDA-Generator performed with the highest net indicated efficiency amongst the simulated strategies. The net indicated efficiency produced by PDFC-EGR remained relatively constant up to λ=1.4 and thereafter decreased at λ=1.6. This indicates a different trend in net indicated efficiency to the throttling and Miller-LIVC strategies, which both resulted in lower efficiency at less lean mixture. Decreasing efficiency with a less lean mixture by throttling could be related to increasing pumping losses due to lower intake manifold pressure than exhaust manifold pressure. This also results in the lowest values of efficiency compared to the other simulated strategies up to λ=1.4. The Miller-LIVC strategy produced higher net indicated efficiency than throttling despite similarly deteriorated efficiency with a less lean mixture, likely due to lower compression ratio by retarded intake valve closing.

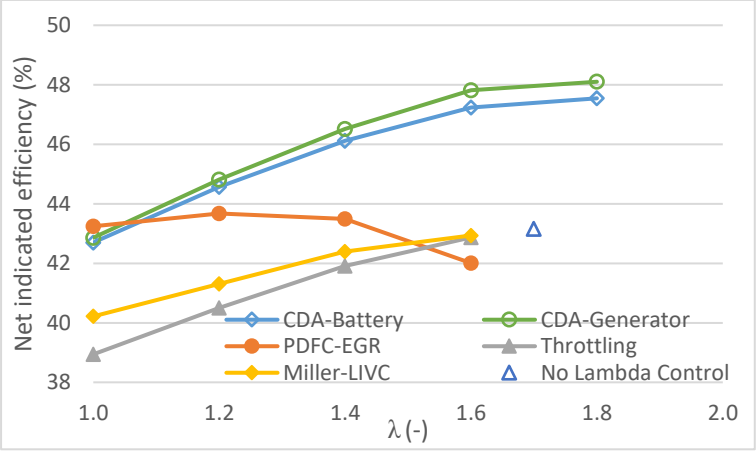


Figure 6.6. Net indicated efficiency of Cylinder 1 at 1200 rpm/6 bar BMEP

The brake efficiencies produced by the simulated strategies are shown in *Figure 6.7*. Brake efficiency generated using the CDA-Battery strategy increased by 4% as the mixture strength was enleaned from λ=1.0 to λ= 1.8 due to increasing pumping benefits. In addition, it also benefited from "free energy" i.e., zero parasitic losses. At the leaner mixture, higher intake charge resulted in a larger discrepancy between the CDA-Battery and CDA-Generator strategies, varying between 1 to 6%. The CDA-Generator indicates optimum efficiency at λ=1.4 and decreased with a leaner mixture, suggests that the reduced pumping could no longer compensate for the parasitic losses of the generator. On the other hand, the optimum operating point of the PDFC-EGR strategy was between λ=1.2 to λ= 1.4, producing higher

brake efficiency than the CDA-Generator mode. It is also shown that the PDFC-EGR strategy performed with highest brake efficiency among the 6-cyl strategies. Meanwhile, the throttling strategy suffered lowest brake efficiency due to higher pumping loss at lower λ, thus deteriorating brake efficiency by 3.2%. Overall, brake efficiency by the simulated strategies indicates that the implementation of the CDA strategy needs to be coupled with battery powered eSupercharger to run most efficiently. Alternatively, the 6-cylinder strategies with PDFC-EGR could be more practical to improve engine performance albeit with uncertainties remaining around combustion and sufficient exhaust temperature for effective methane slip control under real world operation that could not be experimentally validated in the currently reported work.

Plots of Brake Specific Fuel Consumption (BSFC) for the simulated strategies are illustrated in *Figure 6.7*(b) in g/kWh of equivalent fuel energy to diesel. The trend of BSFC by the simulated strategies appears as the inverse of brake efficiency. As CDA-Battery performed with highest brake efficiency, it consumed the lowest fuel quantity. The figure indicates improvement in BSFC by the CDA-Battery mode at leaner mixtures, which decreases from 233 to 210 g/kWh. The PDFC-EGR mode performed with lowest BSFC at 230 g/kWh among the 6-cylinder strategies at λ=1.2 and λ=1.4.

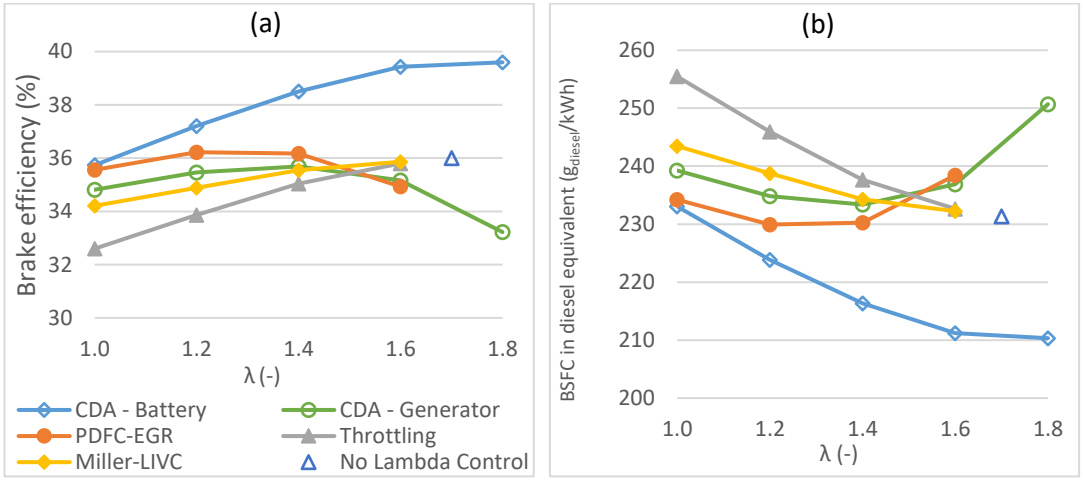


Figure 6.7. (a) Brake efficiency and (b) BSFC at 1200 rpm/6 bar BMEP

6.3.5 In-cylinder Pressure and Heat Release Rate at 1200 rpm/6 bar BMEP

The in-cylinder pressure and gross Heat Release Rate (herein referred to as HRR) of Cylinder 1 during throttling mode with a λ sweep from 1.0 to 1.6 are illustrated in *Figure 6.8*. Increased intake restriction by throttling at lower λ operation decreased intake manifold pressure and thus decreased compression pressure. Lower compression-end temperature and a less lean mixture deteriorated ignition delay, hence resulting in higher premixed diesel combustion as

indicated by the higher first peak of HRR. The impact of λ to ignition delay is discussed in more detail in the next section. The less lean mixture also promoted flame propagation, with accelerated combustion duration and a higher second peak of HRR. HRR by throttling strategy with CDF suggests two stages of combustion, where the first combustion by auto-ignited diesel became flames that propagated into surrounding premixed gaseous fuel within combustion chamber which resulted in higher heat release than the pilot combustion.

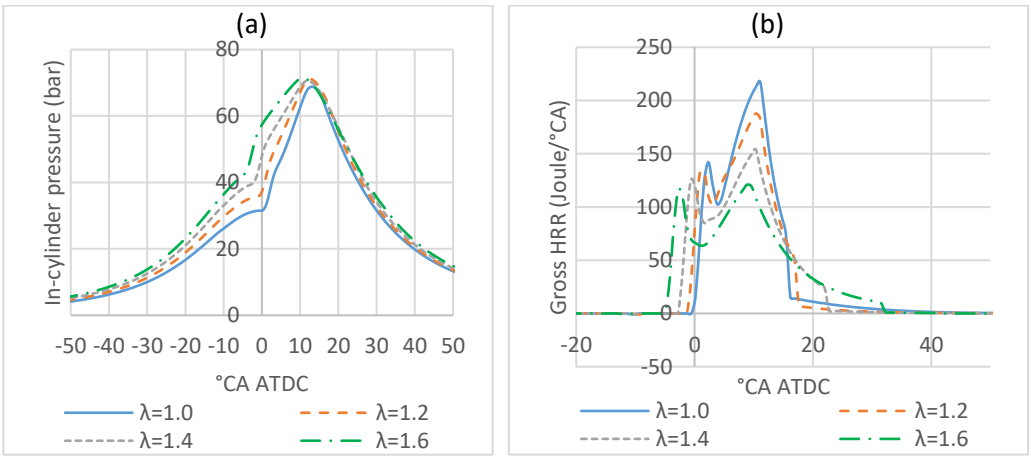


Figure 6.8. (a) The in-cylinder pressure and (b) Gross HRR of Cylinder 1 by throttling with λ sweep at 1200 rpm/6 bar BMEP

The impact of λ sweeps on the in-cylinder pressure and HRR of Cylinder 1 by PDFC-EGR at 1200 rpm/6 bar BMEP is illustrated in *Figure 6.9*. The HRR suggest that in PDFC simulation which used premixed first pilot to provide multiple location of ignition sources initially burned at slower burn rate than initial HRR by CDF as shown in Figure 6.8(b). However, the second pilot injection accelerated combustion by promoting fast flame propagation within gaseous fuel/air mixture, resulting higher peak of HRR. Increasing EGR with lower λ resulted in slightly lower compression-end pressure, since the intake trapped mass was slightly reduced as shown in *Figure 6.2*(a). However, larger EGR fraction increased intake manifold temperature as shown in Figure 6.1(b), resulting in higher compression end temperature as illustrated in Figure 6.10. PDFC-EGR operation with lower λ produced a higher peak of HRR and faster combustion due to higher flame speed within gaseous fuel/air mixture thanks to the less lean mixture strength and higher compression-end temperature as illustrated in *Figure 6.10*.

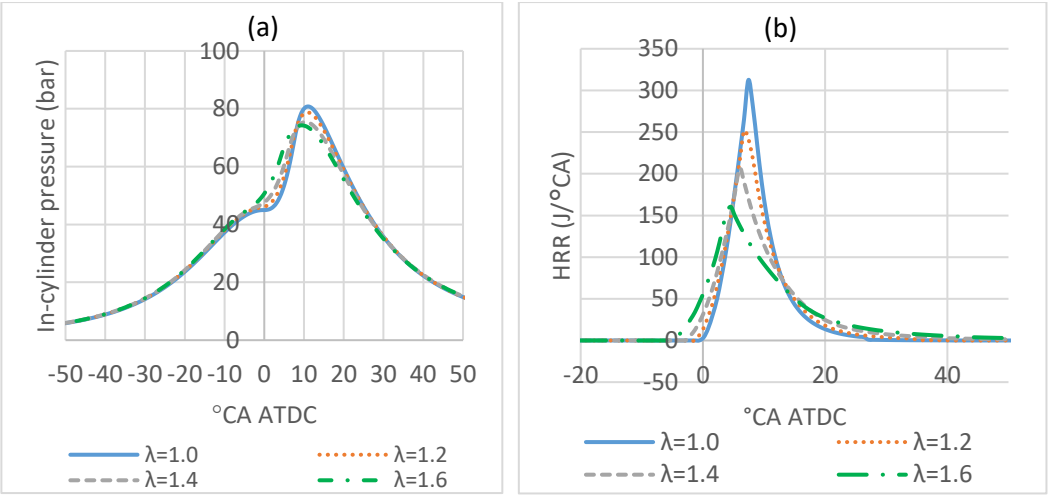


Figure 6.9. (a) The in-cylinder pressure and (b) Gross HRR of Cylinder 1 under 6-cyl PDFC-EGR mode with varying λ at 1200 rpm/6 bar BMEP

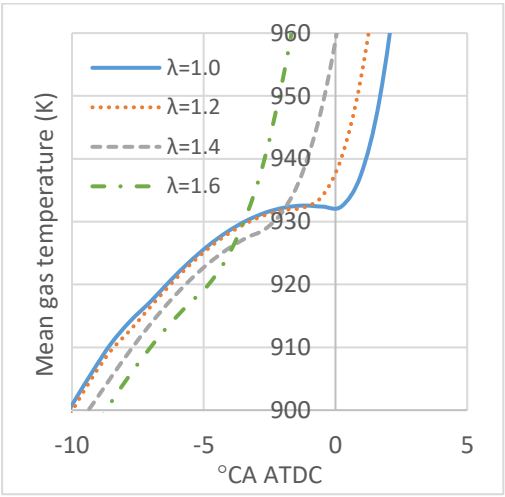


Figure 6.10. Mean gas temperature near TDC by PDFC-EGR at the swept λ

The in-cylinder pressure and HRR during CDA-Battery operation with varying λ values are depicted in *Figure 6.11*. The result produced by CDA-Generator operation is not presented here as the impact of λ sweep to the in-cylinder pressure and HRR indicated a similar trend. The simulation with leaner mixtures trapped more intake charge mass that in turn resulted in higher compression pressure and improved ignition delay of the pilot fuel. However, the leaner mixture decreased the flame propagation speed and hence resulted in lower heat release rate and prolonged combustion duration, as indicated by the HRR curves in *Figure 6.11*(b). Therefore, to locate 50% of Mass Fraction Burned (MFB50) at the same location for all the simulated points (8 °CA ATDC), the leaner mixture required more advanced injection timing of the pilot fuel. In addition, the leaner mixture indicates two stage combustion, with a more noticeable first peak of diesel combustion and second peak of gaseous fuel combustion. Meanwhile, the less lean mixture indicates more simultaneous combustion of

diesel and gaseous fuel, as reflected by the less noticeable peak of the first combustion when using diesel.

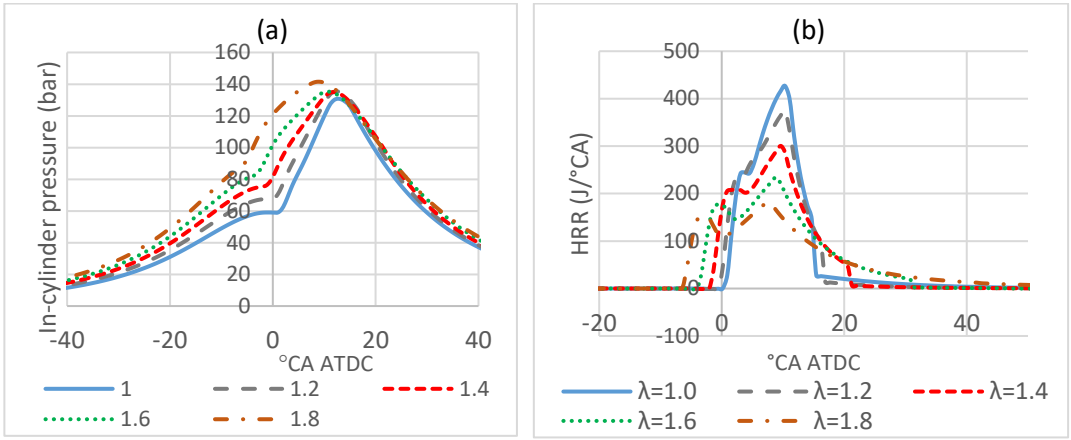


Figure 6.11. (a) The in-cylinder pressure and (b) Gross HRR by CDA-Battery operation with varying λ at 1200 rpm/6 bar BMEP

6.3.6 In-cylinder Pressure and Heat Release Rate at 1200 rpm/6 bar BMEP/λ=1.0

A comparison of the in-cylinder pressure of Cylinder 1 produced by the simulated strategies at 1200 rpm/6 bar/λ=1.0 is presented in *Figure 6.12*(a). The in-cylinder pressure curves generated by the CDA strategies are higher than the other 6-cyl strategies, as it required intake charge mass of approximately double that of the 6-cyl operating modes to generate around twice the Net IMEP. Higher compression pressure resulted in a higher peak of in-cylinder pressure, rising from ~75bar to ~135bar. Meanwhile, among the 6-cyl strategies, PDFC-EGR performed with highest compression pressure, with highest intake charge mass resulting in higher compression pressure than the throttling and Miller-LIVC modes.

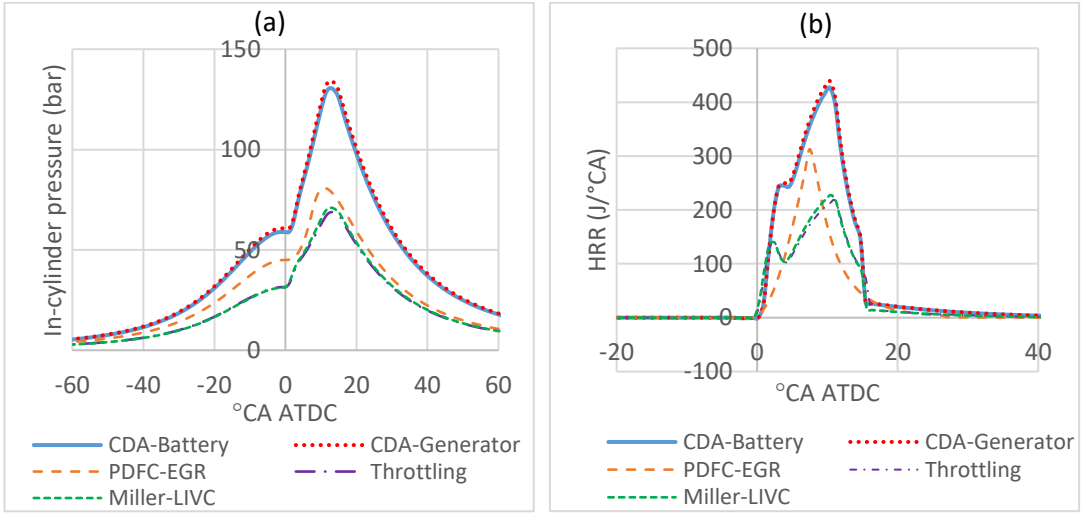


Figure 6.12. (a) The in-cylinder pressure and (b) Gross HRR by CDA and 6-cyls. strategies at 1200 rpm/6 bar BMEP/λ=1.0

The HRR curves of the simulated strategies at λ=1.0 are presented in *Figure 6.12*(b). PDFC indicates more simultaneous combustion of diesel and gaseous fuel, while CDF in the simulated strategies (except PDFC-EGR) suggested diesel combustion followed by flame propagation within the gaseous fuel. With the same combustion scheme, CDA indicates more simultaneous combustion than throttling and Miller-LIVC operation albeit the peak of HRR by diesel combustion is still noticeable. CDA strategies with higher load within Cylinder 1 resulted in significantly higher peak of HRR than the 6-cyl strategies, with slightly shorter combustion duration. Shorter duration between SOC and increasing HRR after the first peak of HRR suggests more simultaneous combustion by CDA than incurred by the 6-cyl strategies at the same λ. In general, HRR curves indicate that the CDA strategy improved both diesel and gaseous fuel combustion. There are several factors that could contribute to the combustion improvement by CDA. Firstly, CDA strategy provided more ignition source due to increased pilot fuel quantity. Secondly, higher in-cylinder pressure and temperature at the end of compression promoted diesel combustion as well as flame propagation of the air/gas mixture. From the two simulated CDA strategies, higher fuel quantity within the charge mass by CDA-Generator mode produced higher HRR than the CDA-Battery strategy.

6.3.7 Mean Gas Temperature at 1200 rpm/6 bar BMEP/λ=1.0

The mean gas temperature profiles of Cylinder 1 for the different simulated strategies are shown in *Figure 6.13*. Higher intake charge mass by CDA mode compared to the 6-cylinder strategies resulted in higher mean gas temperature during compression pre-combustion, combustion and the expansion stroke. PDFC-EGR operation with higher intake temperature resulted in higher compression-end temperature than throttling and Miller-LIVC mode. The Miller-LIVC strategy with reduced compression ratio due to retarded IVC resulted in lowest compression-end temperature. The lowest mean gas temperature produced by PDFC-EGR among 6-cyl strategies was likely due to the lowest fuel consumption as indicated by the lowest BSFC as shown previously in *Figure 6.7*(b).

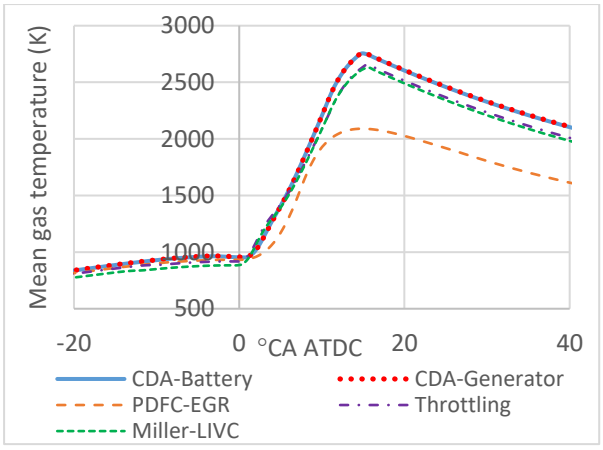


Figure 6.13. Mean gas temperature of Cylinder 1 at 1200 rpm/6 bar BMEP/λ=1.0

6.3.8 Combustion-Related Parameters at 1200 rpm/6 bar BMEP

Set out in Figure 6.13 are values of combustion duration (the duration from 10% to 90% of MFB) for the simulated strategies at 1200 rpm/6 bar BMEP. Combustion duration by all of the simulated strategies indicated that the lower λ shortens the combustion duration due to improved flame propagation. The combustion duration produced by throttling and Miller-LIVC were very similar. This suggests a similar impact of lower intake manifold by throttling and lower compression ratio by Miller-LIVC. Compared to the other simulated strategies, PDFC-EGR operation resulted in the most significant improvement in combustion duration as the mixture got richer, associated with increasing temperature and pressure at the end of the intake stroke. The combustion duration values produced by CDA strategies were generally shorter than the 6-cyl mode values except for the PDFC-EGR mode at λ=1.0. Higher load in the individual firing cylinders produced by CDA operation caused higher in-cylinder pressure and temperature that in turn promoted flame propagation.

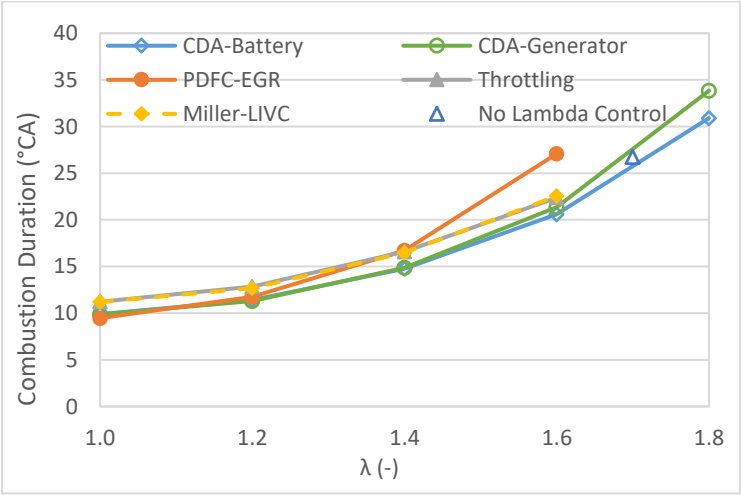


Figure 6.14. Combustion duration at 1200 rpm/6 bar BMEP

The mixture λ directly affected the ignition delay, which is defined by the duration from SOI of the first pilot and 0.1% of MFB. The ignition delay produced by simulated strategies is shown in *Figure 6.15*(a). The CDA strategies improved the ignition delay of the dual-fuel combustion. Higher pressure and temperature at the end of the compression due to higher trapped mass by CDA strategy improved the diesel atomisation, hence shortening the ignition delay. To the contrary, Miller-LIVC suffered the trend of longest ignition delay among the simulated modes. Under less lean mixture, Miller-LIVC trapped less intake air by later (retarded) IVC, reducing compression ratio, lowering the cylinder temperature and thus deteriorating the ignition delay. Meanwhile, the mixture enrichment by throttling operation decreased the intake pressure, which resulted in lower compression-end pressure and temperature and deteriorated ignition delay (despite keeping the original compression ratio). Among the simulated strategies, PDFC-EGR indicated a different trend to the other simulated strategies, with a slightly parabolic trend and shorter ignition delay at λ=1.2. The less significant deterioration of ignition delay by a richer mixture in PDFC-EGR could be related to increased intake charge temperature due to higher EGR.

Since the mixture λ, in-cylinder pressure and temperature affected combustion duration and ignition delay, the SOI of pilot fuel needed to be adjusted accordingly to locate the MFB50 at 8 °CA ATDC for each of the simulated strategies. The SOI values (which refer to the start of the first pilot injection) for the respective operating modes are illustrated in *Figure 6.15*(b). The CDA strategies with shortest combustion duration and ignition delay needed a SOI timing closer to TDC to locate the MFB50 at 8 °CA ATDC. This could be a benefit, improving the diesel combustion processes. In PDFC-EGR, with relatively constant ignition delay but longer combustion duration at higher λ, operation required SOI advancement to result in the same combustion phasing. Meanwhile, the SOI pilot in Miller-LIVC strategy is the most advanced at around -14 CA ATDC and suffered longest ignition delay despite similar combustion duration as the throttling strategy (shown in *Figure 6.14*).

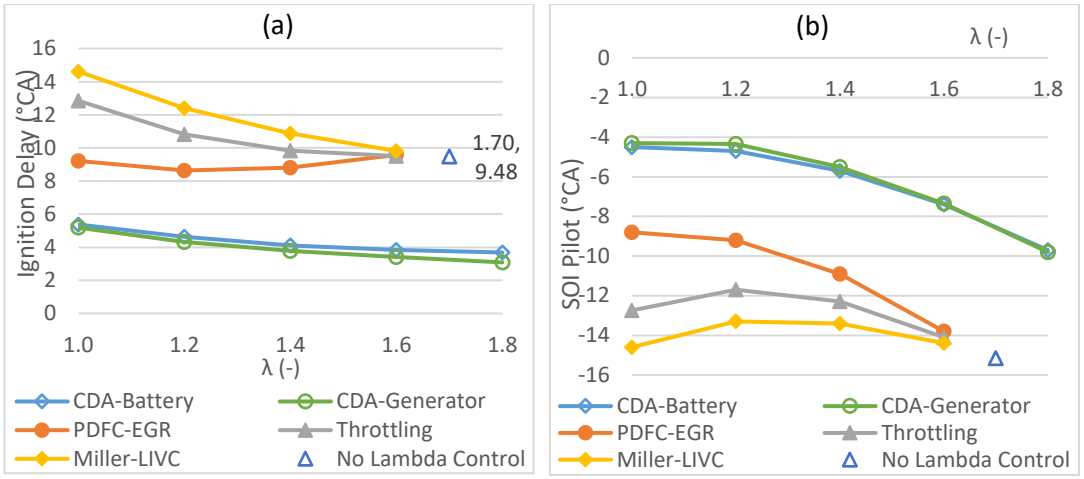


Figure 6.15. (a) Ignition Delay (SOI to 0.1% MFB) and (b) SOI Pilot at 1200 rpm/6 bar BMEP.

6.3.9 Maximum Pressure Rise Rate at 1200 rpm/6 bar BMEP

The maximum Pressure Rise Rates (max. PRR) are shown in *Figure 6.16*. The CDA-Generator mode produced the highest max. PRR at 7 to 8.3 bar/°CA. With 10 bar/°CA set as the threshold, all strategies remained within this limit. The CDA strategy with shortest ignition delay and faster combustion resulted in higher max. PRR than the 6-cyl strategies, which became yet higher as the mixture got less lean. Among the simulated strategies, mixture enrichment with PDFC-EGR caused the most significant increasing of max. PRR. This suggests that more thoroughly premixing the first pilot fuel improved flame propagation and significantly accelerated combustion with higher max. PRR. Meanwhile, simulation with a less lean mixture during throttling and Miller-LIVC operation did not significantly impact max. PRR.

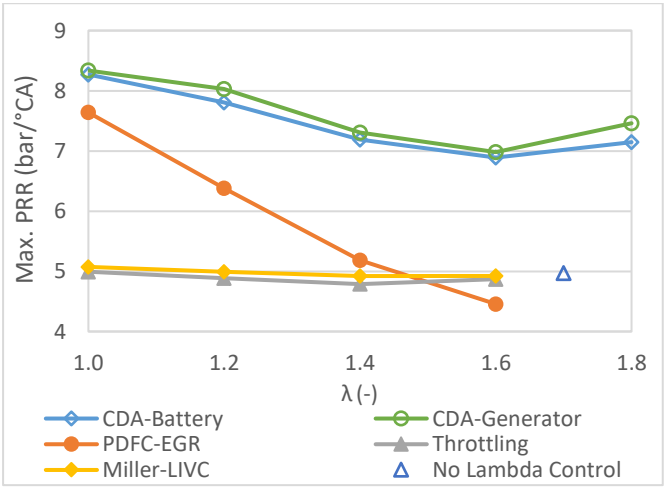


Figure 6.16. Maximum Rate of Pressure Rise (ROPR) at 1200 rpm/6 bar BMEP

6.3.10 Engine Heat Loss at 1200 rpm/6 bar BMEP

The engine's heat loss through cylinder wall heat transfer (herein referred to as engine heat loss) for the simulated strategies is shown in *Figure 6.17*. All of the modes resulted in a similar trend of λ impact to the cylinder wall heat loss, improved with leaner operation. This could be related to lower mean gas temperature as the mixture was enleaned. Among the 6-cyl strategies, throttling suffered the highest trend of cylinder wall heat loss while PDFC-EGR resulted in the lowest trend. The results by CDA strategies demonstrate the benefit of lower heat loss than the 6-cyl strategies, which could be related to less surface area in contact with hot gases due to deactivation. Compared to the throttling strategy, the 6-cyl strategy suffered the highest wall heat loss, while the implementation of CDA-Battery operation reduced heat loss by 22%. Meanwhile, compared to PDFC-EGR mode, CDA-Battery operation suffered similar heat loss at λ=1.0, but improved with leaner mixtures up to 19 % at λ=1.6. Differences in wall heat loss between the simulated strategies can be related to i) the cylinder mean gas temperature, ii) varying fuel consumption and iii) differences in cylinder wall surface area in contact with hotter gases. In 6-cyl mode, as the mean gas temperature increased the cylinder wall heat loss deteriorated. This could be the reason why PDFC-EGR suffered the least heat loss while throttling suffered the highest wall heat loss in comparison between the 6-cyl strategies. On the other hand, reducing hot surface area during the CDA strategy is an effective method to improve the cylinder wall heat loss despite the fact the firing cylinder was running at higher cylinder mean gas temperature. This analysis neglects any transient operation (where the deactivated cylinders initially contain hot trapped residual for the first few cycles, albeit thereafter leaking down to a low steady state).

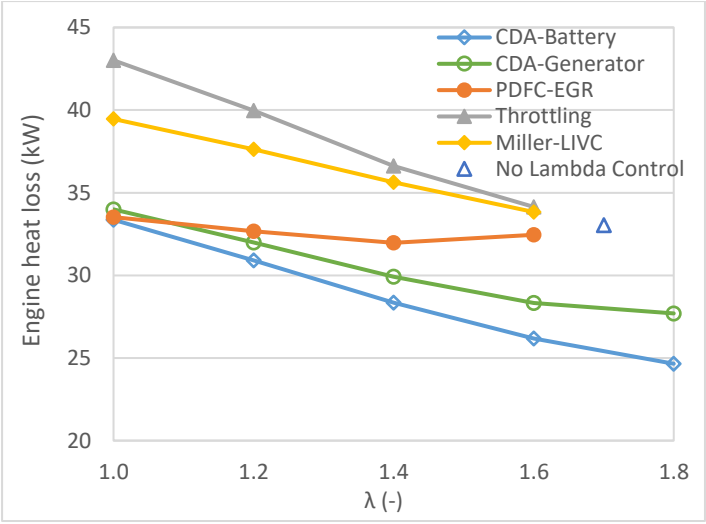


Figure 6.17. Engine heat loss at 1200 rpm/6 bar BMEP

6.3.11 Exhaust Gas Temperature at 1200 rpm/6 bar BMEP

The Exhaust Gas Temperature (EGT) generated by the simulated strategies is depicted in *Figure 6.18*. The presented value is the mass-averaged temperature of exhaust gas at the outlet of the exhaust manifold. As the instantaneous temperature at the outlet of the exhaust manifold fluctuated depending on the exhaust gas flow, the mass-averaged temperature is considered to be a meaningful comparable parameter that indicates exhaust gas energy (as opposed to the time-averaged temperature which neglected the fluctuating flowrate) [166].

It is noticeable in the figure that CDA strategies produced higher exhaust gas temperature than the 6-cylinder strategy up to λ=1.6. In the comparison of the two CDA strategies, CDA-Generator produced higher exhaust gas temperature. The higher fuel consumption for CDA-Generator mode resulted in higher exhaust gas temperature than CDA-Battery operation. Amongst the 6-cylinder strategies, throttling resulted in the highest exhaust gas temperature, while the lowest temperature was produced by PDFC-EGR. Compared to throttling strategy with the same λ, CDA-Battery increased the exhaust gas temperature by up to 48°C. Compared to PDFC-EGR at λ=1.0, CDA-Battery mode resulted in 175°C higher EGT.

For the simulated strategies except PDFC-EGR, lowering λ increased exhaust gas temperature. Meanwhile, increasing λ up to 1.4 for PDFC-EGR operation slightly decreased EGT, but simulation at λ=1.6 increased it. Compared to the results of other strategies, the exhaust gas temperature by PDFC-EGR mode operating up to λ=1.4 was the lowest. However, the relatively higher EGT when using PDFC-EGR mode at λ=1.6 was likely due to longer combustion duration, as shown in *Figure 6.14*, and/or retarded EOC. The EGT strongly related to the BSFC and combustion characteristics where later EOC tended to result in higher EGT. In addition, the lower engine heat loss in CDA mode compared to 6-cyl modes also contributed to higher EGT. The slight changes of EGT during PDFC-EGR operation could be related to relatively constant fuel consumption during the λ sweep, while simulation at lower λ in the other strategies increased fuel consumption. Generally, the higher EGT during CDA can be attributed to higher mean gas temperature of the firing cylinder and lower cylinder wall heat loss.

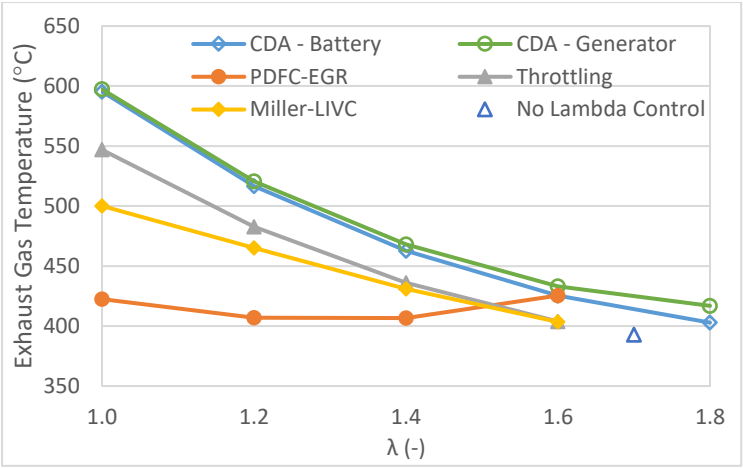


Figure 6.18. Exhaust Gas Temperature at 1200 rpm/6 bar BMEP

6.4 Simulation Results at 1200 rpm/3 bar BMEP

A setting of 3 bar BMEP is a relatively low load operating condition, where a low temperature and lean mixture become challenges for premixed flame propagation during dual-fuel combustion. This study assessed a method to address this problem by implementing CDA to run the firing cylinders at higher individual load, increasing cylinder temperatures and more supportive for intake control to run a less lean mixture. In this section, the simulation results by 6-cyl and CDA strategies at 1200 rpm/3 bar BMEP are presented and discussed. The impact of each strategy will be presented here, including analysis of combustion performance and other key engine parameters. In the figures presented, CDA with CDF without intake control (at the highest λ) is presented on the same curve with CDA-throttling, while CDA with PDFC without intake control was on the same curve as CDA-EGR (PDFC). The results of simulation with PDFC are clearly denoted as PDFC, otherwise the data points shown are CDF simulation results.

6.4.1 Impact of Simulated Strategies upon Intake Parameters at 1200 rpm/3 bar BMEP

The impact of each simulated strategy upon average intake manifold pressure and temperature are presented in *Figure 6.19*. The 6-cyl strategy with throttling at λ=1.8 was simulated with 0.67 barA intake manifold pressure, illustrating how it was not practical to simulate at lower λ. With a combination of throttling and EGR, both throttle-EGR-CDF and throttle-EGR-PDFC, the intake manifold pressure was set at 0.8 barA. The intake temperature reached 36°C due to 16% dilution with EGR. Meanwhile, in PDFC-EGR strategy with 34.5% EGR, the intake manifold temperature was 49°C and the intake manifold pressure was 1 bar. Throttling as a λ controlling method in the implemented CDA strategy reduced the intake

manifold pressure to 0.8 barA at λ=1.0. In CDA-LIVC mode, increasing temperature with a less lean mixture was likely caused by later IVC operation, which in turn caused intake charge preheating during the early stage of compression before IVC, with gases expelled back to the intake manifold. Implementation of EGR as a λ control method in CDA-EGR(PDFC) mode with at less lean mixture (lower λ) increased the intake manifold temperature because of the higher EGR fraction (up to 47°C at λ=1.0 with up to 29.5% EGR) while the intake manifold pressure remained constant.

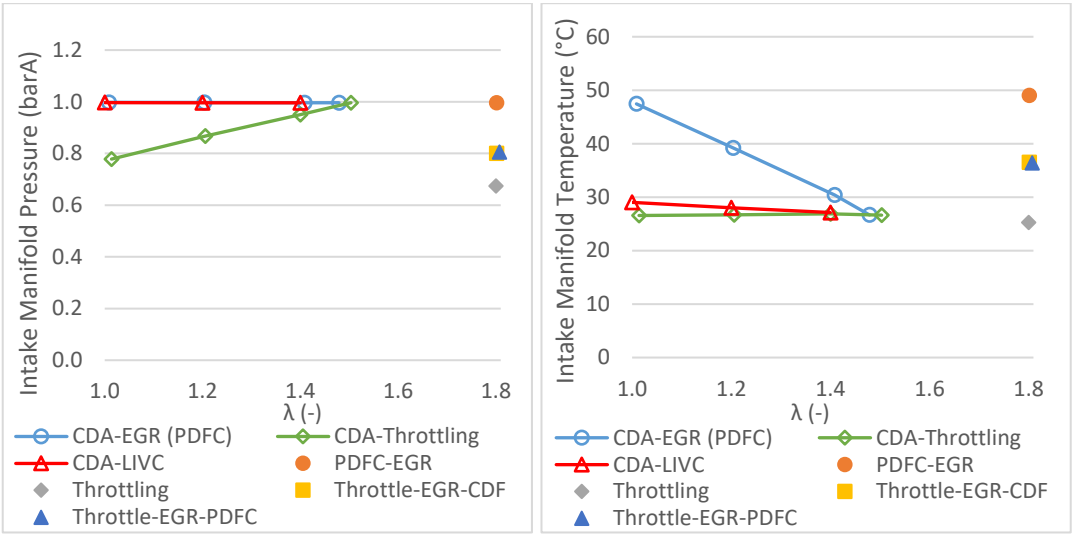


Figure 6.19. (a) Intake manifold pressure and (b) Intake manifold temperature at 1200 rpm/3 bar BMEP

The impact of λ control methods in CDA strategies to intake trapped mass is illustrated in *Figure 6.20*(a). The corresponding EGR percentage in the simulated strategies with EGR is plotted in *Figure 6.20*(b). Reducing trapped air mass with throttling and Miller LIVC operation and a less lean mixture resulted in significant intake trapped mass reduction in a similar manner. Meanwhile, higher EGR percentage with lower λ in CDA-EGR (PDFC) mode slightly reduced the intake trapped mass. In all 6-cyl strategies, PDFC-EGR with 34% EGR trapped the highest intake mass while throttling simulated with the lowest trapped mass. Combination of both throttling-EGR-PDFC and throttling-EGR-CDF was run with ~16% EGR, with higher intake trapped mass and also higher intake manifold pressure and temperature than throttling.

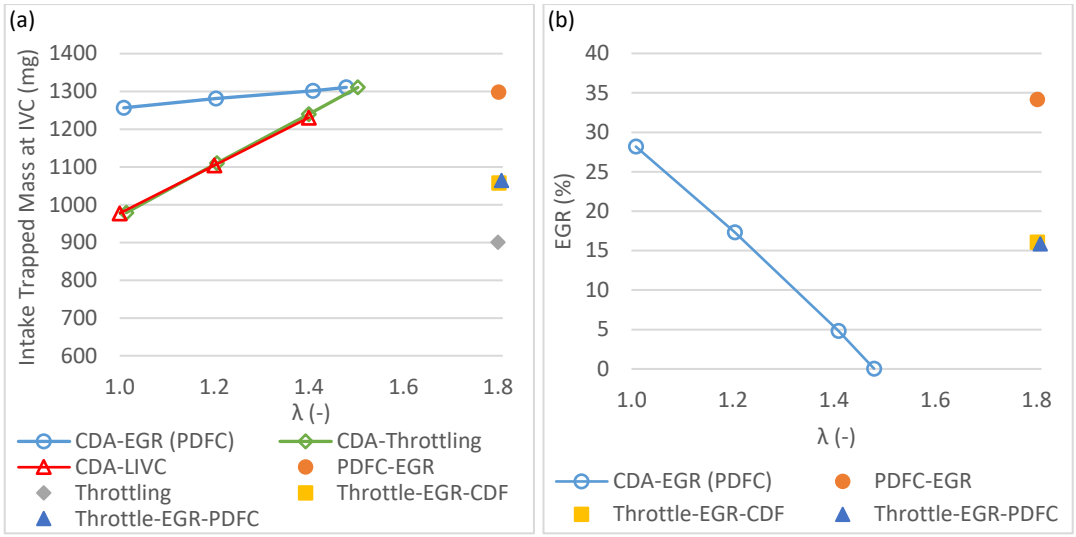


Figure 6.20. (a) Intake trapped mass and (b) EGR percentage in simulated strategies with EGR at 1200 rpm/3 bar BMEP

Shown in *Figure 6.21* is the impact of LIVC at λ to the dynamic compression ratio in CDA-LIVC mode, with the IVC set to simulate a certain λ. Enriching the mixture by LIVC from λ=1.4 to λ=1.0 with IVC at -115 to -84 CA ATDC reduced the dynamic compression ratio from 13.9 to 9.7, while the other strategies with standard IVC (at -158.5 °CA ATDC) were simulated at 17.1.

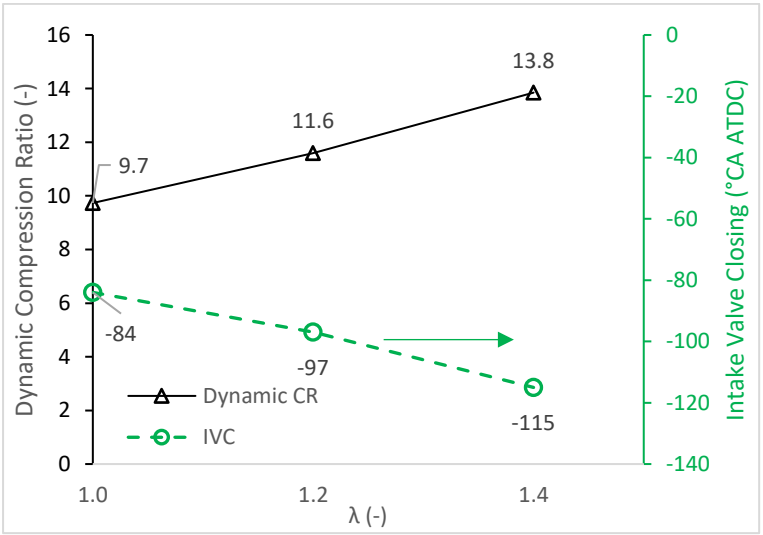


Figure 6.21. Dynamic compression ratio and IVC by CDA-LIVC at 1200 rpm/3 bar BMEP

6.4.2 Net IMEP and PMEP at 1200 rpm/3 bar BMEP

The net IMEP of Cylinder 1 at 1200 rpm/3 bar BMEP is shown in *Figure 6.22*(a). The net IMEP for the 6-cyl modes was ~4.1 bar. Meanwhile, the CDA strategies performed at around 8.1 bar net IMEP, roughly doubled the load of the firing cylinder during 6-cyl mode. In comparing CDA strategies, simulation of an enriched mixture in CDA-throttling resulted in constant net

IMEP, while enrichment in CDA-EGR(PDFC) and CDA-LIVC modes resulted in slightly increased net IMEP due to higher FMEP with a less lean mixture.

To observe the impact of each simulated strategy on pumping work, the PMEP by respective strategies is presented in *Figure 6.22*(b), where the WMEP of the deactivated cylinders was also included in the calculation. More negative PMEP means more significant pumping losses. The CDA strategies resulted in reduced pumping losses even at the richest mixture (λ=1.0), lower than the 6-cylinders strategy at λ=1.8. This indicates a key benefit of CDA mode over 6-cyl operation; being able to run at high substitution ratio with a less lean mixture with the aim of improving flame propagation. CDA with LIVC indicates the lowest pumping losses among the CDA strategies, with relatively constant value despite lowered λ. Meanwhile, PMEP in the CDA with throttling strategy deteriorated with a richer mixture (from -0.07 bar at λ=1.4 to -0.16 bar at λ=1.0) due to lowered intake manifold pressure via less throttle opening. The CDA-EGR (PDFC) mode resulted in slightly more pumping loss than CDA-LIVC operation since higher exhaust back pressure was applied to flow EGR to the intake manifold. Among the 6-cylinder strategies, PDFC-EGR mode performed with the least pumping losses since it required slightly higher exhaust back pressure to flow the EGR and was performed without throttling as implemented in the other 6-cylinder strategies.

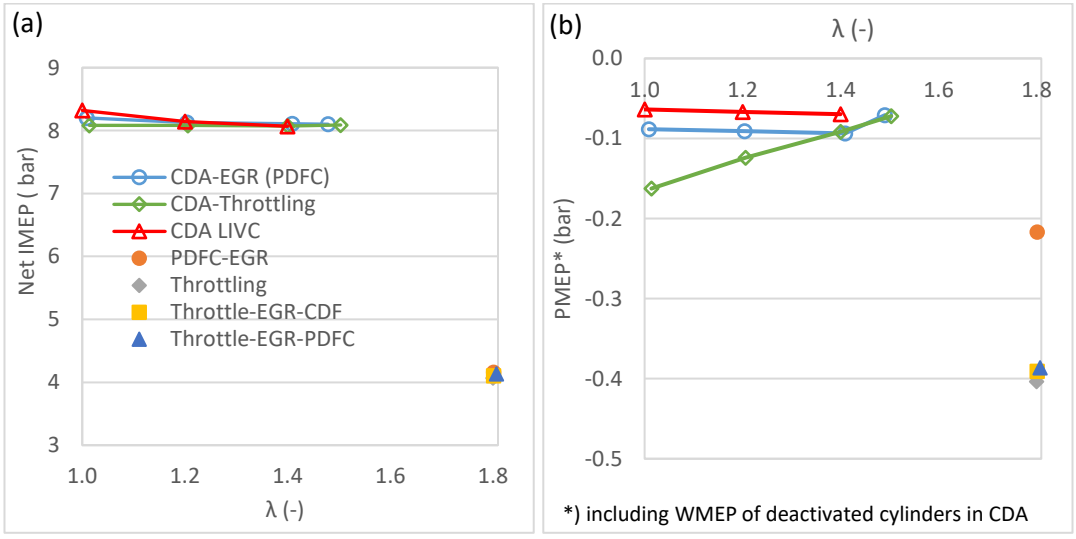


Figure 6.22. (a) Net IMEP of Cylinder 1 and (b) Engine PMEP at 1200 rpm/3 bar BMEP

6.4.3 Brake Efficiency and Fuel Economy at 1200 rpm/3 bar BMEP

Brake efficiency at 1200 rpm/3 bar BMEP is depicted in *Figure 6.23*(a). CDA strategies performed with higher efficiency than the 6-cyl strategies at all simulated points. Among the CDA strategies, CDA-EGR (PDFC) mode performed with optimum brake efficiency at λ=1.2. CDA-Throttling up to λ=1.4 performed the lowest trend of brake efficiency among the

implemented CDA strategies. The comparison of CDA strategies at highest λ indicates that CDA with CDF (in the same curve as CDA-throttling in green) performed with higher brake efficiency at 32.2 than CDA with PDFC without EGR (plotted in the same curve as CDA-EGR(PDFC) in blue) at 31.7. Meanwhile, among the 6-cyl simulated strategies at λ=1.8, PDFC-EGR performed with highest brake efficiency at 29.5% due to lowest pumping losses. On the contrary, the throttling strategy generated the lowest brake efficiency of 28.4 due to significant pumping losses. In conclusion, CDA with the leanest mixture resulted in higher brake efficiency, increased by 3.8% more than the 6-cyl strategies.

To give another perspective of improvement in fuel economy, the corresponding values of BSFC are plotted in *Figure 6.23*(b). The lowest BSFC at λ=1.0 and λ=1.2 was incurred by CDA-EGR (PDFC) mode, with similar BSFC by the three CDA strategies at λ=1.4. CDA simulation at the leanest mixture with CDF generated better fuel economy than CDA with PDFC. At this operating point, CDA-CDF resulted 4% higher brake efficiency than 6-cyl throttling or 12.5% improvement in fuel economy. Generally, CDA performed with better fuel economy than the simulated 6-cyl strategies at λ=1.8. From the comparison of strategy that run at lowest fuel consumption between CDA and 6-cyl (CDA-EGR(PDFC) vs PDFC-EGR), the CDA strategy improved fuel economy by 8% at 1200 rpm/3 bar BMEP.

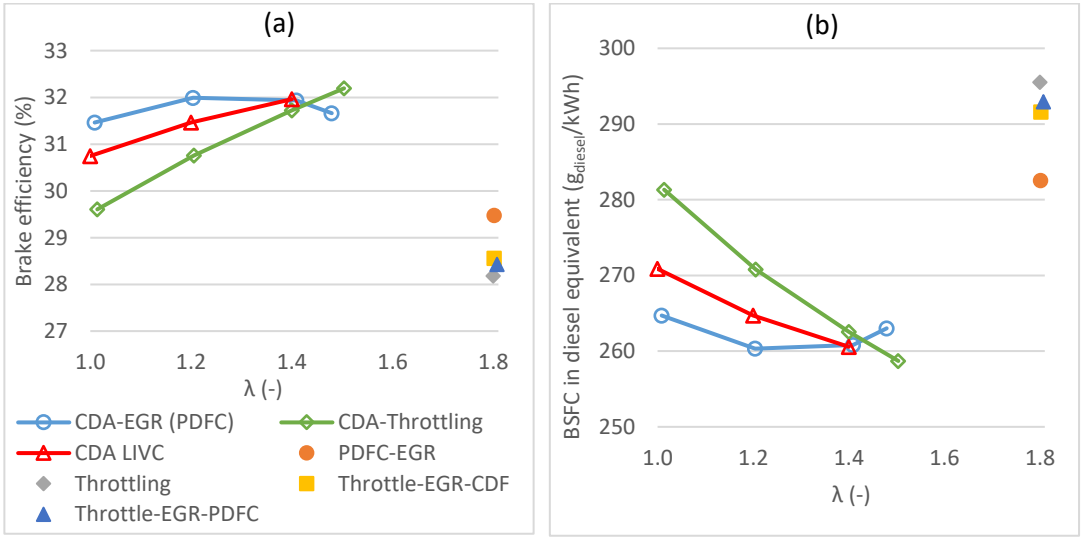


Figure 6.23. (a) Brake efficiency and (b) BSFC at 1200 rpm/3 bar BMEP

6.4.4 In-cylinder pressure and Heat Release Rate at 1200 rpm/3 bar BMEP

The in-cylinder pressure of the 6-cyl strategies at 3 bar BMEP – λ=1.8 is shown in *Figure 6.24*. PDFC-EGR strategy resulted in the highest in-cylinder pressure due to higher intake charge mass and higher intake temperature due to EGR dilution. The in-cylinder pressure and HRR curves indicate that all of the simulated strategies start the combustion before TDC, hence

suffered high pressure during the end of compression (working against the piston). This should be compensated for by higher pressure during the expansion stroke, with deteriorated fuel consumption. Meanwhile, the throttling strategy operated at lowest pressure due to the valve restriction mechanism that reduced intake pressure, deteriorated ignition delay and hence required earliest SOI of the pilot fuel. Implementation of EGR in the Throttle-EGR-CDF strategy improved pumping losses and resulted in higher compression pressure, which in turn improved ignition delay hence retarding the SOI of the pilot fuel and advancing the start of combustion.

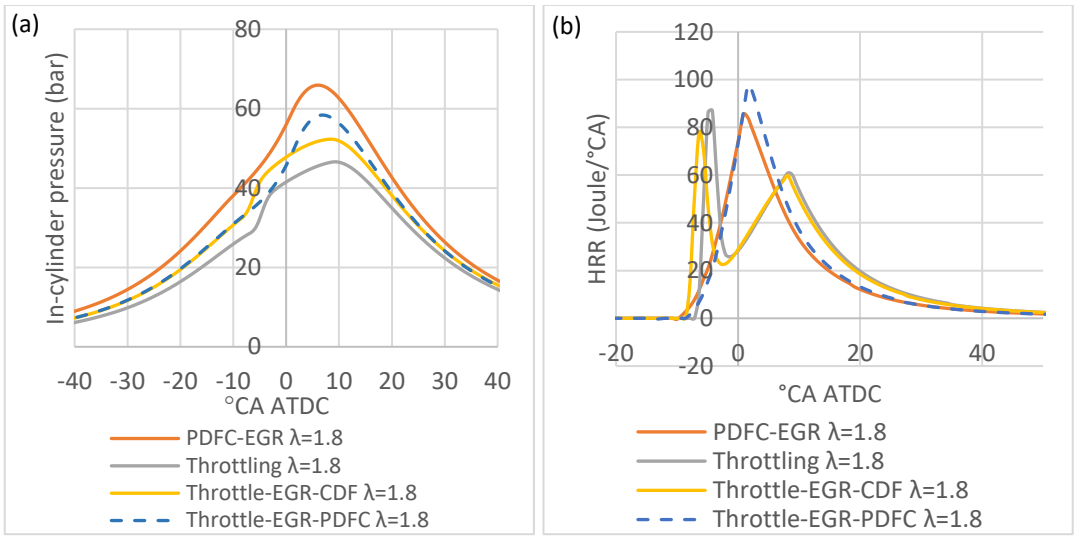


Figure 6.24. (a) In-cylinder pressure and (b) gross HRR by 6-cylinder strategies at 1200 rpm/3 bar BMEP-λ=1.8

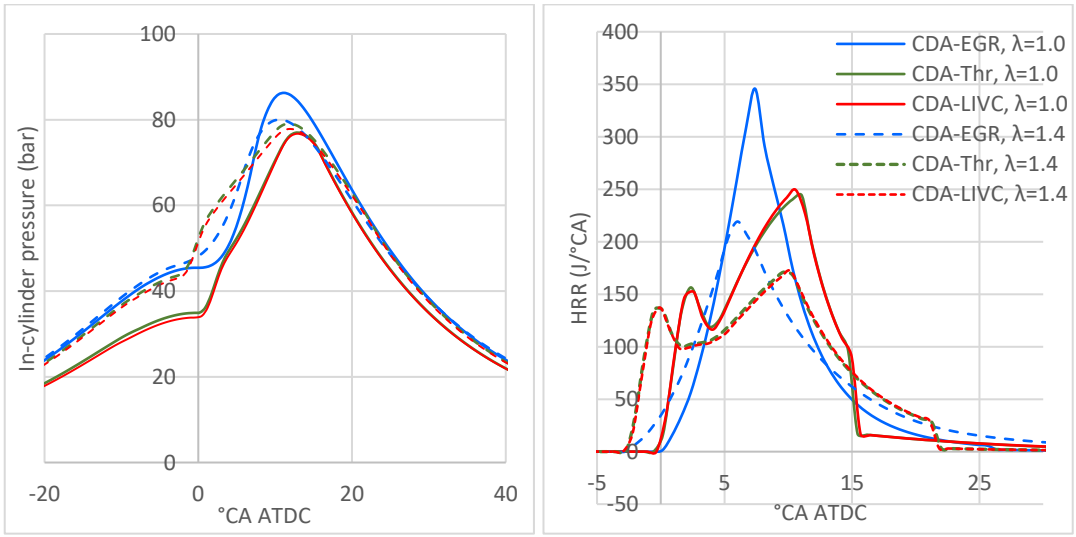


Figure 6.25. (a) In-cylinder pressure and (b) gross HRR by CDA at 1200 rpm/3 bar BMEP at λ=1.0 and λ=1.4

The in-cylinder pressure and HRR by the CDA strategies at 1200 rpm/3 bar BMEP are both shown in Figure 6.25, where the simulation results at λ=1.0 and λ=1.4 are presented to

illustrate the impact of the λ control method. Comparing the same λ, CDA-EGR (PDFC) mode performed with highest compression pressure and also peak in-cylinder pressure, because of higher trapped mass and higher intake manifold pressure. Meanwhile, CDA-LIVC mode resulted in the lowest compression-end pressure due to lowest dynamic compression ratio. In comparison of the respective λ control strategy, simulation with a less lean mixture during CDA-throttling (CDA-Thr) and CDA-LIVC mode significantly decreased the compression pressure due to lower intake trapped mass. In CDA-LIVC, the condition with less lean mixture was deteriorated by lower dynamic compression ratio. The less significant decrease of compression pressure was shown by CDA-EGR(PDFC) operation with a less lean mixture, since the intake trapped mass was not significantly reduced as the intake air was replaced by EGR. In addition, higher EGR percentage in the intake charge increased intake manifold temperature that also contributed to less decrease of compression pressure. From the HRR curves shown, CDA-Throttling and CDA-LIVC with conventional dual-fuel resulted in distinct two stage combustion, where the first autoignition of diesel was followed by flame propagation within premixed gaseous fuel. Meanwhile, CDA-EGR with PDFC with the single peak at higher level of HRR indicated simultaneous combustion. From HRR curves, simulation with a less lean mixture resulted in higher peak and faster combustion because of improved flame speed.

6.4.5 Mean Gas Temperature at 1200 rpm/3 bar BMEP

Mean gas temperature during the 6-cyl strategies at λ=1.8 are depicted in Figure 6.26, while the mean gas temperature by CDA strategies at λ=1.0 and λ=1.4 are shown in Figure 6.27. From comparison of the mean gas temperature by 6-cyl strategies, PDFC-EGR resulted in highest compression-end temperature due to highest trapped mass and highest intake manifold temperature. Meanwhile, throttling strategies resulted in lowest compression-end temperature but highest maximum values of mean gas temperature. The maximum of mean gas temperature can be attributed to the fuel consumption of the respective strategies. From the comparison of mean gas temperature by CDA in Figure 6.27, running the simulation with a less lean mixture with retarded IVC in CDA-LIVC mode resulted in significant drop in mean gas temperature at the end stage of compression, which is attributed to lower dynamic compression ratio. CDA-Throttling with a less lean mixture also decreased compression pressure due to lower intake trapped mass but in a less significant drop. To the contrary, simulation in CDA-EGR (PDFC) mode at λ=1.0 resulted in higher compression-end temperature than at λ=1.4, which could be related to higher intake manifold temperature

due to higher EGR percentage with a less lean mixture. Lower peak of mean gas temperature by CDA-EGR (PDFC) mode resulted due to lower fuel consumption than CDA-Throttling and CDA-LIVC operation.

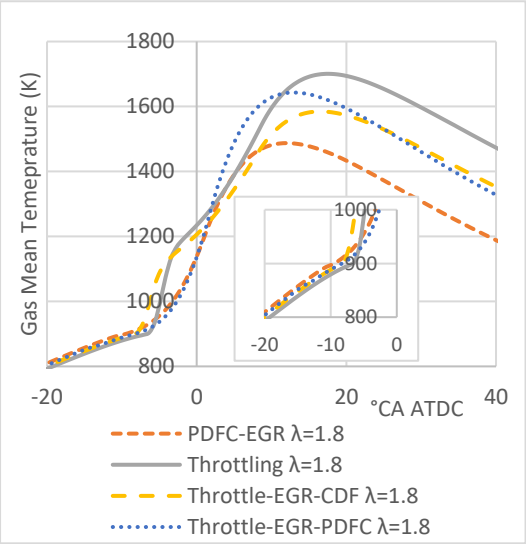


Figure 6.26. Mean gas temperature of Cylinder 1 at 1200 rpm/3 bar BMEP by 6-cylinder Strategies λ=1.8

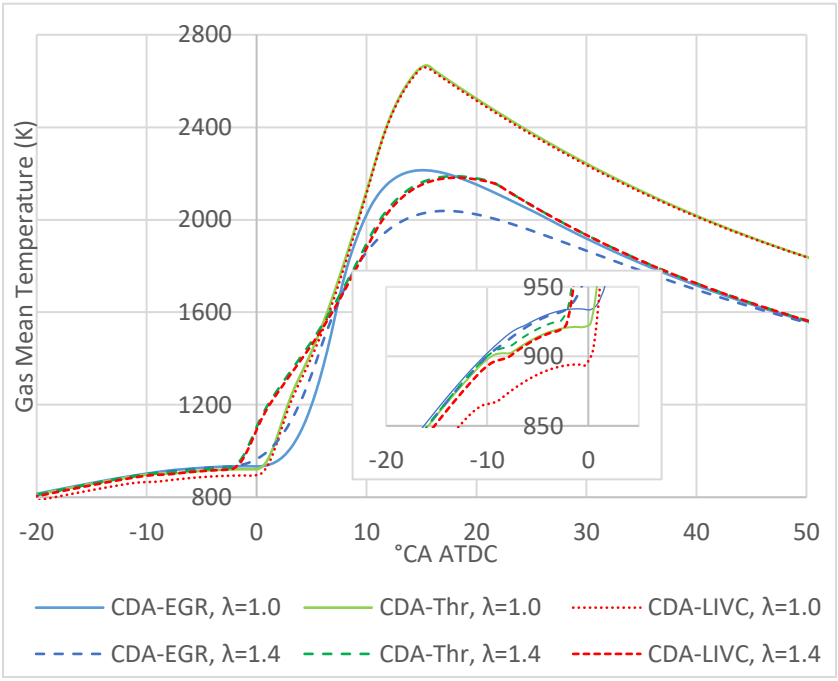


Figure 6.27. Mean gas temperature of Cylinder 1 at 1200 rpm/3 bar BMEP by CDA strategies λ=1.0 and λ=1.4

6.4.6 Combustion Parameters at 1200 rpm/3 bar BMEP

Combustion duration and ignition delay are two key combustion parameters presented in this section. Combustion duration (10% to 90% MFB location) at 3 bar BMEP is depicted in *Figure 6.28*(a), while the ignition delay (duration from SOI to 0.1% MFB) values are depicted

in *Figure 6.28*(b). As the air/fuel mixture in the respective strategies affected ignition delay and combustion, the SOI of the pilot fuel was adjusted accordingly to locate CA50 at 8 °CA ATDC, as shown in *Figure 6.28*(c). Please note that SOI for the PDFC strategy refers to the SOI of the second pilot injection.

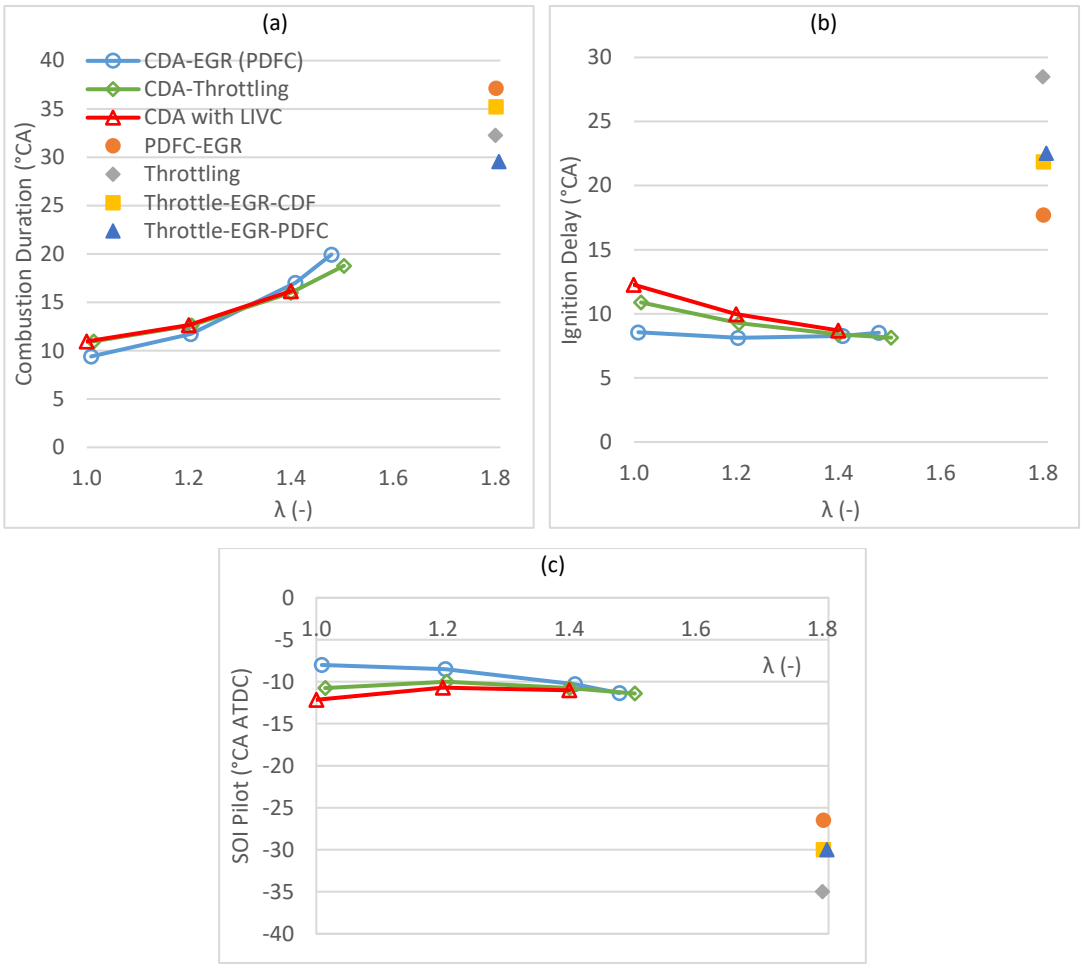


Figure 6.28. (a) Combustion duration, (b) Ignition delay, (c) SOI of pilot fuel, by simulated strategies 1200 rpm/3 bar BMEP

CDA at all simulated strategies performed with shorter combustion duration (between 9 to 27 °CA) and improved ignition delay (between 5 to 20 °CA) than the 6-cyl strategies. The CDA strategies resulted in higher in-cylinder pressure and temperature than the 6-cyl strategies thus improving ignition delay. Simulation of CDA-throttling with a less lean mixture deteriorated ignition delay due to lower intake manifold pressure and thus lower compression pressure and temperature. Meanwhile CDA-LIVC strategy with a less lean mixture was simulated with retarded IVC that decreased dynamic compression ratio, decreased pressure and temperature, hence deteriorated ignition delay. The ignition delay in CDA-EGR (PDFC) mode was relatively constant with a less lean mixture, benefitting from higher compression pressure and higher intake temperature by higher EGR ratio.

Shorter combustion duration indicates that the CDA strategy performed with faster combustion than the 6-cyl strategies between 9 to 27 °CA. The combustion by all CDA strategies was accelerated with a less lean mixture due to increased flame speed. Less lean mixture and higher cylinder temperature by the implemented CDA strategies promoted flame propagation of the gas/air mixture. CDA-EGR (PDFC) mode performed with fastest combustion among the simulated strategies. The higher intake temperature and higher compression temperature due to higher trapped mass by EGR dilution contributed to the improvement of flame propagation. More significant improvement in combustion duration resulted by CDA-EGR (PDFC) mode than any of the other strategies, suggesting the combined effect of EGR that increased charge temperature and more ignition source provided by the premixed first pilot within the gas/air mixture.

In the 6-cyl strategy, PDFC-EGR mode performed with shortest ignition delay but longer combustion duration than throttling. Intake dilution with EGR resulted in higher compression temperature, improved diesel autoignition processes but deteriorated flame propagation within premixed gaseous fuel. Meanwhile, the combination of Throttle-EGR-PDFC benefited from higher intake temperature and premixing of the first injection to accelerate the combustion, with shorter ignition delay than a throttling only strategy.

As the engine operating points and the implemented strategy affected the combustion duration and ignition delay, the injection timing of the pilot fuel was adjusted accordingly to locate CA50 at 8 °CA ATDC. The SOI of the first pilot fuel for the simulated strategies is plotted in *Figure 6.28*(c). The combined benefits of improved ignition delay and faster flame propagation within gaseous fuel by CDA strategy (due to higher pressure and temperature) enabled the retardation of SOI closer to TDC. To the contrary, SOI pilot of the 6-cylinder strategies were at a more advanced timing due to longer ignition delay and slower combustion speed.

6.4.7 Engine Heat Loss at 1200 rpm/3 bar BMEP

The engine heat loss through the cylinder wall heat transfer (herein engine heat loss) by simulated strategies are depicted in *Figure 6.29*. Engine heat loss by CDA strategies at λ=1.4 and higher were lower than by the 6-cyl strategies. However, simulation with a less lean mixture deteriorated engine heat loss due to higher mean gas temperature. This caused the CDA-Throttling and CDA-LIVC at λ=1.0 and λ=1.2 to result in higher engine heat loss than 6-cyl with PDFC-EGR operation. Among the CDA simulated strategies, CDA with throttling-CDF mode up to λ=1.4 indicated the highest trend of engine heat loss which could be related to

highest BSFC. The trend of engine heat loss by CDA-EGR (PDFC) remained lower than by 6-cyl strategies although deteriorated at lower λ. Among all of the simulated strategies, throttling resulted in highest engine heat loss.

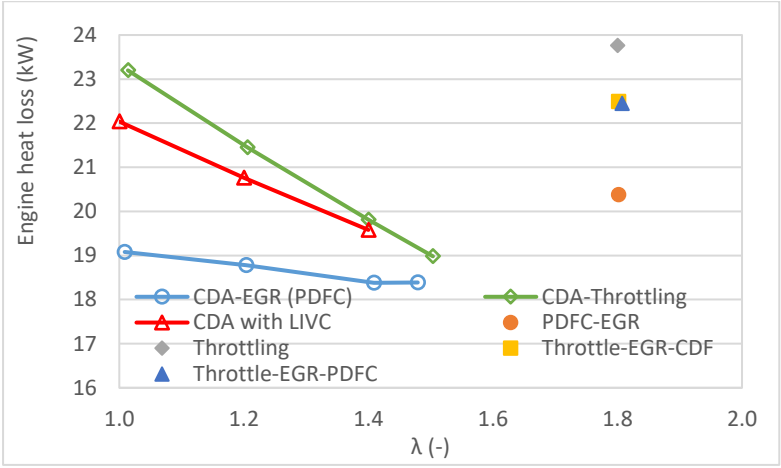


Figure 6.29. Engine's cylinder wall heat transfer rate at 1200 rpm/3 bar BMEP

6.4.8 Exhaust Gas Temperature at 1200 rpm/3 bar BMEP

EGT by simulated strategies at 1200 rpm/3 bar BMEP are shown in *Figure 6.30*. Comparison between strategies in the same number of firing cylinder (either in 6-cyl or CDA) suggests that the EGT strongly related to BSFC, mean gas temperature and cylinder wall heat loss. Comparison between 6-cyl strategies, throttling produced highest EGT, while PDFC-EGR resulted in lowest EGT. From the comparison, CDA strategies produced 30 to 165°C higher EGT than throttling with 6-cylinder strategy. Higher gas mean-temperature in the firing cylinder in CDA give such benefit because of higher load (Net IMEP) in less lean mixture with improved cylinder wall heat loss due to less surface area than 6-cyl strategy. The EGT by CDA-throttling was highest among the simulated strategies due to highest fuel consumption that resulted in highest mean gas temperature. Meanwhile, combination of CDA with PDFC-EGR produced lowest exhaust gas temperature up to 1.2 with relatively constant trend despite λ changes. As summary, contrast to 6-cyl strategy that resulted highest EGT at 377°C, CDA strategies produced EGT more than 400 °C. This means, CDA is beneficial for supporting oxidation process within advanced Methane Oxidation Catalyst (MOC) that requires EGT higher than 380°C [124].

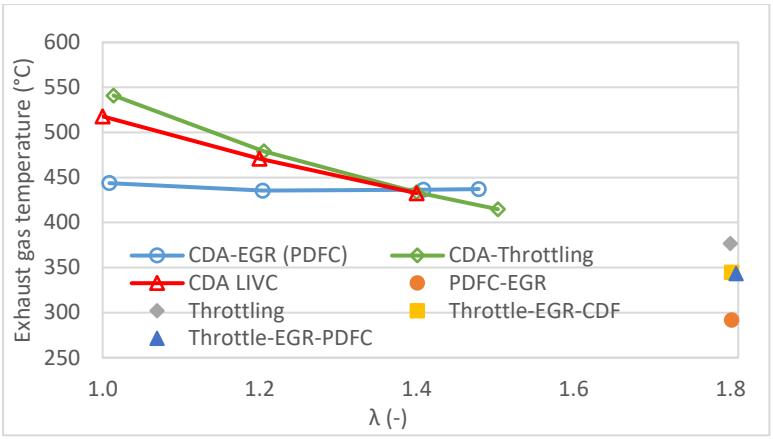


Figure 6.30. Exhaust gas temperature at 1200 rpm/3 bar BMEP

6.5 Summary

The phenomenological modelling of dual-fuel combustion was simulated in a 6-cylinder CI engine model with predictive combustion in GT Power software. The simulations were carried out at 1200 rpm at 6 bar and 3 bar BMEP as representative of low load operating points. The simulations at 6 bar BMEP were performed by implementing 6-cylinder active and CDA strategies with mixture strength variation (λ sweep) to stoichiometric mixture (λ=1.0). Intake charge in the CDA strategies at 6 bar BMEP were varied by adjustment of eSupercharger speed. Meanwhile, simulations at 3 bar BMEP was run by implementing 6-cylinder strategies at λ=1.8 and CDA strategies combined with throttling, EGR, or LIVC as the mixture control strategy.

The implementation of CDA-Battery by deactivating 3 cylinders at 1200 rpm/6 bar BMEP increased the load of firing cylinder at roughly double of the load in 6-cyl active strategies. Therefore, each firing cylinder in CDA strategies required higher fuel quantity thus higher intake charge mass that resulted in higher in-cylinder pressure and temperature during compression. This improved the processes related to the pilot diesel combustion. In addition, it also promoted flame propagation of premixed gaseous fuel. Combination of both shorter ignition delay and faster combustion by CDA strategy required retardation of pilot injection timing closer to the TDC to locate the combustion phasing at 8 °CA ATDC, which is also beneficial to the diesel combustion process. The engine also benefits from the CDA operation by lower cylinder wall heat loss due to halving the number of the firing cylinder. The higher load of individual cylinder in CDA resulted in higher mean gas temperature thus produced higher exhaust gas temperature by 38°C than the highest EGT produced by 6-cylinder strategy. The improved combustion performance and lower cylinder wall heat loss contributed to the improvement of brake efficiency by CDA strategy by 4%. From the

perspective of pumping loss, the CDA strategy benefited higher intake manifold pressure than exhaust manifold pressure during pumping process. However, the CDA strategy requires dedicated valve actuation mechanism. If hardware complexity become an uncompromised factor, PDFC-EGR with 6-cylinders strategy could be the feasible option to improve the performance, where its brake efficiency at λ=1.0 is just slightly lower than CDA-Battery and higher than CDA-Generator.

3 bar BMEP is a very low load operating point, which is challenging for dual-fuel combustion at 90% substitution ratio with 6-cyl active due to very lean mixture. The 6-cyl simulated strategies at λ=1.8 resulted in deteriorated ignition delay and poor combustion performance, hence resulted low brake efficiency. Further mixture enrichment was limited either by very low intake manifold pressure or high EGR fraction required to replace the intake air. Combination of throttling and EGR resulted in higher efficiency than throttling, thanks to improved pumping loss. However, 6-cyl strategies produced EGT lower than 380 °C, less than catalyst light off temperature of MOC.

CDA strategy at 3 bar BMEP was simulated by implementing throttling, EGR and PDFC, or LIVC as λ control method. Combination of CDA with each λ control method cause different consequences. CDA-throttling at richest mixture suffered highest pumping loss that deteriorated the fuel economy. CDA-EGR(PDFC) at less lean mixture used high EGR fraction that resulted in high cylinder temperature that resulted shortest ignition delay and combustion duration, hence performed at highest brake efficiency. Meanwhile, CDA-LIVC at the most retarded IVC to simulate at richest mixture suffered lowest dynamic compression ratio, resulted lower cylinder temperature and shortest ignition delay among CDA strategies. In general, CDA improved combustion performance, both in ignition delay of diesel pilot fuel and shorten the combustion duration, thanks to higher cylinder temperature and less lean mixture that increase flame speed. This resulted improvement in fuel economy by 4% compared to the 6-cylinder strategy with throttling at λ=1.8. The higher individual load in CDA strategies also resulted in higher mean gas temperature of the firing cylinder that produced higher exhaust gas temperature by 165°C than the 6-cylinder strategies with throttling. In addition, simulated CDA strategies at this low load produced EGT higher than 400°C that meet the requirement of MOC.

Chapter 7 Thermal Barrier Coating (TBC) on Piston and Cylinder Head Surface in Dual-Fuel Combustion

7.1 Introduction

In Chapter 6, simulation results of dual-fuel combustion strategies are presented, where CDA resulted in higher brake efficiency and higher exhaust gas temperature than the 6-cylinder active strategy. Further improvement to increase exhaust gas temperature could be an attractive dual-fuel combustion strategy to support the oxidation process within a methane oxidation catalyst. Heat loss from burned gas to the cylinder wall is one key factor that determines the exhaust gas temperature.

Thermal Barrier Coatings (TBC) are not new and can be applied to the piston crown and potentially other surfaces within the combustion chamber as a thermal barrier. A thin coating layer of low thermal conductivity and low heat capacity material is applied to the surface of piston crown or other inner surfaces within the combustion chamber and/or exhaust ports. TBCs have been reported as a successful strategy that reduced heat transfer and increased efficiency in previous studies of gasoline [167], diesel [168,169] and gas engines [170].

In this study, the impact of TBC upon piston and cylinder head surfaces was investigated through phenomenological modelling in GT Power software. Set out in the first section of this chapter is a description of how the TBC method was implemented in the model. This is followed by a description of the simulated points for dual-fuel combustion that were performed in two engine models, with and without TBC (standard piston and head surface). In the second section, the simulation results at 6 bar BMEP are presented and discussed. Following this, in the third section the simulation results at 3 bar BMEP are reported and analysed. Finally, a summary of the results is described with some important findings highlighted.

7.2 Simulation Setting of Dual-Fuel Combustion with TBC

The simulation was performed in the same engine model as described in Chapter 4 but with modification to the piston and cylinder head surfaces by application of a TBC layer. Implementation of the TBC into the model was simulated using the “MaterialThermalProp” template in the “Surface Layer” template. The properties of the TBC material used in this study were taken from the Silica Reinforced Porous Anodised Aluminium (SiRPA) concept developed by the Toyota research team reported by Wakisaka et al. [168]. The material was

developed as a low conductivity and low heat capacity coating, suitable to reduce heat loss during combustion and prevent intake heating during the intake stroke. Thermophysical properties of SiRPA are described in *Table 7.1*. In the engine model, a 100 µm thick surface layer was applied on the piston bowl and inner cylinder head surfaces.

Properties	**Unit**	**Value**
Density	g/cm^3	1.4
Thermal conductivity	W/mK	0.67
Volumetric specific heat capacity	kJ/m^3K	1300

Table 7.1. Thermophysical properties of TBC material (at 500 K) used in the simulation (from Ref. [168]*)*

Dual-fuel combustion with TBC application was simulated at 1200 rpm/6 bar BMEP and was performed only at λ=1.2 with CDA strategies in the following scenarios: CDA-Battery, CDA-Generator and the 6-cylinders strategy with PDFC-EGR, throttling, and Miller-LIVC. The dual-fuel simulation of diesel engine model with TBC at 1200 rpm/6 bar BMEP- λ=1.2 used the same settings of the respective strategy simulated in the standard (non-TBC) model. In the other words, only the material properties of the model were changed in the simulation while all of the operating parameters such as fuel quantity, eSupercharger speed, EGR percentage, throttle valve angle, IVC and combustion multipliers were kept as same as the standard model. Fixing these parameters was done to minimise other effects that might influence the engine performance apart from the TBC application. The simulation was undertaken at λ =1.2 rather than λ =1.0 since if the TBC caused lower intake air mass and an over rich mixture (λ<1.0), the simulation would result in unwanted higher unburned fuel.

Implementation of TBC in the engine model was simulated at 1200 rpm/3 bar BMEP with 3 variations of CDA strategy at λ=1.2 i.e., CDA-EGR (PDFC), CDA-throttling and CDA-LIVC, while 6-cylinder strategies with the TBC model were simulated with PDFC-EGR and throttling at λ=1.8. The strategies were simulated in the same way as 6 bar BMEP above in terms of how the parameters in the standard (non-TBC) model were fixed.

7.3 Simulation Results of Dual-Fuel with TBC at 1200 rpm/6 bar BMEP/λ=1.2

Simulation results with the TBC model are compared to the results from non-TBC model. The change of each parameter as the impact by TBC is presented as a relative value to the non-TBC model. In several parameters resolved on a crank-angle basis the differences are marginal and can be higher or lower, thus producing fluctuated traces.

7.3.1 Changes to The Intake Charge via TBCs at 1200 rpm/6 Bar BMEP

Since the TBC has different properties to the standard metal surface, changes to cylinder wall temperature were expected. In turn, differences in heat transfer rates were expected to influence the in-cylinder pressure and temperature. Changes to in-cylinder pressure and mean gas temperature at 6 bar BMEP for the simulated strategies are illustrated in *Figure 7.1*(a) and *Figure 7.1*(b). The change to in-cylinder pressure by TBC was very little (max. ±0.002 bar), but it is an important phenomenon to be analysed to understand the other impacts upon the intake charge. Higher temperature by all strategies early in the intake stroke indicated higher residual gas, which then dropped as the cylinder volume expanded to draw intake air into the cylinder. In the CDA strategies, the TBC resulted in lower pressure and mean gas temperature than the non-TBC model and remained relatively constant at ~1 °C from ~390 °CA ATDC. To the contrary, the 6-cyl strategies resulted in higher mean gas temperature. In addition, mean gas temperature started to increase from around 480 °CA ATDCF that suggested a heating effect by the cylinder wall.

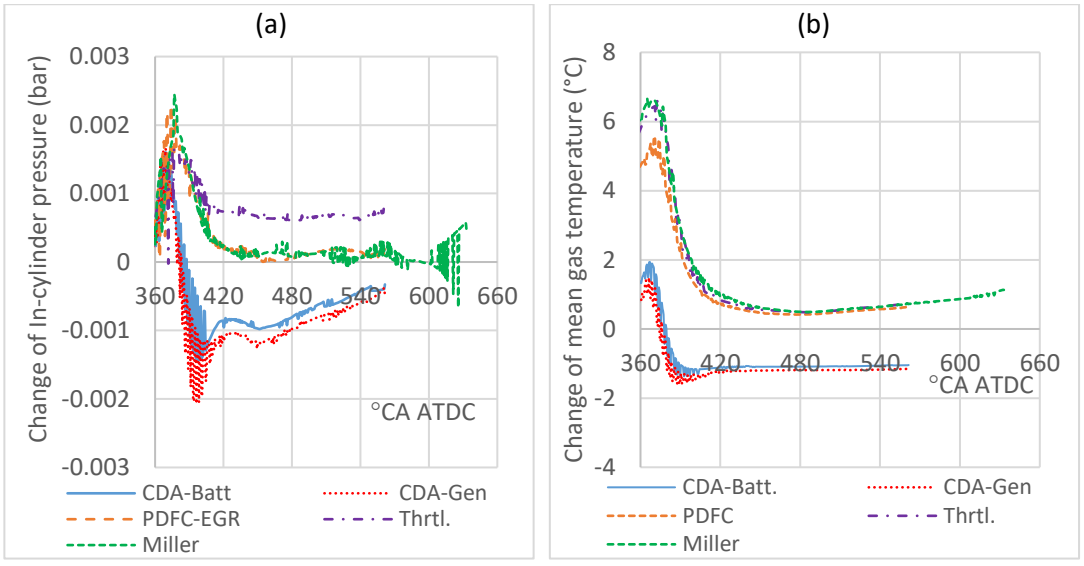


Figure 7.1. (a) change of in-cylinder pressure and (b) change of mean gas temperature during intake and early compression stroke

One consequence of changed in-cylinder pressure and temperature by the TBC was the change in the intake trapped mass. The change of the trapped mass in Cylinder 1 at IVC for each respective operating strategy is illustrated in *Figure 7.2*(a). The TBC piston and cylinder head increased the intake trapped mass in the CDA strategies. CDA-Generator with TBC increased the trapped mass by 0.3%, higher than CDA-Battery with TBC which increased by 0.24% trapped mass. Lower in-cylinder pressure by CDA strategies in the engine model with TBC during suction and the early compression stroke resulted in higher intake air trapped mass for the same operating speed of eSupercharger. On the contrary, TBC application in the

6-cylinder strategies decreased the intake trapped mass due to higher in-cylinder pressure during suction and early on in the compression stroke. Therefore, the implementation of TBC to the 6-cylinder strategies with naturally aspirated (without eSupercharger) trapped less intake mass than the standard engine model. Decreased trapped mass in the throttling strategy was less significant than PDFC-EGR and Miller-LIVC. PDFC-EGR, with higher intake temperature due to EGR dilution which brought a more significant effect of reduced intake trapped mass. Meanwhile, LIVC at the same IVC timing at the highest mean gas temperature resulted in the most significant reduction of trapped mass among the 6-cyl strategies, at 0.25% lower than the non-TBC model.

With the same injected fuel quantity for the respective strategy, the change of air/fuel mixture by simulation in the TBC model relative to the standard model is illustrated in *Figure 7.2*(b). CDA strategies with TBC application increased the air/fuel mixture by as much as 0.05 for CDA-Battery and 0.06 for the CDA-Generator. On the other hand, lower trapped intake air mass by TBC in the 6-cylinders strategies decreased the air/fuel ratio by 0.03 for PDFC-EGR, 0.02 during throttling and 0.05 for the Miller-LIVC strategy.

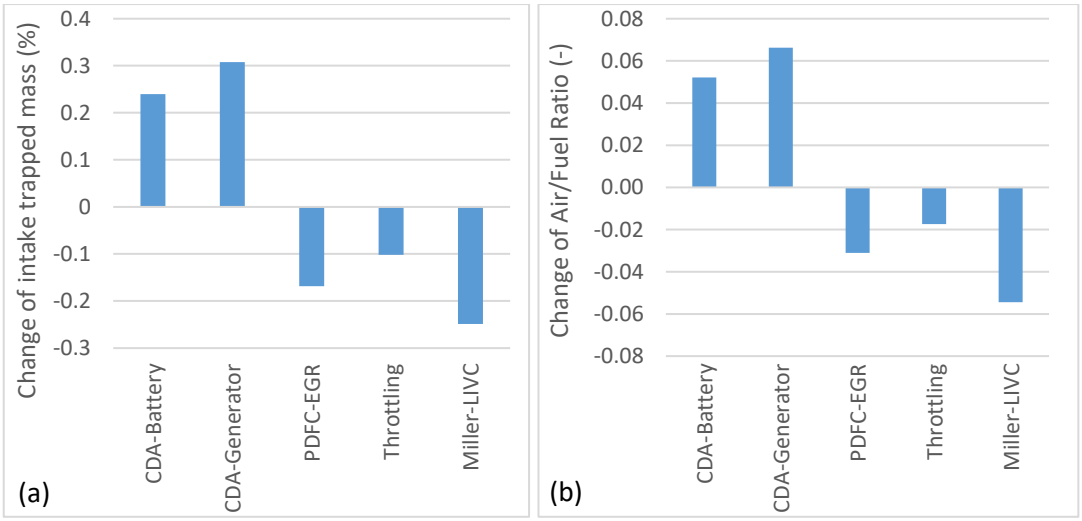


Figure 7.2. (a) Change of intake trapped mass and (b) Change of air/fuel ratio by TBC application in simulated strategies at 1200 rpm/6 bar BMEP, λ=1.2

7.3.2 Changes to In-cylinder Pressure, Mean Gas Temperature and Heat Transfer at 1200 rpm/6 bar BMEP

Changes of intake charge as described in the previous section and the expected change of heat transfer resulted in changes to several other parameters during compression and combustion. Change of in-cylinder pressure and mean gas temperature by the simulated strategies are plotted in *Figure 7.3*(a) and *Figure 7.3*(b) respectively. The application of TBC slightly increased in-cylinder pressure during the end of the compression stroke and mostly

during the expansion stroke. Despite lower intake trapped mass with CDA, lower cylinder wall heat transfer by TBC application increased the in-cylinder pressure. Meanwhile, amongst the simulated strategies, Miller-LIVC with TBC resulted in the highest peak changes to the in-cylinder pressure during combustion. The most significant reduction of intake trapped mass by TBC during the Miller-LIVC strategy resulted in the largest reduction in air/fuel ratio (amongst the 6-cyl strategies) that in turn influenced the combustion and thus produced the greatest changes to in-cylinder pressure.

The 6-cylinders strategies indicate higher mean gas temperature as an effect of TBC during compression and expansion. A richer mixture, as indicated by the reduced air/fuel ratio as shown in *Figure 7.2*(b), contributed to higher mean gas temperature by the 6-cylinder strategies with TBC. On the contrary, TBC application to the CDA-Generator mode produced lower mean gas temperature, while in CDA-Battery operation the TBC performed with the same mean gas temperature. This lower gas temperature could be related to leaner mixture operation by CDA strategies with TBC.

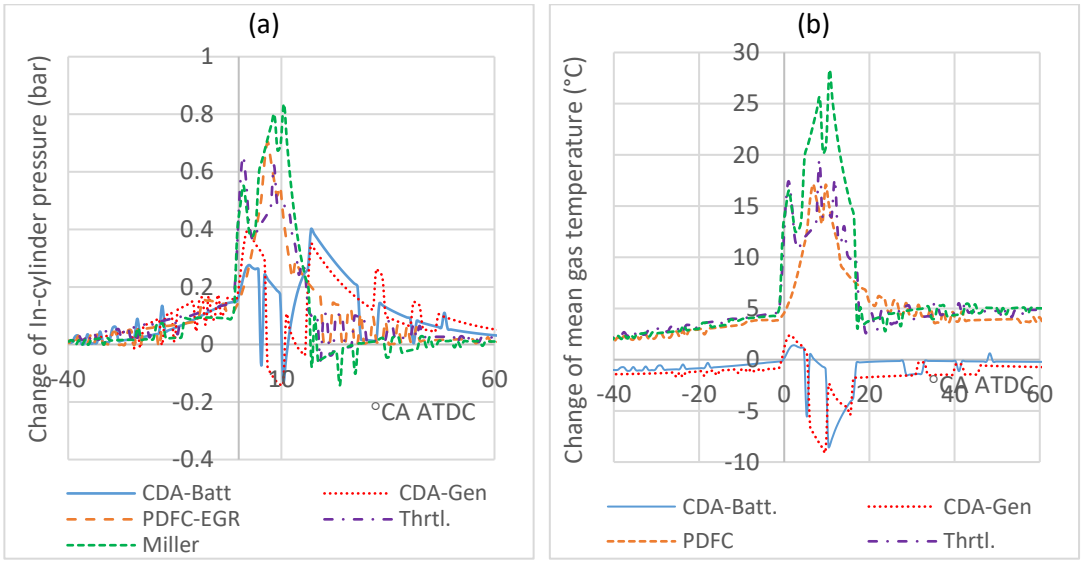


Figure 7.3. (a) Changes to the in-cylinder pressure and (b) Changes to the mean gas temperature by TBC application in the simulated strategies at 1200 rpm/6 bar BMEP- λ=1.2

7.3.3 Combustion Parameters during Dual-Fuel with TBC at 6 bar BMEP

As TBC changed the intake trapped mass, intake pressure and mean gas temperature, it was expected to affect the combustion performance. The impact of TBC on the ignition delay, combustion duration and combustion phasing are depicted in *Figure 7.4*. Positive changes to ignition delay and combustion duration indicate longer duration with TBCs, while positive changes to CA50 indicates retarded combustion phasing.

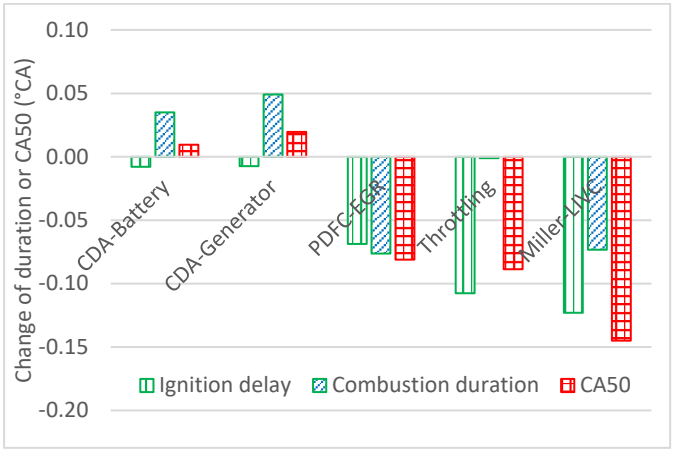


Figure 7.4. Change of ignition delay, combustion duration and CA50 resulted by TBC at 1200 rpm/6 bar BMEP- λ=1.2

In general, TBC improved ignition delay in all strategies, with more significant impact during the 6-cyl strategies. Diesel combustion favours higher pressure that improves the injection process. Lesser effect during CDA with TBC could be related to slightly lower mean gas temperature during the end of compression than the standard model despite higher in-cylinder pressure. TBC in CDA mode resulted in prolonged combustion duration, while TBC in 6-cyl operation with PDFC-EGR and Miller-LIVC shortened the combustion duration by 0.07 °CA. A richer mixture due to reduced intake trapped mass for TBC application in 6-cyl strategies promoted flame propagation. With more reduced ignition delay than TBC in CDA combined with shorter combustion duration by TBC application in 6-cyl strategies, it advanced the combustion phasing. To the contrary, less improvement of ignition delay with longer combustion duration for TBC in CDA resulted in retarded combustion phasing. In summary, although slight changes were observed, TBC application in the respective simulated strategies had several small impacts upon the combustion parameters.

7.3.4 Changes of Cylinder Wall Heat Loss by TBC at 1200 rpm/6 bar BMEP

During the early stage of compression, the in-cylinder gas absorbs heat from the cylinder wall and thus the heat transfer is usually signed as negative. As the pressure and temperature increase during compression, the gas transfers heat to the cylinder wall hence it is signed as positive. The impact of application of TBC to the changes of heat transfer during the end of compression and early expansion stroke is presented in *Figure 7.5*(a). During this period, the gas temperature is higher than the cylinder wall and the gas transferred heat to the cylinder wall. Therefore, the negative change of heat transfer at the end of compression is a benefit of TBC, since the heat transfer is lower than the non-TBC models. The CDA strategies with

TBC indicate higher improvement of the cylinder wall heat loss than the 6-cylinders strategies. The application of TBC to the 6-cylinder strategies results partially in higher heat transfer during the combustion period, where Miller with TBC performed with highest increasing mean gas temperature and also resulted in highest peak heat transfer. This could be related to higher mean gas temperature during combustion as illustrated in *Figure 7.3*(b). In addition, significantly higher mean gas temperature during the peak heat release rate during combustion resulted in higher heat transfer by the TBC model. To the contrary, lower mean gas temperature for TBC with CDA during combustion reduced the heat transfer rate. At the end of combustion and later stage of the expansion stroke, the heat transfer for TBC remained lower than the standard model.

While the effect of TBC during combustion varies depending on the simulated strategies, generally TBC reduces the heat transfer from working gas to the cylinder wall during the expansion stroke. This generally improved the average of engine's cylinder wall heat transfer (herein referred to as engine heat loss), as shown in *Figure 7.5*(b). The negative change indicates the improvement of the engine's heat loss. The TBC on the piston and cylinder head surfaces at 1200 rpm/6 bar BMEP-λ=1.2 improved the cylinder wall heat loss in all of the simulated strategies. It is shown that TBC reduces the cylinder wall heat loss between 0.8 to 1.2%. The most significant improvement among the simulated strategies was produced by PDFC-EGR, with 1.17% reduction in the cylinder wall heat loss. Meanwhile, the least improvement was noted for the CDA-Generator strategy, at 0.8% change.

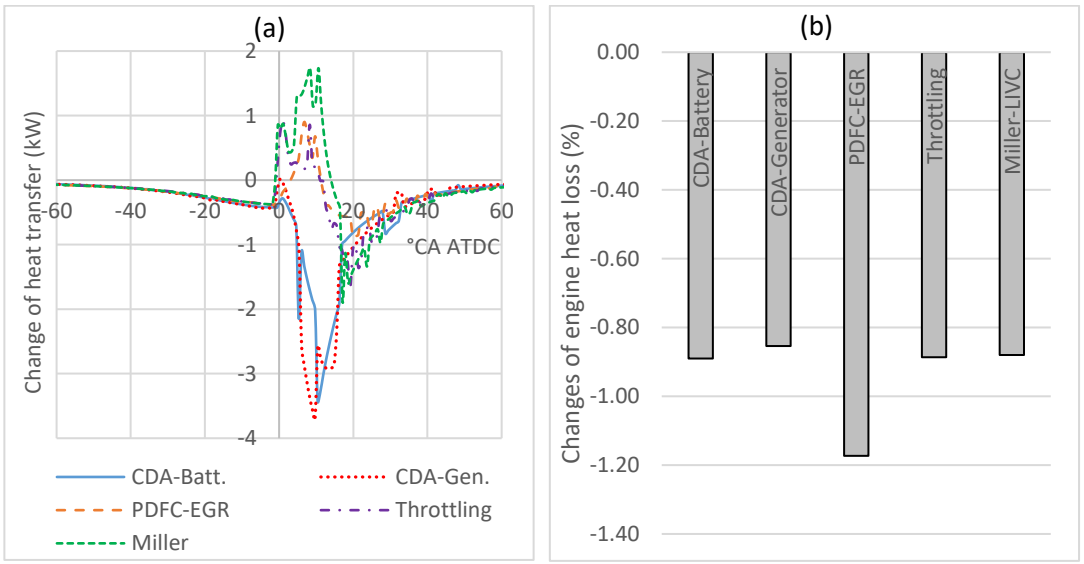


Figure 7.5. (a) Changes of instantaneous heat transfer and (b) Changes of the engine heat loss by TBC application in the simulates strategies at 1200 rpm/6 bar BMEP-λ=1.2

7.3.5 Changes in Net IMEP and BMEP by TBCs at 1200 rpm/6 bar BMEP

Improvement in the cylinder wall heat loss by TBC application contributes to slight improvement in Net IMEP of Cylinder 1 and BMEP for all of the simulated strategies as illustrated in *Figure 7.6*(a). The applied TBC in CDA-Generator mode improved Net IMEP by 0.04 bar and BMEP by 0.02 bar. In the CDA-Battery mode, TBC improve Net IMEP and BMEP by a slightly lower level. Meanwhile, TBC in the 6-cylinder strategies increase at a lower level, by 0.017 bar of Net IMEP and 0.015 of BMEP for the PDFC-EGR mode. The application during Miller-LIVC benefits the lowest improvement of 0.015 bar Net IMEP and 0.01 bar BMEP. The improvement of Net IMEP and BMEP produced a small improvement in the net indicated efficiency (shown as Net Ind. Eff.) and brake efficiency (shown as Brake Eff.), as shown in *Figure 7.6*(b). TBC application improved performance most significantly in CDA-Generator mode, with 0.12% increase in net indicated efficiency and 0.11% in brake efficiency. CDA-Battery, PDFC-EGR, throttling, and Miller-LIVC modes incurred lower percentage benefits. Reduction of cylinder wall heat losses by TBCs increases the in-cylinder pressure, which improves the net indicated efficiency as well as the brake thermal efficiency. The improvement of efficiency can be converted to improvement in fuel economy of around 0.7 g_{diesel}/kWh for TBC in CDA-Generator mode, as illustrated in *Figure 7.7*, while TBC in Miller-LIVC mode exhibited least reduction among the simulated strategies, with BSFC reduced by 0.4 g_{diesel}/kWh.

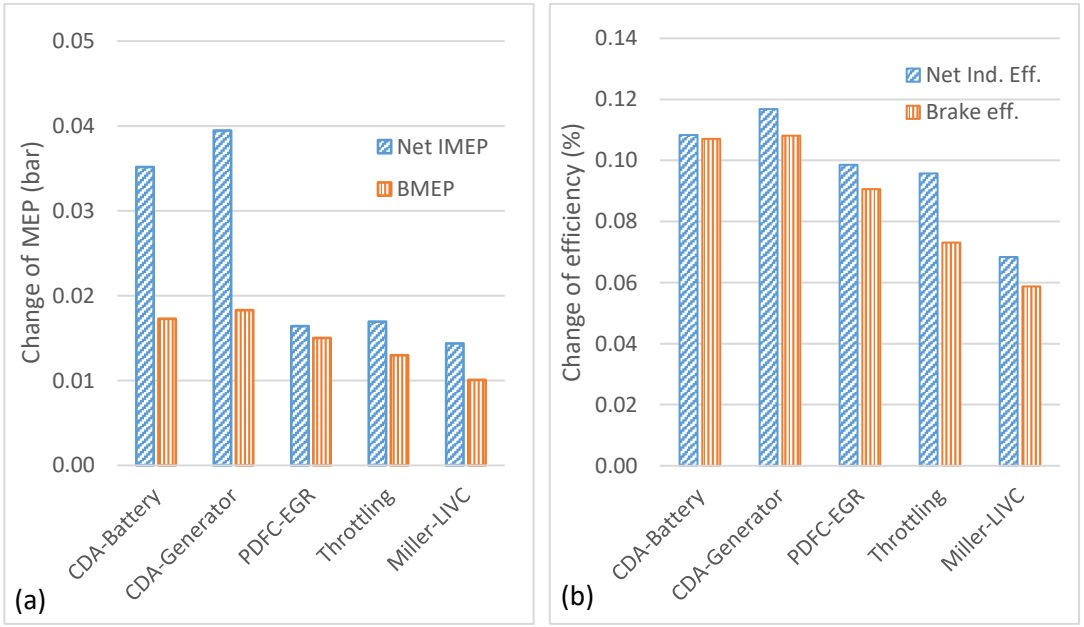


Figure 7.6. (a) Changes of net IMEP of cylinder 1 and BMEP, (b) Changes in net indicated efficiency and brake efficiency by TBC application in the simulated strategies at 1200 rpm/6 bar BMEP- λ=1.2

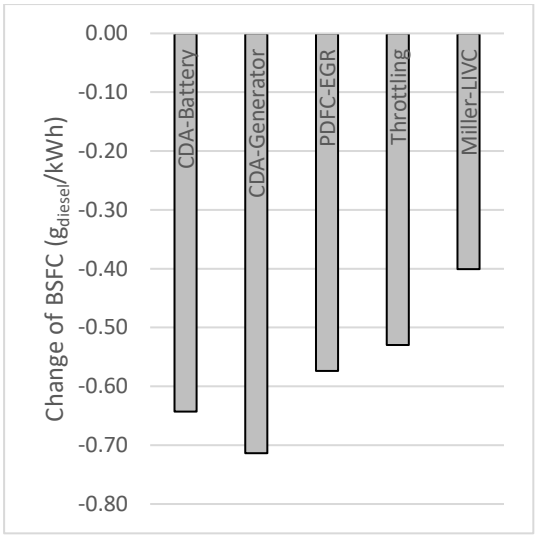


Figure 7.7. Change of BSFC in diesel equivalent by TBC application to the simulated strategies at 1200 rpm/6 bar BMEP- λ=1.2

7.3.6 Changes in Exhaust Gas Temperature by TBCs at 1200 rpm/6 bar BMEP

The impact of TBC upon exhaust gas temperature by the respective simulated strategies is shown in Figure 7.8. The 6-cylinders strategies indicate higher exhaust gas temperature with TBC by 2°C. To the contrary, the CDA strategy with TBC decreases the EGT by 1.4°C in CDA-Battery mode and 1.7°C in CDA-Generator mode. Despite improved cylinder wall heat loss, lower EGTs during CDA can be attributed to combustion with a leaner mixture that decreased mean gas temperature during combustion.

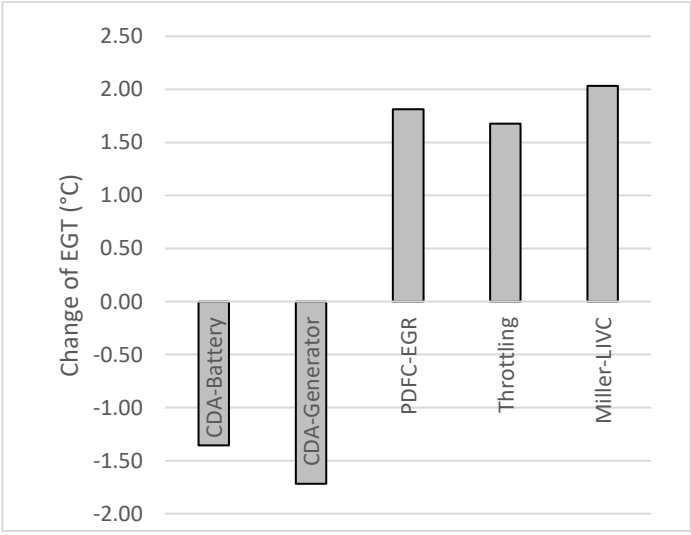


Figure 7.8. Changes of exhaust gas temperature by TBC application in the simulated strategies at 1200 rpm/6 bar BMEP- λ=1.2

7.4 Simulation Results of Dual-Fuel with TBCs at 1200 rpm/3 bar BMEP

The impacts of TBC application upon key parameters in both the CDA strategies (λ=1.2) and 6-cylinder strategies (with PDFC-EGR and throttling at λ=1.8) are described and discussed in this section. This includes some concise discussion on changes in the intake charge, in-cylinder pressure and gas temperature, combustion, heat transfer and EGT.

7.4.1 Changes of The Intake Trapped Mass and Air/Fuel Ratio by Application of TBC at 1200 rpm/3 bar BMEP

The changes in intake trapped mass for all simulated strategies with TBC at 1200 rpm/3 bar BMEP are shown in *Figure 7.9*(a). Application of TBC to the simulated strategies slightly reduced the intake trapped mass by between 0.09% to 0.2%. The TBC application to the CDA-throttling strategy reduced the intake trapped mass by the least quantity. Meanwhile, it reduced the intake trapped mass for CDA-LIVC mode with the most significant percentage. As the injected fuel quantity was fixed for all modes, the simulation with TBC reduces air/fuel ratio in all three simulated strategies as shown in *Figure 7.9*(b). The applied TBC decreased the air/fuel ratio in different values. The largest decrease was produced for the CDA-LIVC and Throttling modes (at 0.043 and 0.040 respectively), while the least decrease was in CDA-throttling mode (at 0.020). Increased mean gas temperature during intake in the LIVC strategy, which pushed gases back to the intake port, increased the intake manifold temperature thus decreasing the density and the intake trapped mass. The effect of intake heating by TBC was less significant in the throttling strategy, hence the intake trapped mass reduction was less significant among the simulated strategies. In summary, TBC application at 3 bar resulted in small reduction in intake trapped mass and air/fuel ratio, thus producing a richer mixture, which is a similar effect as observed in the simulated strategies at 6 bar without a boosting device.

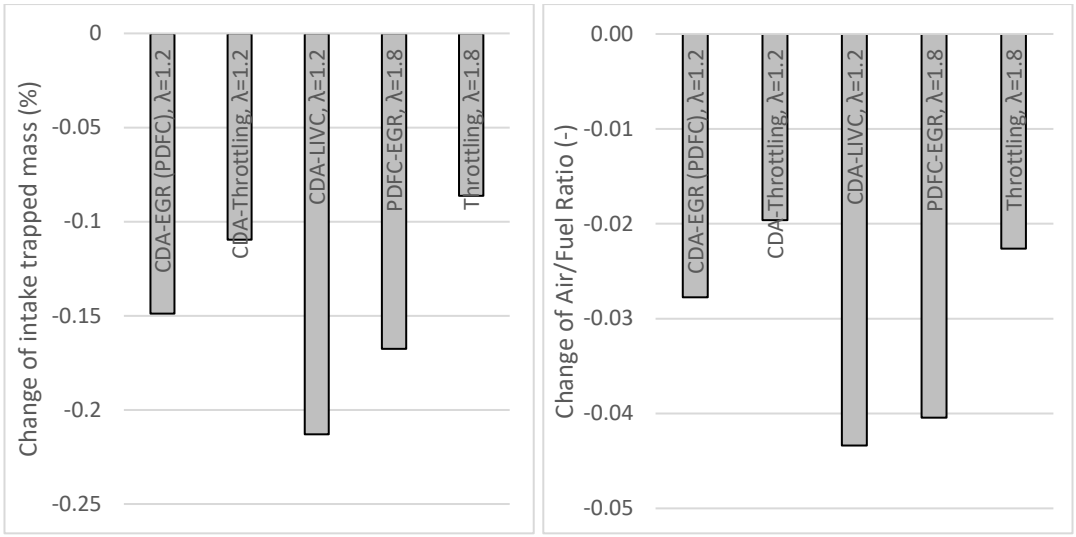


Figure 7.9. (a) Changes of intake trapped mass and (b) Changes of air/fuel ratio by TBC application in simulated strategies at 1200 rpm/3 bar BMEP

7.4.2 Changes of The In-cylinder Pressure, Mean Gas Temperature and Crank-Angle Resolved Heat Transfer Changes by TBCs at 1200 rpm/3 bar BMEP

Despite lower intake air trapped mass as shown before, TBC application to the simulated strategies at 3 bar BMEP increased in-cylinder pressure during the end of compression and combustion as shown in *Figure 7.10*(a), where the application resulted in the highest peak during CDA-EGR (PDFC) at 1.3 bar. At the later stage in the expansion stroke, the change of in-cylinder pressure by TBC application was not significant. The changes of mean gas temperature for the TBC model and simulated strategies are shown in *Figure 7.10*(b). All of the simulated strategies with TBC indicate higher mean gas temperature than the standard model. The highest change of mean gas temperature was produced by application of TBC in the CDA -EGR (PDFC) strategy up to 30 °C. TBC application in 6-cyl strategy with PDFC-EGR slightly increased mean gas temperature by 7 °C. After combustion, the mean gas temperature remained higher than the non-TBC model due to improved heat transfer to the cylinder wall.

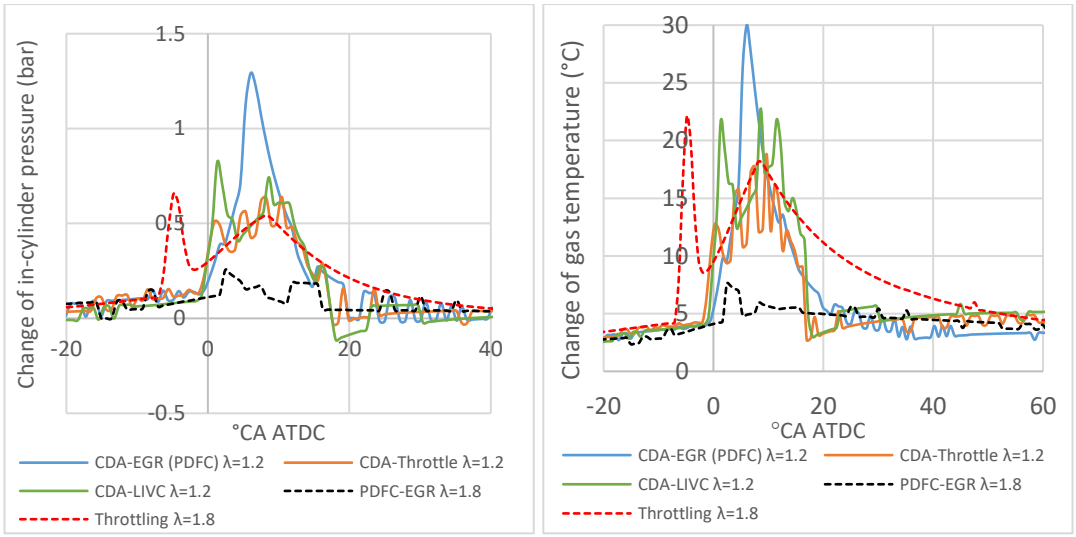


Figure 7.10. (a) Changes of the in-cylinder pressure and (b) Changes of the mean gas temperature by TBC application in the simulated strategies at 1200 rpm/3 bar BMEP

7.4.3 Combustion Parameter by Dual-Fuel with TBCs at 3 bar BMEP

The influence of TBC application upon the combustion parameters is illustrated in *Figure 7.11*. The TBC improved ignition delay, shortened the combustion duration and advanced the combustion phasing. The impact of TBC to shorten the combustion duration was more significant in PDFC-EGR and throttling at λ=1.8 modes than for the CDA strategies. TBC in throttling resulted in the most significant reduction of combustion duration and most advancement of combustion phasing. Higher in-cylinder pressure and mean gas temperature at the end of compression promoted the pilot injection processes and improved ignition delay. Meanwhile, richer mixture with TBC application and higher mean gas temperature became important factors that promoted flame propagation hence shortened the combustion duration and advanced the combustion phasing.

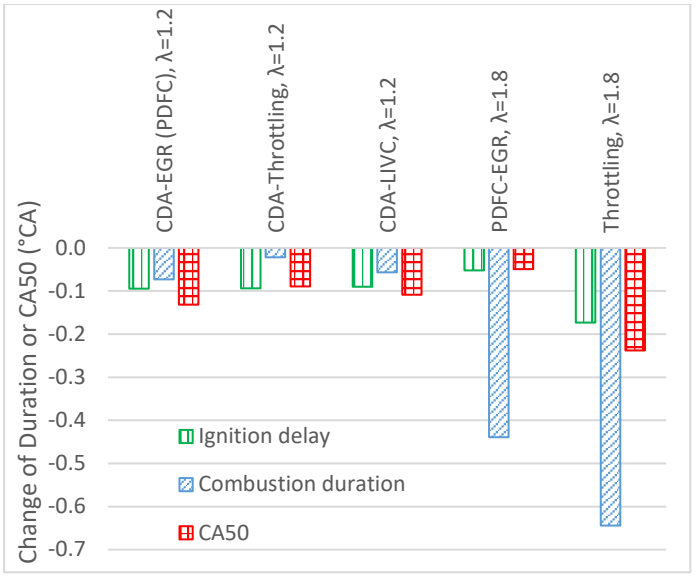


Figure 7.11. Change of ignition delay, combustion duration, and CA50 resulted by TBC at 3 bar BMEP

7.4.4 Changes of Cylinder Wall Heat Loss and Exhaust Gas Temperature by TBCs at 1200 rpm/3 bar BMEP

The change to instantaneous heat transfer by the simulated TBC models during end of compression and expansion stroke is illustrated in *Figure 7.12*(a). The negative changes during the end of compression and expansion stroke means an improvement of heat loss to the cylinder wall. The application of TBC indicates reduction of heat transfer by working gas to the cylinder wall during compression and predominantly during the expansion stroke. Higher heat transfer during combustion (close to TDC) could be attributed to significantly higher peak mean gas temperature by simulated strategies with TBC than the standard model.

Reduction of cylinder wall heat transfer during compression and the expansion stroke in the TBC model improved the overall engine heat loss, as shown in *Figure 7.12*(b). The application of TBC to the CDA -EGR (PDFC) strategy improved the engine's cylinder wall heat loss by 1.1%. In CDA-throttling, applied TBC improved cylinder wall heat transfer by 1%. It reduced the engine's cylinder wall heat loss with the least significance in CDA-LIVC strategy at 0.85%. TBC in PDFC-EGR mode at λ=1.8 resulted in more significant improvement of heat loss at 1.2%, while TBC in throttling mode resulted in the least reduction in heat loss at 0.7%. In general, TBC application in the simulated strategies at 3 bar BMEP improved engine heat loss despite higher mean gas temperature during combustion and expansion.

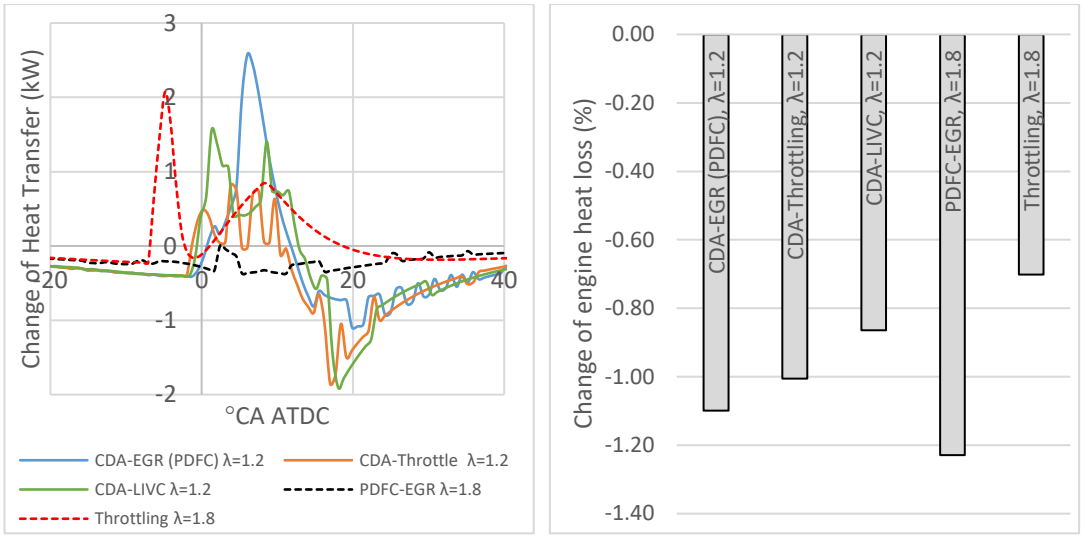


Figure 7.12.(a) Change of instantaneous heat transfer and (b) Changes of the engine heat loss by TBC application in the simulates strategies at 1200 rpm/3 bar BMEP

Significantly higher mean gas temperature during combustion, as shown in *Figure 7.10*(b), resulted in higher heat transfer. However, as the temperature decreased in the later stage of expansion, the heat transfer for TBC became lower despite higher mean gas temperature than the non-TBC model. Predominantly lower heat transfer in the simulated strategies indicates the benefit of TBC application to reduce the engine heat loss through cylinder wall heat transfer, albeit with relatively modest impacts overall.

7.4.5 Changes in Net IMEP and BMEP by TBCs at 1200 rpm/3 bar BMEP

Improved cylinder wall heat loss with TBC changed the in-cylinder pressure during the intake stroke. Higher in-cylinder pressure during expansion resulted in small changes to Net IMEP, BMEP, net indicated efficiency and brake efficiency as shown in *Figure 7.13*. TBC increased Net IMEP of the simulated strategies by between 0.016 to 0.018 bar, increased BMEP by 0.008 bar in the CDA strategies and with higher increase during 6-cyl operation at 0.016. The increase improved net indicated efficiency in CDA mode by 0.09% in CDA-Throttling and CDA PDFC-EGR modes, the 6-cylinder strategy incurred higher improvement by 0.16. This resulted in 0.08% to 0.09% improvement of net indicated efficiency in CDA while 6-cylinder strategies increased this by a higher amount at 0.16%. The change of brake efficiency is around 0.01%, with even lower change than the net indicated efficiency. Since CDA mode was simulated with half the number of firing cylinders, a similar change of net IMEP resulted in lower increase of efficiency than the 6-cyl strategies. Meanwhile, comparison of TBC impact upon BMEP between the simulated strategies showed similar trends in brake efficiency.

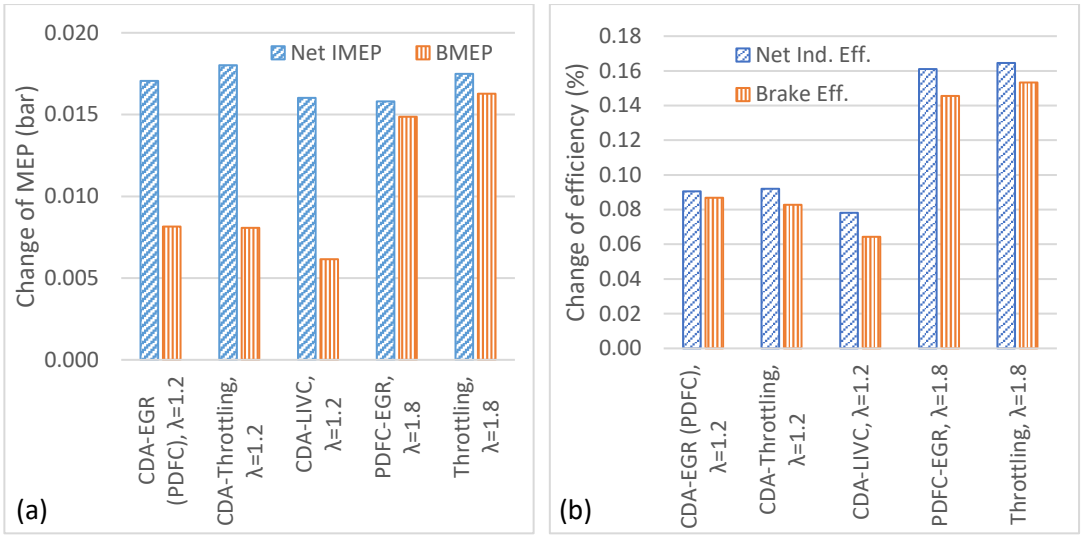


Figure 7.13. (a) Changes of net IMEP of cylinder 1 and BMEP, (b) Changes in net indicated efficiency and brake efficiency by TBC application in the simulated strategies at 1200 rpm/3 bar BMEP

Higher brake efficiency with TBC resulted in improvement in fuel economy as expressed in BSFC in diesel equivalent, shown in *Figure 7.14*. More significant reduction in BSFC was observed with the 6-cylinder strategy than CDA mode, where throttling improved it by 1.6 g_{diesel} /kWh. The least improvement in BSFC was produced by CDA-throttling, with 0.7 g_{diesel}/kWh BSFC reduction.

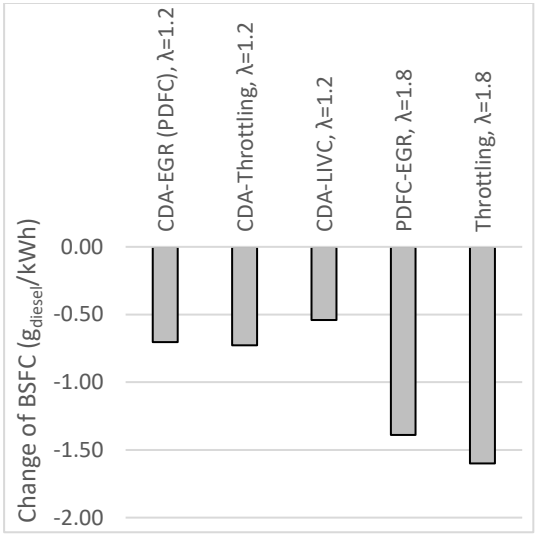


Figure 7.14. Impact of TBC to fuel economy at 1200 rpm/3 bar BMEP

7.4.6 Changes to Exhaust Gas Temperature by TBCs at 1200 rpm/3 bar BMEP

The increased EGT by application of TBC in the simulated CDA strategies at 3 bar BMEP is illustrated in *Figure 7.15*. The TBC model that was at lower intake trapped mass performed with slightly richer mixture and with increased EGT by 1.9°C. The richer mixture for CDA-LIVC

mode resulted in highest increase of EGT. Meanwhile, TBC in throttling mode just slightly increased EGT at 0.1°C. In general, the results indicate that TBC application in the simulated strategies at 1200 rpm/3 bar BMEP did not only improve the efficiency, but also increased the EGT albeit again small in impact.

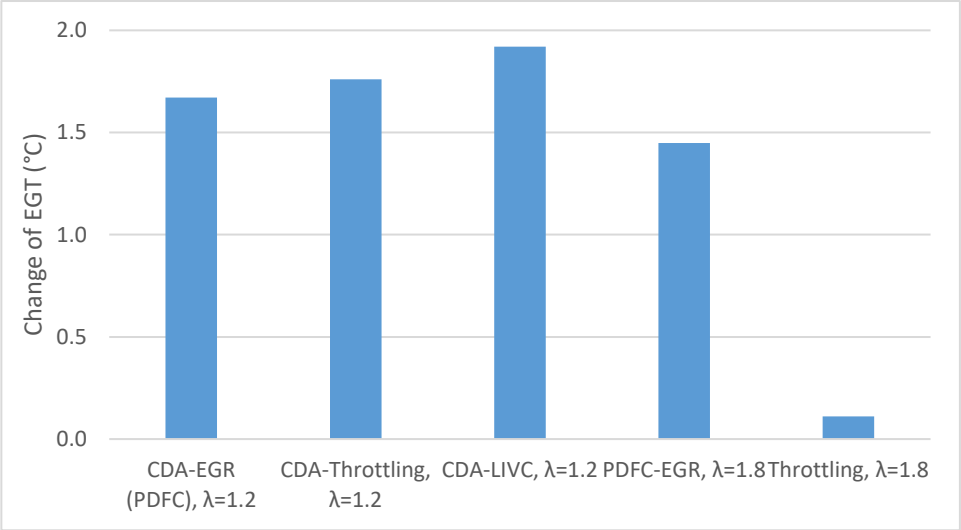


Figure 7.15. Changes of exhaust gas temperature by TBC application in the simulated strategies at 1200 rpm/3 bar BMEP

7.5 Summary

The application of TBCs to the simulated strategies was assessed as a method to reduce cylinder wall heat loss and improve efficiency. TBC application onto the piston crown and cylinder head surfaces was simulated in dual-fuel combustion with several strategies at 1200 rpm, for two load points at 6 and 3 bar BMEP. Apart from the modification on the cylinder head surface, all operating parameters such as fuel quantity, EGR percentage, throttle opening and IVC were set the same for TBC and the standard engine model. Thus, varying intake trapped mass as a consequence of TBC application was one of the observable variables. The impacts of TBC were compared to the standard model and the change of parameters presented as relative values.

TBC application caused varying effects upon the intake charge of the simulated strategies. In CDA strategy with eSupercharger, it increased the intake trapped mass and in turn increased the air/fuel ratio relative to the non-TBC model. Higher in-cylinder pressure during the end of compression improved ignition delay. However, a leaner mixture by TBC in CDA mode resulted in longer combustion duration, retarded combustion phasing and decreased exhaust gas temperature by 1.4 °C in CDA-Battery mode and by 1.7 °C for the CDA-Generator strategy. To the contrary, TBC in the 6-cylinder strategies decreased the intake charged mass,

performed at richer mixture operation and thus increased the EGT by 2 °C. Application of TBC to the simulated strategies (either in CDA or 6-cylinder strategies at 1200 rpm/ 6 bar BMEP λ=1.2) produced 0.8 to 1.2% improvement in cylinder wall heat loss. This contributed to increase in-cylinder pressure during combustion, increased brake efficiency by 0.11 % and improved fuel economy by 0.7 g_{diesel}/kWh.

From simulation at 3 bar BMEP, TBC application to the simulated strategies reduced intake trapped mass and reduced the air/fuel ratio. Due to reduced heat transfer during compression, it resulted in higher in-cylinder pressure and mean gas temperature hence improved ignition delay. These effects in combination with a richer mixture shortened the combustion duration and advanced the combustion phasing. For all strategies, TBC improved cylinder wall heat loss by 1.1% in CDA and by 1.2 % in 6-cylinder strategy. Another benefit of TBC was improvement in brake efficiency by 0.09 % for CDA and 0.16% for 6-cylinder strategy. Converted to fuel economy, TBC in CDA mode reduced the BSFC by 0.9 g_{diesel}/kWh while in 6-cyl throttling it improved BSFC by 1.6 g_{diesel}/kWh. With lower fuel consumption but improved heat loss and lower intake trapped mass, TBC produced 1.9 °C higher EGT in CDA mode. In the 6-cylinder modes, the application to PDFC-EGR operation increased EGT by 1.5 °C but only increased the EGT in throttling by 0.1 °C. In summary, in CDA where the standard model already resulted in EGT more than 400 °C, TBC increased it slightly further. In 6-cylinder strategies where the EGT by standard model were less than 380 °C, TBC did not increase it more than the catalyst light-off temperature although resulted benefit of improved fuel economy. Overall, it can be concluded that the application of such coatings within the combustion chamber had only a modest beneficial impact for part load dual-fuel enhancement (with the benefits well within normal daily variation effects due to changing fuel properties or ambient conditions). However, since this study only focused on low load, the results may not be representative for mid- and high-load operating conditions.

Chapter 8 Thermodynamic Modelling of Water Removal in Exhaust Gas of Dual-Fuel Combustion

8.1 Introduction

Water vapour is one of the main products of combustion. However, its presence within the exhaust can negatively influence the conversion ability of a methane oxidation catalyst by water adsorption, catalyst deactivation and shortens the catalyst's lifetime through sintering which is aided by water at high temperature. In addition, the obstructive effect by water resulted in the oxidation process becomes worse as the gas temperature gets lower at reaction temperature less than 500°C [126]. Back to discussion in Section 2.7, reducing the water vapour concentration from 10 to 1%vol. of the gas passing through the Pd/SnO_2 catalyst could reduce the catalyst light-off temperature (required temperature to result in 50% conversion - T_{50}) by ~60°C. Meanwhile, in Pd/Al_2O_3 catalyst the equivalent benefit rises to ~90°C. It is therefore apparent that innovation which can potentially reduce water content within the exhaust of a dual-fuel engine will enable further reductions in methane slip under low load, cooler exhaust conditions.

In this chapter, thermodynamic simulation results are presented from parametric studies of potential methods to instigate water vapour removal from the exhaust of a dual-fuel engine when operating on the cusp of methane oxidation catalyst light-off under conventional conditions (currently available best in class is a T_{50} of >380°C [124]). In the first sub-section details of the assumptions made on the exhaust gas constituents are presented. Corresponding calculations of variables related to humidity and gas properties such as specific heat and gas constants are described in full detail in Appendix A. This is followed by comparison of two competing methods to aid effective water removal without significant net temperature drop, namely the use of Phase Change Materials (PCMs) to act as a thermal battery versus the approach of adopting an Inverted Brayton cycle as a means of water removal during the cold portion of the cycle.

8.2 Experimental Data for The Thermodynamic Modelling

In order to simulate the art of the possible it was first necessary to obtain real engine test data where water removal would be viable. Set out in *Table 8.1* is a summary of such real engine data for a Volvo D13 operating under conventional dual-fuel operation. This data was produced on an industry standard test bed and used as a baseline in the prior PhD work by

May and Cairns [106] and therefore considered a viable baseline for this analysis (which was conducted ahead of the engine testing reported in this thesis).

Variables	Unit	1	2	3	4	5	6	7	8	9	10	11	12	13
Engine Speed	rpm	1203	1203	1518	1518	1204	1204	1203	1520	1520	1822	1821	1821	1821
Observed Torque	Nm	2071	2071	1093	1648	1063	1568	511	536	1892	1514	450	1261	896
Power	kW	261	261	174	262	134	198	64	85	301	289	86	240	171
Turbine Out Temperature	C	355	355	348	385	360	385	310	275	393	389	293	363	374
Turbine Out Pressure	kPa (abs.)	111	111	108	116	105	109	103	107	120	120	107	116	111

Table 8.1. The operating conditions and respective turbine outlet pressure and temperature at the 13 points steady state test by Clean Air Power

For the simulation work in this study, only the data from point 9 were used in the simulation with the details presented in *Table 8.2*. The point was selected since it has relatively high temperature (> 380°C) to promote an effective process within the MOC with expectation of acceptable lower temperature out of the IBC process while producing relatively high power from IBC process with the turbine out pressure at 120 kPa. The data was post-processed with the Carbon, Oxygen, Hydrogen, and Nitrogen balance calculation including the fuel consumption, λ, and humidity to produce the mass flowrate of each constituent as presented in *Table 8.2*. The H_2 was assumed to be zero due to lean mixture operation [138].

Parameter	Unit	Value
Engine Speed	rpm	1520
Observed Torque	Nm	1892
Observed Power Output	kW	301
Methane Conc. Wet	ppm	2657
Hydrocarbon Conc. Wet	ppm	3093
Carbon Monoxide Conc. Dry	ppm	0
Nitrogen Oxides Conc. Dry	ppm	26
Carbon Dioxide Conc. Dry	$\%_{vol.}$	8.40
Carbon Dioxide Intake Manifold	$\%_{vol.}$	8.32
Oxygen Conc. Dry	$\%_{vol.}$	7.17
Oxygen Conc. Intake Manifold	$\%_{vol.}$	18.58
Air Flow	g/s	398
Diesel Flow	g/s	3.85
CNG Flow	g/s	12.55
Exhaust Mass Flow	kg/min	24.8
CNG Usage	%	78.67
Turbine Out Temp	°C	393
Turbine Out Press	kPa (abs.)	120

Table 8.2. Selected data for simulation of exhaust gas water removal from dual-fuel operation

	CO_2	CO	NO_x	H_2	HC	CH_4	H_2O	O_2	N_2	Ar
Mass flowrate (g/s)	48.193	0	0.015	0	0.079	0.482	33.00	63.62	299.281	5.083

Table 8.3. Post-processed data of exhaust gas for simulation of water removal process

8.3 Cooling and Reheating with PCMs Heat Exchanger as a Thermal Battery

The water removal process was simulated by decreasing temperature of the exhaust gas to lower temperature than its dew point temperature. The maximum water content in exhaust gas at certain temperature and pressure is dictated by saturation humidity ratio. The details of humidity calculation are described in Appendix A and only to be discussed briefly in this section. During the cooling process, the thermal energy of the exhaust gas needed to be stored for the next reheating process. Therefore, the process required a heat exchanger that also worked as thermal battery. The thermal energy from high temperature exhaust gas was stored in the thermal battery during high loads and then later on added back to the exhaust stream when at partial loads. PCMs were selected as both the heat exchanger and thermal battery.

The PCM was assumed to work as a medium in the heat exchanger which at one side works to absorbs heat and another side reheats the exhaust gas. The PCMs were simulated to absorb thermal energy from higher temperature gas during its phase change process from solid to liquid. In the reverse direction, during the gas reheating process the PCMs reject heat to the colder gas and change phase from liquid to solid. The PCMs were assumed to work within its respective phase change process at constant melting temperature. To fulfil its function in the condensing process, multiple PCMs in a cascade configuration were used to simulate cooling and reheating process.

Diagram of the cascade PCMs Heat Exchanger (HE) is illustrated in *Figure 8.1* the selected PCMs are listed in *Table 8.4*. The PCMs with each melting temperature was selected not only for this simulation, but also considering the next simulation with IBC described in the next section.

The engine out exhaust gas was simulated to cools down through each of the PCM heat exchanger sequentially while the heat was stored for reheating process. The last HE selected

for the process depended on the simulated condensing temperature. For instance, the last HE to condense the gas at 40°C was PCM 14 with melting temperature (T_M) of 31°C, then the gas out of the HE (drawn in dash line) flew to the water separator.

The gas out of the water separator was reheated through the PCMs HE sequentially. The first HE for the reheating process was the one that worked at higher temperature than gas (Exhaust Gas Temperature (EGT)>gas temperature). For instance, the simulated condensing temperature of 40 °C was reheated firstly by PCM 13 at 50.6°C, hence drawn in dash line to PCM 13, skipping PCM 14, 15 and 16.

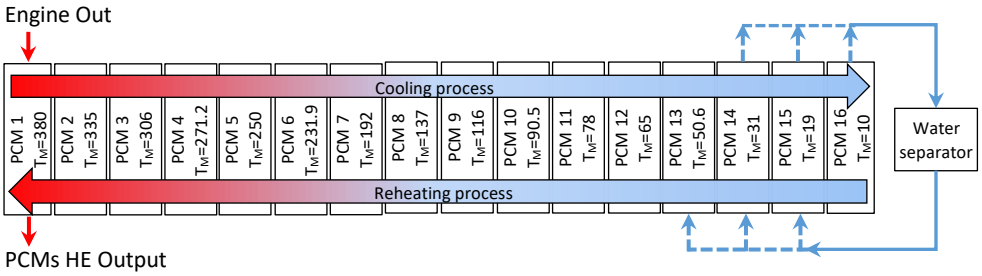


Figure 8.1. Exhaust gas water removal process with PCMs heat exchanger

PCM	Melting Temperature (°C)	Latent heat or Heat of fusion (kJ/kg)	Thermal conductivity (W/m.K)	Density (kg/m^3)
n-Pentadecane [171]	10	205	0.17	768
$K_2HO_4.4H_2O$ [171]	19	231	-	1447
$LiNO_3.2H_2O$ [171]	31	296	-	-
n-Tetracozane (C_{24}) [171]	50.6	255	-	799
$Na_3PO_4.12H_2O$ [171]	65	190	-	-
$Ba(OH)_2.8H_2O$ [171]	78	267	0.68	2070
$KAl(SO_4)_2.12H_2O$ [171]	90.5	183	-	-
MgCl2.6H2O [171]	116	165	-	-
$NaC_2H_3O_2.3H_2O$ [171]	137	172	-	1450
$AlCl_3$ [172]	192	280	-	-
Sn [173]	231.9	60.5	15.08	730
$LiNO_3$ [172]	250	370	-	-
Bi [173]	271.2	53.3	8.1	979
$NaNO_3$ [171]	306	172	0.5	2261
KNO3[171]	335	95	0.5	2109
KOH [171]	380	149.7	0.5	2044

Table 8.4. The selected phase change materials used in this simulation

8.3.1 Heat Transfer during the Cooling Process

The stored heat rate by heat transfer of gas to the PCM heat exchanger was calculated using Equation *(8.1)*. Heat exchanger effectiveness (ε_{HE}) was used in the calculation to define the

ratio of the heat transfer by the heat exchanger to the maximum theoretical heat transfer. This used the same term that was used in a paper by Liu et al. [174] as expressed in equation *(8.2)*. The specific heat of exhaust gas (c_p) was calculated at each step of cooling by using the temperature of PCM heat exchanger for calculation. The details of c_p approximation are described in Appendix A. The simulation of the cooling process with the selected PCM heat exchanger was assumed to result in the temperature out of the heat exchanger being equal to the temperature of the respective heat exchanger, except in the simulation of cooling process by the lowest PCM to achieve the targeted condensing temperature ($T_{condensing}$).

$$\dot{Q}_{stored} = \dot{m}.c_p.\left(T_{gas,in} - T_{HE}\right).\varepsilon_{HE} \qquad (8.1)$$

$$\varepsilon_{HE} = \frac{\left(T_{gas,in} - T_{gas,out}\right)}{\left(T_{gas,in} - T_{PCM}\right)} \qquad (8.2)$$

Where:

ε_{HE} : heat exchanger effectiveness

$\dot{Q}_{stored}$: heat transfer rate from hot gas as the heat stored in the PCM (W)

$\dot{m}$: exhaust gas mass flowrate (kg/s)

c_p : specific heat of exhaust gas (J/kg)

T_{gas} : temperature of working gas (°C)

$T_{condensing}$: targeted condensing temperature (°C)

The cooling process to the targeted condensing temperature was simulated in the PCM heat exchanger which was at lower temperature than the condensing temperature. The gas was simulated to exit the condenser at the targeted condensing temperature, hence the rate of stored heat ($\dot{Q}_{stored}$) to the last PCM heat exchanger was calculated using Equation *(8.3)*.

$$\dot{Q}_{stored} = \dot{m}.c_p.\left(T_{gas} - T_{condensing}\right).\varepsilon_{HE} \qquad (8.3)$$

8.3.2 Heat Transfer during the Reheating Process

In the simulation of the reheating process, the exhaust gas with reduced water content was simulated to enter the first heat exchanger which is at higher temperature than the condensing temperature. So, the heat exchanger with lower temperature than condensing temperature was skipped. The required heat rate for reheating the gas ($\dot{Q}_{reheat,required}$) to achieve the working temperature of corresponding PCM ($T_{PCM\,HE}$) was higher than theoretical required heat rate due to effectiveness less than 100%, as expressed by Equation (8.4).

$$\dot{Q}_{reheat,required} = \frac{\dot{m}.c_p.\left(T_{PCM\ HE} - T_{gas,in}\right)}{\varepsilon_{HE}} \quad (8.4)$$

The reheating power provided by PCM heat exchanger as indicated by stored heat rate ($\dot{Q}_{stored}$) calculated in the previous section should be higher than $\dot{Q}_{reheat,required}$. If the $\dot{Q}_{stored} \geq \dot{Q}_{reheat,required}$, the temperature of gas out of heat exchanger was equal to the PCM heat exchanger temperature ($T_{gas,out} = T_{PCM\ HE}$). If $\dot{Q}_{stored} > \dot{Q}_{reheat,required}$, then there was the surplus of heat rate ($\dot{Q}_{stored}$). Otherwise, if $\dot{Q}_{stored} < \dot{Q}_{reheat,required}$ the gas temperature out of heat exchanger was calculated by Equation *(8.5)*.

$$T_{gas,out} = T_{gas,in} + \frac{\dot{Q}_{stored}.\varepsilon_{HE}}{\dot{m}.c_p} \quad (8.5)$$

8.3.3 Simulated Parameters of the Direct Cooling and Reheating of Exhaust Gas with PCMs

The exhaust gas out of the engine turbocharger for this simulation was assumed to be at 120 kPa (Abs.) and 393°C as mentioned in *Table 8.2*. From the initial calculation of the exhaust gas, its dew point temperature was 48.4°C. Therefore, the process was simulated at the lower condensing temperature, between 10 to 40°C. In the condensing process, the gas was simulated to pass through each of required PCM heat exchanger sequentially to the targeted condensing temperature.

Several assumptions were made for the heat transfer calculation:

- The scope of simulation was limited to the thermodynamic simulation and the heat transfer process within the PCM heat exchanger was not detailed
- The heat transfer rate was assumed as steady in the cooling and reheating process
- The heating and cooling processes to bring and maintain the PCMs at target temperature were not covered in this simulation
- Pressure drop along the heat exchanger was neglected
- The simulations were run at 90% of charging and discharging effectiveness, slightly lower than 92% as reported by Liu et al. [174] considering possible more ineffectiveness in the process
- The lowest possible gas temperature out of respective heat exchanger was assumed as equal to temperature of heat exchanger (at phase change temperature of PCM)

- c_p as function of temperature was calculated by referring to the heat exchanger temperature
- Temperature of heat exchanger surface was equal to the phase change temperature of PCM. The heat exchanger temperature was constant and uniform throughout the heat exchanger section. However, the mechanism to control the PCMs heat exchanger temperature was not simulated in this study

8.3.4 Simulation Results of the Direct Cooling and Reheating of Exhaust Gas with PCMs

The impact of changing the condensing temperature to the final water content was illustrated in *Figure 8.3*. From 7.3%mass (or 11.7%vol.) of initial water content, condensing temperature sweep from 40 to 10°C resulted the remaining water content by 3.7 to 0.7%mass or 6.2 to 1.0%vol. The largest water removal was resulted by condensing the exhaust gas to 10°C, removing 6.7%$_{mass}$ or 10.7%$_{vol.}$ of water content. Looking back to Pd/SnO_2 shown in *Figure 2.16*, this would reduce T_{50} by ~60°C.

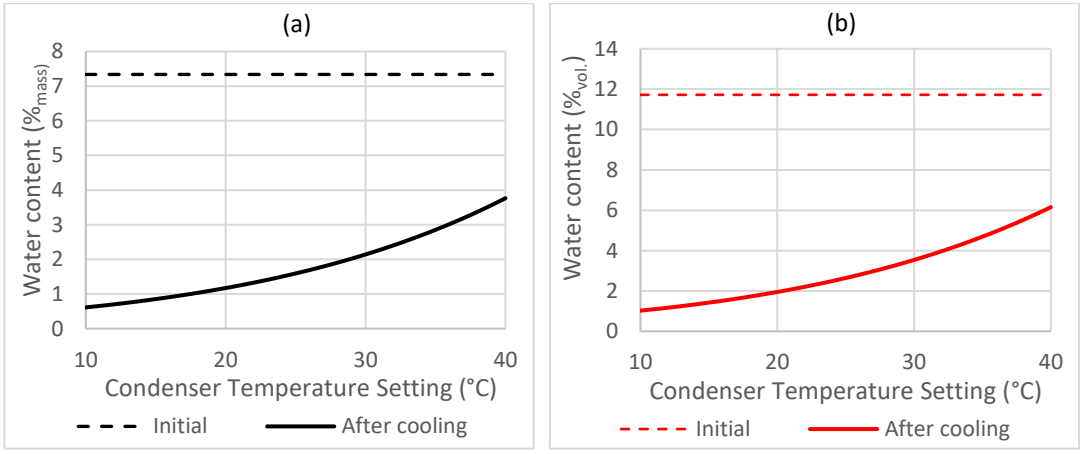


Figure 8.2. Impact of condenser temperature setting to the water content in expressed in %$_{mass}$ (a) and %$_{vol.}$ (b)

The final exhaust gas temperature at the outlet of the reheating heat exchanger at the swept condensing temperature is depicted in *Figure 8.3*. Reducing the condensing temperature from 40 to 10°C increased the final exhaust gas temperature by 11°C. It is important to note that the gas was simulated to be reheated by PCM heat exchanger at higher temperature than the simulated condensing temperature. For instance, in the simulation of 15°C condensing temperature, the gas was reheated firstly by 19°C PCM heat exchanger. The final exhaust gas temperature suggested that lower condensing temperature benefited the lower

mass. Therefore, with the similar stored heat by PCMs thermal battery for any simulated condensing temperature, the reheating process resulted in higher final temperature.

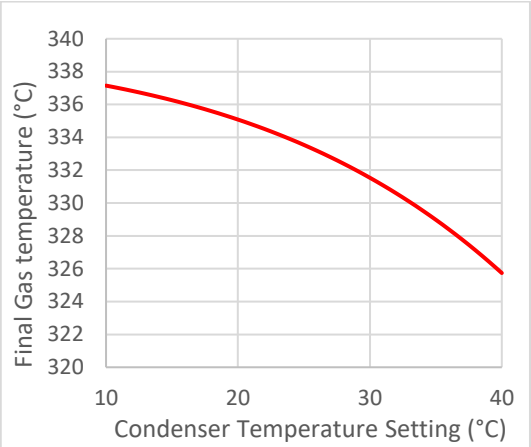


Figure 8.3. Impact of condensing temperature to the final exhaust gas temperature

8.4 Simulation of Water Removal Process with Inverted Brayton Cycle and PCM Thermal Battery

The simulation of the thermodynamic model was performed to assess the application of Inverted Brayton Cycle (IBC) with PCMs thermal battery (as heat exchanger) to remove water content in exhaust gas and generate power from the residual energy. The schematic diagram of IBC process and its temperature - entropy (T-s) diagram are illustrated in *Figure 8.4*. The exhaust gas out of turbocharger (at Point 1) was expanded by IBC turbine with specified expansion ratio (to Point 2) and generated work. Then the low-pressure gas at high temperature was cooled through the PCM thermal battery to the defined condensing temperature. As the turbine outlet temperature varied depended on the simulated expansion ratio, the first heat exchanger used for cooling and storing the heat was selected accordingly (hence the arrow to the HE is drawn in dash line). This means, the first HE should be lower than turbine out temperature. For example, if the turbine out temperature was 370°C, the gas was flown to PCM 2 at T_M =335°C, skipping PCM 1 that worked at T_M=380°C. During cooling and condensing process, the gas passed through the HE sequentially. The lowest PCM HE for condensing the gas was selected according to the simulated condensing temperature, hence the gas out of HE is illustrated in dash line.

The condensed gas from water separator then compressed to 1 atmosphere (atm). The required work to compress the gas was supplied by generated work from turbine or additional power out of the system if needed. Finally, the gas at atmospheric pressure (point 4) was reheated through the PCM heat exchangers. As the selected PCM HE depended on

the compressor out temperature (selected T_M> T4), the line to the corresponding PCM HE was drawn in dash. The gas was sequentially passed through the PCMs to be reheated. The last HE that was used for reheating the gas was the one that firstly absorbed heat from the gas out of turbine. Therefore, the gas flew out of the last HE (point 5) is also indicated in dash line.

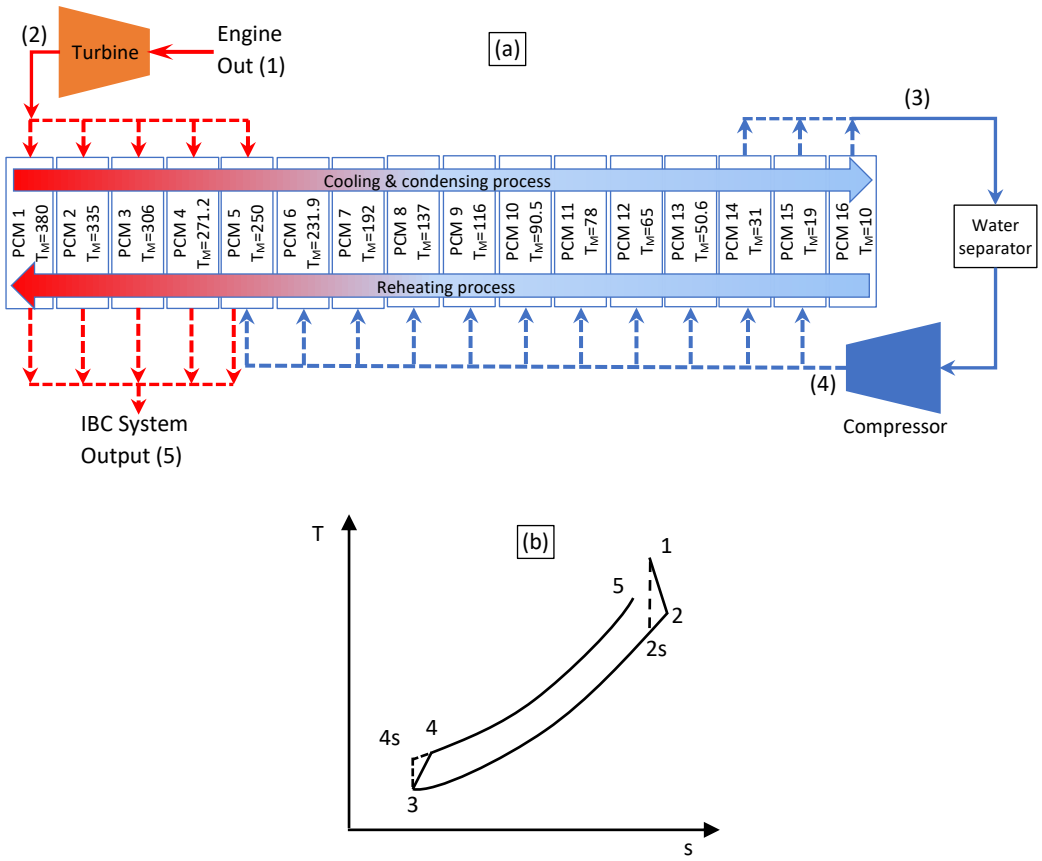


Figure 8.4. (a) Schematic diagram of IBC process, (b) T-s diagram of IBC process

8.4.1 Processes Calculation

Exhaust gas mass flowrate at each point before condensation ($\dot{m}_1$ and $\dot{m}_2$) and after condensation ($\dot{m}_3, \dot{m}_4, \dot{m}_5$) was calculated differently due to reduced water content and the NMHC was assumed to be fully condensed. Calculations for the processes occurring in the turbine and compressor are described here. Meanwhile, calculation of the cooling and reheating processes follows the same equations used in the previous section. Calculation of pressure and temperature of the simulated gas in the expansion and compression process is described in the following sub-section. The water content at each point was calculated accordingly.

8.4.1.1 Expansion process

The expansion ratio of turbine is the ratio of inlet to outlet gas pressure as expressed by Equation *(8.6)*. The non-isentropic gas pressure out of turbine was assumed as equal to the isentropic gas pressure out of turbine.

$$r_t = \frac{p_1}{p_{2s}} \tag{8.6}$$

By assuming isentropic expansion process and constant specific heat ratio, the turbine outlet temperature was calculated by Equation *(8.7)*.

$$T_{2s} = T_1 \left(\frac{p_{2s}}{p_1}\right)^{\frac{\gamma-1}{\gamma}} \tag{8.7}$$

Where γ is ratio of specific heats (c_p/c_v).

$$\frac{\gamma-1}{\gamma} = \frac{\left[\frac{c_p}{c_v} - 1\right]}{\frac{c_p}{c_v}} = \frac{c_p - c_v}{c_p}$$

As $c_p - c_v = R$

$$\frac{\gamma-1}{\gamma} = \frac{R}{c_p}$$

With the substitution above, T_{2s} could be expressed as Equation *(8.8)*.

$$T_{2s} = T_1 \left(\frac{p_{2s}}{p_1}\right)^{\frac{R}{c_p}} \tag{8.8}$$

Due to inefficiency, the gas temperature out of turbine is higher than the temperature of an isentropic process. Therefore, gas temperature out of turbine is expressed in Equation *(8.9)*, where T_1, T_2, T_{2s} are in K, involving turbine isentropic efficiency (η_t).

$$T_2 = T_1 - \eta_t \cdot (T_1 - T_{2s}) \tag{8.9}$$

The power generated by the turbine was calculated by:

$$\dot{W}_T = \dot{m}_1 \cdot c_p \cdot (T_1 - T_{2s}) \cdot \eta_t \tag{8.10}$$

8.4.1.2 Compression Process

Compression ratio is the ratio of gas outlet to inlet pressure as expressed in equation. The compressor outlet pressure by non-isentropic process (p_4) was assumed as equal to the isentropic process (p_{4s}).

$$r_c = \frac{p_{4s}}{p_3} \tag{8.11}$$

Meanwhile, the isentropic outlet temperature of compressor is expressed in Equation *(8.12)*.

$$T_{4s} = T_3 \left(\frac{p_{4s}}{p_3} \right)^{\frac{R}{c_p}} \quad (8.12)$$

Due to inefficiency in the compressor, the outlet temperature is higher than by the isentropic process, hence expressed as in Equation *(8.13)* with T_3, T_4, T_{4S} are in K, involving compressor isentropic efficiency (η_c).

$$T_4 = T_3 + \frac{(T_{4s} - T_3)}{\eta_c} \quad (8.13)$$

The required power by compressor to increase pressure from the cooling pressure to 1 atm was calculated by assuming constant Cp during an isentropic compression process. Due to inefficiency in the process, the required power is higher than that in an isentropic process, as expressed in Equation *(8.14)* with compressor isentropic efficiency (η_c) as the denominator.

$$\dot{W}_C = \dot{m}_3 \cdot c_{p3} \cdot \frac{(T_{4s} - T_3)}{\eta_c} \quad (8.14)$$

8.4.1.3 Simulation Parameter and Assumptions

The simulation was performed with an expansion ratio sweep from 1.2 to 3.0 with increments of 0.1 and condensing temperature from 10 to 40°C with increments of 5°C. Several assumptions made for the simulation were:

- The processes in the IBC were assumed as steady state
- In the calculation of process in the turbine and compressor, c_p was calculated from temperature of inlet condition and assumed as constant. c_p as function of temperature was calculated by including mass fraction of each exhaust gas constituent. Calculation of exhaust gas constant (R) considered mole number of exhaust gas at initial condition and after cooling process
- The pressure loss along the heat exchanger passage was neglected
- The turbine and compressor were assumed to work at 70% efficiency for all of the simulated points
- The same assumptions of the relevant process in the PCMs heat exchanger described in the previous section were also applied in this simulation works

8.4.2 Results and Discussion of Water Removal with IBC

The turbine outlet pressure during the sweep of expansion ratio is illustrated in *Figure 8.5*(a). Considering the outlet temperature illustrated in *Figure 8.5*(a), the selected first PCM thermal battery was the one that works at lower temperature. For illustration purposes, the highest temperature out of the turbine was 371°C that was produced by an expansion ratio of 1.2, the first heat exchanger that absorbs heat from the exhaust gas was T_M=335°C PCM thermal battery. At the simulated higher expansion ratio, as the turbine outlet temperature decreased, the next lower PCM heat exchanger was selected to absorb heat from the exhaust gas. Therefore, between an expansion ratio of 1.7 to 2.2, the first PCM to receive heat from gas was PCM 306°C. Meanwhile, between 2.3 to 3 of expansion ratio, PCM 271°C was the first selected heat exchanger. As the turbine outlet pressure was lowered by increasing expansion ratio, the saturation humidity ratio was expected to be higher as discussed in Appendix A and illustrated in *Figure A.2*. Therefore, the simulation at the same condensing temperature but at lower pressure due to higher expansion ratio resulted in reduced water removal. As a consequence, higher exhaust mass flowrate through compressor increased the gas back to 1 atm resulting in higher compressor outlet temperature as illustrated in *Figure 8.5*(b).

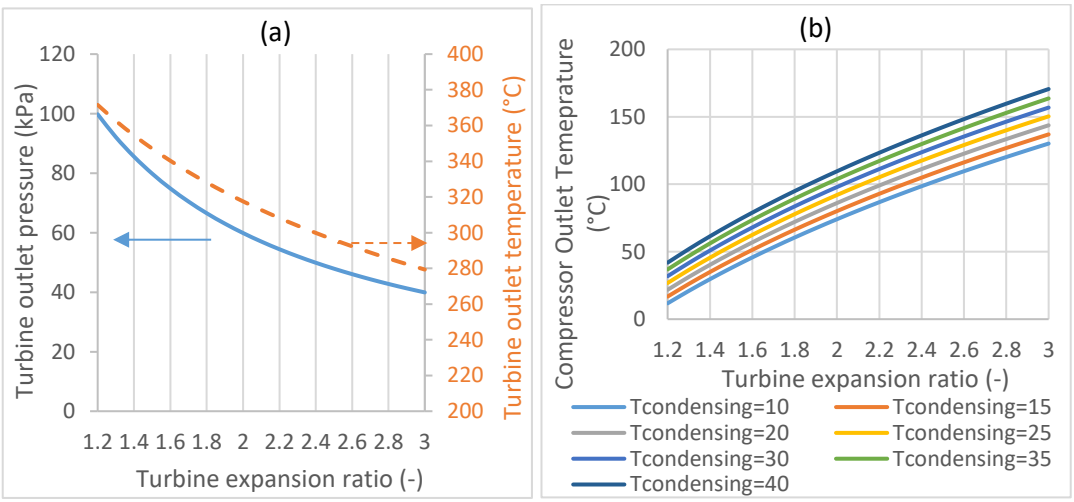


Figure 8.5. (a) IBC turbine outlet pressure and temperature and (b) Compressor outlet temperature at the simulated conditions

The remaining water vapour content in exhaust gas at the outlet of the IBC reheater by the simulated conditions are plotted in *Figure 8.6*. At the same condensing temperature, increasing the expansion ratio resulted in higher water vapour content. In the other words, higher expansion ratio was a less effective way to reduce water vapour in the exhaust gas. The higher expansion ratio resulted in lower gas pressure at the turbine outlet and hence

lower dew point temperature. The trend of deteriorated performance of IBC in removing water vapour content in exhaust gas with increasing expansion ratio was more significant at higher condensing temperature. This is expected as illustrated by the impact of total pressure to the saturation humidity ratio in *Figure A.2* in Appendix A. Therefore, the simulation of IBC with 35 and 40°C condensing temperature only removed water content at an expansion ratio up to 2.5 and 1.9 respectively. The lowest remaining water content by the simulated conditions in the IBC process was produced at 10°C as much as 0.74%$_{mass}$ at an expansion ratio of 1.2 up to 1.86 %$_{mass}$ at an expansion ratio of 3.0. The expression of water remained in the gas in %volume is presented in *Figure 8.7*. From 11.7%$_{vol.}$ of initial water content, the remaining water at expansion ratio of 1.2 was 1.2 %$_{vol.}$, increasing at higher expansion ratio up to 3.1%$_{vol.}$ at expansion ratio of 3.

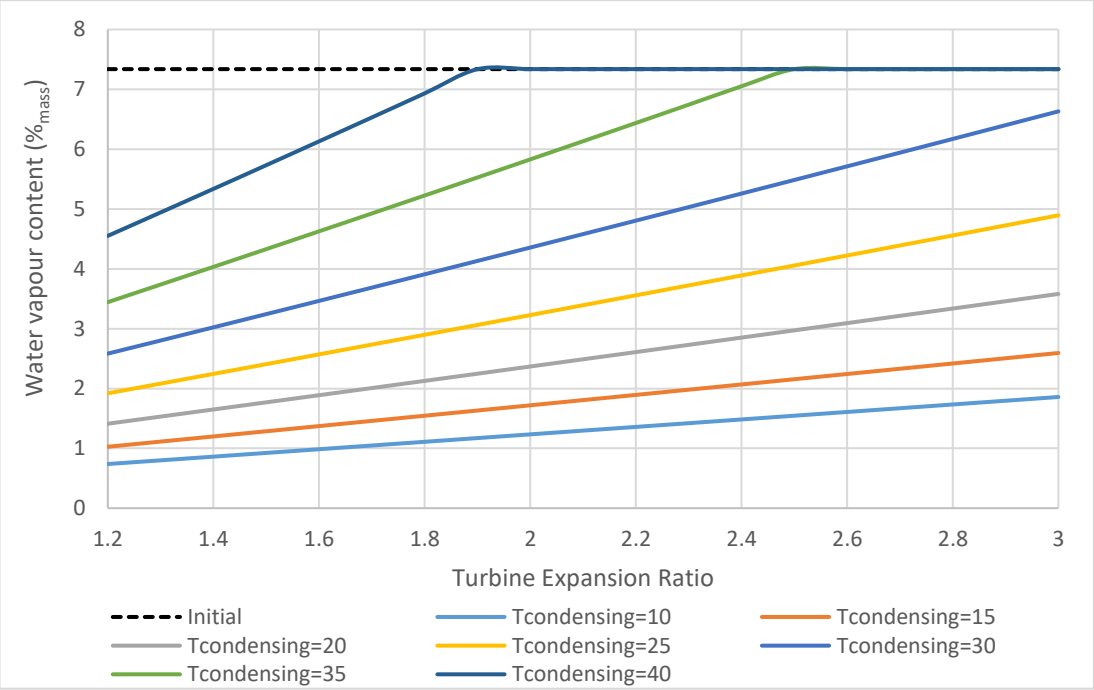


Figure 8.6. Final water content out of IBC process by simulation at different condensing temperature (in °C) with expansion ratio sweep

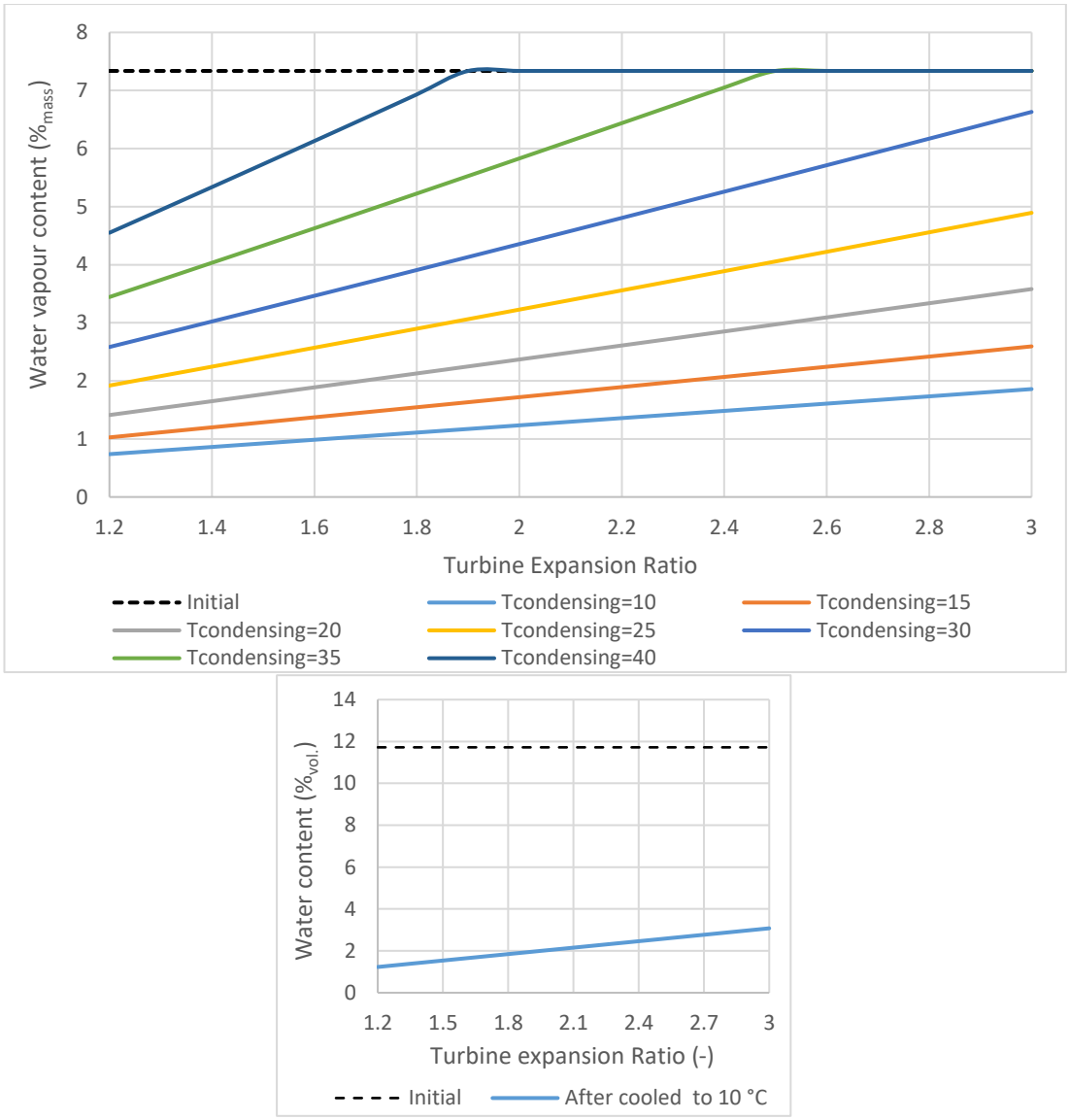


Figure 8.7. Water content remained in the exhaust gas after cooled to 10°C at expansion ratio sweep

The temperature of exhaust gas out of IBC process with the simulated condensing temperatures and swept expansion ratio is shown in *Figure 8.8*. It is apparent that increasing the expansion ratio up to 2.4 decreased the gas temperature out of the IBC system. The IBC process with lower condensing temperature resulted in higher final gas temperature. The highest outlet temperature of the IBC is 305°C with a 10°C condensing temperature and expansion ratio of 1.2.

In the simulation at the same expansion ratio, the PCM stored thermal energy for the reheating process was at the same rate despite the simulated condensing temperature varying. However, the simulation at a lower condensing temperature resulted in lower water content and hence lower mass. Therefore, the same reheated power that was rejected from PCM heat exchanger during reheating process resulted in higher outlet gas temperature for

the lower condensing temperature. Meanwhile, the simulation at the same condensing temperature with increasing expansion ratio resulted in lower temperature out of the IBC due to higher water content in the exhaust gas. Hence, the same heat power in reheating process resulted in lower outlet temperature.

However, the trend of decreasing outlet temperature by increasing expansion ratio changed at further increase of expansion ratio. For instance, simulation at 40°C condensing temperature increased the outlet temperature from expansion ratio 2.5 up to 2.8 and decreased again at higher expansion ratio. The similar trend was shown by lower the condensing temperature that changed the trend at different expansion ratio. This phenomenon could be related to the compressor outlet temperature as shown in *Figure 8.5*(b), where the increasing expansion ratio required higher compression ratio to increase the pressure of the cooled gas at point 3 to point 4, thus increasing the gas temperature at the compressor outlet for all of the simulated condensing temperatures. For the range of expansion ratio with changing trend, the higher simulated condensing temperature indicated higher compressor outlet temperature. With higher mass of gas after condensation (due to less removed water vapour), the same compression ratio at higher condensing temperature resulted higher compressor outlet temperature. Therefore, the same absorbed heat from the PCM thermal battery resulted in higher final temperature than the lower condensing temperature. Then during the reheating process, the same heat power from the PCM thermal battery (by the same expansion ratio) increased the exhaust gas temperature of higher condensing temperature more significantly despite higher mass than by the lower condensing temperature. However, the thermal energy stored by PCM is reduced at further increase of expansion ratio due to lower turbine outlet temperature as well as the lower PCM heat exchanger that absorbed the heat and reheat the gas. Therefore, the final temperature reached its optimum for the respective condensing temperature then decreasing at further higher expansion ratio.

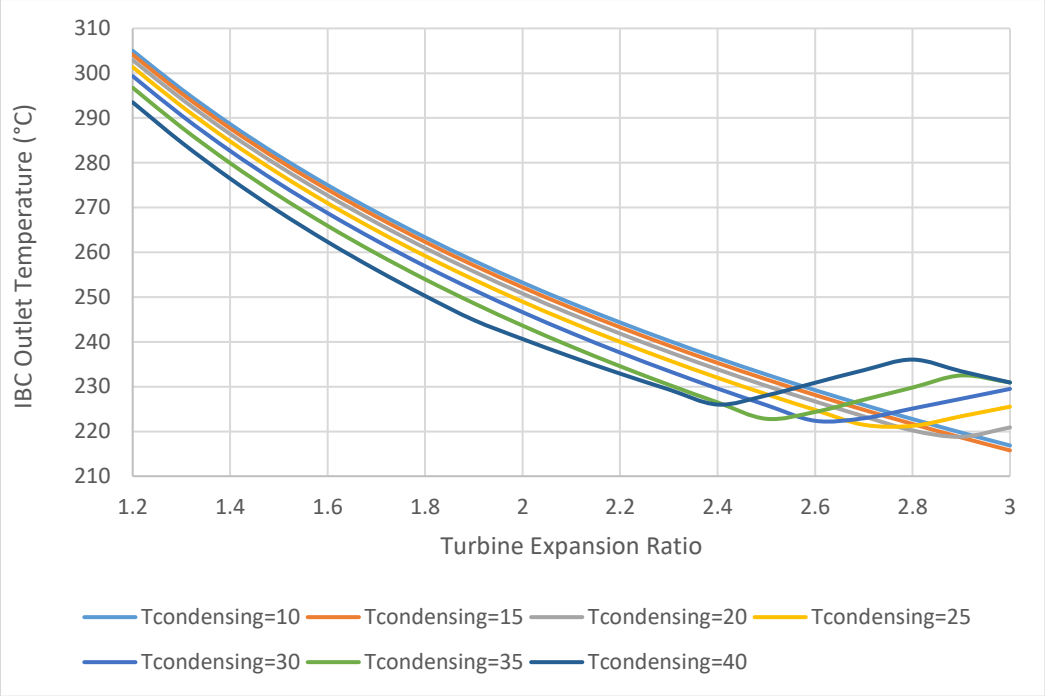


Figure 8.8. IBC final temperature at the simulated condensing temperature with expansion ratio sweep

The net power produced by IBC at the simulated condensing temperature and expansion ratio sweep is shown in *Figure 8.9*. Despite the net power by simulations at different condensing temperature at expansion ratio 1.2 look similar, the net power by lower condensing temperature was actually higher than the net power produced by the higher condensing temperature. The trend of higher net power by lower condensing temperature became more noticeable at higher expansion ratio. The simulation at the same condensing temperature with increasing expansion ratio produces higher net power then decreased after certain expansion ratio, indicated its optimum condition for the respective condensing temperature. The simulation at 10°C condensing temperature produced 12.07 kW maximum net power at expansion ratio 1.7. With 301 kW of the engine power, it equalled to 4% of additional benefit to the engine power. Meanwhile, the simulation at higher condensing temperature produced lower maximum net power at lower expansion ratio.

Since the gas was expanded prior to the condensing process, the power generated by the turbine at the same expansion ratio for all simulated condensing temperatures were the same. However, the saturation humidity ratio increases at lower pressure, thus less water was removed from the exhaust gas during a cooling process at higher expansion ratio (reduced turbine outlet pressure). In turn, the compressor required more power to increase the pressure of higher mass flowrate of exhaust gas back to 1 atm. In terms of the required power for compressing the gas, the condensing process at higher pressure and lower

condenser outlet temperature were beneficial conditions for removing water content from the working gas.

The negative net power produced as shown in *Figure 8.9* indicated larger power consumed by the compressor than the one generated by the turbine, which means it became parasitic to the engine operation. As the expansion ratio and the condensing temperature determined the net power produced, the point where the IBC process became no longer beneficial at different expansion ratio depended on the condensing temperature. The simulation results at condensing temperature 10 to 25 indicated that the net power was produced positively at the swept expansion ratio between 1.2 to 3.0.

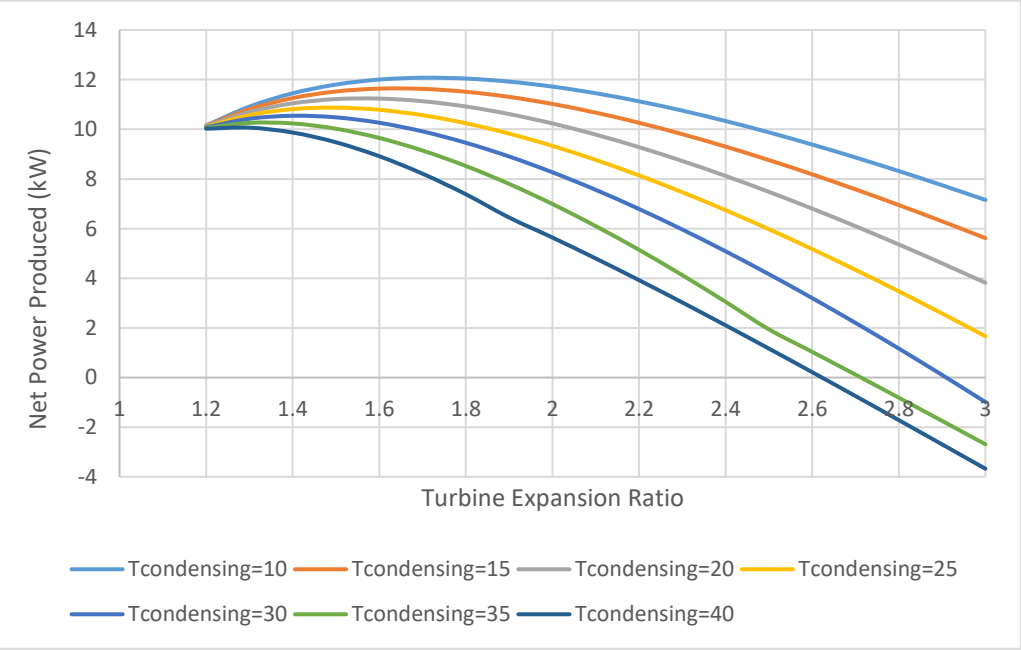


Figure 8.9. Net power produced (kW) by IBC at simulated condensing temperature with expansion ratio sweep

8.5 Summary

Removing water content in the exhaust gas is a strategy that could increase the effectiveness of a methane oxidation catalyst for the aftertreatment of exhaust gas from dual-fuel combustion in compression ignition engines. This study proposed two processes of exhaust gas water removal: i) direct cooling and reheating processes via a PCM matrix thermal battery and ii) inverted Brayton cycle with PCM thermal battery to produce the net power from the residual energy within the exhaust gas. The simulation was performed using basic thermodynamic models to get the result of both strategies for the exhaust gas with 7.34 % mass of water content at 393°C and 1.20 kPa (absolute) of the turbocharger outlet temperature and pressure.

The direct cooling and reheating processes with a PCM heat exchanger in a cascade configuration was simulated at condensing temperature ranges from 10 to 40°C at the specified heat exchanger effectiveness of 90%. This resulted in water vapour removal of 6.7%$_{mass}$ or 10.6%$_{vol.}$ and a final temperature by 337°C with a 10°C condensing temperature. The simulation at higher condensing temperature resulted in lower temperature due to less water content removal.

Meanwhile, the removal process of water vapour content with IBC produced net power depending on the simulated condition. Despite IBC process producing power that could improve the engine's brake efficiency, in its utilisation the removed water content needs to be compromised. If the highest final temperature at the outlet of IBC system is chosen as priority, the simulated condition resulted in highest outlet temperature of 305°C by 10°C of condensing temperature at expansion ratio of 1.2. On the other hand, the simulated conditions resulted maximum net power 12.07 kW by 10°C condensing temperature at expansion ratio of 1.7 with 6.29 %$_{mass}$ or 10.8%$_{vol.}$ of removed water content and 269°C of gas temperature at the IBC outlet.

Overall, the largest reduction of water vapour content by 10.7%$_{vol.}$ resulted by direct cooling and reheating process potentially provide the benefit of reduced Pd/SnO_2 catalyst light-off temperature (T_{50}) by ~60°C.

Chapter 9 Conclusions and Recommendations for Future Work

9.1 Conclusions

Decarbonisation of the heavy-duty transport sector could be implemented by utilising lower carbon fuel in an internal combustion engine (ICE) as a mature technology, electrification, or using an alternative powertrain (such as a fuel cell). Battery electric heavy duty vehicles reliant upon lithium ion incur excessive powertrain weight, that reduces the payload and is not an immediate favourable solution for long range transportation. Despite fuel cells potentially resulting in zero tank-to-wheel GHG emission in the long term, current hydrogen production which is dominated by steam methane reforming from fossil-based natural gas with otherwise higher GHG emission. Natural gas with methane as main constituent that has a higher H/C ratio, can help reduce CO_2 emissions. In addition, biomethane as a renewable version of natural gas could significantly impact upon net-zero GHG emissions targets set by government. Therefore, this study focused upon natural gas utilisation in the ICE, which is expected to be an immediate solution for decarbonising the HDV sector.

Port injection of natural gas for dual-fuel operation in a compression ignition engine is a dual-fuel option that has the possibility to revert back to fully functioning diesel operation. The low load operating range is a challenging operating condition for dual-fuel mode due to the lean mixture and low in-cylinder temperature. On the other hand, unburned methane emissions are also a concerning problem that must be curtailed. Therefore, an innovative method is required to promote oxidation within a methane oxidation catalyst as a final solution to minimise associated tail-pipe emissions. Both improving low-load combustion performance and promoting processes within MOC are topics of interest in this study to mitigate the methane slip from dual-fuel operation in the CI engine.

Several methods to improve dual-fuel combustion performance at low load were evaluated in this study. This included testing of an alternative pilot fuel to improve combustion performance and reduce emissions. The potential of performance improvement by cylinder deactivation (by deactivating both fuel injection and valve actuation as per recent light duty applications) was quantified through simulation work using a new GT-Power phenomenological model of dual-fuel combustion for a 6-cylinder heavy duty engine. Implementation of new Thermal Barrier Coatings (TBC) as a heat loss reduction strategy was also simulated in the same model to assess potential improvement in engine performance, fuel economy and emissions. In final work, thermodynamic modelling was used to simulate highly novel exhaust gas water removal processes to promote the oxidation process within

a methane oxidation catalyst (MOC). The key conclusions of all of these experimental and parametric modelling are presented by sub-section below.

9.1.1 CDC with Diesel or GTL and PDFC with Diesel or GTL as A Pilot Fuel

The experimental tests in a light duty engine were conducted under conventional diesel combustion (CDC) with ultra-low sulphur diesel (diesel) and Gas-to-Liquid diesel fuel (GTL) at 1200 rpm, 5.3 bar BMEP. The engine was run at 60 and 100 MPa rail pressure with injection timing sweeps undertaken, where the interval between SOI of pilot and main injection was 10 °CA. The following key conclusions were made during CDC operation:

- GTL generally resulted in better combustion quality than diesel, as indicated by lower THC at the same injection timing and reduced CO at most injection timings. Therefore, GTL resulted in slightly higher combustion efficiency than diesel (between 0.04 to 0.37 %)
- GTL resulted in lower brake efficiency by 1.3% although at the latest injection timing with SOI_{Main}=15 °CA ATDC it resulted in higher brake efficiency than diesel by 0.47%. Shorter ignition delay by GTL improved both combustion and brake efficiency with such late injection timing
- HRR analysis indicated that GTL performed with shorter ignition delay, with reduced premixed combustion and longer combustion duration than diesel. On the other hand, the longer ignition delay of diesel resulted in faster combustion due to higher heat release during premixed main combustion
- From the comparison of NOx emissions at 60 MPa rail pressure, GTL at all swept injection timings produced lower NO_x (by up to 5.1 %). However, GTL with 100 MPa rail pressure resulted in similar NO_x as diesel, except with SOI_{Main}=15 °CA ATDC where GTL resulted in lower NO_x by 34%
- At the same injection timing and rail pressure, GTL produced lower soot than diesel by up to 55% (in FSN value)
- A typical NO_x-soot trade-off was produced by changing rail pressure either in CDC with GTL or diesel, where lower rail pressure improved NO_x but deteriorated filter smoke number. On the other hand, despite both fuels exhibiting NO_x improvement with retarded injection timing at both 60 and 100 MPa rail pressure, retarding injection timing did not always deteriorate filter smoke number. At 60 MPa rail pressure, retarding SOI_{Main} by up to 5 °CA ATDC deteriorated filter smoke number,

albeit SOI_{Main}=15 °CA ATDC resulted in improvement. Meanwhile, soot emissions for either GTL or diesel at 100 MPa rail pressure was less sensitive to injection timing, with the highest FSN produced at SOI_{Main}=0 °CA ATDC

- Lower soot generation with GTL can probably be attributed to its lower sulphur content, lower aromatic content and/or larger portion of combustion with a less rich mixture as indicated by a reduced premixed portion of the main combustion from the HRR analysis. In addition, the longer combustion duration could provide longer duration for soot oxidation
- Lower aromatic content probably also contributed to lower NO_x emissions with GTL. On the other hand, the calculated gas mean temperature with GTL was higher than diesel because of higher fuel energy for a corresponding operating condition. Hence the reduced NO_x values occurred despite less favourable temperature conditions
- GTL produced higher EGTs, increased by 5 °C compared to diesel at the earliest injection timing. At the latest injection timing the trend reversed with EGT value 20°C lower than diesel. The EGT with SOI_{Main} at TDC and 5 °CA ATDC were similar

Diesel or GTL was used as pilot fuel in premixed dual-fuel combustion (PDFC) tests at 1200 rpm/5.3 bar BMEP at 58% (±2) gas substitution ratio. From the test results, the following conclusions were made:

- GTL-PDFC GTL resulted in higher combustion efficiency by 3.2% and increased brake efficiency by 0.8%.
- GTL-PDFC resulted in lower exhaust gas emissions than diesel-PDFC in all measured constituents. It resulted in THC improvement by 34% and CO by 40%. GTL-PDFC also reduced NO_x by 18% and FSN by 42%.
- Utilisation of GTL as a pilot fuel in PDFC improved ignition delay and improved combustion stability, although with longer combustion duration than diesel
- GTL slightly increased EGT by ~1°C at 40 and 50 °CA pilot separation but ~6°C lower EGT at 60 °CA pilot separation

9.1.2 Dual-Fuel Simulation with Cylinder Deactivation

This study evaluated the cylinder deactivation strategy through phenomenological modelling in GT Power commercial software. In the application of CDA, the fuel injection and valve actuation of three out of six cylinders are deactivated by implementing a minimum trapped

mass deactivation strategy after the last exhaust valve closing event. The simulation was run at 1200 rpm at 6 and 3 bar BMEP as representation of low load operation in a HDV compression ignition engine. Dual-fuel combustion was simulated at 90% substitution ratio of fuel energy.

At 6 bar BMEP, conventional operation (6-cylinder) was simulated with PDFC-EGR, throttling and Miller-LIVC as λ controlling methods, while CDA strategy was simulated with eSupercharger that was simulated to be powered with either a Battery (CDA-Battery) or a crank-driven generator (CDA-Generator). Conclusions from the simulation results can be drawn as follows:

- The CDA strategy performed with roughly double the Net IMEP in the firing cylinders. For instance, with the 6-cyl strategy running at ~7.2 bar Net IMEP, CDA-Battery mode operated with 14.4 bar Net IMEP, while CDA-Generator mode operated with 14.8 to 17.4 Net IMEP (from λ=1.0 to λ=1.8) because of the power required to drive the eSupercharger motor.
- As CDA strategy doubles the individual cylinder load, trapping higher mass which in turn resulted in higher compression pressure and temperature. This promoted shorter ignition delay and improved flame propagation with shorter combustion duration
- The CDA strategy with eSupercharger as boosting device and leaner mixtures provides a pumping benefit. Therefore, CDA performed with higher net indicated efficiency than the 6-cylinder strategy at most simulated points, except for PDFC-EGR mode at λ=1.0. As the pumping benefit increased with leaner mixture, the net indicated efficiency of CDA got higher. CDA-Generator mode incurred the highest net indicated efficiency since it benefits from pumping higher than CDA-Battery to perform at higher net IMEP. Amongst 6-cyl operations, throttling suffered higher pumping loss as the throttle opening gets smaller to simulate the less lean mixture, resulting in the lowest net indicated efficiency up to λ=1.4
- The brake efficiency by CDA-Battery mode was highest amongst the simulated strategies, increasing from 35.6% at λ=1.0 up to 39.6% at λ=1.8. This improvement was attributed to battery utilisation in driving the eSupercharger, pumping benefits and improved combustion performance. Meanwhile, CDA-Generator reaches 35.69% maximum brake efficiency at λ=1.4 then decreased with leaner mixtures as the parasitic loss to generate power for motor of eSupercharger got higher and

exceeded the benefit from higher net indicated efficiency. Between the 6-cylinder strategies, brake efficiency for PDFC-EGR mode up to λ=1.4 was between 35.56% to 36.17%, the highest of those simulated at 6 bar BMEP (which is also higher than CDA-Generator). Throttling that suffered the highest pumping loss performed with lowest brake efficiency up to λ=1.4, while Miller-LIVC that improved the pumping loss performed with higher brake efficiency

- Although the firing cylinder in CDA modes performed with higher mean gas temperature due to increased fuel quantity, halving the number of firing cylinders in CDA reduced heat transfer surface area. CDA-Battery reduced heat loss by ~21% and CDA-Generator by ~22% compared to throttling as a strategy that suffered the highest heat loss. Compared to PDFC-EGR mode, which suffered the least heat loss, CDA Battery mode reduced by 0.4% to 19%, while heat loss in CDA-Battery mode was 1.4% higher at λ=1.0 but lower with leaner mixtures by 12.75% at λ=1.6

- Higher mean gas temperature and lower engine heat loss in CDA simulation resulted in higher exhaust gas temperature (as mass-averaged). CDA at λ=1.0 resulted in higher exhaust gas temperature by 48°C compared to throttling, which resulted in the highest EGT amongst the 6-cyl strategies. Meanwhile, compared to PDFC-EGR mode at λ=1.0 as the most efficient strategy among 6-cyl simulation, CDA resulted in 178°C higher EGT

- As simulation with CDA at a less lean mixture accelerated the combustion, it resulted in higher PRR where the highest value at λ=1.0 was still at an acceptable level for the engine noise (less than 10 bar/°CA set as a threshold in this study)

- Amongst the 6-cyl strategies, PDFC-EGR mode up to λ=1.4 resulted in the highest brake efficiency, but lowest exhaust gas temperature as a consequence of lowest fuel consumption. Therefore, if hardware complexity related to valve actuation becomes a constraint for realising the CDA strategy, PDFC-EGR can be chosen as fuel efficient strategy to run dual-fuel operation with compromised exhaust gas temperature

This study also simulated dual-fuel operation at 1200 rpm/3 bar BMEP, which is a challenging operating point due to very low load conditions where the methods of air/fuel mixture control to run the engine at less lean mixture have particular consequences. The 6-cylinder strategies were simulated at λ=1.8 with several intake control methods. Less lean mixture was considered as not feasible due to excessively low intake manifold temperature by

throttling or very high EGR fraction in PDFC-EGR mode. A combination of throttling-EGR-CDF and throttling-EGR-PDFC were simulated as alternatives to improve the pumping loss and reduce EGR. At this operating point, Miller-LIVC mode was not a feasible option in 6-cylinder simulation as the retarded LIVC resulted in too low compression ratio to sustain the pilot diesel auto-ignition. At 3 bar BMEP, dual-fuel with a less lean mixture was simulated under CDA strategy with CDF or PDFC without any intake restriction (at the leanest mixture) and several intake control methods to sweep the λ: CDA-EGR(PDFC), CDA-Throttling and CDA-LIVC. The following conclusions can be drawn from the simulation results:

- To produce the same BMEP, the firing cylinders in 6-cyl strategies run at ~4.1 bar Net IMEP, while CDA must run the remaining firing cylinder at 8.1 to 8.3 of Net IMEP.
- The engine benefited from lower pumping losses during CDA operating strategies when compared to the 6-cylinder strategies. This enabled less lean mixture operation to improve combustion performance by implementing EGR, throttling, or LIVC to control the intake charge. For instance, to simulate λ=1.0, CDA-LIVC was run at a dynamic compression ratio of 9.7, CDA-Throttling was simulated with average of intake manifold pressure at 0.8 barA, and CDA-EGR(PDFC) utilised 28% of EGR
- The lowest fuel consumption was performed by CDA-CDF mode with a leaner mixture without intake restriction, which improved fuel consumption by 12.5%, equivalent to 4% higher brake efficiency compared to 6-cylinder throttling operation
- CDA-EGR(PDFC) mode improved fuel economy by 8% relative to PDFC-EGR as the lowest fuel consumption for the 6-cyl strategies. As a strategy that performed at lowest fuel consumption at λ=1.0, CDA-EGR(PDFC) mode produced EGT at 66°C higher than 6-cyl Throttling, with 3.3% higher brake efficiency or 10.4 % improvement in fuel economy (in diesel equivalent). CDA-Throttling at λ=1.0 resulted in 165°C higher EGT than 6-cyl Throttling at λ=1.8, that was achieved with 1.5% higher brake efficiency or 4.4 % improvement in fuel economy
- CDA-EGR(PDFC) from λ=1.4 to λ=1.0 performed with lower heat loss by 6.3 to 9.8% than the 6-cyl strategies with PDFC-EGR mode. CDA-Throttling and CDA-LIVC at λ=1.4 also performed at lower heat loss than PDFC-EGR. However, at lower λ the heat loss worsened due to higher mean gas temperature as fuel consumption increased
- In comparing the simulated strategies at λ=1.0 under CDA modes, CDA-Throttling suffered the largest pumping loss, highest fuel consumption, highest engine heat loss and yet resulted in highest EGT. CDA-LIVC performed with lowest pumping loss,

longest ignition delay, less engine heat loss and lower EGT than CDA-Throttling. CDA-EGR(PDFC) mode performed at lower pumping loss than CDA-Throttling (but larger than CDA-LIVC), lowest fuel consumption, lowest heat loss and lowest EGT

- The simulated CDA strategy produced 415°C lowest EGT, while 6-cyl strategies produced highest EGT at 377°C
- Improvement in fuel economy, heat loss reduction and increased EGT became encouraging factors to implement CDA as an innovative strategy at 1200 rpm/3 bar BMEP to extend the limit of dual-fuel under typically urban operating conditions

9.1.3 Thermal Barrier Coating (TBC) Strategy in Dual-Fuel Combustion

Further improvement of dual-fuel combustion at low load was simulated with application of TBC on the surface of the piston and cylinder head to reduce the cylinder wall heat loss. At 6 bar BMEP, TBC reduced engine heat loss between 0.8% to 1.2%. TBC in the simulated CDA strategies with eSupercharger increased the intake air quantity that increased the air/fuel ratio. This caused leaner mixture combustion that decreased EGT by 1.7°C. From the simulation results with 6-cylinder strategies, TBC reduced the trapped air mass that resulted in higher EGT by 2°C. TBC marginally increased brake efficiency by 0.11% or equivalent to an improvement in fuel economy of 0.7 g_{diesel}/kWh.

At 3 bar BMEP, TBC with CDA strategies reduced cylinder wall heat loss by 1.1%. Its implementation in 6-cyl strategies reduced heat loss by 1.25%. Implementation of TBC in the simulated strategies at 3 bar BMEP increased brake efficiency in CDA mode by 0.09% (improvement of 0.7 g_{diesel}/kWh in BSFC), while in 6-cyl strategies by 0.16% (equivalent to 1.6 g_{diesel}/kWh reduction in BSFC). As TBC reduced the intake trapped air mass, combustion at richer mixture combined with reduced heat loss resulted in higher EGT by 1.5°C in the 6-cyl strategy and 1.9°C in the CDA strategy. While TBC increased EGT of the simulated strategies at 3 bar BMEP, the marginal increase did not result in higher EGT than the catalyst light-off temperature (380°C).

9.1.4 Exhaust Gas Water Removal Process

Removing water content in the exhaust gas can increase the efficiency of the methane oxidation process within a MOC by changing the catalyst's light off temperature (T_{50}). Two methods of water removal process were simulated via basic thermodynamic modelling: i) direct cooling and reheating via a PCM heat exchanger and ii) the Inverted Brayton cycle (IBC) process with PCMs as a heat exchanger.

Direct cooling and reheating via the PCMs heat exchanger at 10°C of condensing temperature reduced water content from 7.3%$_{mass}$ (or 11.7 %$_{vol.}$) to 0.6%$_{mass}$ (or 1.0%$_{vol.}$) and resulted in a final temperature at 337°C. The reduction in water content can reduce T_{50} of Pd/SnO_2 catalyst by ~60°C.

The water removal process with IBC was simulated with condensing temperature sweep from 10 to 40°C (in 5°C increments) and an expansion ratio sweep from 1.2 to 3.0. The lowest water vapour content in the final outlet of the IBC system was produced with 10°C condensing temperature, from 0.7%$_{mass}$ (or 1.2%$_{vol.}$) at expansion ratio 1.2 up to 1.9 %$_{mass}$ (or 3.1%$_{vol.}$) at an expansion ratio of 3. It produced 304°C for a maximum IBC outlet temperature with expansion ratio 1.2 with 10 kW of net power generated. The IBC system at this simulation condition resulted in the highest net power among the simulated condensing temperature, with a maximum 12.07 kW at an expansion ratio of 0.7, which produced a final gas temperature at 269°C. Although it produced lower maximum outlet temperature than the direct cooling and reheating process, the IBC process generated power by 4% of the engine brake power.

Overall, the work has indicated that CDA is a highly effective strategy for improving low load dual-fuel performance, with promising results obtained indicating a future IC engine utilising GTL pilot fuel and biogas may be a highly sustainable option to explore in future work. The TBCs were relatively ineffective at the light load conditions examined but may offer other benefits across the wider speed/load map. The water removal concept is relatively novel and potentially offers promise in future stationary power generation and/or dual-fuel marine engine applications.

9.2 Recommendations for Future Work

GTL with higher cetane number and LHV than diesel could provide more flexibility in the pilot injection strategy. If diesel utilisation as pilot fuel suffers longer ignition delay in dual-fuel combustion under less lean mixture as reported in previous studies [7], the sensitivity of GTL to the mixture strength in dual-fuel operation needs to be investigated further.

The potential of GTL fuel to improve dual-fuel combustion needs to be explored further in wider operating conditions in real heavy duty engines. Future studies can be conducted with optimisation of the first and second pilot injection such as in quantity ratio, combustion phasing and substitution ratio. In addition, as a synthetic fuel which can be produced from different feedstocks, future potential of Biomass-to-Liquid (BTL) as a candidate for a pilot

fuel in dual-fuel using biomethane should be investigated to realise the net-zero carbon emission targets.

The simulation of dual-fuel combustion with normal operation or cylinder deactivation can be improved by additional works such as:

- Validation of EGR flow by various intake and exhaust manifold pressures
- Despite the usage of injection profile from GT Power library considered to produce low level of error as it is in low quantity, using the measured injection profile as input for future simulation works can increase the prediction accuracy
- Blowby simulation to examine the effect of pumping work to the deactivated cylinder
- Calibration could also improve accuracy in prediction of several parameters such as: blowby, heat transfer, friction and EGR characteristics
- Improving capability to model crevice volume contribution to the unburned methane

There are several aspects of CDA operation which were not covered in this study. The potential of CDA strategy can be explored further by investigating its impact on the engine thermal load and the engine structure. As the cylinder fires with longer intervals than 6-cylinder firing, its impact upon noise, vibration and harshness needs to be assessed, where this topic has not yet been investigated. Simulation of a hybrid of compression ignition engine and a battery electric vehicle that runs in dual-fuel combustion and electrification at idle and very low load (<3 bar BMEP) would also be highly relevant.

The combustion modelling work was performed using standard burning velocity correlations without any combination of diesel and natural gas, which needs to be taken into account in future modelling. The flow filed in the engine will also impact upon the multipliers. This study assumed same set of combustion multipliers between the standard and TBC model. This was applied considering similar pattern of heat release rate of diesel combustion with standard and TBC model as shown by Wakisaka et al. [168]. A calibration of combustion multipliers using experimental results would improve prediction accuracy.

The basic modelling performed in this study is considered as preliminary study that evaluated the relative potential of the water removal process upon the exhaust gas during dual-fuel combustion. More detailed simulation of heat exchanger performance should be undertaken including heat absorption and rejection within the thermal battery material. Last but not

least, the CDA strategy should be implemented in a real engine and evaluated across the full speed load map, including cold start operation.

Appendix A Formulae for Calculating Humidity and Exhaust Gas Properties

In this appendix, the formulae for calculating humidity and gas properties for simulation of exhaust gas water removal process are described. The water vapour content in a gas mixture has a strong relationship with the temperature and pressure. Decreasing the temperature below dew point temperature reduces the water vapour content. If the temperature is decreased to the dew point temperature at its pressure, the water vapour condenses to the humidity ratio at saturation that is expressed in kilogram of water vapour per kilogram of dry air ($kg_{water}/kg_{dry\ air}$). In other words, the water vapour does not condense unless the temperature of gas mix at certain pressure below the dew point temperature. If the gas pressure kept constant during cooling down process to decrease temperature lower than dew point temperature, the water condenses, hence humidity ratio decreases. The dew point calculation, humidity ratio, and the other relevant parameters are described in this section. The formulae used in this appendix refer to several literatures [1–3] with adaptation for exhaust gas instead of atmospheric air.

A.1 Water Vapour Pressure and Water Vapour Pressure at Saturation

According to Dalton law, water vapour partial pressure (p_w) can be calculated from the multiplication of mole fraction of water in exhaust gas and pressure of gas mix. Alternatively, if the humidity ratio and gas pressure are known, p_w can be calculated from Equation *(A.1)* [175]. Humidity ratio (W_{humid}) is water vapour mass per unit of dry gas mixture.

$$p_w = (pW_{humid})/(r_{M_{H2O}/M_{gas}} + W_{humid}) \qquad (A.1)$$

Where:

p : gas pressure

W_{humid} : humidity ratio (in $kg_{water}/kg_{dry\ gas}$)

$r_{M_{H2O}/M_{gas}}$: mole ratio of water to dry exhaust gas ($M_{H2O}/M_{dry\ gas}$)

Saturation pressure of water vapour at certain temperature is calculated by Equation *(A.2*) according to Wagner et al. [177] for the temperature range between 0 to 373°C. The calculated saturation pressure of water (p_{ws}) at the range between 0 to 100°C is illustrated in *Figure A.1*.

$$\ln\left[\frac{p_{ws}}{p_c}\right] = \frac{T_c}{T}(C_1\vartheta + C_2\vartheta^{1.5} + C_3\vartheta^3 + C_4\vartheta^{3.5} + C_4\vartheta^4 + C_6\vartheta^{7.5}) \qquad (A.2)$$

$$\vartheta = 1 - \frac{T}{T_c}$$

As

$$\ln\left[\frac{p_{ws}}{p_c}\right] = \ln p_{ws} - \ln p_c$$

$$\ln p_{ws} = \ln p_c + \frac{T_c}{T}(C_1\vartheta + C_2\vartheta^{1.5} + C_3\vartheta^3 + C_4\vartheta^{3.5} + C_4\vartheta^4 + C_6\vartheta^{7.5})$$

Hence,

$$p_{ws} = e^{\left[\ln p_c + \frac{T_c}{T}(C_1\vartheta + C_2\vartheta^{1.5} + C_3\vartheta^3 + C_4\vartheta^{3.5} + C_4\vartheta^4 + C_6\vartheta^{7.5})\right]} \quad (A.3)$$

Where:

e : Euler number (2.71828)

T : Temperature in K

p_{ws} : saturation pressure of water vapour (hPa)

T_c : Critical temperature, 647.096 K

p_c : Critical pressure, 220640 hPa

C_i : Coefficient, where $C_1 = -7.85951783$, $C_2 = 1.84408259$, $C_3 = -11.7866497$, $C_4 = 22.6807411$, $C_5 = -15.9618719$, $C_6 = 1.80122502$

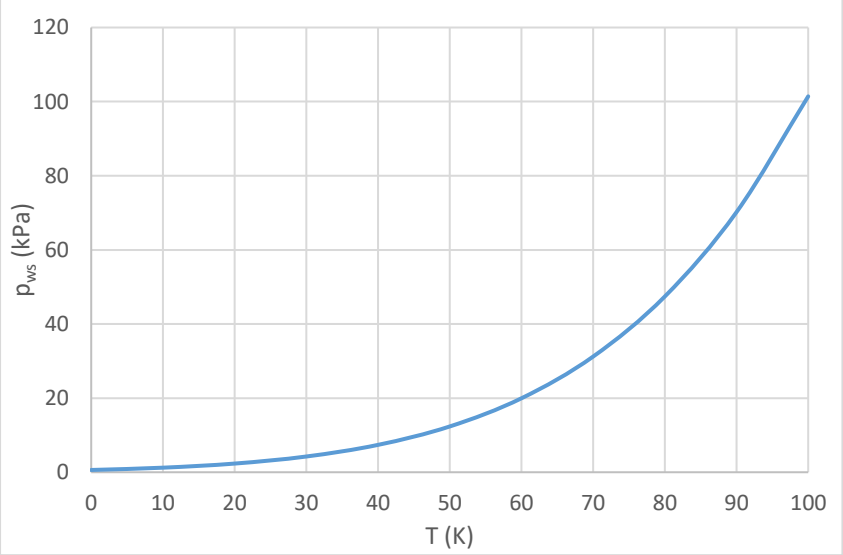


Figure A.1. Saturation pressure of water at temperature between 0 to 100°C

A.2 Saturation Humidity Ratio

The saturation humidity ratio ($W_{saturation}$) is the maximum water content in exhaust gas at certain pressure and temperature as expressed by Equation *(A.4)*, adapted from Ref. [175].

$$W_{saturation} = r_{M_{H2O}/M_{gas}} \times \frac{p_{ws}}{p - p_{ws}} \quad (A.4)$$

Where:

$W_{saturation}$: saturation humidity ratio ($kg_{water}/kg_{Dry\ Gas}$)

p_{ws} : saturation pressure of water vapour (kPa)

p : total pressure of gas mixture (kPa)

Gas pressure and temperature determine the maximum water content in a gas mixture. As illustration, the saturation humidity ratio at total pressure of air (as an example of gas mixture) at 20 and 30°C with pressure range between 10 to 100 kPa(abs.) are shown in *Figure A.2*. It is noticeable that reducing pressure at the constant temperature results in higher saturation humidity ratio. In addition, higher temperature at the same pressure increases the saturation humidity ratio.

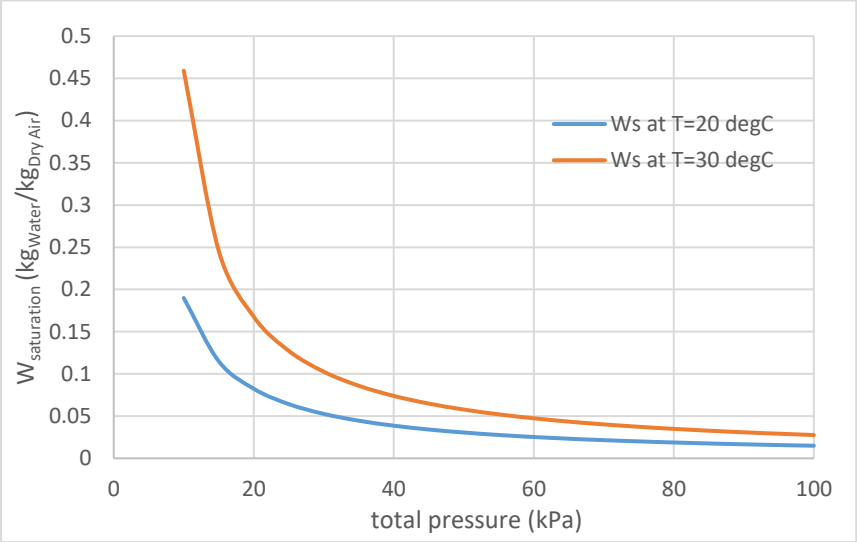


Figure A.2. Saturation humidity ratio ($W_{saturation}$ in $kg_{Water}/kg_{Dry\ Air}$) at 20 and 30 °C between 10 to 100 kPa of total pressure

If the saturation humidity ratio at the specified temperature and pressure after condensing process is higher than humidity ratio of exhaust gas, the water content in the exhaust gas does not condense. Therefore, the gas needs to be cooled down to temperature with lower than humidity ratio of gas mix. The temperature where saturation humidity ratio of gas at certain pressure is equal to the humidity ratio of gas mix is called as dew point temperature which is described in the following section.

A.3 Dew Point temperature

Dew point temperature is the temperature at which the water content in the gas mix at certain pressure starts to condense. Dew point temperature (T_d) in °C can be calculated using Equation *(A.5*) [176].

$$T_d = \frac{T_n}{\left[\frac{m}{\log_{10}\left(\frac{p_w}{A}\right)} - 1\right]} \quad (A.5)$$

Where:

T_d= dew point temperature in °C

p_w = water vapour partial pressure in hPa

A, m, T_n are defined in *Table A.1*.

Temperature Range (°C)	A	m	T_n
-20 to 50	6.116441	7.591386	240.7263
50 to 100	6.004918	7.337936	229.3975
100 to 150	5.856548	7.27731	225.1033
150 to 200	6.002859	7.290361	227.1704
200 to 350	9.980622	7.388931	263.1239

Table A.1. A, m, T_n for the respective range of temperature [176]

A.4 Specific Heat (Cp) and Constant (R) of Gas Mix

Specific heat (Cp) of each species (i) for thermodynamic modeling is calculated using Equation *(A.6*) and the value of each coefficients for each gas are described in the *Table A.2*. Meanwhile, cp and R of Argon are constant at 0.5203 and 0.20813 kJ/kg.K. R and $a_{i,n}$ are presented in the *Table A.2* that is valid for 300 to 1000 K.

$$\frac{c_{p,i}}{R} = a_{i1} + a_{i2}T + a_{i3}T^2 + a_{i4}T^3 + a_{i5}T^4 \quad (A.6)$$

Where:

c_p : Heat capacity (J/mol.K)

T : Temperature (K)

Gas	R	a_{i1}	a_{i2}	a_{i3}	a_{i4}	a_{i5}
CO	0.296829	3.7101	- 0.16191* 10^{-2}	0.36924*10^{-5}	-0.2032*10^{-8}	0.23953*10^{-12}
CO_2	0.188919	2.4008	0.8735* 10^{-2}	-0.66071*10^{-5}	0.20022*10^{-8}	0.63274*10^{-15}
H_2	4.1244	3.0574	0.26765* 10^{-2}	-0.58099*10^{-5}	0.5521*10^{-8}	-0.18123*10^{-12}
H_2O	0.46151	4.0701	-0.11084* 10^{-2}	0.41521*10^{-5}	-0.29637*10^{-8}	0.80702*10^{-12}
O_2	0.25983	3.6256	-0.18782* 10^{-2}	0.70555*10^{-5}	-0.67635*10^{-8}	0.21556*10^{-11}
N_2	0.2968	3.6748	-0.12082 * 10^{-2}	0.2324 *10^{-5}	-0.63218 *10^{-9}	-0.22577 *10^{-12}
CH_4	0.51826	3.826	-0.3979 * 10^{-2}	2.4558 *10^{-5}	-22.733 *10^{-9}	0.6963 *10^{-11}

Table A.2. R and coefficients a used for cp calculation of selected gases [45,178]

The gas constant (R) is calculated from the universal gas constant ($\tilde{R}$=8.3143 J/mol.K) divided by molar mass of gas as expressed in Equation *(A.7*).

$$R = \tilde{R}/M_{gas} \quad (A.7)$$

Cp of NO_x is calculated with Equation *(A.8)*[179] by assume it as NO, where $t = \mathrm{T(K)}/1000$

$$c_p = 23.83491 + 12.58878t - 1.139011t^2 - 1.497459t^3 + 0.214194/t^2 \quad (A.8)$$

In the simulation, the c_p of Non-Methane Hydrocarbon (NMHC) is approximated by c_p of hexadecane, which is calculated by Equation *(A.9)* [180].

$$c_{p,hexadecane} = 66.9822 + 184.951\left[\frac{(1616.65/\mathrm{T})}{\sinh(1616.65/\mathrm{T})}\right]^2 + 142.19\left[\frac{(777.742/\mathrm{T})}{\cosh(777.742/\mathrm{T})}\right]^2 \quad (A.9)$$

Illustrated in *Figure A.3*, the influence of temperature to Cp of selected gas in kJ/kg.K.

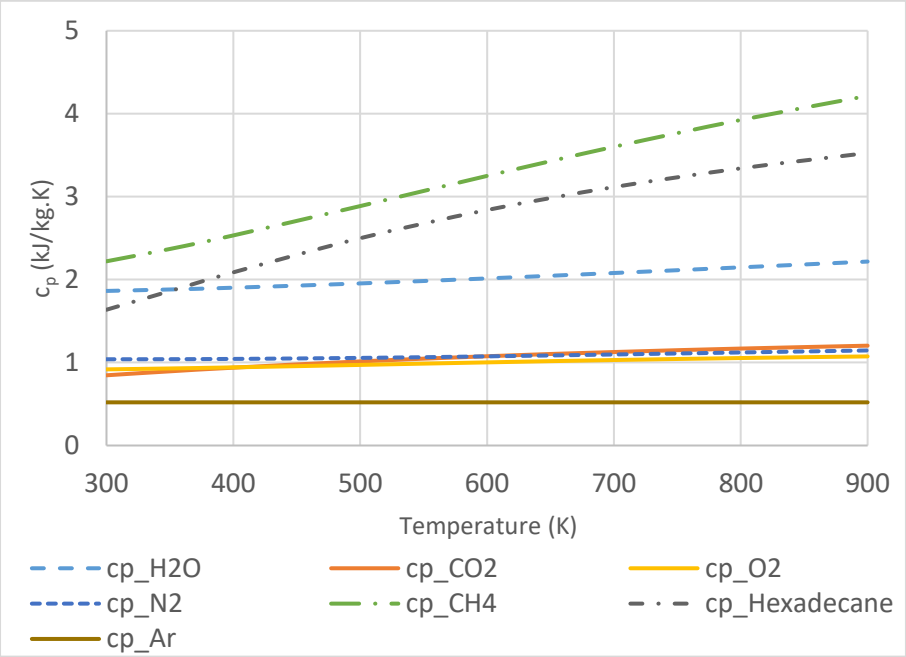


Figure A.3. c_p of gas species at temperature

c_p of a gas mixture ($c_{p,gas\ mix}$) is the sum of multiplication of gas mass fraction ($mass\ fraction_{gas,i}$) and its c_p ($c_{p\ gas,i}$) as expressed in Equation *(A.10)*. The gas constant ($R_{gas\ mix}$) is calculated in a similar way as shown in Equation *(A.11)*.

$$c_{p,gas\ mix} = \sum(c_{p\ gas,i}.mass\ fraction_{gas,i}) \quad (A.10)$$

$$R_{gas\ mix} = \sum(R_{gas,i}.mass\ fraction_{gas,i}) \quad (A.11)$$

References

[1] E. and I.S. Department for Business, 2018 UK greenhouse gas emissions: final figures - data tables, (2020). https://assets.publishing.service.gov.uk/government/uploads/system/uploads/attachment_data/file/875508/final-greenhouse-gas-emissions-tables-2018.xlsx.

[2] The European Parliament and the Council of the European Union, Regulation (EU) 2019/1242 of the European Parliament and of the Council of 20 June 2019 Setting CO2 emission performance standards for new heavy-duty vehicles and amending Regulations (EC) No 595/2009 and (EU) 2018/956 of the European Parliament, 2019. https://eur-lex.europa.eu/eli/reg/2019/1242/oj.

[3] European Commission, Climate Action - Reducing CO2 emissions from Heavy-Duty Vehicles, (2015). https://ec.europa.eu/clima/policies/transport/vehicles/heavy_en#tab-0-0 (accessed October 5, 2018).

[4] Science and Technology Committee - House of Common, Clean Growth: Technologies for meeting the UK's emissions reduction targets, n.d. https://publications.parliament.uk/pa/cm201719/cmselect/cmsctech/1454/145402.htm.

[5] A. Smallbone, B. Jia, P. Atkins, A.P. Roskilly, The impact of disruptive powertrain technologies on energy consumption and carbon dioxide emissions from heavy-duty vehicles, Energy Convers. Manag. X. 6 (2020) 100030. https://doi.org/10.1016/j.ecmx.2020.100030.

[6] R. Sacchi, C. Bauer, B.L. Cox, Does Size Matter? The Influence of Size, Load Factor, Range Autonomy, and Application Type on the Life Cycle Assessment of Current and Future Medium? The Heavy-Duty Vehicles, Environ. Sci. Technol. 55 (2021) 5224–5235. https://doi.org/10.1021/acs.est.0c07773.

[7] S. Schlatter, B. Schneider, Y. Wright, K. Boulouchos, Experimental Study of Ignition and Combustion Characteristics of a Diesel Pilot Spray in a Lean Premixed Methane/Air Charge using a Rapid Compression Expansion Machine, in: SAE 2012 World Congr. Exhib., SAE International, 2012. https://doi.org/https://doi.org/10.4271/2012-01-0825.

[8] G.A. Karim, Dual-Fuel Diesel Engines, 1st ed., CRC Press, Boca Raton, 2015.

[9] British Petroleum, Statistical Review of World Energy - all data, 2021, (2021). https://www.bp.com/content/dam/bp/business-sites/en/global/corporate/xlsx/energy-economics/statistical-review/bp-stats-review-2022-all-data.xlsx.

[10] US Department of Energy, Clean Cities Alternative Fuel Price Report, 2022. https://afdc.energy.gov/files/u/publication/alternative_fuel_price_report_april_2020.pdf.

[11] Michela Cappannelli, C. McGlade, P. Zeniewski, P. Le Feuvre, T. Gould, Outlook for biogas and biomethane: Prospects for organic growth, IEA, 2020. https://iea.blob.core.windows.net/assets/03aeb10c-c38c-4d10-bcec-de92e9ab815f/Outlook_for_biogas_and_biomethane.pdf.

[12] CENEX, Dedicated to Gas: An Innovate UK Research Project to Assess the Viability of Gas Vehicles, 2019. https://www.cenex.co.uk/app/uploads/2019/11/324-003-004-Dedicated-to-Gas-Assessing-the-Viability-of-Gas-Vehicles.pdf.

[13] H. Schlick, Potentials and challenges of gas and dual-fuel engines for marine applications, in: 5th CIMAC CASCADES, Busan, 2014. https://www.cimac.com/cms/upload/events/cascades/cascades_2014_busan/presentations/Presentation_Session2_AVL_CASCADES_Busan_Oct2014_Harald_Schlick.pdf (accessed January 12, 2019).

[14] R.G. Papagiannakis, D.T. Hountalas, Combustion and exhaust emission characteristics of a dual fuel compression ignition engine operated with pilot diesel fuel and natural gas, Energy Convers. Manag. 45 (2004) 2971–2987. https://doi.org/10.1016/j.enconman.2004.01.013.

[15] T. Korakianitis, A.M. Namasivayam, R.J. Crookes, Natural-gas fueled spark-ignition (SI) and compression-ignition (CI) engine performance and emissions, Prog. Energy Combust. Sci. 37 (2011) 89–112. https://doi.org/10.1016/j.pecs.2010.04.002.

[16] A. Cozzolini, D. Littera, R. Ryskamp, J. Smallwood, M. Besch, M. Velardi, H. Kappanna, D. Carder, M. Gautam, Characteristics of Exhaust Emissions from a Heavy-Duty Diesel Engine Retrofitted to Operate in Methane/Diesel Dual-Fuel Mode, (2013). https://doi.org/https://doi.org/10.4271/2013-24-0181.

[17] S. Di Iorio, A. Magno, E. Mancaruso, B.M. Vaglieco, Performance, Gaseous and Particle Emissions of a Small Compression Ignition Engine Operating in Diesel/Methane Dual Fuel Mode, in: SAE 2016 World Congr. Exhib., SAE International, 2016. https://doi.org/https://doi.org/10.4271/2016-01-0771.

[18] A. Sarkar, U.K. Saha, Role of global fuel-air equivalence ratio and preheating on the behaviour of a biogas driven dual fuel diesel engine, Fuel. 232 (2018) 743–754. https://doi.org/10.1016/j.fuel.2018.06.016.

[19] F. Königsson, J. Kuyper, P. Stalhammar, H.-E. Angstrom, The Influence of Crevices on Hydrocarbon Emissions from a Diesel-Methane Dual Fuel Engine, SAE Int. J. Engines. 6 (2013) 2013-01–0848. https://doi.org/10.4271/2013-01-0848.

[20] M.S. and R.V.D. Forster, P., V. Ramaswamy, P. Artaxo, T. Berntsen, R. Betts, D.W. Fahey, J. Haywood, J. Lean, D.C. Lowe, G. Myhre, J. Nganga, R. Prinn, G. Raga, Changes in Atmospheric Constituents and in Radiative Forcing, in: Clim. Chang. 2007 Phys. Sci. Basis. Contrib. Work. Gr. I to Fourth Assess. Rep. Intergov. Panel Clim. Chang. [Solomon, S., D. Qin, M. Manning, Z. Chen, M. Marquis, K.B. Averyt, M.Tignor H.L. Mill. , Cambridge University Press, Cambridge, United Kingdom and New York, NY, USA., 2007: p. 996. https://www.ipcc.ch/site/assets/uploads/2018/02/ar4-wg1-chapter2-1.pdf.

[21] M. Holweg, The Evolution of Competition in the Automotive Industry, in: G. Parry, A. Graves (Eds.), Build To Order Road to 5-Day Car, Springer London, London, 2008: pp. 13–34. https://doi.org/10.1007/978-1-84800-225-8_2.

[22] C.R. Ferguson, A.T. Kirkpatrick, Internal Combustion Engines: Applied Thermosciences, Third, Wiley, 2015. https://books.google.co.uk/books?id=9rLLCQAAQBAJ.

[23] P. (ICCT E. Mock, European Vehicle Market Statistics, Pocketbook 2019/20, (2019) 105.

https://de.statista.com/download/MTYwNDE0MDMwNyMjMTA0NzI1IyM2OTY5OCMjMSMjbnVsbCMjU3R1ZHk=.

[24] C. Brand, Beyond 'Dieselgate': Implications of unaccounted and future air pollutant emissions and energy use for cars in the United Kingdom, Energy Policy. 97 (2016) 1–12. https://doi.org/10.1016/j.enpol.2016.06.036.

[25] European Commission, New and improved car emissions tests become mandatory on 1 September, (2017) 1–7. https://ec.europa.eu/commission/news/new-and-improved-car-emissions-tests-become-mandatory-1-september-2017-aug-31-0_en.

[26] K. Engeljehringer, Emission Regulation Trends, in: AVL Emiss. TechDay 2018, Mattsee, Osterr., 2018. https://www.avl.com/documents/10138/8665616/02+AVL+India+Seminar+May+2018_Regulation+Trends_Engeljehringer.pdf.

[27] European Commission, E. Commission, Reducing CO2 emissions from heavy-duty vehicles, (2019). https://ec.europa.eu/clima/policies/transport/vehicles/heavy_en (accessed July 23, 2019).

[28] R. Kawamoto, H. Mochizuki, Y. Moriguchi, T. Nakano, M. Motohashi, Y. Sakai, A. Inaba, Estimation of CO2 Emissions of internal combustion engine vehicle and battery electric vehicle using LCA, Sustain. 11 (2019). https://doi.org/10.3390/su11092690.

[29] ACEA, Vehicles in use Europe 2019, 2019. https://www.acea.be/uploads/statistic_documents/ACEA_Report_Vehicles_in_use-Europe_2017.pdf.

[30] P. Atkins, G. Milton, A. Atkins, R. Morgan, A Local Ecosystem Assessment of the Potential for Net Negative Heavy-Duty Truck Greenhouse Gas Emissions through Biomethane Upcycling, Energies. 14 (2021) 806. https://doi.org/10.3390/en14040806.

[31] E. Emilsson, L. Dahllöf, Lithium-Ion Vehicle Battery Production, C444, IVL Swedish Environmental Research Institute, 2019. https://www.ivl.se/download/18.14d7b12e16e3c5c36271070/1574923989017/C444.pdf.

[32] Q. Dai, J.C. Kelly, L. Gaines, M. Wang, Life cycle analysis of lithium-ion batteries for automotive applications, Batteries. 5 (2019). https://doi.org/10.3390/batteries5020048.

[33] J.C. Kelly, Q. Dai, M. Wang, Globally regional life cycle analysis of automotive lithium-ion nickel manganese cobalt batteries, Mitig. Adapt. Strateg. Glob. Chang. (2019) 371–396. https://doi.org/10.1007/s11027-019-09869-2.

[34] S. Wolff, M. Seidenfus, K. Gordon, S. Álvarez, S. Kalt, M. Lienkamp, Scalable life-cycle inventory for heavy-duty vehicle production, Sustain. 12 (2020). https://doi.org/10.3390/su12135396.

[35] R. Edwards, L. Jean-Francois, R. David, W. Weindorf, G. Simon, H. Hass, A. Krasenbrink, L. Lonza, H. Maas, R. Nelson, A. Reid, K.D. Rose, H. Hamje, WELL-TO-TANK Report version 4.a: JEC WELL-TO-WHEELS ANALYSIS, Publications Office of the European Union, Luxembourg (Luxembourg), 2014. https://doi.org/10.2790/95629.

[36] Royal Society, Options for producing low-carbon hydrogen at scale, 2018.

https://royalsociety.org/-/media/policy/projects/hydrogen-production/energy-briefing-green-hydrogen.pdf.

[37] E. Bianco, H. Blanco, R. Ferroukhi, Green Hydrogen, IRENA, Abu DHabi, 2016. https://www.irena.org/-/media/Files/IRENA/Agency/Publication/2020/Nov/IRENA_Green_hydrogen_policy_2020.pdf.

[38] D.T. Ainalis, C. Thorne, D. Cebon, White Paper Decarbonising the UK 's Long-Haul Road Freight at Minimum Economic Cost, 2020. http://www.csrf.ac.uk/2020/07/white-paper-long-haul-freight-electrification/%0Ahttp://www.csrf.ac.uk/wp-content/uploads/2020/07/SRF-WP-UKEMS-v2.pdf.

[39] C.S. and A.B. (E4tech). Nikolas Hill, Sofia Amaral, Samantha Morgan- Price, Tom Nokes, Judith Bates (Ricardo Energy & Environment), Hinrich Helms, Horst Fehrenbach, Kirsten Biemann, Nabil Abdalla, Julius Jöhrens (ifeu), Eloise Cotton, Lizzie German, Anisha Harris, Sebastien Haye, Determining the environmental impacts of conventional and alternatively fuelled vehicles through LCA - Interim Report, 2020. https://doi.org/10.2834/91418.

[40] M. Kane, Germany: A5 Autobahn Gets Catenary Overhead Lines For xEV Trucks, (2020). https://insideevs.com/news/440388/germany-a5-autobahn-catenary-overhead-lines-trucks/ (accessed November 13, 2020).

[41] BP Energy Economics, BP Energy Outlook: 2019 Edition, 2019. https://www.bp.com/content/dam/bp/business-sites/en/global/corporate/pdfs/energy-economics/energy-outlook/bp-energy-outlook-2019.pdf (accessed June 25, 2019).

[42] EPA, An Overview Of Renewable Natural Gas from Biogas, EPA, 2020. https://www.epa.gov/sites/default/files/2020-07/documents/lmop_rng_document.pdf.

[43] S. Mokhatab, W.A. Poe, J.Y. Mak, Handbook of Natural Gas Transmission and Processing, 2015. https://doi.org/10.1016/B978-0-12-801499-8.00002-X.

[44] T.L. Alleman, R.L. McCormick, E.D. Christensen, G. Fioroni, K. Moriarty, J. Yanowitz, Biodiesel handling and use guide, 2016. https://afdc.energy.gov/files/u/publication/biodiesel_handling_use_guide.pdf.

[45] J.B. Heywood, Internal Combustion Engine Fundamentals, 2nd Editio, McGraw-Hill Education, New York, 2018.

[46] U. Leiker, M., Christoph, K., Rankl, M., Cartellieri, W., and Pfeifer, The Evaluation of the Antiknocking Property of Gaseous Fuels by means of the Methane Number and its Practical Application to Gas Engines, in: 9th Int. Congr. Combust. Engines, Stockholm, Sweden, 1971.

[47] D.G. Van Alstine, D.T. Montgomery, T.J. Callahan, R.C. Florea, Ability of the Methane Number Index of a Fuel to Predict Rapid Combustion in Heavy Duty Dual Fuel Engines for North American Locomotives, (2015). https://doi.org/10.1115/ICEF2015-1119.

[48] Euromot, Methane Number Calculation (MWM Method), (2019). https://www.euromot.eu/wp-content/uploads/2019/07/MWM-MN-Code-for-

distribution-2016-04-22.zip (accessed February 7, 2021).

[49] ISO, ISO/TR 22302:2014(en) Natural gas — Calculation of methane number, 2014.

[50] Cummins-Westport, Fuel Quality Calculator, (n.d.). https://www.cumminswestport.com/fuel-quality-calculator (accessed March 2, 2021).

[51] Caterpillar, CAT Methane Number Calculator, (n.d.). https://www.cat.com/en_US/articles/solutions/oil-gas/Cat-Methane-Number-Calculator.html (accessed March 2, 2021).

[52] Wartsila, Wärtsilä Methane Number Calculator, (n.d.). https://www.wartsila.com/marine/build/gas-solutions/methane-number-calculator (accessed March 1, 2021).

[53] International Group of Liquefied Natural Gas Importers (GIIGNL), Position paper on the impact of including methane number in natural gas regulation, 2015. https://giignl.org/publications/position-paper-impact-including-methane-number-natural-gas-regulation.

[54] International Group of Liquefied Natural Gas Importers (GIIGNL), GIIGNL Annual Report 2018, 2018. https://giignl.org/sites/default/files/PUBLIC_AREA/Publications/rapportannuel-2018pdf.pdf.

[55] M. Lambert, Biogas: A significant contribution to decarbonising gas markets?, Oxford, 2017. https://www.oxfordenergy.org/wpcms/wp-content/uploads/2017/06/Biogas-A-significant-contribution-to-decarbonising-gas-markets.pdf.

[56] IRENA, Technology Brief: Biogas for Road Vehicles, 2018. https://www.irena.org/publications/2017/Mar/Biogas-for-road-vehicles-Technology-brief.

[57] H.M. Cho, B.-Q. He, Combustion and emission characteristics of a lean burn natural gas engine, Int. J. Automot. Technol. 9 (2008) 415–422. https://doi.org/10.1007/s12239-008-0050-5.

[58] P. Lott, O. Deutschmann, Lean-Burn Natural Gas Engines: Challenges and Concepts for an Efficient Exhaust Gas Aftertreatment System, Emiss. Control Sci. Technol. (2020) 1–6. https://doi.org/10.1007/s40825-020-00176-w.

[59] Y. Dong, C.M. Vagelopoulos, G.R. Spedding, F.N. Egolfopoulos, Measurement of laminar flame speeds through digital particle image velocimetry: Mixtures of methane and ethane with hydrogen, oxygen, nitrogen, and helium, Proc. Combust. Inst. 29 (2002) 1419–1426. https://doi.org/10.1016/S1540-7489(02)80174-2.

[60] E. Toulson, H.J. Schock, W.P. Attard, A Review of Pre-Chamber Initiated Jet Ignition Combustion Systems, in: SAE 2010 Powertrains Fuels Lubr. Meet., SAE International, 2010. https://doi.org/https://doi.org/10.4271/2010-01-2263.

[61] M.A. V Ward, High-Energy Spark-Flow Coupling in an IC Engine for Ultra-Lean and High EGR Mixtures, in: SAE 2001 World Congr., SAE International, 2001. https://doi.org/https://doi.org/10.4271/2001-01-0548.

[62] X. Yu, X. Zhang, T. Zhang, G. Chen, J. Tjong, M. Zheng, Combustion Stability

Improvement via Multiple Ignition Sites on a Production Engine, in: WCX SAE World Congr. Exp., SAE International, 2020. https://doi.org/https://doi.org/10.4271/2020-01-1115.

[63] B. Almansour, S. Vasu, S.B. Gupta, Q. Wang, R. Van Leeuwen, C. Ghosh, Performance of a Laser Ignited Multicylinder Lean Burn Natural Gas Engine, J. Eng. Gas Turbines Power. 139 (2017) 1–7. https://doi.org/10.1115/1.4036621.

[64] H. Zhu, X. Yu, L. Liang, M. Zheng, G. Reader, Investigation of multi-event spark discharge strategy for lean methane-air combustion, Proc. Inst. Mech. Eng. Part D J. Automob. Eng. (2021) 1–18. https://doi.org/10.1177/0954407020984599.

[65] W.P. Attard, E. Toulson, A. Huisjen, X. Chen, G. Zhu, H. Schock, Spark Ignition and Pre-Chamber Turbulent Jet Ignition Combustion Visualization, in: SAE 2012 World Congr. Exhib., SAE International, 2012. https://doi.org/https://doi.org/10.4271/2012-01-0823.

[66] Z.H. Kyaw, H.C. Watson, Hydrogen assisted jet ignition for near elimination of NOx and cyclic variability in the S.I. Engine, Symp. Combust. 24 (1992) 1449–1455. https://doi.org/https://doi.org/10.1016/S0082-0784(06)80169-4.

[67] M. Bunce, H. Blaxill, William Attard, Turbulent jet ignition pre-chamber combustion system for spark ignition engines, US 9,353,674 B2, 2016. https://patents.google.com/patent/US8857405B2/en.

[68] N. Peters, M. Bunce, H. Blaxill, The Impact of Engine Displacement on Efficiency Loss Pathways in a Highly Dilute Jet Ignition Engine, in: WCX SAE World Congr. Exp., SAE International, 2019. https://doi.org/https://doi.org/10.4271/2019-01-0330.

[69] P. Soltic, T. Hilfiker, S. Hänggi, Efficient light-duty engine using turbulent jet ignition of lean methane mixtures, Int. J. Engine Res. 0 (2019) 146808741988983. https://doi.org/10.1177/1468087419889833.

[70] A. Cooper, A. Harrington, M. Bassett, S. Reader, M. Bunce, Application of the Passive MAHLE Jet Ignition System and Synergies with Miller Cycle and Exhaust Gas Recirculation, in: WCX SAE World Congr. Exp., SAE International, 2020. https://doi.org/https://doi.org/10.4271/2020-01-0283.

[71] N. Peters, S.K.P. Subramanyam, M. Bunce, H. Blaxill, Optimization of the Mechanical and Thermodynamic Efficiency Loss Dynamic in a Lean Single Cylinder Natural Gas-Fueled Jet Ignition Engine, (2019). https://doi.org/10.1115/ICEF2019-7213.

[72] N. Peters, S.K.P. Subramanyam, M. Bunce, H. Blaxill, S. Krishna, P. Subramanyam, M. Bunce, H. Blaxill, Optimization of The Mechanical and Thermodynamic Efficiency Loss Dynamic in A Lean Single Cylinder Natural Gas-Fueled Jet Ignition Engine, in: Proc. ASME 2019 Intern. Combust. Engine Div. Fall Tech. Conf., 2019: pp. 1–8. https://doi.org/10.1115/ICEF2019-7213.

[73] A. Shah, Improving the Efficiency of Gas Engines using Pre-chamber Ignition, Lund University, 2015. https://portal.research.lu.se/portal/files/3706218/8228492.pdf (accessed March 13, 2019).

[74] J.E. Dec, A Conceptual Model of DI Diesel Combustion Based on Laser-Sheet Imaging*, in: Int. Congr. Expo., SAE International, 1997. https://doi.org/https://doi.org/10.4271/970873.

[75] A. Velji, M. Ĺüft, S. Merkel, Mixture formation, combustion and pollutant emissions

in high-speed direct-injection diesel engines, Adv. Direct Inject. Combust. Engine Technol. Dev. (2010) 105–154. https://doi.org/10.1533/9781845697457.1.105.

[76] M.P.B. Musculus, Measurements of the Influence of Soot Radiation on In-Cylinder Temperatures and Exhaust NOx in a Heavy-Duty DI Diesel Engine, in: SAE 2005 World Congr. Exhib., SAE International, 2005. https://doi.org/https://doi.org/10.4271/2005-01-0925.

[77] K.B. Binder, Diesel Engine Combustion BT - Handbook of Diesel Engines, in: K. Mollenhauer, H. Tschöke (Eds.), Springer Berlin Heidelberg, Berlin, Heidelberg, 2010: pp. 61–75. https://doi.org/10.1007/978-3-540-89083-6_3.

[78] K. Akihama, Y. Takatori, K. Inagaki, S. Sasaki, A.M. Dean, Mechanism of the Smokeless Rich Diesel Combustion by Reducing Temperature, in: SAE 2001 World Congr., SAE International, 2001. https://doi.org/https://doi.org/10.4271/2001-01-0655.

[79] T. Kitamura, T. Ito, J. Senda, H. Fujimoto, Mechanism of smokeless diesel combustion with oxygenated fuels based on the dependence of the equivalence ration and temperature on soot particle formation, Int. J. Engine Res. 3 (2002) 223–248. https://doi.org/10.1243/146808702762230923.

[80] G.D. Neely, S. Sasaki, Y. Huang, J.A. Leet, D.W. Stewart, New Diesel Emission Control Strategy to Meet US Tier 2 Emissions Regulations, in: SAE 2005 World Congr. Exhib., SAE International, 2005. https://doi.org/https://doi.org/10.4271/2005-01-1091.

[81] K. Ohsawa, T. Kamimoto, Advanced Diesel Combustion, in: C. Arcoumanis, T. Kamimoto (Eds.), Flow Combust. Reciprocating Engines, Springer Berlin Heidelberg, Berlin, Heidelberg, 2009: pp. 353–380. https://doi.org/10.1007/978-3-540-68901-0_7.

[82] S.L. Kokjohn, R.M. Hanson, D.A. Splitter, R.D. Reitz, Fuel reactivity controlled compression ignition (RCCI): A pathway to controlled high-efficiency clean combustion, Int. J. Engine Res. 12 (2011) 209–226. https://doi.org/10.1177/1468087411401548.

[83] R.D. Reitz, G. Duraisamy, Review of high efficiency and clean reactivity controlled compression ignition (RCCI) combustion in internal combustion engines, Prog. Energy Combust. Sci. 46 (2015) 12–71. https://doi.org/10.1016/j.pecs.2014.05.003.

[84] J. Speirs, P. Balcombe, P. Blomerus, M. Stettler, P. Achurra-Gonzalez, M. Woo, D. Ainalis, J. Cooper, A. Sharafian, W. Merida, D. Crow, S. Giarola, N. Shah, N. Brandon, A. Hawkes, Natural gas fuel and greenhouse gas emissions in trucks and ships, Prog. Energy. 2 (2020) 012002. https://doi.org/10.1088/2516-1083/ab56af.

[85] N. Dronniou, J. Kashdan, B. Lecointe, K. Sauve, D. Soleri, Optical Investigation of Dual-fuel CNG/Diesel Combustion Strategies to Reduce CO 2 Emissions, SAE Int. J. Engines. 7 (2014) 2014-01–1313. https://doi.org/10.4271/2014-01-1313.

[86] K. Nithyanandan, Y. Gao, H. Wu, C.-F. Lee, F. Liu, J. Yan, An Optical Investigation of Multiple Diesel Injections in CNG/Diesel Dual-Fuel Combustion in a Light Duty Optical Diesel Engine, SAE Tech. Pap. 2017-March (2017). https://doi.org/10.4271/2017-01-0755.

[87] G. McTaggart-Cowan, K. Mann, J. Huang, A. Singh, B. Patychuk, Z.X. Zheng, S. Munshi, Direct Injection of Natural Gas at up to 600 Bar in a Pilot-Ignited Heavy-

Duty Engine, SAE Int. J. Engines. 8 (2015) 2015-01–0865. https://doi.org/10.4271/2015-01-0865.

[88] Volvo, Fact sheet Engine G13C420, EU6SCR, 035 (2019) 1–3. https://stpi.it.volvo.com/STPIFiles/Volvo/FactSheet/G13C420, EU6SCR_Eng_01_309253875.pdf.

[89] R. Vermeulen, Emissions testing of a Euro VI LNG-diesel dual fuel truck in the Netherlands, 2019. https://publications.tno.nl/publication/34633965/pl7KqC/TNO-2019-R10193.pdf.

[90] P. Fasching, F. Sprenger, H. Eichlseder, Experimental Optimization of a Small Bore Natural Gas-Diesel Dual Fuel Engine with Direct Fuel Injection, SAE Int. J. Engines. 9 (2016) 2016-01–0783. https://doi.org/10.4271/2016-01-0783.

[91] F. Sprenger, P. Fasching, C. Granitz, H. Eichlseder, New Dual-fuel Combustion Process for Passenger Car Engines, MTZ Worldw. 79 (2018) 60–67. https://doi.org/10.1007/s38313-018-0037-1.

[92] A. Kikusato, H. Fukasawa, K. Nomura, J. Kusaka, Y. Daisho, A Study on the Characteristics of Natural Gas Combustion at a High Compression Ratio by Using a Rapid Compression and Expansion Machine, (2012). https://doi.org/https://doi.org/10.4271/2012-01-1651.

[93] S. Schlatter, B. Schneider, Y.M. Wright, K. Boulouchos, Comparative Study of Ignition Systems for Lean Burn Gas Engines in an Optically Accessible Rapid Compression Expansion Machine, in: 11th Int. Conf. Engines Veh., SAE International, 2013. https://doi.org/https://doi.org/10.4271/2013-24-0112.

[94] Z. Liu, G.A. Karim, An Examination of the Ignition Delay Period in Gas-Fueled Diesel Engines, J. Eng. Gas Turbines Power. 120 (1998) 225–231. http://dx.doi.org/10.1115/1.2818080.

[95] M.S. Lounici, M.A. Benbellil, K. Loubar, D.C. Niculescu, M. Tazerout, Knock characterization and development of a new knock indicator for dual-fuel engines, Energy. 141 (2017) 2351–2361. https://doi.org/10.1016/j.energy.2017.11.138.

[96] M. Kirsten, G. Pirker, C. Redtenbacher, A. Wimmer, F. Chmela, Advanced Knock Detection for Diesel/Natural Gas Engine Operation, (2016). https://doi.org/https://doi.org/10.4271/2016-01-0785.

[97] G. Anderson, Characterization of abnormal dual-fuel combustion, in: W. Siebenpfeiffer (Ed.), Heavy-Duty-, On- Und Off-Highway-Motoren 2017, Springer Fachmedien Wiesbaden, Wiesbaden, 2018: pp. 79–98.

[98] S. Weber, R. Stegmann, M. Prager, G. Wachtmeister, The Effect of Inlet Valve Timing and Engine Speed on Dual Fuel NG-Diesel Combustion in a Large Bore Engine, SAE Int. J. Engines. 11 (2018) 229–246.

[99] M.E.J. Stettler, W.J.B. Midgley, J.J. Swanson, D. Cebon, A.M. Boies, Greenhouse Gas and Noxious Emissions from Dual Fuel Diesel and Natural Gas Heavy Goods Vehicles, Environ. Sci. Technol. 50 (2016) 2018–2026. https://doi.org/10.1021/acs.est.5b04240.

[100] J. Norris, C. Brannigan, B. White, A. Demurtas, A. Sale, I. Dawson, Provision of HGV Emissions Testing, Final Report, Report for Department for Transport, 2015. https://assets.publishing.service.gov.uk/government/uploads/system/uploads/attac

hment_data/file/468172/hgv-emissions-testing.pdf.

[101] J. Liu, F. Yang, H. Wang, M. Ouyang, S. Hao, Effects of pilot fuel quantity on the emissions characteristics of a CNG/diesel dual fuel engine with optimized pilot injection timing, Appl. Energy. 110 (2013) 201–206. https://doi.org/10.1016/j.apenergy.2013.03.024.

[102] J.M.S. Mattson, C. Langness, C. Depcik, An Analysis of Dual-Fuel Combustion of Diesel with Compressed Natural Gas in a Single-Cylinder Engine, in: WCX World Congr. Exp., SAE International, 2018. https://doi.org/https://doi.org/10.4271/2018-01-0248.

[103] H. Park, E. Shim, C. Bae, Improvement of combustion and emissions with exhaust gas recirculation in a natural gas-diesel dual-fuel premixed charge compression ignition engine at low load operations, Fuel. 235 (2019) 763–774. https://doi.org/10.1016/j.fuel.2018.08.045.

[104] United Nations, UNECE Regulation 49, Revision 7. Uniform provisions concerning the measures to be taken against the emission of gaseous and particulate pollutants from compression-ignition engines and positive ignition engines for use in vehicles., 2015. http://www.unece.org/trans/main/wp29/wp29wgs/wp29grpe/grpeinf71.html (accessed August 19, 2018).

[105] I. May, V. Pedrozo, H. Zhao, A. Cairns, S. Whelan, H. Wong, P. Bennicke, Characterization and Potential of Premixed Dual-Fuel Combustion in a Heavy Duty Natural Gas/Diesel Engine, in: SAE 2016 World Congr. Exhib., SAE International, 2016. https://doi.org/https://doi.org/10.4271/2016-01-0790.

[106] I.A. May, An experimental investigation of lean-burn dual-fuel combustion in a heavy duty diesel engine, Brunel University London, 2018. http://bura.brunel.ac.uk/handle/2438/16398.

[107] E. Shim, H. Park, C. Bae, Intake air strategy for low HC and CO emissions in dual-fuel (CNG-diesel) premixed charge compression ignition engine, Appl. Energy. 225 (2018) 1068–1077. https://doi.org/10.1016/j.apenergy.2018.05.060.

[108] H. Park, E. Shim, C. Bae, Injection Strategy in Natural Gas–Diesel Dual-Fuel Premixed Charge Compression Ignition Combustion under Low Load Conditions, Engineering. 5 (2019) 548–557. https://doi.org/10.1016/j.eng.2019.03.005.

[109] A. Yousefi, H. Guo, M. Birouk, An experimental and numerical study on diesel injection split of a natural gas/diesel dual-fuel engine at a low engine load, Fuel. 212 (2018) 332–346. https://doi.org/10.1016/j.fuel.2017.10.053.

[110] F. Königsson, Advancing the Limits of Dual Fuel Combustion, 2012.

[111] P. Garcia Valladolid, P. Tunestal, Effects of Intake Manifold Conditions on Dual-Fuel CNG-Diesel Combustion in a Light Duty Diesel Engine Operated at Low Loads, in: SAE 2016 World Congr. Exhib., SAE International, 2016. https://doi.org/https://doi.org/10.4271/2016-01-0805.

[112] R. Miller, High Expansion, Spark Ignited, Gas Burning, Internal Combustion Engines, USA Patent 2,773,490, 11 December 1956, 1956. https://patentimages.storage.googleapis.com/5b/03/cc/c65bb7001db064/US2773490.pdf.

[113] H. Song, C. Liu, Y. Li, Z. Wang, L. Chen, X. He, J. Wang, An exploration of utilizing low-pressure diesel injection for natural gas dual-fuel low-temperature combustion, Energy. 153 (2018) 248–255. https://doi.org/10.1016/j.energy.2018.04.041.

[114] S. Dev, H. Guo, S. Lafrance, B. Liko, An Experimental Study on the Effect of Exhaust Gas Recirculation on a Natural Gas-Diesel Dual-Fuel Engine, in: WCX SAE World Congr. Exp., SAE International, 2020. https://doi.org/https://doi.org/10.4271/2020-01-0310.

[115] J. Konrad, T. Lauer, M. Moser, E. Lockner, J. Zhu, Engine Efficiency Optimization under Consideration of NOX- and Knock-Limits for Medium Speed Dual Fuel Engines in Cylinder Cut-Out Operation, in: WCX World Congr. Exp., SAE International, 2018. https://doi.org/https://doi.org/10.4271/2018-01-1151.

[116] W.F. Oy, Wärtsilä 34DF, Product Guide, 2020. https://cdn.wartsila.com/docs/default-source/product-files/engines/df-engine/product-guide-o-e-w34df.pdf?sfvrsn6.

[117] D.E. Sommer, M. Yeremi, J. Son, J.C. Corbin, S. Gagné, P. Lobo, J.W. Miller, P. Kirchen, Characterization and Reduction of In-Use CH 4 Emissions from a Dual Fuel Marine Engine Using Wavelength Modulation Spectroscopy, Environ. Sci. Technol. 53 (2019) 2892–2899. https://doi.org/10.1021/acs.est.8b04244.

[118] M. McGhee, Z. Wang, A. Bech, P.J. Shayler, D. Witt, The effects of cylinder deactivation on the thermal behaviour and fuel economy of a three-cylinder direct injection spark ignition gasoline engine, Proc. Inst. Mech. Eng. Part D J. Automob. Eng. 233 (2019) 2838–2849. https://doi.org/10.1177/0954407018806744.

[119] A. Grob, C. Brinkmann, J. Königstedt, The new Audi 4.0-L V8 TFSI engine. Part 2: Thermodynamics and Calibration, MTZ Worldw. 74 (2013) 34–39. https://doi.org/10.1007/s38313-013-0028-1.

[120] K. Küpper, J. Linsel, B. Pingen, C. Weber, Cylinder Deactivation for Three-cylinder Engines, MTZ Worldw. 77 (2016) 46–51. https://doi.org/10.1007/s38313-016-0132-0.

[121] K.R. Vos, G.M. Shaver, A.K. Ramesh, J. McCarthy, Impact of Cylinder Deactivation and Cylinder Cutout via Flexible Valve Actuation on Fuel Efficient Aftertreatment Thermal Management at Curb Idle, Front. Mech. Eng. 5 (2019) 52. https://www.frontiersin.org/article/10.3389/fmech.2019.00052.

[122] A.K. Ramesh, D.B. Gosala, C. Allen, M. Joshi, J. McCarthy Jr, L. Farrell, E.D. Koeberlein, G. Shaver, Cylinder Deactivation for Increased Engine Efficiency and Aftertreatment Thermal Management in Diesel Engines, in: WCX World Congr. Exp., SAE International, 2018. https://doi.org/https://doi.org/10.4271/2018-01-0384.

[123] A. Archer, J. McCarthy Jr, Quantification of Diesel Engine Vibration Using Cylinder Deactivation for Exhaust Temperature Management and Recipe for Implementation in Commercial Vehicles, (2018). https://doi.org/https://doi.org/10.4271/2018-01-1284.

[124] P. Tanev, M. Soorholtz, Methane Oxidation Catalyst, Process to Prepare the Same and Method Of Using the Same, WO 2016/139283 Al, 2016. https://patentimages.storage.googleapis.com/55/04/ca/454acedcacfe38/WO2016139283A1.pdf.

[125] D.J. Worth, M.E.J. Stettler, P. Dickinson, K. Hegarty, A.M. Boies, Characterization and Evaluation of Methane Oxidation Catalysts for Dual-Fuel Diesel and Natural Gas Engines, Emiss. Control Sci. Technol. 2 (2016) 204–214. https://doi.org/10.1007/s40825-016-0047-x.

[126] R. Gholami, M. Alyani, K. Smith, Deactivation of Pd Catalysts by Water during Low Temperature Methane Oxidation Relevant to Natural Gas Vehicle Converters, 2015. https://doi.org/10.3390/catal5020561.

[127] P. Gélin, L. Urfels, M. Primet, E. Tena, Complete oxidation of methane at low temperature over Pt and Pd catalysts for the abatement of lean-burn natural gas fuelled vehicles emissions: Influence of water and sulphur containing compounds, Catal. Today. 83 (2003) 45–57. https://doi.org/10.1016/S0920-5861(03)00215-3.

[128] R. Kikuchi, S. Maeda, K. Sasaki, S. Wennerström, K. Eguchi, Low-temperature methane oxidation over oxide-supported Pd catalysts: Inhibitory effect of water vapor, Appl. Catal. A Gen. 232 (2002) 23–28. https://doi.org/10.1016/S0926-860X(02)00096-0.

[129] Y. Zhang, P. Glarborg, K. Johansen, M.P. Andersson, T.K. Torp, A.D. Jensen, J.M. Christensen, A Rhodium-Based Methane Oxidation Catalyst with High Tolerance to H2O and SO2, ACS Catal. 10 (2020) 1821–1827. https://doi.org/10.1021/acscatal.9b04464.

[130] I. May, A. Cairns, H. Zhao, H.C. Wong, S. Whelan, P. Bennicke, The Development of Low-Carbon Combustion Systems for Heavy-Duty Dual-Fuel Engines, in: Futur. Powertrain Conf. 2016, 2016. https://futurepowertrains.co.uk/wp-content/uploads/2016/01/Future-Powertrain-Conference-2016-Vayon-Brunel.pdf.

[131] A.H.I. Hegab, Combustion Characteristics of Methane-Diesel Dual-Fuel Engines at Light Load Conditions with Different Injection Strategies, University of Nottingham, 2017.

[132] M.J. McGhee, N. Sully, Clean Air Power CNG Supply System Operational Instruction, 2018.

[133] Micro Motion, Product Data Sheet PS-00374, Rev AF, Micro Motion ® ELITE ® Coriolis Flow and Density Meters, (2018).

[134] T.L. Alleman, L. Eudy, M. Miyasato, A. Oshinuga, S. Allison, T. Corcoran, S. Chatterjee, T. Jacobs, R.A. Cherrillo, R. Clark, I. Virrels, R. Nine, S. Wayne, R. Lansing, Fuel Property, Emission Test, and Operability Results from a Fleet of Class 6 Vehicles Operating on Gas-To-Liquid Fuel and Catalyzed Diesel Particle Filters, in: 2004 Powertrain Fluid Syst. Conf. Exhib., SAE International, 2004. https://doi.org/https://doi.org/10.4271/2004-01-2959.

[135] Shell, Knowledge Guide - Shell GTL Fuel Synthetic Technology for Cleaner Air, (2016). https://www.shell.com/business-customers/commercial-fuels/shell-gtl-fuel/technical-information/_jcr_content/par/relatedtopics.stream/1496056917944/5bbe2047ad53280f54ce84ba3f824c68ef8be723/shell-gtl-fuel-knowledge-guide-en.pdf (accessed June 30, 2018).

[136] Z. Hua, N. Ladommatos, Engine Combustion Instrumentation and Diagnostics, Society of Automotive Engineers, 2001.

[137] U. Nations, UNECE Regulation No. 49, Revision 6. Uniform provisions concerning the measures to be taken against the emission of gaseous and particulate pollutants from compression-ignition engines and positive ignition engines for use in vehicles., 2013. https://www.unece.org/fileadmin/DAM/trans/main/wp29/wp29regs/2013/R049r6e.pdf.

[138] M. Adachi, H. Nakamura, Engine Emissions Measurement Handbook, SAE International and Horiba Ltd., 2013.

[139] MAHLE, Flow Test Results RHAC - Volvo Duet Diesel Inline 6, Northampton, UK, n.d.

[140] Aeristech, Aeristech Electric Superchargers, (n.d.). https://www.aeristech.co.uk/electric-supercharger/ (accessed October 4, 2019).

[141] Ashwoods, IPM-L50, (2019). https://ashwoodselectricmotors.com/wp-content/uploads/2017/12/IPM-L50.pdf (accessed September 18, 2019).

[142] J. Sohn, M. Sunwoo, K. Min, J. Shin, M. Han, POWER MANAGEMENT STRATEGY FOR THE 48 V MILD HYBRID ELECTRIC VEHICLE BASED ON THE CHARGE-SUSTAINING CONTROL, Int. J. Automot. Technol. 20 (2019) 37–49. https://doi.org/10.1007/s12239−019−0004−0.

[143] Gamma Technologies, GT Suite Help, (2020).

[144] R. Payri, F.J. Salvador, P. Martí-Aldaraví, J. Martínez-López, Using one-dimensional modeling to analyse the influence of the use of biodiesels on the dynamic behavior of solenoid-operated injectors in common rail systems: Detailed injection system model, Energy Convers. Manag. 54 (2012) 90–99. https://doi.org/10.1016/j.enconman.2011.10.004.

[145] G. Woschni, A universally applicable equation for the instantaneous heat transfer coefficient in the internal combustion engine, SAE Tech. Pap. 76 (1967) 3065–3083. https://doi.org/10.4271/670931.

[146] S.K. Chen, P.F. Flynn, Development of a single cylinder compression ignition research engine, SAE Tech. Pap. (1965). https://doi.org/10.4271/650733.

[147] Gamma Technologies, Engine Performance Manual 2019, Westmont, Illinois, 2019.

[148] R. Amirante, E. Distaso, P. Tamburrano, R.D. Reitz, Laminar flame speed correlations for methane, ethane, propane and their mixtures, and natural gas and gasoline for spark-ignition engine simulations, Int. J. Engine Res. 18 (2017) 951–970. https://doi.org/10.1177/1468087417720018.

[149] S. Tüchler, P. Dimitriou, On the capabilities and limitations of predictive, multi-zone combustion models for hydrogen-diesel dual fuel operation, Int. J. Hydrogen Energy. 44 (2019) 18517–18531. https://doi.org/10.1016/j.ijhydene.2019.05.172.

[150] A. Hockett, G. Hampson, A.J. Marchese, Development and Validation of a Reduced Chemical Kinetic Mechanism for Computational Fluid Dynamics Simulations of Natural Gas / Diesel Dual-Fuel Engines, Energy & Fuels. (2016). https://doi.org/10.1021/acs.energyfuels.5b02655.

[151] H. An, W. Yang, J. Li, A. Maghbouli, K.J. Chua, S.K. Chou, A numerical modeling on the emission characteristics of a diesel engine fueled by diesel and biodiesel blend fuels, Appl. Energy. 130 (2014) 458–465.

https://doi.org/10.1016/j.apenergy.2014.01.004.

[152] Y. Li, G. Tian, J. Zhang, H. Xu, Comparative Experimental Study on Microscopic Spray Characteristics of RME, GTL and Diesel, in: SAE 2010 Powertrains Fuels Lubr. Meet., SAE International, 2010. https://doi.org/https://doi.org/10.4271/2010-01-2284.

[153] U. Azimov, K.-S. Kim, Visualization of Gas-to-Liquid (GTL) Fuel Liquid Length and Soot Formation in the Constant Volume Combustion Chamber*, J. Therm. Sci. Technol. 3 (2008). https://doi.org/10.1299/jtst.3.461.

[154] G.S. Forman, T.E. Hahn, S.D. Jensen, Greenhouse gas emission evaluation of the GTL pathway, Environ. Sci. Technol. 45 (2011) 9084–9092. https://doi.org/10.1021/es202101b.

[155] O.P.R. van Vliet, A.P.C. Faaij, W.C. Turkenburg, Fischer-Tropsch diesel production in a well-to-wheel perspective: A carbon, energy flow and cost analysis, Energy Convers. Manag. 50 (2009) 855–876. https://doi.org/10.1016/j.enconman.2009.01.008.

[156] C.M. Liu, N.K. Sandhu, S.T. McCoy, J.A. Bergerson, A life cycle assessment of greenhouse gas emissions from direct air capture and Fischer-Tropsch fuel production, Sustain. Energy Fuels. 4 (2020) 3129–3142. https://doi.org/10.1039/c9se00479c.

[157] J.P. Zammit, M.J. McGhee, P.J. Shayler, I. Pegg, The influence of cylinder deactivation on the emissions and fuel economy of a four-cylinder direct-injection diesel engine, Proc. Inst. Mech. Eng. Part D J. Automob. Eng. 228 (2014) 206–217. https://doi.org/10.1177/0954407013506182.

[158] Department for Business Energy and Industrial Strategies - UK, Digest of UK Energy Statistics (DUKES): calorific values and density of fuels, Natl. Stat. (2021). https://assets.publishing.service.gov.uk/government/uploads/system/uploads/attachment_data/file/1060149/DUKES_A.1-A.4.xls (accessed July 30, 2021).

[159] Q. Xu, M. Xu, D. Hung, S. Wu, X. Dong, H. Ochiai, Z. Zhao, C. Wang, K. Jin, Diesel Spray Characterization at Ultra-High Injection Pressure of DENSO 250 MPa Common Rail Fuel Injection System, in: WCX™ 17 SAE World Congr. Exp., SAE International, 2017. https://doi.org/https://doi.org/10.4271/2017-01-0821.

[160] M.K. Le, S. Kook, Injection Pressure Effects on the Flame Development in a Light-Duty Optical Diesel Engine, SAE Int. J. Engines. 8 (2015) 609–624. https://doi.org/https://doi.org/10.4271/2015-01-0791.

[161] Y. Kidoguchi, C. Yang, K. Miwa, Effects of Fuel Properties on Combustion and Emission Characteristics of a Direct-Injection Diesel Engine, in: CEC/SAE Spring Fuels Lubr. Meet. Expo., SAE International, 2000. https://doi.org/https://doi.org/10.4271/2000-01-1851.

[162] Y. AKASAKA, Y. SAKURAI, Effects of Fuel Properties on Exhaust Emission from DI Diesel Engine, JSME Int. J. Ser. B. 41 (1998) 13–18. https://doi.org/10.1299/jsmeb.41.13.

[163] G.K. Lilik, A.L. Boehman, Effects of fuel composition on critical equivalence ratio for autoignition, Energy and Fuels. 27 (2013) 1601–1612. https://doi.org/10.1021/ef3016014.

[164] DUKES, Dukes 2019, 2019.

https://assets.publishing.service.gov.uk/government/uploads/system/uploads/attachment_data/file/840015/DUKES_2019_MASTER_COPY.pdf.

[165] S. Saxena, I.D. Bedoya, Fundamental phenomena affecting low temperature combustion and HCCI engines, high load limits and strategies for extending these limits, Prog. Energy Combust. Sci. 39 (2013) 457–488. https://doi.org/10.1016/j.pecs.2013.05.002 Review.

[166] J.A. Caton, Comparisons of thermocouple, time-averaged and mass-averaged exhaust gas temperatures for a spark-ignited engine, SAE Tech. Pap. (1982) 20–22. https://doi.org/10.4271/820050.

[167] J. Chérel, J. Zaccardi, B. Bouteiller, A. Allimant, Experimental assessment of new insulation coatings for lean burn spark-ignited engines, Oil Gas Sci. Technol. – Rev. d'IFP Energies Nouv. 11 (2020). https://doi.org/https://doi.org/10.2516/ogst/2020006.

[168] Y. Wakisaka, M. Inayoshi, K. Fukui, H. Kosaka, Y. Hotta, A. Kawaguchi, N. Takada, Reduction of Heat Loss and Improvement of Thermal Efficiency by Application of "Temperature Swing" Insulation to Direct-Injection Diesel Engines, SAE Int. J. Engines. 9 (2016) 1449–1459. https://doi.org/https://doi.org/10.4271/2016-01-0661.

[169] A. Kawaguchi, H. Iguma, H. Yamashita, N. Takada, N. Nishikawa, C. Yamashita, Y. Wakisaka, K. Fukui, Thermo-Swing Wall Insulation Technology; - A Novel Heat Loss Reduction Approach on Engine Combustion Chamber -, in: SAE 2016 Int. Powertrains, Fuels Lubr. Meet., SAE International, 2016. https://doi.org/https://doi.org/10.4271/2016-01-2333.

[170] M. Andrie, S. Kokjohn, S. Paliwal, L.S. Kamo, A. Kamo, D. Procknow, Low Heat Capacitance Thermal Barrier Coatings for Internal Combustion Engines, in: WCX SAE World Congr. Exp., SAE International, 2019. https://doi.org/https://doi.org/10.4271/2019-01-0228.

[171] K.S. Reddy, V. Mudgal, T.K. Mallick, Review of latent heat thermal energy storage for improved material stability and effective load management, J. Energy Storage. 15 (2018) 205–227. https://doi.org/10.1016/j.est.2017.11.005.

[172] K. Pielichowska, K. Pielichowski, Phase change materials for thermal energy storage, Prog. Mater. Sci. 65 (2014) 67–123. https://doi.org/10.1016/j.pmatsci.2014.03.005.

[173] J. Radcliffe, Y. Li, Thermal energy storage in Scotland, Birmingham, 2014. https://www.climatexchange.org.uk/media/1393/thermal_energy_storage_in_scotland.pdf.

[174] M. Liu, N.H.S. Tay, M. Belusko, F. Bruno, Investigation of Cascaded Shell and Tube Latent Heat Storage Systems for Solar Tower Power Plants, Energy Procedia. 69 (2015) 913–924. https://doi.org/10.1016/J.EGYPRO.2015.03.175.

[175] ASHRAE, 2013 ASHRAE Handbook: Fundamentals, ASHRAE, Atlanta, GA, 2013.

[176] Vaisala, HUMIDITY CONVERSION FORMULAS Calculation formulas for humidity, 2013. www.vaisala.com (accessed August 19, 2018).

[177] W. Wagner, A. Pruß, The IAPWS formulation 1995 for the thermodynamic properties of ordinary water substance for general and scientific use, J. Phys. Chem. Ref. Data. 31 (2002) 387–535. https://doi.org/10.1063/1.1461829.

[178] M.J. Moran, Fundamentals of engineering thermodynamics / Michael J. Moran, Howard N. Shapiro., 5th ed., Hoboken, N.J. : John Wiley & Sons, Hoboken, N.J., 2004.

[179] NIST, Nitric oxide, (n.d.). https://webbook.nist.gov/cgi/cbook.cgi?ID=C10102439&Type=JANAFG&Plot=on#ref-1.

[180] F.A. Aly, L.L. Lee, Self-consistent equations for calculating the ideal gas heat capacity, enthalpy, and entropy, Fluid Phase Equilib. 6 (1981) 169–179. https://doi.org/10.1016/0378-3812(81)85002-9.